EPFL

Experimental Study on Bedload Transport and Bedforms: Behaviour and Interplay in Steep Turbulent Streams

Ivan PASCAL

2022

"N'aurèi pas pro de la mia vita,

N'aurèi pas pro de cent cançons,

Entà'us tornar ua petita

Part de çò qui m'an balhat, tots.

Que son los mens,

Drets sus la tèrra,

Que van tot doç suu caminau,

Lo camp laurat que huma encuèra,

Que son los mens, los de qui cau."

— de "Los de qui cau", Nadau

Alle persone care partite durante questi anni.

Acknowledgements

Les remerciements d'une thèse sont probablement la partie la plus difficile à écrire mais celle que l'on fait avec le plus de plaisir. D'abord, je veux remercier tous les membres du jury pour avoir pris le temps de lire le manuscrit, participer à la défense et donner leur avis critique sur ce travail. Vous avez rendu le jour de la défense un moment très enrichissant pour moi du point de vue scientifique mais aussi du point de vue humain. Merci François pour avoir accepté le rôle de président mais surtout pour m'avoir donné il y a 4 ans deux conseils qui ont été précieux aux cours de ces années. Merci Christophe pour m'avoir donné la possibilité d'entreprendre cette thèse au Laboratoire d'Hydraulique Environnementale (LHE), une voie pas équipée mais où l'on peut créer ses propres équipements, où le rocher est finalement beau même s'il ne faut pas avoir peur de jouer avec des graviers pour arriver au sommet et redescendre. Merci Alain pour les questions qui étaient à la fois des signes de curiosité et des conseils avisés. Grazie Riccardo del tempo dedicato, della tua competenza e della tua gentilezza. Spero di poter mettere in pratica i tuoi consigli e di trovare il tempo e il modo di collaborare nel futuro prossimo. Merci François pour tout le temps et l'énergie dépensés pour réviser ce manuscrit et me donner tes retours. Certains conseils n'ont pas pu être développés dans cette thèse mais j'espère de pouvoir le faire dans une continuation de ce parcours de recherche. Merci à Martina pour l'aide et la patience avec toutes les démarches administratives liées à l'EDME.

On arrive au LHE, ce bastion rocheux où j'ai débarqué en visite un jour de début mars entre la pluie et la neige. On y étudie les écoulements de toutes sortes de fluides et matériaux granulaires. J'ai fini par y entreprendre ce parcours d'observateur d'antidunes et compteur de cailloux. Ce laboratoire magique rassemble parfois aux mélanges de matériaux qu'on y étudie, un peu comme le gravier—composé de "pierrailles de toutes natures" (Surell, 1841). On y trouve Bob, ce brillant ingénieur avec qui on peut tout construire et réparer entre une rigolade

Acknowledgements

I want to thank the inspiring people I met at conferences and workshops. It would be too long and difficult to list you all. If you read these lines, well, you know that I owe you a beer.

A big "thank you" to all the people with whom I shared a rope, a hike, a running outing, a snow track or slope, a meat, a beer, or a sail across the Lake during these five years here in Switzerland. In more or less random order, Matteo, Cesco, Giovanni B., Johanne (encore), Marion, Olivier, Patrick, Blandine, Lorenzo, Tara, Yannick, Carrie, Seth, Charlotte, Aurélien, Romain M., Lara, Fabio, Silvia, Romain C., Ettore, Cecilia, Michele, Giulio, Corentin, Mateo, Barnaby, Jacques, Séverin, Oscar, Alberto, Gianluca, Alessandro, Candelaria, Laura, Claire, Sylwia, Mathieu, Steffen, Kevin, Andrea, Sara, Davide W., Giovanni D. C., Romain D., Christian, Antonio, Johan, Nicolas, Mélanie, Etienne, Arnaud et Bertil (toujours vous), Bruno, JB, Valentina, Laura, Tano, Luca, Fabrizio... *e chi più ne ha più ne metta.* I am probably forgetting someone in this paragraph, I apologise for that.

Grazie alle persone con le quali ho condiviso momenti importanti ai tempi degli studi al Politecnico. Un ringraziamento speciale per tutti gli insegnamenti, il tempo dedicato e i preziosi consigli al Prof. Adriano Fiorucci, al Prof. Luigi Sambuelli, al Prof. Luca Ridolfi, al Prof. Paolo Dabove e a Diego Franco. Un sentito ringraziamento a Paolo Perona per aver generosamente risposto alle mie domande ormai più di cinque anni fa. Una menzione speciale va anche al gruppo di via Torricelli. Grazie a Giovanni, per le discussioni sull'analisi dei segnali tramite trasformate e soprattutto per la nostra amicizia.

Un ringraziamento a tutti gli amici "delle Valli". In particolare, ringrazio i miei amici d'infanzia con i quali ho inconsciamente iniziato questo percorso di studi più di 25 anni fa. La costruzione e la distruzione di dighe al *biàl* per osservare gli effetti delle piene erano le nostre specialità (insieme all'allagamento degli orti...).

Grazie a tutta la mia famiglia per i sacrifici e gli insegnamenti che mi hanno portato un giorno a poter iniziare questo dottorato. Il vostro costante supporto è stato fondamentale durante tutti questi anni. *Merci!*

Grazie infine a te, Giulia. Ci sosteniamo e mi sopporti da ormai più di quattro anni. Un diploma dovrebbero darlo a te! Ti sono grato di essere al mio fianco e incoraggiarmi anche nei momenti meno positivi. Questo traguardo è anche tuo. I nostri sentieri si sono incontrati e proseguono insieme per mari e monti.

Lausanne, June 30, 2022   Ivan Pascal

Abstract

In mountain regions, steep streams play an important role in water and sediment connectivity. In these highly dynamic systems, water flow features, sediment fluxes and stream morphologies are tightly interlinked over a broad range of temporal and spatial scales. Understanding their interactions is key to forecast, prevent and mitigate the impacts of stream-related hazards on human population and facilities as well as to manage the resources connected to the rivers. Sediment clasts at rest on the bed surface may be eroded, transported and deposited by the water flow. Grains that move in rolling and saltation regimes close to the bed compose the 'bedload', which is considered the main mode of sediment transport when studying morphodynamics of mountain rivers. The fate of these particles is of primary interest for river scientists and engineers as bedload predominantly drives the river morphology evolution and responds to it in a complex manner. Therefore, measuring and predicting bedload transport rates are fundamental concerns for many works of research and applications. Bedload transport rates may exhibit large non-Gaussian fluctuations, even under steady-state conditions, especially when bedload transport intensity is weak. These fluctuations may originate from different phenomena and affect the accuracy of bedload transport rate estimates. Particles transported by the water flow can destabilise other particles at rest on the bed surface. Under weak bedload transport conditions, this positive feedback can lead to large bedload pulses. When grains settle, they often organise in small clusters or larger bedforms. Bedform migration has been identified as one of the potential causes of bedload transport fluctuations. Trains of upstream-migrating antidunes may develop in steep coarse-bedded streams when the water discharge is sufficiently high to ensure fully supercritical flow conditions. In this dissertation, I present an experimental investigation on the behaviour of bedload transport fluctuations and antidunes in steep supercritical flows. The experiments were conducted in narrow flumes under well-controlled conditions with high-resolution image-based bedload transport and bed topography monitoring. The dependence of mean bedload transport rate uncertainty on the averaging time interval was analysed. Furthermore, I performed experimental runs with increasing transport intensity and a nearly constant mean bed slope angle to study how antidune sequences composed by bedforms of variable shape typically responded to the mean bedload flux imposed under steady-state conditions. Spectral analysis of the bed elevation perturbation in time and space allowed us to quantify the variability ranges of antidune shape and celerity. Scaling the spectra with opportune reference scales made it possible to identify a consistent dimensionless relationship between antidune geometry and migration celerity, which includes the dependencies on flow and sediment supply forcings. I studied how the

Abstract

bedload transport rate fluctuates in presence of migrating bedforms. The effects on the bedload transport rate periodicity due to non-uniformities in the antidune migration period and to deviations from the steady-state transport conditions were also investigated. This work is a further step on the way towards a complete understanding of the interplay between bedload transport fluctuations and bedforms in mountain streams.

—

Keywords: *bedload transport; gravel-bed rivers; mountain streams; antidunes; morphodynamics; bedload pulses; intermittent processes; experimental work; image analysis.*

Résumé

Dans les régions de montagne, les cours d'eau à forte pente jouent un rôle important dans les transferts d'eau et des sédiments tout au long des bassins versants. Dans ces systèmes fortement dynamiques, les caractéristiques de l'écoulement, les flux de sédiments et les morphologies des cours d'eau sont étroitement liés, et ce sur une large gamme d'échelles temporelles et spatiales. Comprendre leurs interactions est essentiel pour prévoir, prévenir et atténuer les impacts des aléas naturels liés aux cours d'eau sur la population et les installations, ainsi que pour gérer les ressources liées aux rivières. Les sédiments au repos sur la surface du lit peuvent être érodés, transportés et déposés par l'écoulement de l'eau. Les grains qui se déplacent dans des régimes de roulement et de saltation à proximité du lit composent la 'charge de fond'. Ce transport de sédiments par charriage est considéré comme la principale forme de transport solide lors de l'étude de la morphodynamique des rivières de montagne. Le sort de ces particules est d'un intérêt primordial pour les scientifiques et les ingénieurs fluviaux car cette charge est la plus morphogène et elle répond à l'évolution de la rivière de manière complexe. Par conséquent, la mesure et la prédiction du débit solide par charriage sont des préoccupations fondamentales pour de nombreux travaux de recherche et applications. Les débits solides peuvent présenter des grandes fluctuations, même dans des conditions proches d'un état d'équilibre, surtout lorsque l'intensité moyenne du charriage est faible. Ces fluctuations peuvent être causées par des différents phénomènes et influencer la précision des estimations du débit solide moyen représentatif. Les particules transportées par le courant peuvent en déstabiliser d'autres. Dans des conditions de faible charriage, cette rétroaction positive peut conduire à de grandes pulsations du débit solide. Lorsque les grains se déposent, ils s'organisent souvent en petites agglomérations de particules ou en morphologies du lit plus grandes. La migration des morphologies du lit a été identifiée comme l'une des causes potentielles des fluctuations du débit solide par charriage. Des séquences d'antidunes qui migrent vers l'amont peuvent se développer dans les torrents à forte pente à lit grossier lorsque le débit d'eau est suffisamment élevé pour assurer des conditions d'écoulement totalement supercritiques sur un bief. Dans cette thèse je présente une étude expérimentale sur le comportement des fluctuations de transport de charriage et des antidunes dans des écoulements supercritiques à forte pente. Les expériences ont été menées dans des canaux étroits dans des conditions contrôlées. Le suivi du débit solide et de la topographie du lit était basé sur des techniques d'imagerie à haute fréquence et haute résolution. L'influence du temps d'échantillonnage sur l'incertitude du débit solide moyenné a été analysée. De plus, j'ai effectué des essais avec une intensité de transport croissante et une pente moyenne du

lit presque constante pour étudier comment des séquences d'antidunes composées par des formes à longueur d'onde variable répondaient généralement au débit solide moyen imposé par l'alimentation du système. L'analyse spectrale de la perturbation de la topographie du lit (dans le temps et dans l'espace) nous a permis de quantifier les plages de variabilité de la forme et de la vitesse de migration des antidunes. La normalisation de ces spectres avec des échelles de référence opportunes a permis d'identifier une relation (de type adimensionnel) entre la géométrie de l'antidune et sa vitesse de migration. Cette relation inclut des dépendances par rapport aux débits d'alimentation (solide et liquide) imposés au système. J'ai étudié comment le transport solide par charriage varie en présence de ces morphologies du lit qui se déplacent. Les effets sur la périodicité des pulsations du débit solide dus aux non-uniformités dans la période de migration des antidunes—ainsi qu'aux écarts par rapport aux conditions de transport "à l'équilibre"—ont également été étudiés. Ce travail est un pas en avant vers une meilleure compréhension de l'interaction entre les fluctuations du débit solide par charriage et les morphologies du lit dans les cours d'eau de montagne.
—

Mots clés : *transport solide par charriage ; rivières à lit de gravier ; torrents de montagne ; antidunes ; dynamique des formes du lit ; pulsations du débit solide ; processus intermittents ; expériences de laboratoire ; analyse d'image.*

Riassunto

Nelle regioni montuose, i corsi d'acqua a forte pendenza svolgono un ruolo importante nel trasferimento di acqua e sedimenti attraverso i bacini idrografici. In questi sistemi altamente dinamici, le caratteristiche idrauliche della corrente, i flussi di sedimenti e le morfologie dei letti torrentizi sono strettamente collegati su un'ampia gamma di scale temporali e spaziali. Comprendere le interazioni di questi fattori è essenziale per prevedere, prevenire e mitigare gli impatti sulle persone e sulle strutture dei rischi naturali legati ai fiumi, nonché per gestire le risorse a loro connesse. I sedimenti a riposo sulla superficie del letto possono essere erosi, trasportati e depositati dal flusso d'acqua. I grani che si muovono in prossimità del letto ed entrano frequentemente in contatto con esso costituiscono il 'carico di fondo'. Questo trasporto solido di fondo è considerato la principale forma di trasporto di sedimenti quando si studia la morfodinamica dei fiumi di montagna. Il destino di queste particelle (tipicamente di taglia grossolana) è di interesse primario per ricercatori e ingegneri fluviali perché questo carico è quello che maggiormente influenza l'evoluzione del fiume e risponde a questa in maniera complessa. Pertanto, la misurazione e la previsione della portata solida di fondo sono problematiche fondamentali per molti lavori di ricerca e applicazioni. I flussi di sedimenti possono presentare grandi fluttuazioni, anche in condizioni prossime allo stato stazionario, soprattutto quando l'intensità del trasporto è debole. Queste fluttuazioni possono essere causate da diversi fenomeni e influenzare la precisione delle stime di portata solida di fondo media (rappresentativa delle condizioni). Le particelle trasportate dalla corrente possono destabilizzarne altre. In condizioni di trasporto solido debole, questo meccanismo di retroazione positiva può portare a grandi fluttuazioni del flusso di sedimenti. Quando i grani si depositano, spesso si organizzano in piccoli agglomerati di particelle o in forme di fondo più grandi. La migrazione delle forme di fondo è stata identificata come una delle potenziali cause delle fluttuazioni della portata solida di fondo. Sequenze di antidune che migrano verso monte possono svilupparsi in torrenti ripidi con fondo composto da sedimenti di taglia grossolana quando la corrente è sufficientemente intensa da garantire condizioni di flusso completamente supercritiche su un tratto. In questa tesi presento uno studio sperimentale sul comportamento delle fluttuazioni di trasporto solido di fondo e delle antidune in correnti di tipo torrentizio. Gli esperimenti sono stati condotti in canali stretti in condizioni controllate. Il monitoraggio del flusso di sedimenti e della topografia del letto è stato basato su tecniche di fotografia ad alta frequenza e ad alta risoluzione. È stata analizzata l'influenza del tempo di campionamento sull'incertezza del portata solida media stimata. Inoltre, ho effettuato esperimenti con diverse intensità di trasporto e pendenza media del letto quasi costante per

studiare come le sequenze di antidune (composte da forme a lunghezza d'onda variabile) rispondessero generalmente al flusso medio di sedimenti imposto a monte. L'analisi spettrale delle ondulazioni del letto di sedimenti (nel tempo e nello spazio) ci ha permesso di quantificare gli intervalli di variabilità della forma dell'antiduna e della velocità di migrazione. La normalizzazione di questi spettri con opportune scale di riferimento ha permesso di individuare una relazione (di tipo adimensionale) tra la geometria dell'antiduna e la sua velocità di migrazione. Questa relazione include le dipendenze dalle portate di alimentazione (solide e liquide) imposte al sistema. Infine, ho studiato come varia il trasporto solido di fondo in presenza di queste forme di fondo migranti. Sono stati studiati gli effetti sulla periodicità della fluttuazione della portata sedimentaria dovuti alle non uniformità nel periodo di migrazione delle antidune, nonché alle deviazioni dalle condizioni di trasporto solido "di equilibrio". Questo lavoro rappresenta un passo in avanti verso una migliore comprensione dell'interazione tra le fluttuazioni della portata solida di fondo e le forme di fondo nei torrenti di montagna.
—

Parole chiave: trasporto solido di fondo; fiumi a letto ghiaioso; torrenti di montagna; antidune; dinamica delle forme di fondo; fluttuazioni del trasporto solido di fondo; processi intermittenti; esperimenti di laboratorio; analisi d'immagine.

Contents

Contents

List of Figures

List of Tables

1 Introduction

1.1 Motivation

Mountain rivers are key elements of the landscape that govern the transfer of water and sediments from high-altitude areas (occasionally enriched by glaciers) to lowland rivers, plains and seas (Milliman and Syvitski, 1992). As rivers, they are not simply transport machines but dynamic entities that evolve over time by interacting with their boundaries. Flowing water can erode, transport and deposit sediments (sand, gravel, boulders, wood, etc.). Sometimes, these phenomena are relatively slow and the changes induced by a stream on the surrounding environment may be almost imperceptible at the human-life time scale. The inexperienced observer might think of such a river as the quiet element of a postcard, whose path and water flow can be easily constrained if needed. In other cases, the same stream could behave differently, displacing large sediment volumes, flooding inhabited areas and completely changing the image of the postcard in few hours (or even minutes). Such extreme events are often triggered by an increase in the water discharge due to a rainfall or to the intense snow melt during a sunny day. However, the hydraulic behaviour and the morphodynamic evolution of these streams are the result of a complex interplay between flow, transported sediments and river boundaries. Therefore, understanding the sediment transport and morphodynamic processes in mountain streams is fundamental for the societies that populate mountainous and pre-alpine areas. This would provide more solid bases to prevent and mitigate stream-related hazards that threaten human lives and infrastructures—resulting in heavy human and economic costs (e.g. Badoux et al., 2016, 2014). Moreover, better knowledge of the hydrological, hydraulic and sedimentary behaviour of mountain streams would help protect this riverine environment and manage the resources associated to it. These aspects are particularly important in a context of climate change in which increasingly extreme dry and wet periods will alternate and have negative consequences on water bodies, the economy and society (FOEN, 2021).

In mountain rivers, the sediment phase is typically composed of coarse particles (such as gravel, pebbles and boulders) that are transported as 'bedload'—a term that indicates particles

that travel close to the bed and experience frequent contacts with it. Bedload transport has been studied in detail since the end of the nineteenth century (e.g. du Boys, 1879). After more than 140 years of research efforts, bedload transport rate predictions in mountain rivers, based on the available tools, are hardly closer than one order of magnitude to the measured rates (see Ancey, 2020b). Moreover, the predictive power is particularly poor under weak transport conditions (e.g. Gomez and Church, 1989; Barry et al., 2004). These unsatisfactory performances have drawbacks on our capacity to predict (i) the volume of sediments transported by a river over a given time interval and (ii) the river hydraulic and morphodynamic responses to precipitation and sedimentary inputs (just to provide two key examples). The difficulty in predicting bedload transport rates partly lies in the fact that they may fluctuate widely and intermittently (in time and space); these fluctuations should be taken into account in both bedload transport monitoring and bedload transport modelling (see Ancey et al., 2014; Furbish et al., 2017; Ancey, 2020b; Gomez et al., 2022).

Figure 1.1: An example of steep mountain stream: the Germanasca in Prali (Piemonte, Italy) during an intense flood (end of May 2008). Flow from left to right. ©Susy Pascal.

This dissertation presents an experimental study in which we specifically investigated (i) how variable are the bedload transport rates and the antidune morphodynamic features and (ii) how their variabilities are interrelated in steep coarse-bedded streams under supercritical flow conditions. It would be presumptuous to pretend that five years of research work in an underground laboratory might produce a major breakthrough in our understanding of bedload transport in real-world streams—a topic on which generations of brilliant engineers and scientists have already spent time and effort in a steady, slow progress. This thesis is not about game-changing achievements. It summarises hours of passionate observation

(and a bit of elbow grease) spent around a simplified stream in which small grains travelled downstream, while strange dunes migrated upstream. These observations eventually provided some useful data, stimulated a couple of papers and might inspire some new idea. Who knows if these seeds will one day contribute to a better prediction of bedload transport processes in steep streams? In the meanwhile, Figure 1.1 shows a mountain stream that did not like its engineered left bank.

1.2 Scientific background

In this section, I review the scientific literature on sediment transport and river morphodynamics. The focus is on concepts, models and methods applicable to systems characterised by shallow flow over coarse-grained bed (conditions typical of mountain streams) and weak to moderate bedload transport intensities.

1.2.1 Bedload transport

Role of sediment transport in rivers and bedload transport mechanism

In rivers, mass and momentum exchanges occur between the water flow, its sediment load, and the flow boundaries (i.e. atmosphere, river bottom and banks). Assuming that the friction at the air-water interface is negligible, the motion of the gravity-driven surface flow is mainly affected by the 'skin friction' (the shear stresses acting at the scale of the bed sediments) and 'form friction' (the dissipations induced by bed and bank morphologies). Conversely, the moving flow exerts a shear stress on the solid boundaries. Natural river beds are usually composed of granular material that can be eroded, transported and deposited by the stream flow. This sediment displacement modifies the bed topography, which in turn affects the flow dynamics, creating a complex feedback. This mutual interplay links together water flow, sediment fluxes and stream morphology (see Church and Ferguson, 2015). The coarsest fraction of sediments transported by the stream flow in rolling, saltating, or sliding motion close to the bed is usually called 'bedload', whereas the finer fraction can be classified as 'suspended load'. In mountain gravel-bed rivers, bedload is generally the main form of sediment transport (Church, 2010) or, at least, the fraction of the sediment load that drives the morphodynamic evolution.

Bedload transport rate: Definition examples and descriptive approaches

Bedload transport rate has been defined in a multitude of different forms depending on the context (e.g. theoretical models or field measurements) and the purpose of the work (see Campagnol et al., 2012; Furbish et al., 2012; Ballio et al., 2014; Furbish et al., 2017; Ballio et al., 2018; Ancey, 2020a). I briefly present some definitions that give the opportunity to introduce

some key aspects regarding the variables used in bedload transport rate expressions and the possible approaches.

Usually, bedload transport rates measured with basket samplers in flume and field studies are computed as the ratio between the amount of sediment collected—weight,volume or number of grains—at a given cross-section and the temporal interval of collection. Another relationship inspired by the definition of flux through a control surface in continuum mechanics (Ballio et al., 2014) reads as

$$Q_s = \int_{\mathscr{S}} \gamma(\mathbf{x}, t) u_p(\mathbf{x}, t) \mathrm{d}\mathscr{S}, \tag{1.1}$$

where Q_s [$L^3\,T^{-1}$] is the volumetric transport rate, $\mathscr{S}$ is the control surface, $\gamma(\mathbf{x}, t)$ is a 'clipping function' (which takes value 1 if the point $\{\mathbf{x}, t\}$ is located in a solid particle and 0 otherwise, see Coleman and Nikora, 2009) and $u_p(\mathbf{x}, t)$ is the velocity component normal to the surface $\mathrm{d}\mathscr{S}$ of the solid that occupies the $\mathbf{x}$ position at time t. Unfortunately, in most applications, the $\gamma(\mathbf{x}, t)$ function is hardly measurable and this definition results seldom useful. Choosing between the many available alternatives, I report two examples of definitions that might appear equivalent at a first look. First, the expression that Bridge and Dominic (1984) considered to derive a bedload transport formula on the basis of theoretical considerations. This definition, when expressed in terms of volumetric bedload transport rate per unit width ($q_s = Q_s/W$ [$L^2\,T^{-1}$]), reads

$$q_s = \frac{\mathscr{W}'_s}{g(\rho_s - \rho)} U_b, \tag{1.2}$$

where $\mathscr{W}'_s$ is the immersed weight of the moving grains per unit bed area, U_b is 'the mean speed of bed load grains' (based on a theoretical expression, see Bridge and Dominic, 1984), g is the gravitational acceleration, $(\rho_s - \rho)$ is the density difference between sediment and water. Second, Ancey et al. (2008) defined the bedload transport rate in a control volume as

$$q_s = \frac{V_p N}{LW} U_p, \tag{1.3}$$

where V_p is the characteristic particle volume (constant for uniform sediments), L is the length of the control volume in streamwise direction, $U_p(t) = \sum_{i=1}^{N} u_{p,i}(t)$ is the averaged velocity of the particles (with instantaneous velocity $u_{p,i}(t)$) present in the control window at time t and $N(t)$ is the number of moving particles. Note that Eq. 1.2 and Eq. 1.3 share similar structures but some variables can be defined in notably different ways and by considering different spatial and temporal references (e.g. the mean particle velocities U_b and U_p or the concentration of moving particles). Such structural similarities accompanied by more or less subtle differences in the definitions of important variables are very frequent in the volume-averaged

expressions of q_s. These differences may significantly affect the q_s values (and their meaning) depending on the context (e.g. fixed or mobile bed in the control volume, well-sorted or poorly sorted sediments), thus they deserve particular attention. This is particularly important when comparing results from different investigations and different measurement procedures.

Bedload transport rates (independently of their definition) may be expressed in a dimensionless form proposed by Einstein (1950):

$$\varphi = \frac{q_s}{[g(s-1)]^{0.5}d^{1.5}}, \tag{1.4}$$

where $d \simeq d_{50}$ is the characteristic particle size and $s = \rho_s/\rho$ is the sediment-to-water density ratio. This form is useful when comparing sediment transport rates for different sediments or environments (e.g. different g) and many bedload transport formulae are usually expressed in terms of φ. The symbol Φ is usually attributed to the dimensionless bedload transport rate; here I use φ for this variable to avoid confusion with the particle flux Φ_s.

The use of tracers (tagged particles) in flume and field studies has been largely inspired by the work of Einstein (1937a) and has attracted remarkable interest during the last decades (e.g. Hassan and Church, 1991; Wilcock, 1997b; Ganti et al., 2010). It is accompanied by a different type of definitions for the bedload flux, in which the key elements are usually the distances travelled by particles between entrainment and deposition events, the times of rest and motion experienced by each particle (or the entrainment rate for the particles at rest in a certain bed area) and the depth at which the bed is reworked by erosion and deposition (e.g. Einstein, 1950; Crickmore and Lean, 1962; Wong et al., 2007). Mentioning these definitions leads to specify an important difference in the approaches adopted to observe and describe the bedload transport process. Two different and complementary approaches are possible: Lagrangian and Eulerian (see Ancey, 2010; Ballio et al., 2018). The Lagrangian approach focuses on the properties (hop lengths, resting times, etc.) of the individual particles along their trajectories (e.g. Campagnol et al., 2013). The Eulerian approach is focused on a reference location (control volume or surface) and on the assessment of variables defined at that location to express q_s (see Eq. 1.3). Mixed Lagrangian-Eulerian approaches have been proposed and used, especially for bedload transport investigations based on tracers (see expressions presented in Wong et al., 2007). Ballio et al. (2018) demonstrated that Lagrangian variables of interest can be inferred from Eulerian variables and proposed a unified framework for these descriptions. The bedload transport investigations conducted by the candidate and presented in this dissertation were based on an Eulerian point of view.

To define bedload transport rates and describe bedload transport processes it is natural to make use of temporal, spatial (and ensemble) averaging operations (simple or combined) (see Bunte and Abt, 2005; Ballio et al., 2014; Ancey and Heyman, 2014; Fathel et al., 2015). In

most cases, the monitoring systems provide time-averaged bedload transport rates rather than instantaneous rates. Extending the averaging time window during data post-processing may prove useful to reduce the rate uncertainty or to estimate the representative bedload transport rate of a system under steady-state conditions—i.e. the conditions under which the system experiences a balance between erosion and deposition over certain spatial and temporal scales. These sampling- and averaging-related aspects are the leitmotif of Chapter 2 (Ancey and Pascal, 2020).

First attempts of bedload transport rate prediction with deterministic equations

As just mentioned, many definitions of bedload transport rate exist. Interestingly, their number is vastly overtaken by the quantity of formulae advanced for predicting bedload transport rates. The first known formula was proposed by du Boys (1879), a French engineer that worked on the River Rhone (Hager, 2005). This formula is based on the idea of a riverbed made of superposed parallel layers of grains that may be entrained in sliding motion (one layer over the other) by the flow-induced bed shear stress $\tau_b = \rho h \tan \psi$ (where h is the flow depth and ψ is the bed slope angle). The bed layers slide if and only if τ_b exceeds a certain threshold value τ_c. Originally, this criterion was expressed as comparison between an entrainment force and a resistive force that depended on the stability angle of the granular material (see Hager, 2005). In case of entrainment, du Boys (1879) stated that the translation velocities of the layers are linearly distributed over a basal layer at rest. Although this idealized bedload transport model does not match the real bedload motion conditions, it remarkably led to express the bedload transport rate as proportional to the shear stress τ_b and to its excess over a threshold value τ_c:

$$q_s = \chi \tau_b (\tau_b - \tau_c), \tag{1.5}$$

where χ is a coefficient to be determined experimentally. Interestingly, this structure (or very similar ones, in which $q_s \propto (\tau_b)^a (\tau_b - \tau_c)^b$) can be retrieved in many empirical or semi-empirical bedload transport formulae proposed during the following decades (e.g. Eq. 1.6 by Meyer-Peter and Müller, 1948). Indeed, the available q_s datasets—progressively enriched with data collected during flume studies (e.g. Gilbert and Murphy, 1914) and field observations—approximately confirmed this proportionality and were intensively used for empirically-fitted formulae. Other attempts to formulate predictive relationships in slightly different forms were made. For instance, Schoklitsch (1934) considered q_s proportional to the water discharge q_w (or the stream power) and the excess of q_w above a critical discharge threshold and then fitted the relationship on experimental and flume data. Bagnold (1956) approached the problem from an entirely theoretical point of view. He considered the system in which bedload transport occurs "as a fluid-dynamic transporting machine" and found a physical justification for the proportionality $q_s \propto \sqrt{\tau_b}(\tau_b - \tau_c)$—even if his reasoning was totally different from that followed by du Boys (1879). This proportionality is not exactly the same retrieved empirically by other authors but is very similar. Consider, for instance, the formula proposed by Meyer-

Peter and Müller (1948) with its original coefficients (see Wong and Parker, 2006):

$$\varphi = 8(\Theta - \Theta_{\text{c}})^{3/2}, \quad \text{with} \quad \Theta = \frac{\tau_{\text{b}}}{\rho g (s-1) d_{50}}, \tag{1.6}$$

where the bed shear stress is expressed with the dimensionless Shields parameter Θ (Shields, 1936) and the dimensionless critical shear stress $\Theta_{\text{c}} = 0.047$. Reporting this expression is instrumental to highlight that most pioneering deterministic formulae included a fixed critical threshold Θ_{c} for sediment transport initiation and assumed equilibrium conditions with full transport capacity. The fitting of the three coefficients that appear in this empirical formula was based on a large dataset of bedload transport rate observations, which included data collected by Gilbert and Murphy (1914) and Meyer-Peter et al. (1934), as well as auxiliary data produced during flume experiments conducted at ETHZ (Zurich) with uniform flows over well-sorted coarse sediments (see Meyer-Peter and Müller, 1948). This aspect should be conscientiously taken into account before applying this formula or similar ones under conditions out of their calibration domains. Note that Shields (1936) also proposed a diagram that implicitly links the Θ_{c} to the particle Reynolds number Re^* (for smooth, transitional and rough turbulent flow conditions). Defining the value of Θ_{c} (intended as critical threshold for sediment entrainment and motion) attracted the attention of many researchers during the twentieth century (see Buffington and Montgomery, 1997).

Factors that affect the uncertainty of bedload flux predictions

During the second part of the twentieth century, researchers and practitioners began to realise that the deterministic relationships for q_{s} may lead to large estimation errors (several orders of magnitude), especially in gravel-bed rivers and flume experiments under weak bedload transport conditions (e.g. Gomez and Church, 1989; Barry et al., 2004). It is worth specifying that prediction issues are usually less severe for field and experimental systems under intense bedload transport conditions. For instance, in the tests conducted by Gomez and Church (1989), Bagnold's formula (Bagnold, 1956) gave satisfactory results for cases characterised by relatively intense bedload transport rates. Because of the shortcomings of the deterministic approach, the criteria used for determining Θ_{c} and the very same notion of fixed Θ_{c} threshold for incipient particle motion were questioned (see Lavelle and Mofjeld, 1987; Buffington and Montgomery, 1997; Recking, 2009). Many factors can be claimed for the difficulties in establishing an empirical (or semi-empirical) relationship for bedload transport rate prediction with good performances and wide application domains. During the recent decades, many researchers reconsidered the concept of bedload transport initiation in coarse-bedded rivers and the related effects on bedload transport rate predictions. These efforts were mainly dedicated to better understand and model: size-selective bedload transport due to poorly sorted sediments and bed armouring (e.g. Parker et al., 1982; Wilcock, 1988, 1997a; Frey et al., 2003; Recking, 2006), form drag quantification for bedload transport predictions (e.g. Gomez and Church, 1989; Recking, 2013a), changes in the hydraulics (velocity profiles and flow resistance)

of shallow flows with high relative roughness (e.g. Rickenmann, 2001), and non-linearity effects in the bedload transport (often neglected by considering hydraulic parameters averaged over the cross-sections) (Recking, 2013a). Many authors also found that part of the errors made when predicting bedload flux in mountain streams may be due to limitations in the actual sediment supply to the system (e.g. D'Agostino and Lenzi, 1999; Almedeij and Diplas, 2003; Bravo-Espinosa et al., 2003; Gomez, 2006; Rickenmann and Koschni, 2010; Comiti and Mao, 2012). Classic deterministic bedload transport formulae (e.g. Meyer-Peter and Müller, 1948; Smart and Jaeggi, 1983) often lead to over-estimations of the bedload transport rate in a given stream if such stream does not have availability of mobilisable sediment sufficient to cover the so-called 'transport capacity' of the water flow (e.g. D'Agostino and Lenzi, 1999; Rickenmann and Koschni, 2010). Therefore, taking into account the case-specific sediment availability (limited or unlimited) and supply conditions is of paramount importance when estimating bedload fluxes and studying channel morphology evolution (Comiti and Mao, 2012). The reader is referred to the work by Yager et al. (2007) for an example of framework that accounts for the local sediment availability and the effects on the shear stress partitioning of large particles with low (or null) mobility. A limited bedload income from upstream in a stream reach does not necessarily imply a mean bedload transport rate lower than the transport capacity at the reach outlet. The in-reach availability of erodible sediment (from channel bottom and banks) and the boundary conditions have to be considered as well. An interesting insight on this aspect is presented in Chap. 4, in which data collected during flume experiments with and without active sediment feeding are presented.

A change of paradigm: probabilistic approaches to bedload transport

Apart from the factors mentioned in the previous section, another fundamental ingredient was neglected in the first deterministic approaches: the bedload transport intrinsic randomness. In the 1930s and 1940s, despite the first observations of temporal and spatial fluctuations in bedload transport rates (e.g. Ehrenberger, 1931; Mühlofer, 1933), the bedload transport rate was considered to be in substantial one-to-one relationship with mean flow conditions (see Gomez, 1991). After many hours spent observing sediments transported by water in laboratory flumes at ETHZ, Hans A. Einstein understood that "the dislodgement and subsequent motion of a bed particle are a matter of chance" under the effects of near-bed flow turbulence (Ettema and Mutel, 2004). Einstein summarized his point of view in his PhD thesis (Einstein, 1937a), the first work that introduced the concept of probability in bedload transport investigations. Subsequently, Einstein (1950) proposed the first dimensionless relationship that links the bedload transport rate in a system to the entrainment probability of a particle at rest on the bed surface sheared by a turbulent flow. His implicit relationship includes three coefficients whose values were determined by fitting the expression on data collected by Gilbert and Murphy (1914) and Meyer-Peter et al. (1934) (see also Smart and Jaeggi, 1983). This expression has the merit of performing reasonably well (with only few adjusted parameters) over a range of dimensionless rate φ (Eq. 1.4) that spans five orders of magnitude (Ancey, 2020a).

Although Einstein's model cannot be considered a strictly stochastic or probabilistic framework (Ancey, 2020a), his approach brought novelty in this field with statistical considerations on particle motion that somehow challenged the dominant conception of bedload flux as univocal function of mean flow conditions. Therefore, Einstein's works inspired the investigations of many researchers, who later studied bedload transport by considering its intermittent nature and the influence of turbulence on particle entrainment and motion (Ancey, 2020a). Bedload transport fluctuations received growing interest during the last decades (see Furbish et al., 2017; Ancey, 2020a,b; Gomez et al., 2022). A number of authors formulated probabilistic and stochastic bedload transport models to improve bedload flux prediction performances or to study bedload transport processes such as the dispersion of tracers (e.g. Parker et al., 2000; Ancey et al., 2008; Turowski, 2010; Furbish et al., 2012). For given flow and bed conditions, stochastic frameworks may provide probability distributions of bedload transport rate (or of other variables of interest) rather than one single estimate. Therefore, they are particularly well-suited for describing (and hopefully predicting) intermittent bedload transport processes under weak sediment transport conditions—which represent the typical situation in which the performances of deterministic formulae are the most unsatisfactory. The stochastic approaches also make it possible to formulate macroscopic conservation equations for a physical system by starting from minimalistic descriptions of the key physical mechanisms at the grain scale (e.g. Furbish et al., 2012; Ancey and Heyman, 2014; Heyman, 2014). From these approaches, it appeared that "noise" induced by bedload intermittency (pulses alternated with periods of weak or no sediment transport) is intrinsic in the discrete nature of particle motion—at least under weak transport conditions—and may affect the bedload transport mean behaviour (e.g. Ancey and Heyman, 2014; Heyman et al., 2014; Ancey et al., 2015; Furbish et al., 2017).

Ancey's stochastic model (2008) and its extensions

Ancey et al. (2006) demonstrated that Einstein's model (1950), which considers only individual particle entrainment and motion events, cannot predict the large non-Gaussian fluctuations of instantaneous bedload transport rates that have been observed at approximately constant water discharge (e.g. Bunte and Abt, 2005), also in well-controlled flume experiments (e.g. Kuhnle and Southard, 1988; Böhm et al., 2004). Starting from their previous observations, Ancey et al. (2008) proposed a stochastic model of bedload transport based on an Eulerian approach. They considered a control volume $\mathscr{V}$ that includes the bed and the water stream between two cross-sections spaced of L in streamwise direction (see Fig. 3, Chapter 2). The dynamics of the population of moving particles N in $\mathscr{V}$ was modelled as an immigration–emigration birth–death Markov process. Immigration and emigration events are the inflow and outflow of particles across the upstream and downstream boundaries of $\mathscr{V}$, respectively, whereas death and birth events are the particle depositions and entrainments, respectively. The individual entrainment of particles from the bed is one possible mechanism that produces 'birth' events.

The rate of this individual entrainment is proportional only to the size of $\mathcal{V}$. Moreover, Ancey's (2008) framework includes a 'collective entrainment' mechanism that yields an additional contribution to the number of births. This mechanism mimics the entrainment of particles from the bed surface under the direct or indirect influence of moving particles (due to collisions, modification of the near-bed instantaneous velocity, etc.) (Ancey et al., 2008). Therefore, this form of entrainment—whose rate depends also on the number of moving particles at time t—produces a positive feedback to fluctuations in the particle activity. The number of moving particles $N(t) = n$ (with $n = 0, 1, 2, ...$) evolves in time under the effects of the above-mentioned mechanisms, which are characterised by their specific rates. Ancey et al. (2008) studied the probability $P(N = n, t)$ of observing $N = n$ at time t. The authors assumed to study a Markovian random jump process, which means that (i) $P(N = n, t)$ depends only on the state of the system at time $t - \delta t$ (with $N(t - \delta t)$) and not on the previous states, and (ii) N can experience only jumps of amplitude +1, 0 or -1 between observation times spaced by δt (with δt sufficiently short). These assumptions appear reasonable for studying the particle exchanges between stream and bed under weak bedload transport conditions and made it possible to use advantageous analytical tools developed for this family of stochastic processes (Ancey et al., 2008). The probability $P(N = n, t)$ under steady-state conditions can be calculated analytically by using such tools. Ancey et al. (2008) demonstrated that the stochastic process formulated in these terms leads to a negative binomial distribution of $P(N = n, t)$ if the collective entrainment mechanism is active. The negative binomial distribution is characterised by a thick right-hand tail and thus may justify relatively frequent large fluctuations of bedload transport rate (where 'large' means that the fluctuation amplitude may be larger than the mean bedload transport rate) (Ancey et al., 2008). The authors also presented results from idealized bedload transport experiments that showed overall good agreement with model predictions.

This stochastic framework was later extended to an array of adjacent control volumes of size Δx and generalised to the continuum form for the limit $\Delta x \to 0$ (Ancey and Heyman, 2014). The continuous variable of this process is a particle activity defined as $c = \lim_{\Delta x \to 0} (N / \Delta x)$. Ancey and Heyman (2014) managed to generalise the process from the discrete space (with N) to the continuous space by using the Poisson representation (Gardiner and Chaturvedi, 1977; Gardiner, 1983). Ancey and Heyman (2014) showed that the Poisson density (which reflects c in the Poisson space) is governed by a stochastic advection equation. An overview of the usefulness of such extension for applications is given by Ancey (2020a) (for details, see Ancey and Heyman, 2014; Ancey et al., 2015). Furthermore, Heyman et al. (2016) proposed closure relationships for the stochastic model based on flume experiments conducted in a narrow range of flow and bedload transport conditions.

Bedload flux predictions in steep mountain streams: the additional issue due to the peculiar flow configuration

In steep mountain streams, shallow free-surface water flows over relatively steep slopes ($\tan \psi \geq 0.01$, where ψ is the bed slope angle) made of coarse sediments—d_{50} is typically in the

size range spanning from gravel to boulders ($d_{50} = \mathscr{O}(10^{-3})$–$\mathscr{O}(10^{0})$ m). In these streams, the roughness size (usually expressed as the median sediment size) is of the order of magnitude of the flow depth. This feature can be described in terms of relative roughness $d_{50}/\overline{h}$ (i.e. the ratio between median grain size and mean flow depth). This aspect is crucial because the dynamics of flows characterised by high relative roughness ($d_{50}/\overline{h} \approx 1$–$10$) notably differ from those of deeper rough flows for which the classical (log-law) flow equations have been developed and tested (e.g. Ferguson, 2007; Rickenmann and Recking, 2011). Over the last three decades, some authors proposed and tested specific empirical frameworks for flow resistance estimation and partitioning (resistance associated to form or macro-roughness drag, and skin drag) in steep streams with high relative roughness (e.g. Ferguson, 2007; Rickenmann and Recking, 2011; Ferguson, 2021).

Recking et al. (2008) also proposed a relationship for estimating Θ_c in steep coarse-bedded streams (used in the investigation presented in Chapter 3 of this dissertation). The key feature of this relationship is the one-to-one proportionality $\Theta_c \propto (\tan\psi)^{0.275}$, which empirically synthesises the steepness effects on the critical shear stress Θ_c in flows with high relative roughness (see also Lamb et al., 2008).

Several authors proposed relationships for bedload transport rate prediction which do not consider threshold values for incipient transport. They were designed (and fitted over field and/or flume data) for improving predictive performances under specific conditions encountered in coarse-bedded rivers, in which the available formulae gave unsatisfactory results (e.g. Barry et al., 2004; Recking, 2010). An interesting example is the empirical formula proposed by Recking (2013b) for predicting q_s (in φ form), which unified two complementary relationships previously proposed by Recking (2010). These two relationships were fitted on a large dataset of field and laboratory observations (see also Recking et al. (2008)). One expression was specifically adjusted for flow conditions that correspond to partially mobilized grains and is a power law of (Θ/Θ_c). The second expression is a power law of Θ with no dependence on Θ_c and is expected to hold for conditions in which the bed sediments are fully mobilized. The resulting unified formula (Recking, 2013b) is

$$\varphi = \frac{14\Theta_{84}^{2.5}}{1 + (\Theta_m/\Theta_{84})^4}, \quad \text{with} \quad \Theta_m = (5\tan\psi + 0.06)\left(\frac{d_{84}}{d_{50}}\right)^{4.4\sqrt{\tan\psi}-1.5} \quad \text{for gravel,} \qquad (1.7)$$

where Θ_m is the Shields parameter that corresponds to the transition from partial to full sediment mobility and Θ_{84} is the Shields parameter calculated for d_{84}. This relationship proved to describe with reasonably small error ranges (< 100 %) the behaviour of the bedload transport rates (φ vs. Θ) observed at the Zinal monitoring station on the River Navisence (Canton du Valais, Switzerland) (see Fig. 2 in Ancey, 2020b). When applied to field cases without preliminary tests, the performances of such type of bedload transport formulae

might be conditioned by the methods used to estimate flow resistance and shear stresses (as highlighted by Recking (2010)). Motivated by these issues, Rousseau (2019) investigated the dynamics of very shallow turbulent flows over coarse sediments by taking into account the role played by the porous bed structure in determining the velocity profiles. He formulated a model that considers the momentum exchanges that occurs in the roughness layer between surface and subsurface flows (see also Rousseau et al., 2020; Rousseau and Ancey, 2020). This novel approach, which specifically considers the typical conditions of mountain streams, is promising but requires further developments to facilitate the implementation in field cases. Indeed, one limitation is related to the difficulties of defining representative volumes and measuring bed porosity profiles in mountain rivers. Another feature that complicates the hydraulic modelling of mountain streams is the pronounced flow non-uniformity often encountered in these systems, a non-uniformity tightly related to sudden changes in the channel slope and width along the reach and to the presence of bedforms.

1.2.2 Bedload-bedforms interplay

Fluctuations of the bedload transport rates

Already during the 1930s, some studies reported pronounced temporal fluctuations in the bedload transport rates, even at approximately constant water discharges. For instance, Ehren-berger (1931) and Mühlofer (1933) measured periodical oscillations in the bedload transport during field measurements conducted with basket samplers at fixed locations in the rivers Danube and Inn. These authors observed bedload transport rate fluctuations that exhibited periods in the 5–20-minutes range and associated them to the transit of downstream migrating bedforms (Gomez, 1991). Also Schoklitsch (1914, 1934) and Einstein (1937b) observed periodic fluctuations of bedload transport rates caused by dune migration in laboratory experiments but, unfortunately, these particular features did not attract much interest in the scientific community during the following years. At that time, the concerns about the uncertainty of the sampling techniques and the pursuit of a universal bedload transport formula likely contributed to the lack of interest for these important observations (Gomez et al., 1989).

In the case of gravel-bed rivers, several phenomena have been indicated as potential causes of bedload pulses under constant hydraulic forcing. At particle scale relatively large fluctuations of the bedload transport rate can originate from mechanisms of entrainment and motion that involve groups of particles (e.g. Drake et al., 1988; Ancey et al., 2008). The formation and destruction of micro-forms (e.g. Strom et al., 2004), reticulate structures (e.g. Church et al., 1998) or armor layers (e.g. Recking, 2006), the migration of bedforms (e.g. Gomez et al., 1989; Mettra, 2014; Dhont and Ancey, 2018; Palucis et al., 2018) and low-relief bedforms—such as sediment waves (e.g. Ashmore, 1991a) and bedload sheets (e.g. Kuhnle and Southard, 1988)—as well as the collapse of step structures (e.g. Recking et al., 2012a; Saletti et al., 2015) and the variations in the sediment supply (e.g. Benda and Dunne, 1997; Recking, 2012) are other examples of phenomena that may generate bedload pulses. The variety of spatial and

temporal scales of these phenomena and the fact that they may occur simultaneously (Gomez et al., 1989) give a good idea of the complexity of bedload transport processes in gravel-bed rivers. These intermittent pulses affect the convergence of the bedload transport rate towards its representative mean value (e.g. Gomez, 1991; Bunte and Abt, 2005; Singh et al., 2009; Campagnol et al., 2012; Recking et al., 2012b). Moreover, bedload pulses may deeply affect the evolution of the macroscopic system—since they may represent considerable fractions of the total bedload flux that travels along a reach (e.g. Drake et al., 1988; Mettra, 2014; Dhont and Ancey, 2018).

Typical bedforms under supercritical or transcritical flow regimes in steep streams

The Froude number Fr represents the ratio between gravity and inertial forces acting on a unity volume of fluid (see for instance Graf and Altinakar, 1993). Consider an open-channel flow characterised by depth h and flow velocity U. In such a flow, Fr is usually expressed as

$$Fr = \frac{U}{(gh)^{1/2}}, \tag{1.8}$$

The dimensionless number Fr may also be interpreted as the ratio between mean flow velocity and surface wave celerity. Therefore, depending on the Froude number, free-surface flows can be distinguished in subcritical ($Fr < 1$) or supercritical ($Fr > 1$). Since in supercritical flows a small free surface perturbation can only travel in downstream direction, such flows are driven—from an hydraulic point of view—by the upstream boundary conditions. Conversely, subcritical flows are driven by the downstream boundary conditions.

Steep streams may exhibit supercritical, transcritical (with transitions from $Fr < 1$ to $Fr > 1$ and vice-versa) and near critical ($Fr \approx 1$) flow regimes along their reach depending on hydraulic forcing (energy gradient and flow discharge) and bed characteristics (slope, grain-size distribution, arrangement) but also on how they combine to determine flow competency and consequently bed morphologies and actual channel width (see Grant, 1997; Comiti and Lenzi, 2006; Comiti et al., 2009; Lamb et al., 2017; Piton and Recking, 2019). Grant (1997) hypothesised that steep mobile-bed streams, whose flow is competent enough (in terms of erosion and bedload transport capacity) to rework bed and banks, naturally tend towards the critical flow configuration ($Fr = 1$, with $h = h_c$) as this corresponds to the most efficient flow condition for transferring the incoming water flux downstream. Recently, Piton and Recking (2019) produced detailed experimental results concerning the case of unconfined competent flows on steep alluvial fans and substantially confirmed Grant's hypothesis. The flow in such systems likely reaches transcritical and near critical flow regimes rather than a precisely critical configuration (Chanson, 1998; Tinkler, 1998; Piton and Recking, 2019). In case of supercritical flows, features such as standing waves and hydraulic jumps often arise and dissipate flow energy, thereby favouring a flow regime relatively close to the critical conditions (Grant, 1997; Piton and Recking, 2019). These authors agree that fully supercritical flows are

usually transient or limited to short stretches and specific stream configurations. One can more easily observe extensive supercritical flow conditions in steep streams that are laterally constrained (see Discussion in Piton and Recking, 2019).

Depending on the combination of hydraulic, sedimentary and boundary conditions, mountain streams exhibit different bed morphologies (e.g. Palucis and Lamb, 2017). Bedforms may also be responsible of significant fractions of total drag and energy dissipation experienced by the flow. In the following part of this section, I outline the main bedform configurations that can be encountered in steep coarse-bedded streams. The main focus is on antidunes, which are the bedforms studied in this research. Micro-forms (i.e. the smallest bedforms, such as particle clusters) are not described in this short overview; the interested reader may find useful information in the paper by Strom et al. (2004) (and references cited therein).

Bar and pool sequences

In gravel-bed rivers with moderate slope ($\lesssim 2\%$), the most common morphology includes bars and pool-riffle sequences (Fig. 1.2) (Montgomery and Buffington, 1993; Church and Rice, 2009). The configuration is commonly identified as 'alternate bar' where the bars and pools are regularly spaced and alternated near the two banks. Bars are classified as 'free' when they arise from the intrinsic instability of the cohesion-less bed in straight channels with fixed banks and constant width (Colombini et al., 1987).

Figure 1.2: Bars in the River Navisence near Zinal (Canton du Valais, Switzerland) on 24.07.2018 (downstream view). The standing and breaking waves indicate a near critical flow regime. The mean slope was approximately 2% along the visible reach. The scour on the left bank was mainly shaped by an intense flood occurred on 02.07.2018. The bar unit near the right bank emerged during the following weeks.

According to the linear stability analysis conducted by Colombini et al. (1987), free alternate

bars are expected to form in channels in which the width-to-depth ratio exceeds a critical value (see also Redolfi, 2021). Alternate bars can also be triggered or enhanced by a local external forcing, such as channel curvature (Seminara, 1998) and asymmetric bed roughness (Redolfi et al., 2021). In such cases, bars are usually called 'forced' (or 'point') bars. Additionally, bars are often classified as 'macro-forms' (e.g. Jackson, 1975) because their longitudinal size typically scales with channel width (e.g. Seminara, 1998). In gravel-bed rivers, bars and pools are often considered fundamental morphological units, whose sequences may experience a transition towards multiple bars and braided river patterns (e.g. Parker, 1976; Ashmore, 1991b; Ferguson, 1993). For detailed reviews of the scientific literature regarding these morphologies (bars and braided networks), I invite the reader to consult the dissertations by Dhont and Ancey (2018); Papa (2020).

Antidunes

The term 'antidune' is commonly used to identify a bedform characterised by in-phase undulations of bed and water free surface (Kennedy, 1961), which can be observed in supercritical or near critical flows. Despite the term 'antidune' was first proposed by Gilbert and Murphy (1914), the first documented observation of upstream migrating antidunes is probably attributable to Cornish (1899) (see Kennedy, 1961).

Over the last century, antidunes have been studied by a number of researchers, who were likely fascinated by the peculiar upstream migration of such bedforms. An overview of references regarding previous experimental, theoretical and numerical research works is available in the introductory section of Chapter 3. For the sake of minimising repetitions, in the following part of this section is mainly dedicated to the antidune occurrence domain and to the main bedform features. The last two paragraphs concern experimental and field studies with observations of antidunes on steep slopes under flows characterised by high-relative roughness.

Antidunes are usually organised in trains (i.e. sequences aligned in streamwise direction). Figure 1.3 shows a train of upstream migrating antidunes with indications of the bedform wavelength λ and amplitude H_{AD}. A given antidune migrates upstream when sediment erosion and deposition occur predominantly on the bedform lee side and stoss side, respectively (see Fig. 1.3).

In his seminal works, Kennedy (1961, 1963, 1969) presented his theoretical analyses as well as his experimental and field observations regarding both two-dimensional ('long-crested') or three-dimensional ('short-crested') antidunes. According to his studies, three-dimensional antidunes arise from the superposition of longitudinal waves and transversal waves and tend to exhibit shorter wavelength and "rooster tails"—i.e. free surface waves that take a highly three-dimensional shape (elongated in streamwise direction with a sharp shrinkage in the transversal plane) above the antidune crests.

The fundamental step in Kennedy's modelling of dune and antidune mechanics lies in the
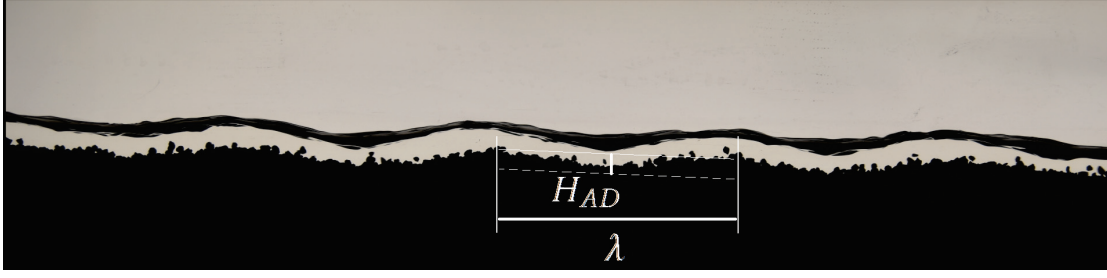
Figure 1.3: Train of upstream migrating antidunes in the experimental setup presented in Chapter 4. Flow from left to right. Flow depth $h \approx 1$ cm, median sediment size $d_{50} = 2.5$ mm.

consideration of a phase lag between bed shear stress and bedload flux over a wavy bed. He proposed (Kennedy, 1963) a relationship—based on potential flow theory—that identifies lower limit of the antidune occurrence domain in the $Fr - k^*$ space:

$$Fr_{\text{cr,low}} = \left(k^*\right)^{-1/2} \left(\tanh k^*\right)^{1/2},$$ (1.9)

where $k^* = 2\pi \overline{h}/\lambda$ is the dimensionless wavenumber.

A second relationship for the upper limit—commonly proposed in stability diagrams—was refined by Reynolds (1965) and reads:

$$Fr_{\text{cr,up}} = \left(k^* \tanh k^*\right)^{-1/2}.$$ (1.10)

Antidunes are predicted in the domain above the Eq. 1.9 curve, whereas dunes are predicted below. Other similar equations for these limits were also proposed by Anderson (1953). According to Kennedy (1963) and Fuchs (1952) the minimum wavelength for long-crested antidunes is given by

$$\lambda_{\text{min K63}} = 2\pi Fr^2 \overline{h}.$$ (1.11)

Therefore, antidunes with $\lambda < \lambda_{\text{min K63}}$ are expected to have 3D morphology. Figure 1.4 displays the antidune occurrence domain (in the $Fr - k^*$ space) and the conditions in which antidunes were observed during the experiments presented in the following chapters of this dissertation.

Antidunes may also experience downstream migration or maintain an approximately stationary position (e.g. Kennedy, 1961). Kennedy (1963) also studied the conditions associated to these different migration behaviours. Unfortunately, considering the potential flow approximation only—with the assumption of the phase lag—does not allow to correctly discriminate
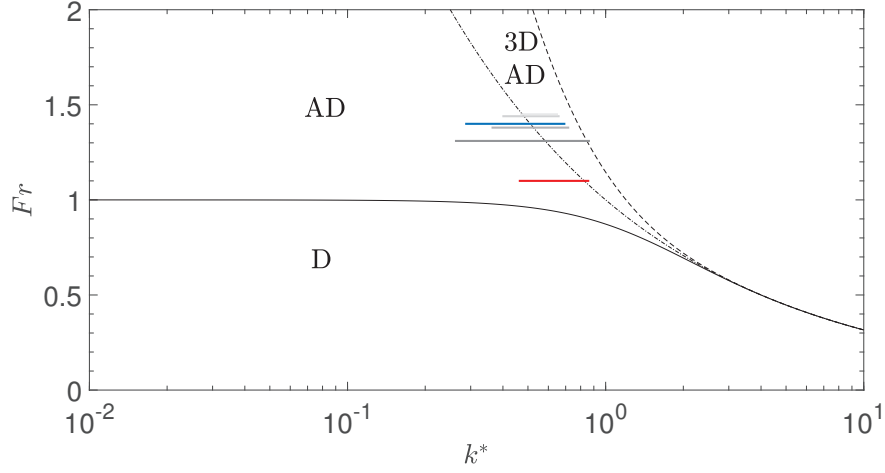
Figure 1.4: Antidune stability diagram (in the $Fr - k^*$ space) according to Kennedy (1963) and Reynolds (1965). The horizontal lines indicate the observations of antidunes conducted during the experimental runs P1 (red), E1–4 (grey shades) and ES1 (blue) presented in Chap. 2, Chap. 3 and Chap. 4, respectively. The continuous, dashed and dash-dotted lines indicate Eq. 1.9, Eq. 1.10 and Eq. 1.11, respectively.

the migration regimes (see Sec. 3 in Bohorquez et al., 2019). Indeed, antidune migration direction results from the flow depth configuration above bed crests and troughs, which ultimately determines the bed shear stress distributions and thus the position of the preferential zones of erosion and deposition—even in absence of phase lag between shear stress and bedload flux (Núñez-González and Martín-Vide, 2011). For instance, downstream migrating antidunes are associated to a deeper flow over antidune trough than over crest, which corresponds to an accelerating flow (preferential erosion) over the antidune stoss side and to a decelerating flow over the lee side (preferential deposition). Upstream migrating antidunes present the inverse situation. Núñez-González and Martín-Vide (2011) analysed the problem by applying Bernoulli's theorem to the streamlines between the cross-sections above the antidune crest and the trough. They found that an 'antidune mobility number' F_a can be used to distinguish antidunes that migrate upstream, downstream or remain stationary. This mobility parameter is expressed as

$$F_a = k_a Fr, \tag{1.12}$$

where $k_a = 2\pi H_m / \lambda$ is a modified dimensionless wavenumber and $H_m = \sqrt{H_{cr} H_{tr}}$ is the geometric mean of the flow depth values over the antidune crest and the trough. Antidunes migrate upstream if $F_a < 1$ and downstream if $F_a > 1$, whereas for $F_a = 1$ the bedform is stationary.

In some cases, antidunes may also experience an hysteresis cycle (Alexander et al., 2001;

Deigaard, 2006). According to these authors, during its growth an antidune may reach a critical steepness that corresponds to a transcritical flow condition above the bedform crest. This transition results in the surface wave breaking and in the bedform obliteration, and the cycle may restart. Form drag related to non-breaking upstream migrating antidunes is expected to be negligible if flow expansion is relatively small (e.g. Fredsøe, 1974).

Other frameworks have been proposed in the recent decades to infer the stability domains of antidunes. In some cases, these models were also able to predict the occurrence domains of other types of bedforms. Among them, the model proposed by Colombini (2004) is based on the application of linear stability analysis to a system of equations composed of the two-dimensional Reynolds averaged Navier-Stokes equations coupled with the Exner equation (Exner, 1925; Paola and Voller, 2005; Coleman and Nikora, 2009). The bedload transport rate was calculated according to the equilibrium relationship proposed by Meyer-Peter and Müller (1948). The major novelty in the approach taken in this work was the calculation of the shear stress at the upper interface of the 'bedload layer' (i.e. an idealised thin layer occupied by the bedload particles that move by saltation) and not at the static bed surface. This minimalistic formulation of the physical interactions between flow, bedload and bed appeared sufficient to 'grasp at least the main features of the mechanism' that leads to bedform instability (Colombini, 2004) and made it possible to predict the formation of two-dimensional (2D) dunes and antidunes. Colombini and Stocchino (2005) showed that decoupling bed and flow dynamics (Kennedy, 1963, an approach introduced by) provides stability fields similar to the coupled analysis for dunes and antidunes but do not predict the instability potentially associated to roll waves for $Fr > 2$. The same authors also extended the stability analysis from the linear to the weakly nonlinear level (Colombini and Stocchino, 2008). An approach that made it possible to estimate equilibrium amplitudes at least for dunes. Later, Colombini and Stocchino (2012) refined Colombini's (2004) theoretical framework by accounting for transversal waves and obtained a unified model for predicting the formation of both two- and three-dimensional bedforms.

Andreotti et al. (2012) built their model with the Reynolds averaged Navier–Stokes equations and modelled the sediment transport with the non-equilibrium formulation by Charru et al. (2004). The resulting model is able to predict the appearance of different bedform types (antidunes but also ripples, rhomboid patterns and bars) for realistic ranges of the Froude number. In the same year, Vesipa et al. (2012) demonstrated that a 1D approximation of the problem based on the combination of the Dressler equations—which include the influence of the flow curvature in the hydraulic modelling—with a non-equilibrium mechanistic sediment transport model is well-suited to predict the antidune marginal stability curves and the most unstable modes of perturbation. In case of hydraulic modelling based on the "shallow-water" (depth-averaged) Saint-Venant equations, instabilities arise only for $Fr > 2$ in the form of roll waves (Balmforth and Provenzale, 2001), unless the shear stress or the sediment transport relationship are modelled in a way that allows the onset of the bedform instabilities (see Bohorquez et al., 2019; Ancey, 2020a). It is important to mention that the generalisation of the Ancey's (2008) model to the continuum form (Ancey and Heyman, 2014) made it possible to

conduct stochastic-deterministic modelling with the Exner equation—expressed in terms of ensemble-averaged particle activity $\langle \gamma \rangle = \langle c \rangle\, V_p / W$—coupled to the Saint-Venant equations (Bohorquez and Ancey, 2015, 2016). Bohorquez and Ancey (2015) showed that this system of equations is unstable and antidunes develop also for $Fr < 2$. The occurrence of instability in these models under slightly supercritical flow conditions is fundamental for predicting antidune formation and for simulating antidunes observed in most flume experiments—in which $1 \lesssim Fr < 2$ (see Bohorquez et al., 2019).

A further advance in the understanding of the bedform instabilities came from taking into account the role of the relative roughness (d/h). Carling and Shvidchenko (2002) proposed a three-dimensional characterisation for dunes and antidunes occurrence domains that includes the relative submergence parameter (i.e. the inverse of the relative roughness) in addition to Fr and k^* and allows for a better description of the dune-antidune transition. Considering this aspect is particularly important in shallow steep streams in which the high relative roughness notably influences the hydraulic resistance experienced by the flow and thus the sediment transport conditions (recall Sec. 1.2.1). Since in flows with relatively high relative roughness ($d/H \gtrsim 0.05$) over coarse sediments ($d \gtrsim 2$ mm) the onset of sediment motion approximately corresponds to near critical or supercritical flow conditions, the unstable two-dimensional bedforms are likely antidunes and not dunes (see Bohorquez et al., 2019) but transitional bedforms may persist depending on boundary conditions and previous history (Carling and Shvidchenko, 2002). The effects on the dune, antidune and roll-waves instabilities related to the combination of Fr, d/h and k^* with the bed shear stress conditions ($\Theta \leftrightarrow \Theta_c$) were effectively synthesised by Bohorquez et al. (2019) in their model.

Antidunes in steep streams characterised by high relative roughness ($d/H \gtrsim 0.1$) were studied in flume experiments (Cao, 1985; Recking et al., 2009; Mettra, 2014; Inoue et al., 2020) and seldom in field cases (e.g. Froude et al., 2017). Observations regarding bedforms in these conditions are extremely valuable for comparisons with results of theoretical and numerical models in which hydraulic and sediment transport modellings has necessarily to be based on relatively large approximations. Experimental data may prove directly useful to understand the dependencies of certain processes or bedform features on physical parameters. Concerning upstream migrating antidunes, Recking et al. (2009) proposed a formula for estimating the dominant antidune wavelength. The authors formulated this relationship (reported in Chap. 3) on the basis of dimensional analysis supported by a large experimental dataset. Another example of the usefulness of experimental studies comes from the documented observation of the coexistence between sequences of 3D downstream migrating antidunes and bars in flume experiments recently conducted by Inoue et al. (2020), who also proposed an analytical model to predict the number of antidune trains in presence of bars. Figure 1.5 shows a similar case with bars coexisting with upstream migrating and nearly stationary antidunes observed by the candidate during a flume experiment (not presented in this dissertation).

In gravel-bed streams and rivers, direct observation and recognition of antidunes is often complicated by the opaque water conditions and by possible difficulties in accessing the
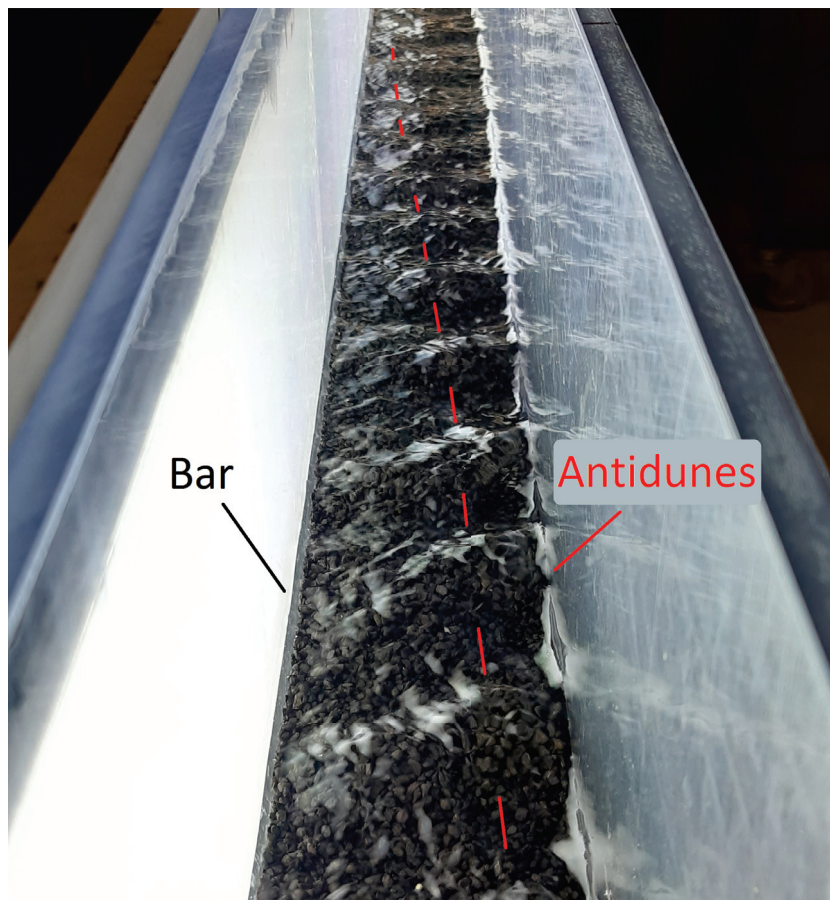
Figure 1.5: Coexistence of bars with a train of antidunes. The flume was 8 cm wide. The flow depth values ranged between 0.5 and 1.5 cm. The sediments were well-sorted with median diameter d_{50} = 2.7 mm. Flow from bottom to top.

sites during floods. Even when a site is accessible, monitoring the bed topography remains technically difficult and may be hazardous for both the operators and the equipment due to the fast sediment-laden flow. Therefore, the presence of antidunes is usually deduced by observing the geometry and behaviour of trains of surface waves potentially associated with these bedforms (e.g. Tinkler, 1997) and/or by analysing the sedimentary structures after the event (e.g. Shaw and Kellerhals, 1977). Isolated observations based on these indirect methods are prone to large uncertainties but in some cases image-based monitoring of the wave trains and sedimentary record analysis could be advantageously combined to obtain more robust results (see Froude et al., 2017). For other examples of trains of surface waves see Fig. 1.6 (River Dora Baltea, Fénis, Valle d'Aosta, Italy), the video https://youtu.be/hDTjCkXrpGA?t=137 from 2'17" to 2'27" by Zufferey (2018) (River Navisence, Zinal, Canton du Valais, Switzerland) and Fig. 2 by Recking et al. (2009) (Arveyron, Chamonix, Haute-Savoie, France).

Figure 1.6: Train of standing waves potentially associated with antidunes in the River Dora Baltea observed on 10.07.2020 near Fénis (Valle d'Aosta, Italy). The surface waves (4 to 6) were nearly stationary but they broke irregularly. Flow from left to right. The triangles indicate the wave crests. The picture was taken right after the wave under the left-hand side triangle experienced a sudden amplitude decrease. The distance in streamwise direction between the first and the fourth wave was approximately 20 m. The slope of this reach is approximately 1%.

Step-pool type sequences

Steps are transversal alignments of coarse sediments (usually cobbles and boulders) across the stream that separate pools partially filled by finer sediments (Chin and Wohl, 2005). An example of step-pool sequence is presented in Fig. 1.7. Some authors classify as "cascade morphology" a configuration in which the steps do not span the entire channel width and the flow assumes a marked three-dimensional pattern (e.g. Montgomery and Buffington, 1993, 1997). Step-pool morphology is common in steep mountain rivers, especially where bed slope values exceed 3–5% (Montgomery and Buffington, 1993, 1997; Church, 2006) and the size of sediments (and wood debris) is large compared to the typical flow depth and channel width (Chin and Wohl, 2005). Steps are typically formed, destroyed and reshaped under intense flood events that mobilise also the coarsest grain fraction (Montgomery and Buffington, 1997; Lenzi, 1999, 2001; Turowski et al., 2009; Molnar et al., 2010; Recking et al., 2012a). After these infrequent events, the longitudinal stepped profile may undergo minor adjustments, pool scouring and armouring during minor floods (Lenzi, 2001).

Flow configuration in step-pool sequences may vary depending on their specific slope and geometry, on their grain distribution and on the flow discharge (see Comiti and Lenzi, 2006; Church and Zimmermann, 2007). In case of transcritical flow regime (with critical or super-critical flow over the steps and subcritical flow in the pools), the 'spill resistance' (Leopold et al., 1960) related to hydraulic jumps or to large turbulent eddies (generated by the flow that plunges in the pool) may dissipate a large fraction of the flow energy (e.g Curran and Wohl, 2003).

Different hypotheses on the formation mechanisms of step-pool sequences were proposed and discussed during the last decades (see Richardson and Carling, 2021). For instance, Whittaker and Jaeggi (1982) observed in flume experiments that step-pool sequences may originate from antidune sequences following depositions of large grains on the antidune crests, whereas Grant (1994) hypothesised that they may arise from antidune merging events. For others, the jamming of the largest grains at random locations along a relatively narrow reach (with subsequent imbrication of other sediments) is the most probable formation mechanism (e.g. Zimmermann and Church, 2001; Church and Zimmermann, 2007). Given the importance of steps and pools for the ecology and dynamics of steep streams, the origin and evolution of step-pool morphology still stimulate research works and debate (see the recent works by Golly et al., 2019; Richardson and Carling, 2021).
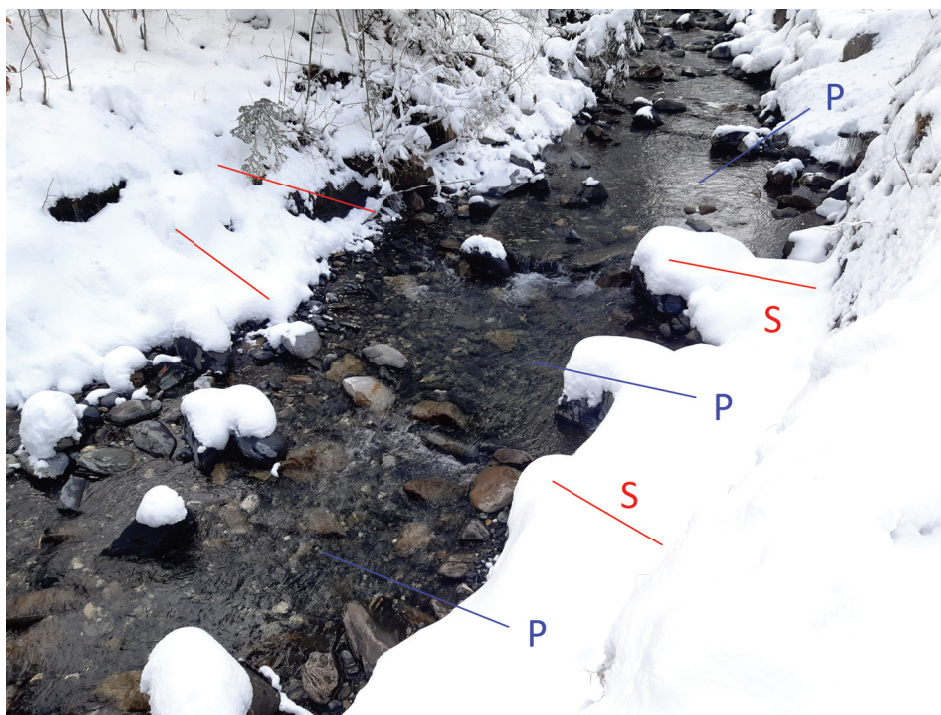
Figure 1.7: Short step-pool sequence in the Avançon de Nant near Les Plans-sur-Bex (Canton Vaud, Switzerland). The step axes (S) and the positions of the pools (P) are indicated.

This short overview does not cover cyclic steps and similar forms. Such bedforms—whose sequences are strictly associated with sequences of persistent hydraulic jumps—share similarities with antidunes and step-pool configurations but their onset requires a predominantly suspended sediment load (Yokokawa et al., 2011). The interested reader is invited to consult the review on cyclic steps that was recently written by Slootman and Cartigny (2020).

Bedform migration and bedload pulses

A number of investigations were dedicated to bedload pulses caused by bedform migration and to the associated bedload transport intermittency in presence of bedforms (e.g. Hamamori, 1962; Gomez et al., 1989; Bunte and Abt, 2005; Singh et al., 2009). Interestingly, bedload transport rate fluctuations induced by migration of meso-forms (i.e. bedforms whose typical size scales with flow depth such as dunes) or macro-forms (such as bars) usually exhibit a periodical behaviour (see Gomez et al., 1989). The periodicity of the pulses might be more or less constant depending on the variability of bedform shape and migration celerity and on the possible superimposition of the bedforms (see Gomez et al., 1989).

In the 1960s, the studies regarding bedform-induced pulses focused on dunes and mild slope rivers. The first formula for estimating the mean bedload transport rate associated with the downstream migration of dunes was proposed by Richardson et al. (1961); Simons et al. (1965) in the form:

$$\overline{q}_\mathrm{s} = \frac{1}{2}\left(1-p\right)H_{dune}\,c_{dune},\tag{1.13}$$

where p is the porosity of the sediment mixture, H_{dune} is the mean dune amplitude and c_{dune} is the mean dune celerity in downstream direction. It is worth mentioning that this expression was conceived during a campaign of flume experiments in which the bed elevation times series were collected at a fixed point by using an echo sounder (Richardson et al., 1961; Simons et al., 1965).

Always in the 1960s and inspired by experimental observations, Hamamori (1962) derived a relationship for the probability distribution of bedload transport rate fluctuations caused by the downstream migration of fast triangular bedforms superimposed on a 'primary' dune (for details and discussion see Turowski, 2011). The cumulative probability distribution of bedload transport rate fluctuations according to Hamamori (1962) is

$$F\left(\frac{q_\mathrm{s}}{\overline{q}_\mathrm{s}}\right) = \frac{q_\mathrm{s}}{4\overline{q}_\mathrm{s}}\left[\ln\left(\frac{4\overline{q}_\mathrm{s}}{q_\mathrm{s}}\right)+1\right],\tag{1.14}$$

where F is defined for $0 \le (q_\mathrm{s}/\overline{q}_\mathrm{s}) \le 4$.

Later, other authors investigated the characteristics of superimposed ripple-dune patterns in sandy beds (e.g. Nordin and Algert, 1966; Hino, 1968; Jain and Kennedy, 1974; Nikora et al., 1997; van der Mark et al., 2008) and understood that synthesising these patterns with mean estimates of dune amplitude and celerity was an oversimplification. These studies stimulated the understanding of the multi-scale nature of ripple-dune fields, in which bedforms usually do not behave as travelling waves with constant geometry and migration celerity (Nikora et al., 1997; Singh et al., 2011; Guala et al., 2014). Accordingly, relationships for estimating the

mean bedload transport rate from spectral analysis of the bed elevation perturbation data were proposed (e.g. Nikora, 1984; Guala et al., 2014). These integral expressions account for the different contributions to $\overline{q}_s$ of different wave modes that compose the bedform pattern, which are characterised by variable size and scale-dependent celerity.

Hamamori's pioneering formula (Eq. 1.14) predicts a maximum amplitude of $4\,\overline{q}_s$ for the q_s fluctuations. Unfortunately, this relationship cannot explain the large bedload pulses (q_s peaks up to $10\,\overline{q}_s$) observed during flume experiments (with gravels, constant water discharge and steady sediment supply) in presence of alternate bars (Dhont and Ancey, 2018) or upstream migrating antidunes (see run *2deg3v* in Mettra, 2014).

Concerning the case of upstream migrating antidunes in steep streams, Mettra (2014) analysed the scatter of antidune geometry and celerity values. He also proposed two relationships (inspired by Simons' formula (1965)) for estimating the maximum (and mean) magnitude of the local bedload pulses from the maximum (and mean) values of antidune amplitude and celerity. Remarkably, Mettra (2014) suggested that large bedload pulses may be also caused by episodic granular avalanches on the antidune lee sides, especially on steep slopes under weak bedload transport intensity. Since the antidune migration direction is opposite to the bedload flux direction, the relative antidune celerity depends not only on the lee-side erosion but also on the fraction of bedload that deposits over each stoss side. Therefore, the application of the framework based on travelling waves proposed by Simons et al. (1965) requires precise information on the bedload fractions eroded and deposited locally. For the same reason, the integral relationships proposed by Nikora (1984) and Guala et al. (2014) are not directly applicable for quantifying the contributions of upstream migrating antidunes to the mean bedload transport rate.

1.2.3 Experimental facilities and techniques

The contributions presented in this dissertation were driven by a predominantly experimental approach. In this section, I outline the reasons that guided me to choose the setups and techniques used for my experiments. I provide a brief review of facilities and techniques that have been used in similar studies for setting the physical conditions of the experiments and for monitoring bedload transport rates and bed topography. To avoid redundancy with the main chapters of the dissertation, the detailed descriptions of the specific experimental setups and methods (techniques and data processing procedures) used for each experimental campaign of this research work are provided in a dedicated section of each chapter.

Narrow flumes and setups

As I will detail in the next section, the focus of this experimental investigation is on bedload transport fluctuations and their relationships with bedform dynamics under conditions that are representative of those encountered mountain streams. The reference conditions that

I considered for reproducing bedload transport and bed morphodynamic phenomena in simplified flume experiments are:

(i) shallow turbulent flows in supercritical regime ($1.1 < Fr < 1.5$ and $d_{50}/\overline{h} \approx 0.25$–$0.4$);

(ii) steep bed slope (mean bed slope $\overline{\psi} = 1$–$3°$);

(iii) erodible bed composed of well-sorted coarse sediments;

(iv) weak to moderate bedload transport intensities ($1 \simeq \Theta/\Theta_c \leq 1.6$);

(v) quasi two-dimensional (2D) bedforms (antidunes);

(vi) flow resistance and turbulence primarily influenced by the bed roughness.

The main experiments were conducted under steady-state conditions (that is, constant water discharge and steady sediment supply) and near-constant mean bed slope angle (no significant trend of net bed erosion or deposition at the flume scale during the experimental run). The bedload transport rate and bed topography data presented for each experiments were collected after the system reached steady-state conditions (unless otherwise indicated). Basket sampling at the flume outlet as well as visual analyses of the bed profile were conducted during the preliminary phase of each experiment to assess the proximity to these quasi-equilibrium conditions. The adjustment time interval before reaching quasi-equilibrium was in some case longer than 10 hours (e.g. E1, Chap.2). Only one experiment presented in this dissertation (see Chap. 4) was deliberately conducted under bed degradation conditions, after the interruption of the active sediment supply at the flume inlet. Concerning the bedload transport intensity, the lowest mean bedload transport rate imposed during the experiments corresponded to $\overline{q}_s = 2.5 \cdot 10^{-6}$ m^2 s^{-1} (run P with $\Theta/\Theta_c = 1.02$), whereas the highest corresponded to $\overline{q}_s = 6.1 \cdot 10^{-5}$ m^2 s^{-1} (run E4 with $\Theta/\Theta_c = 1.62$).

To study the interplay between the fluctuations in the bedload transport rate and the antidune morphodynamics as much isolated as possible from collateral processes, I paid particular attention to avoid the onset of unsteady flows, irregularities in the sediment supply, grain sorting processes and three-dimensional macro-forms. These constraints had to be combined with the available laboratory space, the budget and the facilities already available in the laboratory at the beginning of this research. Since the steadiness of the sediment supply is a fundamental factor to ensure steady-state conditions (especially at weak bedload transport intensity), I decided to use well-sorted fine gravel (d_{50} in the 2–3-mm range) that was compatible with a recent modular feeder already available (see Fig. 3.1 and details in Section 3.2). For given well-sorted coarse sediments, respecting the conditions (i-vi) previously mentioned implies the use of relatively narrow flumes ($d_{50}/W \lesssim 0.2$). A tilting flume setup was already available at the beginning of my doctoral studies—it was built by Mettra (2014) and used also by Heyman (2014). During preliminary tests with the available setup, I verified that using well-sorted fine gravel ($d_{50} \simeq 3$ mm) I could only conduct experiments in which antidunes coexisted with alternate bars in the original flume configuration ($W = 8$ cm, see Fig. 1.5). After these preliminary

tests, I decided to adapt this setup by adding a 2.5-–m-long 4–cm-wide transparent flume inside the existing one (see Fig. 3.1). This flume was used for the experiments presented in Chapter 2 and Chapter 3 (see the specific arrangements in Sec. 2.3 and Sec. 3.2). We designed and built a second flume setup (total length of 6.5 m, width of 4 cm), which was used for the investigation presented in Chapter 4 and will be used for future experimental campaigns. During all the experiments presented in this dissertation, the water flow recirculation was controlled with centrifugal pumps and the sediments were not recirculated.

The experiments performed in such narrow flumes are extremely simplified models of natural streams. They were designed to study bedload transport and bed morphodynamics with a reasonable compromise between physical representativeness of phenomena that occur in steep streams and ease of collection of accurate data with high spatial and temporal resolution—which were essential also for assessing the experimental conditions. I did not design the experiments to reproduce a specific real-world stream. Steep and narrow stream reaches with man-made concrete banks (or bedrock banks) and bed composed of well-sorted coarse sediments are the river systems that may likely experience flow, bed morphology and bedload transport processes the most similar to those investigated in this dissertation.

Methods for bedload flux monitoring

Nowadays, two families of techniques are conventionally used for high-resolution bedload transport measurements in laboratory experiments: image-based techniques and techniques based on impact plates (and accelerometers) for particle impulse detection (see Dhont et al., 2017). A remarkable example of different technique is the system based on load cells developed by Singh et al. (2009). Imaging techniques were successfully used over the last two decades to monitor bedload fluxes or particle motion in many research works, that covered a variety of flow conditions and specific requirements (e.g. Frey et al., 2003; Radice et al., 2006; Zimmermann et al., 2008; Roseberry et al., 2012; Heyman et al., 2016; Terwisscha van Scheltinga et al., 2021). It is also worth mentioning the pioneering field observations conducted by Drake et al. (1988). The main advantages of the image-based techniques in laboratory settings are (i) their application flexibility (provided the possibility of collecting images of reasonable quality at suitable temporal frequency) and (ii) the type and quality of information (e.g. particle trajectory, grain size, velocity) to which they give access, especially in case of particle tracking measurements. Particle tracking (or PTV, for Particle Tracking Velocimetry) is a term that indicates a class of sophisticate methods that can provide highly accurate particle trajectory data—also over mobile bed (e.g. Roseberry et al., 2012; Heyman, 2019)—provided good imaging conditions. Its main negative points are the computational and economic costs of implementation (Dhont et al., 2017).

Impact-plate techniques were also used, particularly in cases that required cost-effective solutions for long-lasting monitoring (Dhont, 2017). Dhont et al. (2017) demonstrated that impact-plate bedload flux monitoring can provide results as accurate as particle tracking if the impact plates are installed vertically (e.g. Mettra, 2014; Dhont, 2017), an original technique

that was developed at the EPFL-LHE Laboratory (see Mettra, 2014; Heyman et al., 2013). Different systems with geophones and plates (installed horizontally) were previously developed specifically for field monitoring by Rickenmann and McArdell (2008). Generally, both techniques (image-based and vertical impact plates) may provide accurate results under low to moderate bedload transport conditions and the choice of the better solution is often driven by the specific experimental setup and by the investigation purposes (Dhont et al., 2017).

Concerning the experimental study presented in this dissertation, we wanted to compute both particle fluxes (across a control surface) and volume-averaged transport rates (see Chap. 2 and Chap. 4). As volume-averaged transport rates require the estimation of particle activity and velocity (e.g. Eq. 1.3), the image-based methods were selected. We also tested the impact-plate technique—to use it as a complement to particle imaging—but we concluded that the fine gravel ($d_{50} \simeq 3$ mm) did not produce a signal-to-noise ratio sufficiently high to obtain a satisfactory accuracy. The signal-to-noise ratio could be improved but this would have requested additional tests to find the most suitable plate stiffness and plate-accelerometer coupling. We applied image-based methods for bedload transport monitoring in all the experiments presented in this dissertation together with basket sampling. The specific settings and procedures are described in each chapter. Image analysis and particle tracking were used also to monitor the sediment supply rate (during the calibration and preliminary tests and continuously during the runs ES1 and ES2).

Methods for bed topography monitoring

Concerning the monitoring of the bed topography and of the flow depth distribution, the choice of the method in our setup was relatively simple. We took advantage of the flume narrowness and of the quasi-2D configuration of flow and bed topography; we monitored the bed elevation and the flow depth by continuously filming the bed profile from the side. This kind of technique (already used by other researchers, e.g. Mettra, 2014; Heyman, 2014) involves image processing operations with detection of the bed-water and water-air interfaces. Simple binarisation filters or other segmentation techniques can be applied quite easily with good results, provided the use of back-lights to ensure sharpness and contrast of the interfaces. The lateral camera can be operated with long or short exposure times to improve the sharpness of the image or to get rid of the moving grains, respectively. Mettra (2014) opted for the second solution. During the experimental campaign presented in Chap. 3 we tested a different approach. We combined sequences of images collected at short time intervals (framerate $\geq$ 60 fps) to recover an image similar to those collected with longer exposure times. According to these tests, using long-exposure images or single images (sharper, with post-filtering) produced only minor differences in the resulting bed topography profiles (in terms of antidune wavelength distribution). The difference appeared more pronounced for the flow depth monitoring. The long-exposure images resulted in depth profiles that were more uniform than those calculated from the single sharp images. This result for the flow depth was expected because the oscillations of free surface were obviously smoothed. The

two techniques have advantages and disadvantages. Using longer exposure times provides bed topography data that are less affected by the noise due to moving grains and errors in the detection of the free surface. On the other hand, this "noise" can be helpful to interpret the changes in the topography over time (it indicates the zones in which particle bursts likely occurred). Details concerning the specific monitoring setups and procedures can be found in Chap. 3 and Chap. 4.

In wider flumes, bed morphologies and flow field are often three-dimensional (e.g. bars, three-dimensional dunes, etc.). This difference makes the topographic monitoring more difficult. Bed topography and flow depth monitoring in such cases can be conducted by using arrays of ultrasonic probes, sonar probes or a combination of ultrasonic probes and laser-sheet imaging techniques (e.g. Singh et al., 2011; Visconti et al., 2012; Dhont, 2017; Vesipa et al., 2017). The techniques developed by Visconti et al. (2012), Dhont (2017) and Vesipa et al. (2017) make it possible to collect bed topography data and water depth data without necessarily interrupting the water flow. An additional issue that arises with this type of laser scanning techniques is related to a sampling problem in which the sampling frequency should be carefully adjusted to properly capture the variations in the morphologies (see Vesipa et al., 2017). This sampling issue would be particularly difficult to tackle in case of 3D monitoring of rapidly changing antidunes (see also Inoue et al., 2020). Inoue et al. (2020) adopted an original technique based on laser-induced fluorescence (LIF) (with a laser sheet projected vertically at a cross-section) and high-speed imaging (from both the downstream direction and the side) to monitor the shape of the flow free surface over 3D antidunes and bars (at a fixed location). Another photogrammetric technique, called Structure-from-Motion, has been developed recently (Westoby et al., 2012) and already proved useful in many experimental setups, especially with braided morphology (e.g. Papa, 2020) but also in presence of dunes (e.g. Terwisscha van Scheltinga et al., 2020).

1.3   Objectives and research contributions

The purpose of this dissertation is to improve the understanding of bedload transport processes and bed morphodynamics in steep streams. Since bedform migration has been identified as one of the causes of large bedload pulses, the focus of this research work is on bedload transport rate fluctuations and their interplay with upstream migrating antidunes at low to moderate bedload transport intensity (mostly under steady-state conditions). Although antidunes are not the only bedforms that can develop in steep streams (recall Sec. 1.2.2), they are taken as the reference bedform type for this study as the investigation focuses on streams under supercritical flow conditions.

The main goal is to investigate the links between the temporal scales of bedload transport rate fluctuations and those of antidune migration. The study is articulated in four main objectives that are functional to achieve this goal:

(i) To define and test a framework for assessing the sampling-time-dependent uncertainty of mean bedload transport rates.

(ii) To assess the variability ranges of antidune wavelength and celerity on steep slopes.

(iii) To identify consistent relationships for describing the antidune morphodynamics based on the analysis of antidune wavelength and celerity ranges and of their dependency on bedload supply and hydraulic forcing under steady-state conditions.

(iv) To assess how the sampling time required for the convergence of the time-averaged bedload transport rate towards the bedload supply rate is interconnected with the migration period of antidunes.

1.4 Dissertation outline

After this introductory chapter, this dissertation continues with three main chapters that precede the conclusive chapter. The thesis is structured as a compilation of articles following the EPFL guidelines. The next two chapters are published articles, whereas the third (Chapter 4) is a manuscript under preparation for submission to a peer-reviewed journal.

Chapter 2 is the contribution that addresses the first objective outlined in the previous section. It presents a study on how mean and variance of bedload transport rates are influenced by the sampling time and by other variables—depending on how the bedload transport rate is defined and measured and on the bedload transport conditions. A protocol for estimating mean bedload transport rates and especially their variance is presented. New data from a flume experiment in which bedload transport was monitored at high-temporal resolution are presented. The protocol was tested in this best-case scenario in which detailed information on particle motion was available but also in other cases of interest for laboratory and field applications.

Chapter 3 describes the experimental investigation devoted to the variability of antidune geometry and migration celerity (the second objective of this dissertation). Four experimental runs in which antidunes developed and migrated upstream under steady-state conditions are presented. Processing the bed topography data collected during each experiment made it possible to obtain the wavelength-celerity spectrum of the antidune pattern. These spectra were analysed with the aim to address the third objective of this thesis. This analysis provided a dimensionless relationship between antidune wavelength and celerity that embeds the effects of the bedload flux forcing on antidune morphodynamics.

Chapter 4 regards a study on the interplay between bedload transport rate fluctuations and antidune migration in which I combined methods already used or proposed in the two previous chapters with some complementary method. The analyses of new experimental data (bedload fluxes and bed topography data) are presented. This chapter covers the research work conducted to achieve the fourth objective of this thesis and to corroborate the findings

of the two previous articles.

In Chapter 5, the main outcomes of this dissertation are summarised and their contribution to a better understanding of bedload transport processes and bed morphodynamics in steep streams is outlined. I also provide some perspectives for future developments.

2 Estimating Mean Bedload Transport Rates and Their Uncertainty

Christophe Ancey[1] **and Ivan Pascal**[1]

[1] Laboratory of Environmental Hydraulics, École Polytechnique Fédérale de Lausanne, Lausanne, Switzerland.

Doctoral candidate's contribution

For this chapter, the theoretical framework and the protocol with the application of the bootstrap method were ideas developed by Prof. Ancey, who wrote most of the manuscript. The candidate designed the experiment (after discussions with Prof. Ancey), carried out the experiment and processed the image data to obtain the dataset of the particle trajectories. The candidate post-processed the trajectories to obtain the data regarding particle flux, number of moving particles in the control windows and their velocities, which were then used by Prof. Ancey to develop and test the protocol. The candidate provided few comments on the manuscript draft and mainly wrote the sections related to the experimental setup, the particle tracking method and the influence of bedforms. The supplementary material related to the tracking method was also authored by the candidate. The modification of the LAP algorithm available in the Track-Mate platform was an original idea of the candidate and was implemented in the code by Jonas Jaggy during his semester project, supervised by the candidate.

Abstract

Measuring bedload transport rates usually involves measuring the flux of sediment or collecting sediment during a certain interval of time Δt. Because bedload transport rates exhibit significant non-Gaussian fluctuations, their time-averaged rates depend a great deal on Δt. We begin by exploring this issue theoretically within the framework of Markov processes. We define the bedload transport rate either as the particle flux through a control surface or as a quantity related to the number of moving particles and their velocities in a control volume. These quantities are double-averaged, that is, we calculate their ensemble and time averages. Both definitions lead to the same expression for the double-averaged mean rate and to the same scaling for the variance's dependence on the length of the sampling duration Δt. These findings lead us to propose a protocol for measuring double-averaged transport rates. We apply this protocol to an experiment we ran in a narrow flume using steady-state conditions (constant water discharge and sediment feed rates), in which the time variations in the particle flux, the number of moving particles, and their velocities were measured using high-speed cameras. The data agree well with the previously defined theoretical relationships. Lastly, we apply our experimental protocol to other flow conditions (a long laboratory flume and a gravel-bed river) to show its potential across various contexts.

2.1 Introduction

2.1.1 Bedload Transport Rate and Fluctuations

Whether measuring bedload transport rates in the field or the laboratory, we are faced with a three-part problem. Firstly, there is no universally accepted definition of the bedload transport rate $\mathcal{Q}_s$, and various definitions have been used depending on the context (Ballio et al., 2014; Furbish et al., 2017; Ballio et al., 2018). For instance, in the laboratory, it has long been common to collect the sediment transported to the flume outlet over a given time interval and weigh it to deduce a time-averaged value of $\mathcal{Q}_s$. Today, techniques based on impact plates, acoustic sensors and image processing enable high-frequency measurements of $\mathcal{Q}_s$ (Singh et al., 2009; Gray et al., 2010; Tsakiris et al., 2014; Rickenmann et al., 2014; Mendes et al., 2016; Geay et al., 2017). In both cases, $\mathcal{Q}_s$ is defined as the particle flux through a surface. Alternatively, in the field, using tagged particles (tracers) has long been the simplest way of measuring transport rates(Wilcock, 1997b), with $\mathcal{Q}_s$ reflecting the complex history of the particles entrained by the flow and subsequently deposited (or possibly buried) on the streambed (Einstein, 1950). Secondly, measuring sediment transport rates (i.e., the displacements and velocities of sediment, and the number of moving particles) remains an enormous technical challenge. Geophones and seismic sensors can only provide proxy calculation methods, which can be related to $\mathcal{Q}_s$ after signal processing (Gray et al., 2010). Discriminating between the various processes (multiple impacts, differently sized sediment, rolling or saltating sediment) is fraught with difficulty (Wyss et al., 2016; Dhont et al., 2017; Dietze et al., 2019). Thirdly, recorded transport rates exhibit very significant non-Gaussian fluctuations even under steady-state flow conditions (Ancey et al., 2008; Ancey and Heyman, 2014). When both the sediment feed rate and water discharge vary over time, it becomes extremely difficult to separate the various random particle movement and bedform migration components of fluctuation and to disentangle the timescales associated with each process (Dhont and Ancey, 2018).

Although the existence of wide fluctuations in bedload transport rates—and their influence on their mean rate estimates—has long been known (Gomez, 1991; Bunte and Abt, 2005; Singh et al., 2009; Recking et al., 2012b), some scientists show little awareness of the crucial influence of measurement protocols, particularly the definition of sampling duration, when estimating mean transport rates and their associated uncertainties. Very few experimental papers have specified how accurate their bedload transport rate measurement was. In many cases, authors mentioned that because they had achieved steady-state conditions, collecting sediment at the flume outlet over durations of 1 min or so, was sufficient to obtain the mean transport rate. Setting an arbitrary sampling duration is, however, seldom satisfactory. Figure 2.1 provides a typical example of how sensitive the time-averaged particle flux $\overline{\Phi}_s$ is to sampling durations (see the captions of Fig. 2.1 or Eq. (2.1) for the definition of $\overline{\Phi}_s$). The mean particle flux was measured in the middle of the flume using image processing (see Sec. 2.3 and Sec. 2.4 for further information). Although the feed rate Q_{in} was constant at the flume inlet (set to 10.3 grains/s), the instantaneous particle flux exhibited fluctuations as large as $5Q_{in}$, causing the time-averaged particle flux $\overline{\Phi}_s$ to deviate substantially from its steady-state value Q_{in}.
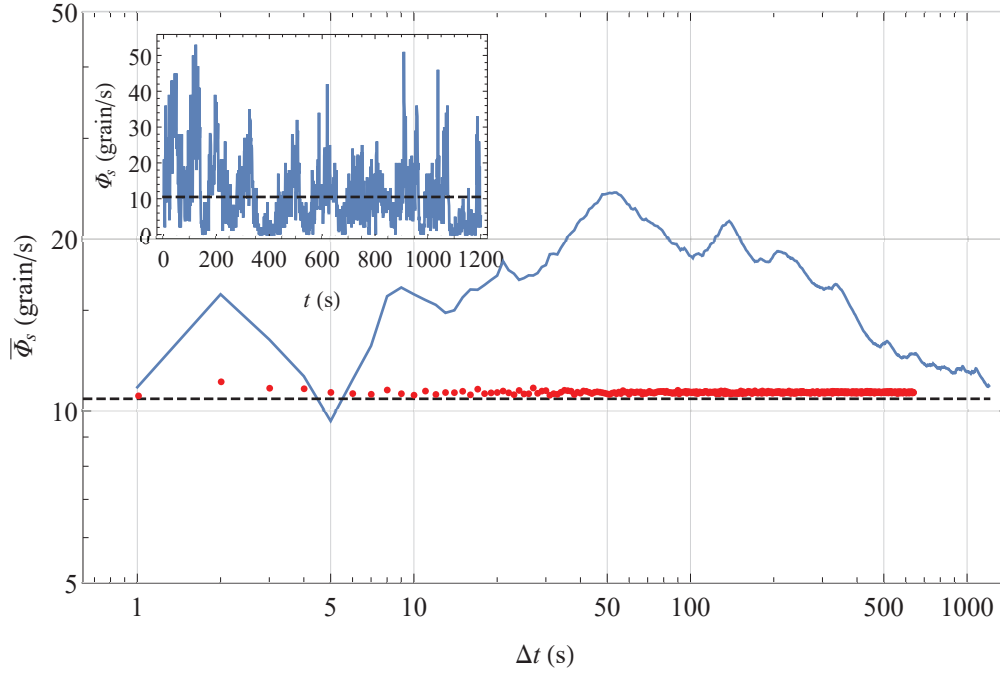
Figure 2.1: Variation in the time-averaged particle flux (solid line) $\overline{\Phi}_s = (\Delta t)^{-1} \int_0^{\Delta t} \Phi_s(t)\mathrm{d}t$ with sampling duration Δt. The instantaneous particle flux $\Phi_s(t)$ was measured by counting the number of particles crossing a control surface located at the flume outlet during a time interval $\delta t = 4$ ms. The flume was 2.5 m long and tilted at $1.55°$ to the horizontal (see Sec. 2.3 for further information on the experiment). The horizontal dashed black line shows the feed rate $Q_{in} = 10.3$ grains/s. The inset shows the time variations in the instantaneous particle flux Φ_s. The red dots show the mean particle fluxes computed using our proposed protocol based on the bootstrap method (see Sec. 2.2.7).

Convergence towards the steady-state value Q_{in} was quite slow: sampling durations should exceed 20 min to get the mean particle flux to within 5%; with other flumes and experimental conditions, we had to wait 100 hours (Dhont and Ancey, 2018). Thus, although it has often been overlooked in research papers to date (Ancey, 2020b), we believe that proper estimation of the uncertainties associated with bedload transport measurements should be a central issue in any experimental protocol.

The uncertainty principles in physics (e.g., Heisenberg's principle) and signal processing (e.g., Gabor's principle) set limits to the precision with which certain physical properties can be measured simultaneously. One can intuitively understand that calculating bedload transport also involves a trade-off between the level of noise and the representativeness of time-averaging: if a short sampling duration is selected, the time-averaged flux $\overline{\Phi}_s$ is representative of the mean local bedload transport rate, but it is also associated with a lot of noise ($\overline{\Phi}_s$ variance is large). On the contrary, if a long sampling duration is selected, the variance of $\overline{\Phi}_s$ is small, but $\overline{\Phi}_s$ may be biased, especially under time-dependent flow conditions (Ballio et al., 2014).

2.1.2 Objectives

The present paper proposes a method for estimating the average and variance of a particle transport rate $\mathscr{Q}_s$ when a $\mathscr{Q}_s$ time series is available. We consider two definitions of bedload transport rate (see Sec. 2.2): firstly, measuring a particle flux through a control surface (e.g., using geophones or image processing), or secondly, measuring particle displacements and velocities in a control window (e.g., using a high-speed camera or an acoustic doppler velocimetry profiler). We are aware that these definitions may not cover all conditions and measurement techniques, but at least they correspond to techniques commonly in use today. The theoretical underpinnings are based on the stochastic bedload transport model developed by Ancey et al. (2008). When sufficient statistical information can be inferred from experimental data, an alternative to calculating the time-averaged particle flux is the use of renewal theory (see Appendix B). Both methods involve high-frequency measurement of the instantaneous transport rate (typically higher than 1 Hz). When high acquisition frequencies are impossible, the central limit theorem provides the asymptotic variation of the $\overline{q}_s$ variance with sampling duration Δt. This method has been successfully applied to various set-ups in well-controlled laboratory experiments (see Sec. 2.4). We present two other applications to demonstrate that the proposed method can be used in various settings (see Sec. 2.5).

2.1.3 A Toy Model

To give a foretaste of the ideas developed in this paper, we consider a virtual experiment. Particles arrive randomly in a flume at a rate $\nu = 1$ grain/s and cross a control surface $\mathscr{S}$ (see Fig. 2.2(a)). By counting the number N of particles that have crossed $\mathscr{S}$ during the time interval Δt, we can estimate the mean particle flux as $\overline{\Phi}_s = N/\Delta t$. Because bedload transport exhibits large non-Gaussian fluctuations, even under steady state conditions, we obtain different $\overline{\Phi}_s$ values depending on when we start the measurement or which path is selected. Figure 2.2(b) shows eight replicates from the same experiment: particle arrival is described as a Poisson process (as we will see later, this is a fair assumption when bedload transport is weak), all paths are realizations of the Poisson process with rate $\nu = 1$ grain/s, and thus the number of particles crossing $\mathscr{S}$ over a time interval Δt varies from one run to another. If we consider the specific run whose endpoint is B (at time $t = 20$ s) in Fig. 2.2(b), we find that $N = 4$ for $\Delta t = 10$ s (point A), and thus $\overline{\Phi}_s = 4/10 = 0.4$ grains/s, a value 60% off the mean rate ν.

How can we improve accuracy? The simplest idea is to increase the time interval Δt. By taking $\Delta t = 20$ s, we find $N = 15$ (point B) and thus $\overline{\Phi}_s = 15/20 = 0.75$ grains/s. The error has dropped to 25%. This is consistent with what (Bunte and Abt, 2005) and (Singh et al., 2009) showed in their field and laboratory experiments: the sample mean and variation vary with increasing sampling durations, and the longer the sampling duration, the lower the error. There are two problems with this approach. Firstly, in practice, it is difficult to take long sampling durations, especially if the flow is time dependent. Secondly, when computing the time-averaged flux
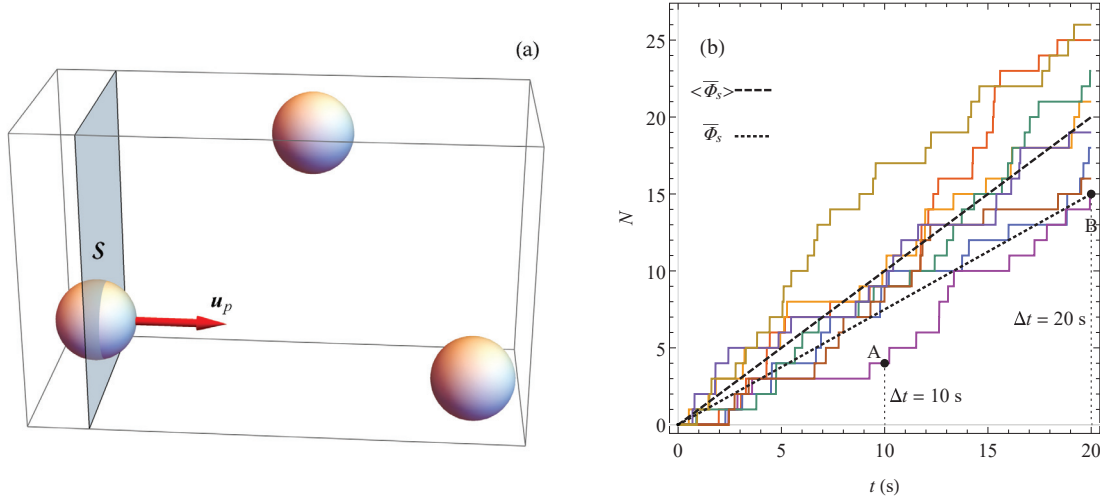
Figure 2.2: (a) Illustration of the virtual experiment: particles move randomly at velocity $\mathbf{u}_p$ and cross the control surface $\mathscr{S}$. (b) Time variations in the number of particles $N(t)$ that have crossed the control surface $\mathscr{S}$ until time t. Here we simulated eight paths of the Poisson process $N(t)$ with rate $\nu = 1$ grains/s and a sampling rate $\delta t = 5$ ms (thus generating $M = 4000$ values of N for each path).

$\overline{\Phi}_s = N/\Delta t$, we have no idea how close this estimate is to the actual rate ν. Indeed, the sample variance is computed by using the Φ_s values along a particular path, and it does not tell us anything about the relative error $\epsilon = |1 - \overline{\Phi}_s/\nu|$. For instance, for path AB, the sample variance is $\sigma_\Phi^2 = \sum_{k=1}^{M}(N(t) - \overline{\Phi}_s t)^2 = 3.72$ grains^2/s^2 (M is the number of sampled values), yielding a coefficient of variation $\sigma_\Phi/\overline{\Phi}_s = 12.8\%$, which is lower than the relative error $\epsilon = 25\%$ by a factor 2.

Another approach involves replicating the initial run to refine the estimate $\overline{\Phi}_s$. The average of the eight runs provides a mean rate $\overline{\Phi}_s = 0.95$ grain/s for $\Delta t = 10$ s, and $\overline{\Phi}_s = 1.02$ grain/s for $\Delta t = 20$ s, with the relative error thus dropping to 2%–5%. This shows that by combining time and run averages, we can reduce uncertainties when measuring bedload transport. Run averaging is close to ensemble averaging $\langle \overline{\Phi}_s \rangle = \lim_{n \to \infty} \sum_{i=1}^{n} N/\Delta t$, which is the tool we will be using in this paper. At this stage of the example, one might doubt that much progress has been made if, in practice, one has to reiterate measurements instead of extending the sampling duration Δt. This is where theory comes in.

We will show that uncertainties (expressed here in terms of ensemble-variance var$\overline{\Phi}_s$) vary as var$\overline{\Phi}_s = K/\Delta t$. The proportionality factor K depends on the measurement protocol and transport stage. When measuring low transport rates, K is equal or close to the mean flux $\overline{\Phi}_s$. If we go back to the example in Fig. 2.2 and consider path AB again, we measure $\overline{\Phi}_s = 15/20 = 0.75$ grains/s, thus deducing that the ensemble variance is approximated by var$\overline{\Phi}_s =$

$\overline{\Phi}_s/\Delta t = 0.0375$ grains^2/s^2 and expecting the actual rate to fall within or close to the range $\overline{\Phi}_s \pm \sqrt{\mathrm{var}\overline{\Phi}_s} = [0.56, 0.94]$ grains/s. The ensemble-averaged variance $\mathrm{var}\overline{\Phi}_s$ thus provides a better estimate of the uncertainties of $\overline{\Phi}_s$ than the sample mean.

We have been able to estimate the ensemble-averaged variance from a single path because we have taken advantage of our knowledge of sediment transport: it behaves like a Markov process at low transport rates. At higher transport rates, the assumption of a Markov process breaks down, but our statistical approach is still possible. It requires more statistical information about $\overline{\Phi}_s$ to implement renewal theory and determine the value of K. High-resolution data were needed for this. Admittedly, replicating measurements is usually difficult (and often impossible), but we will see that statistical techniques such as bootstrapping allow us to estimate the ensemble mean and variance. In the absence of high-resolution data, applying the central limit theorem provides an estimate of K.

2.2   Theory

2.2.1   Definitions and Notation

The present paper uses two different definitions of the bedload transport rate $\mathscr{Q}_s$ from among the numerous forms currently in use (Ancey, 2010; Furbish et al., 2012; Ballio et al., 2014). We have tailored these definitions to the specific analysis developed in this paper (see the end of this section for how these definitions can be generalized in real-world applications). First, for most theoretical developments, we will express $\mathscr{Q}_s$ in grains/s. Second, we will consider a flow per unit width. Although many of the equations presented seem to have been formulated for a two-dimensional problem, the third spatial dimension should not be forgotten. For this reason, we will refer to "control volume" even though this volume is two-dimensional in Fig. 2.3 (the same holds for the control surface and streambed area below).

- Flux of particles across a control surface (see Fig. 2.3). We count the number of particles crossing the control surface $\mathscr{S}$ during the sampling duration Δt:

$$\overline{\Phi}_s(\Delta t \mid t) = \frac{1}{\Delta t}\int_t^{t+\Delta t} \phi_s(\tau)\mathrm{d}\tau, \tag{2.1}$$

  where $\phi_s(\tau)\mathrm{d}\tau$ gives the number of particles intersecting the control surface $\mathscr{S}$ between time τ and $\tau + \mathrm{d}\tau$. Thereafter, we will mostly work with Markov processes that describe weak sediment transport: in such cases, the probability of observing two particles crossing the control surface at the same time drops to zero, and $\phi_s\mathrm{d}\tau$ can either be zero (no particle crossing $\mathscr{S}$) or unity (one particle crossing $\mathscr{S}$). The arrival of individual particles will be described as a Poisson process in Sec. 2.2.3. When this assumption breaks down at sufficiently high transport rates, ϕ_s can take any integer value, and we describe particle arrival as a renewal process (see Appendix B). Equation (2.1) is probably the most natural definition in fluid mechanics because particle transport rates

usually reflect mass fluxes. Indeed, it is equivalent to the definition used in continuum mechanics $\mathcal{Q}_s = \int_{\mathcal{S}} H(\mathbf{x})\mathbf{u}_p(\mathbf{x}, t) \cdot \mathbf{n}\mathrm{d}S$ (where $H(\mathbf{x})$ is unity when point $\mathbf{x}$ is occupied by a particle and zero otherwise, $\mathbf{u}_p$ is the particle velocity field at $\mathbf{x}$, and $\mathbf{n}$ is the outward-oriented normal to $\mathcal{S}$).

- Volume-averaged particle transport rate. By averaging particle motion through a control volume, we relate the bedload transport rate to the volume-averaged particle velocity $\mathcal{U}_p = \sum_{i=1}^{N} u_{p,i}$ (where $u_{p,i}$ is the instantaneous particle velocity) and the number of moving particles N (Ancey and Heyman, 2014):

$$q_s = \frac{N}{A}\mathcal{U}_p, \tag{2.2}$$

where N/A is called the *particle activity* (that is, the number of moving particles per unit of streambed area A) (Furbish et al., 2012). Counting the number of moving particles and determining their mean velocity leads to the instantaneous volume-averaged transport rate q_s. We can calculate its time average:

$$\overline{q}_s(\Delta t \mid t) = \frac{1}{\Delta t} \int_{t}^{t+\Delta t} q_s(\tau)\mathrm{d}\tau, \tag{2.3}$$

where Δt is the sampling duration. If we assume that particles move at a constant velocity, then computing the bedload transport rate involves determining the number of moving particles N. Calculating the time-averaged bedload transport rate $\overline{q}_s$ is tantamount to calculating the time integral of $N(t)$. This is what we will do below by using some general results for Markov processes (see Appendix A) and by applying renewal theory (see Appendix B).

We introduce three averages:

- The *ensemble average* $\langle f \rangle$ of the random quantity f is obtained by averaging f over all possible realizations (Herczynski and Pienkowska, 1980; Lhuillier, 1992; Drew and Passman, 1999)—the electronic supplement to (Ancey and Heyman, 2014) provides a more formal introduction to this average. If f depends on time t, then $\langle f \rangle$ is also a function of t. We denote the steady-state ensemble-averaged value of f by $\langle f \rangle_{ss}$, which is the value reached by $\langle f \rangle$ at sufficiently long time intervals for the initial condition's influence to be negligible.

- The time average $\overline{f}$ is defined as the time integral over the sampling duration Δt:

$$\overline{f}(\Delta t \mid t) = \frac{1}{\Delta t} \int_{t}^{t+\Delta t} f(\tau)\mathrm{d}\tau. \tag{2.4}$$

- We can combine both averages to produce the double-averaged (time- and ensemble-averaged) quantity $\langle \overline{f} \rangle$.

To keep the notation less cluttered, we did not introduce any special symbol to refer to the volume-average underpinning the derivation of Eq. (2.2). When sediment transport involves grains of the same size, we can readily convert transport rates expressed in grains/s into rates expressed in kg/s or m^3/s. When considering grains of different sizes, the definitions (2.1) and Eq. (2.3) can be generalized by partitioning the grain size-distribution into classes and computing particle transport rates for each class.
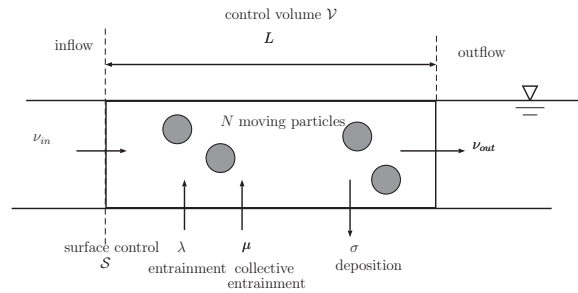
Figure 2.3: Notation and illustration of the exchange processes considered. The water flow transports particles. The mean particle flux is ν_{in}. The number of moving particles N in the control volume $\mathcal{V}$ varies as a result of particles entering and leaving the volume and being entrained or deposited on the bed. Bed particles can be dislodged by the water drag (there is a probability λdt that this occurs within a short time interval dt) or because of interactions with moving particles (as there are N moving particles, the resulting probability of entrainment is $\mu N dt$).

2.2.2 Assumptions

We consider a one-dimensional system under steady-state conditions, corresponding to a narrow, tilted flume with a constant feed rate at its inlet (the flow geometry that will be investigated experimentally in Sec. 2.4). Under these flow conditions, particles move in the same direction as the water flow, and cross-stream diffusion—observed in wider flumes (Seizilles et al., 2014)—can be neglected. The influence of bedforms on flow dynamics and bedload transport is supposed to be negligible, and thus the bed is in equilibrium with no significant elevation variation along its interface with the flow (neither aggradation nor degradation). Particles move at velocity u_p, which may fluctuate over time. The mean particle velocity is denoted by $\overline{u}_p$. Velocity fluctuations are assumed to be Gaussian, with standard deviation σ_u. The probability P_u of observing a given value w for the particle velocity is thus:

$$P_u(w) = \text{prob}(u = w) = \frac{1}{\sqrt{2\pi}\sigma_u} \exp\left(-\frac{(w - \overline{u}_p)^2}{2\sigma_u}\right). \tag{2.5}$$

This assumption has been validated experimentally (Martin et al., 2012; Ancey and Heyman, 2014; Heyman et al., 2016), but not systematically; authors have observed an exponential velocity distribution instead (Lajeunesse et al., 2010; Roseberry et al., 2012). The exact form is not crucial to the rest of the developments.

The central element of our theoretical development is the calculation of the number N of particles crossing a control surface or contained in a control volume. To that end, we use the stochastic bedload transport model proposed by (Ancey et al., 2008). The number of moving particles N varies with time as a result of (i) deposition and (ii) entrainment. Particles come to rest at a rate σ [1/s]. The *deposition rate D* is thus $D = \sigma N$ [grains/s]. We introduce two forms of entrainment:

- *Individual entrainment* at a rate λ [grains/s], which reflects the classic mechanism of entrainment by the water flow.

- *Collective entrainment* at a rate μ [1/s], which takes particle–particle interactions into account.

The number of particles entrained per unit time is thus: $E = \lambda + \mu N$, where E is the *entrainment rate* [grains/s]. To accurately count particles, the system's dimensions must be specified. We consider a control window $\mathcal{V}$ of length L. The window's downstream (or equivalently, upstream) face is the control surface $\mathcal{S}$ (see Fig. 2.3).

We assume that the particle flux can be described as a Markovian process. This implies that the probability of observing N moving particles depends only on recent flux history (there is no memory effect). Differently put, the probability P that one particle crosses the control surface $\mathcal{S}$ during the time interval $[t, t + \delta t]$ is $P = \nu_{in}\delta t$ (where ν_{in} is the feed rate), and thus that probability depends solely on the time interval δt. When δt is infinitesimally small, then only

one particle can cross the control surface (Markovian process theory cannot deal with multiple events). Equivalently, it can be shown that the waiting time τ between two particle-arrivals is exponentially distributed, with parameter $\Lambda = \nu_{in}$ [grains/s] (or equivalent with a mean waiting time $t_w = \nu_{in}^{-1}$):

$$P_\tau(\tau) = \Lambda\exp(-\Lambda\tau). \tag{2.6}$$

2.2.3 Time-Averaged Particle Flux

With these assumptions, we deduce immediately that the number of particles that have crossed the control surface $\mathscr{S}$ up to time t is a Poisson process (Cox and Miller, 1965; Gillespie, 1992). It is straightforward to show that the ensemble average and variance are (Gillespie, 1992):

$$\langle N \rangle = \Lambda t \text{ and } \mathrm{var}N = \Lambda t. \tag{2.7}$$

Using Eq. (2.1), we then deduce that the mean (double-averaged) flux is

$$\langle \overline{\Phi}_s \rangle (\Delta t \mid t) = \frac{\langle N \rangle (t + \Delta t) - \langle N \rangle (t)}{\Delta t} = \Lambda, \tag{2.8}$$

regardless of Δt, whereas the variance is

$$\mathrm{var}\overline{\Phi}_s(\Delta t \mid t) = \frac{\Lambda}{\Delta t}. \tag{2.9}$$

Interestingly, we note that according to the Poisson process, the fluctuation strength varies linearly with the mean particle flux Λ and is inversely proportional to the sampling duration Δt.

2.2.4 Volume-Averaged Bedload Transport Rate for $\sigma_u = 0$

Let us first consider the simplest case, in which the particle velocity fluctuations are negligible relative to their mean velocity $\overline{u}_p$ (that is, we assume that $\sigma_u = 0$). The number N of moving particles in the control window $\mathscr{V}$ can be described as a birth–death immigration–emigration Markov process (Cox and Miller, 1965): entrainment and deposition correspond to birth and death, respectively, whereas immigration and emigration reflect the arrival and departure of particles. The immigration rate is ν_{in}, and the emigration rate is

$$\nu_{out} = \frac{\overline{u}_p}{L}, \tag{2.10}$$

where L is the length of the control window. Under steady-state conditions, the probability of observing N particles in the control volume $\mathscr{V}$ can be calculated analytically. Here we summarize the main results and refer the reader to an earlier publication for the proofs (Ancey et al., 2008).

When the collective entrainment rate μ is non-zero, this probability is the negative binomial

distribution:

$$P_n(n) = \text{prob}(N = n) = \binom{q+n-1}{q-1} p^q (1-p)^n \tag{2.11}$$

with parameters p and q:

$$q = \frac{\lambda + v_{in}}{\mu} \text{ and } p = 1 - \frac{\mu}{v_{out} + \sigma - \mu} \tag{2.12}$$

The autocorrelation function of the time series $N(t)$ is

$$\rho(\tau \mid t) = \frac{\text{cov}(N(t), N(t+\tau))}{\text{var} N(t)} = e^{-\tau/t_c}, \tag{2.13}$$

where $t_c = 1/(v_{out} + \sigma - \mu)$ is the autocorrelation time. Under steady-state conditions, the ensemble average and mean of N are thus

$$\langle N \rangle_{ss} = \frac{\lambda + v_{in}}{v_{out} + \sigma - \mu} \text{ and } \text{var}_{ss} N = \frac{(\lambda + v_{in})(v_{out} + \sigma)}{(v_{out} + \sigma - \mu)^2}. \tag{2.14}$$

The instantaneous bedload transport in the control volume $\mathcal{V}$ is given by Eq. (2.2). As we assume that particles move at constant velocity $\overline{u}_p$, then all the q_s fluctuations result solely from the time variations in the number of moving particles N. Combining Eqs. (2.2) and (2.14), we find that under steady-state conditions, the ensemble-average bed transport rate is

$$\langle q_s \rangle_{ss} = \frac{\overline{u}_p}{L} \langle N \rangle_{ss} = \frac{\lambda + v_{in}}{v_{out} + \sigma - \mu} \frac{\overline{u}_p}{L}. \tag{2.15}$$

Because under steady-state conditions we have $\overline{u}_p \langle N \rangle_{ss}/L = v_{in} = \Lambda$, the steady-state mean transport rate (2.15) matches the mean particle flux (2.8). The variance takes a more complicated form:

$$\text{var}_{ss} q_s = \frac{\overline{u}_p^2}{L^2} \text{var}_{ss} N = \frac{\overline{u}_p^2}{L^2} \frac{(\lambda + v_{in})(v_{out} + \sigma)}{(v_{out} + \sigma - \mu)^2}. \tag{2.16}$$

Calculating the double-averaged bedload transport rate $\langle \overline{q}_s \rangle$ requires more work. First, we can derive the governing equation specific for $\langle N(t) \rangle$, its higher moments, and its time integral $\int_t N(t) dt$ (see Appendix A for the mathematical detail). By using Eq. (2.55) and assuming that particles were initially still ($N_0 = N(t = 0) = 0$) in the control volume, we find that

$$\langle \overline{q}_s \rangle(\Delta t \mid t) = \frac{\overline{u}_p}{L} \frac{\lambda + v_{in}}{v_{out} + \sigma - \mu} \left(1 - \frac{t_c}{\Delta t} (1 - e^{-\Delta t/t_c}) \right), \tag{2.17}$$

which tends to $\langle q_s \rangle_{ss}$ when the sampling duration Δt is sufficiently long relative to the autocorrelation duration t_c. Asymptotically, the variance is deduced by taking the limit $\Delta t \gg t_c$ in Eq. (2.58):

$$\text{var} \overline{q}_s(\Delta t \mid t) = \frac{\overline{u}_p^2}{L^2 \Delta t} \frac{(\lambda + v_{in})(v_{out} + \sigma)}{(v_{out} + \sigma - \mu)^3} = \frac{\overline{u}_p^2}{L^2} \text{var}_{ss} N \frac{t_c}{\Delta t}. \tag{2.18}$$

Contrary to the average (2.17), the double-averaged variance does not converge to the steady-state ensemble-averaged variance (2.16) when $\Delta t \gg t_c$. We also note that, contrary to the particle flux, the fluctuation strength depends on many parameters and does not seem to be trivially related to the mean bedload transport rate. The particle flux, however, is inversely proportional to the sampling duration. We can intuitively estimate that the proportionality factor $\overline{u}_p^2 \text{var}_{ss} N t_c / L^2$ in Eq. (2.18) should be close to Λ. As shown in Sec. 2.4, this link between $\overline{u}_p^2 \text{var}_{ss} N t_c / L^2$ and Λ was observed experimentally, but we have no theoretical argument with which to rigorously demonstrate it.

2.2.5 Volume-Averaged Bedload Transport Rate for $\sigma_u > 0$

Calculations become more involved when considering velocity fluctuations, but they are still tractable analytically. We assume that the number of moving particles is distributed according to a negative binomial distribution (2.11), whose parameters are given by Eq. (2.12). We also assume that the instantaneous particle velocity $u_{p,i}$ is normally distributed (see Eq. (2.5)). We assume that the two marginal probabilities P_n and P_u fully describe the process or, to put it differently, there is no correlation between N and $u_{p,i}$. We define U as the sum of the particle velocities:

$$U = \sum_i^N u_{p,i}. \tag{2.19}$$

As the volume-averaged particle transport rate in the control window $\mathcal{V}$ is $q_s = U/L$, the probability density function of q_s is related to that of U:

$$P_{q_s} = L P_U(L q_s). \tag{2.20}$$

The probability P_U of U is obtained by summing the elementary probabilities of observing k particles, in the control window, whose velocity sum equals U:

$$P_U = \sum_{k=1}^{\infty} P_n(k) P_k(U), \tag{2.21}$$

where P_k denotes the probability of observing that the velocity sum is equal to U. As the sum of normally distributed random variables is also normally distributed, P_k is the normal distribution $\mathcal{N}$, with mean $k\overline{u}_p$ and standard deviation $\sqrt{k}\sigma_u$. We then deduce:

$$P_{q_s} = L P_U(L q_s) = L \sum_{k=1}^{\infty} P_n(k) P_k(L q_s)$$

$$= \sum_{k=1}^{\infty} L \binom{q+n-1}{q-1} p^q (1-p)^n \mathcal{N}(k\overline{u}_p/L, \sqrt{k}\sigma_u/L)(L q_s). \tag{2.22}$$

43

It is then straightforward to infer the mean and variance of q_s even though there is no closed-form expression for the probability P_{q_s}:

$$\langle q_s \rangle = \int_{\mathbb{R}} q_s P_{q_s} \mathrm{d}q_s = \frac{N_{ss}}{L} \overline{u}_p, \tag{2.23}$$

$$\mathrm{var}\, q_s = \int_{\mathbb{R}} (q_s - \langle q_s \rangle)^2 P_{q_s} \mathrm{d}q_s = \mathrm{var}_{ss} N \frac{\overline{u}_p^2 + p\sigma_u^2}{L^2}. \tag{2.24}$$

When $\sigma_u = 0$, we retrieve the variance given by Eq. (2.18). In Appendix C, we show that if we select an exponential distribution for the particle velocities, then there is no change in the ensemble average and only a slight change in the ensemble variance.

If we assume that events (particle velocity and particle number) are independent, then we can generalize the variance equation (2.18) to take velocity fluctuations into account in the double-averaged variance by following the same reasoning as that used for deriving Eq. (2.18):

$$\mathrm{var}\, \overline{q}_s(\Delta t \mid t) = \frac{\overline{u}_p^2 + p\,\mathrm{var}\,u}{L^2 \Delta t} \frac{(\lambda + v_{in})(v_{out} + \sigma)}{(v_{out} + \sigma - \mu)^3} = \mathrm{var}_{ss} N \frac{\overline{u}_p^2 + p\,\mathrm{var}\,u}{L^2} \frac{t_c}{\Delta t}. \tag{2.25}$$

2.2.6 Summary of Results

When we considered that a steady-state system in which the particle flux across a vertical control surface $\mathscr{S}$ was a Poisson process with rate Λ, we found that the double-averaged particle flux (2.8) was Λ, independently of the sampling duration Δt. Under steady-state conditions, mass conservation imposes that $v_{in} = v_{out}\langle N \rangle_{ss}$ in the control window $\mathcal{V}$. Using Eq. (2.10), we then deduced that the double-averaged bedload transport rate (2.15) or (2.23) was also Λ in the limit $\Delta t \gg t_c$. We thus concluded that, on average, both transport rate definitions provided identical results:

$$\langle \overline{q}_s \rangle = \langle \overline{\Phi}_s \rangle. \tag{2.26}$$

These results, however, differed with regards to the variance of q_s or Φ_s: the variance of the double-averaged flux $\langle \overline{\Phi}_s \rangle$ varied as $\Lambda/\Delta t$, whereas the variance of the double-averaged transport rate $\langle \overline{q}_s \rangle$ varied like $v_{out}^2 \mathrm{var}_{ss} N t_c/\Delta t$ given by Eq. (2.18) (or like Eq. (2.25) if velocity fluctuations were taken into account). The fact that the variance varied like $1/\Delta t$ comes as no surprise because the central limit theorem states that the scaled sum S_n of n *independent and identically distributed random* variables Y_i (with finite mean μ_y and standard deviation σ_y) converges in distribution to a normal distribution with mean 0 and variance 1 (Grimmett and Stirzaker, 2008):

$$\frac{S_n - n\mu_y}{\sqrt{n}\sigma_y} \xrightarrow{d} \mathcal{N}(0, 1). \tag{2.27}$$

If we apply the central limit theorem to a long time-series ($t_i = i\delta t, y_i$), where $1 \le i \le n$ and

where δt denotes the time interval between two measurements, with $y_i = \mathcal{Q}_i$ the transport rate at time t_i, then the time-averaged bedload transport rate is $\overline{q}_s(t_n) = S_n \delta t / \Delta t$. Furthermore, when n is large, we have: $\overline{S}_n \to n\mu_y$ and $\mathrm{var} S_n \to n\sigma_y^2$, thus $\overline{\mathcal{Q}}_s \to \mu_y$ and $\mathrm{var}\mathcal{Q}_s \to \sigma_y^2 \delta t / \Delta t$ because $n \propto \Delta t / \delta t$. Asymptotically, for any sample that satisfies the application conditions of the central limit theorem, then the relation $\mathrm{var}\overline{q}_s \propto \Delta t^{-1}$ also holds true. The difference between this scaling and Eqs. (2.18) and (2.9) is that in the Markovian case, the variation $\mathrm{var}\overline{q}_s \propto \Delta t^{-1}$ holds exactly for any sampling duration Δt. Furthermore, in the case of a Poisson process, the steady-state variance in Eq. (2.9) is entirely controlled by the mean particle flux Λ, and there is no need to introduce another parameter σ_y to find its value.

2.2.7 Protocol for Measuring the Sediment Transport Rate and its Variance

In Eqs. (2.8) and (2.15), the transport rates $\langle \overline{\Phi}_s \rangle$ and $\langle \overline{q}_s \rangle$ are based on ensemble averages. The problem is that it is difficult to calculate ensemble averages directly in experiments (unless many runs of the same experiment can be made). There is, however, a fairly simple technique that mimics the ensemble average and makes it possible to deduce the sample mean and variance with high precision: the *bootstrap method* (Davison and Hinkley, 1997). Like the jackknife, this is a resampling technique, which involves repeatedly drawing random subsamples from a single original sample and generating new samples with similar statistical properties to those exhibited by the original one (Davison and Hinkley, 1997). We assume a time series $(t_i = i\delta t, y_i)$ $(1 \leq i \leq n)$, where the variables y_i are independent and identically distributed random values drawn from an underlying distribution F. We assume that we do not know F, but we can get an empirical estimate $\widehat{F}$ by using the sample $(y_1, y_2, \cdots, y_n)$. We can then draw M samples of n values from $\widehat{F}$. We use these M samples to compute the sample mean and variance.

Thus, the key point is starting with a sample of independent and identically distributed data. The tests are detailed in Sec. 2.4. Here, we would like to highlight a simple test of stationarity, which turns out to be robust and useful in a variety of settings. Because of the existence of fluctuations in the q_s time series, it may be difficult to distinguish between stationarity, weak stationarity, and absence of stationarity. Below, we plot the cumulative amount of sediment $S_n = \sum_{i=1}^{n} y_i \Delta t$ (here y_i denotes the particle flux Φ_s or volume-averaged transport rate q_s) as a function of time (see Fig. 2.4 for an example). If the steps (t_n, S_n) come close to a straight line of slope $\widehat{\Lambda}$, then the process is probably stationary: the mean flux will be close to $\widehat{\Lambda}$. Should only some groups of intervals (t_n, S_n) form segments of the line, then the process is weakly stationary. These groups can then be used to identify the periods during which the process was reasonably close to a stationary process. If there is no good match between these groups and the line representing steady state, the protocol cannot be applied.

Our protocol for defining the mean bedload transport rate and its variance is the following:

- If we can acquire data at a sufficiently high frequency, then we resolve the times at which particles cross the control surface $\mathscr{S}$ or move within the control window $\mathscr{V}$. We can then

determine the waiting time between particle arrivals, or measure particle velocity. This is the ideal case against which we will test the theory outlined in this section. Although an emphasis is placed on Markovian processes, particles may behave differently; notably, many particles cross the control surface $\mathscr{S}$ within a short time-interval ("many" here means that the number of particles crossing the surface cannot be described using the Poisson law). Appendix B shows how renewal theory can be used in these cases.

- In the opposite case, when the data acquisition rate is low (typically below 1 Hz), we can still apply the protocol, but it will be difficult to verify whether the theory described above captures the flux behavior well. The central limit theorem is, however, sufficient to deduce the key information of the bedload transport rate's mean and variance. There is, of course, no free lunch. The price paid for low-frequency measurements is that the fluctuation strength is independent of the mean particle flux. Naturally, this does not cause trouble when working under steady-state conditions (one can estimate σ_y), but it becomes more problematic under time-dependent flow conditions.

The steps are the following:

1. Plot the cumulated amount of sediment on a graph $(t_n, S_n = \delta t \sum_{i=1}^{n} y_i)$ and identify the periods T during which the steps are close to a straight line of slope $\widehat{\Lambda}$, that is, the period during which the process was stationary or quasi-stationary. The slope $\widehat{\Lambda}$ represents the mean transport rate over time T, and S_n is a time discretization of $\int y(t)\mathrm{d}t$.

2. From this period T, we can extract a sample (t_i, y_i) involving $n_T \sim T/\delta t$ values. Because we need to handle independent and identically distributed random variables y_i, we must check that this assumption is satisfied. In practice, if one measures volume-averaged transport rates q_i, the assumption of independent and identically distributed data implies that the time interval δt should be larger than the autocorrelation time, otherwise neighboring values would be correlated. The "training" sample $(t_i, y_i)_{1 \le i \le n_T}$ is used to generate random samples, using the bootstrap resampling technique (Davison and Hinkley, 1997).

3. We can estimate the variance of $\langle \overline{y} \rangle (\Delta t)$ by generating M samples (typically $M = 100$ is recommended) of size $n_r = \Delta t/\delta t$ from the training sample (e.g., see (Davison and Hinkley, 1997) on how to use the bootstrap method) and estimating the variance $\mathrm{var}\,\widehat{y}$ of this group.

4. When plotted as a function of Δt, the empirical variance $\mathrm{var}\,\widehat{y}$ should lie on the curve $\widehat{\Lambda}/\Delta t$, by virtue of Eqs. (2.18) or (2.9), if the data were collected at a sufficiently high frequency. If they were not, we can use the central limit theorem (2.27), and the data should be close to the curve $\sigma_y \delta t/\Delta t$.

5. The empirical variance curve $\mathrm{var}\,\widehat{y}(\Delta t)$ makes it possible to specify the accuracy associated with the measurement of the double-averaged transport rate over the duration Δt

or, reciprocally, to select the value of Δt that corresponds to the desired accuracy (i.e., the prescribed σ_y).

2.3 Experimental Procedure (P run)

2.3.1 Experimental Set-up

The flume used was 2.5 m long, 40 mm wide, and tilted at an angle of 1.55° from the horizontal. Water discharge at the flume inlet was set to $Q_w = 0.2$ L/s, and flow depth was 1.1 cm (the hydraulic radius was $R_h = 71$ mm). The flow was supercritical (with a Froude number $Fr = 1.1$). This choice of the flow regime was driven by our desire to approach the flow conditions found in mountain streams (the subject of our research) and to limit the effects of sidewall friction on flow turbulence. Well-sorted gravel (mean diameter $d_{50} = 3$ mm, density $\rho_p = 2550$ kg/m³) was layered along the flume bottom to a thickness of 4 cm, and the same gravel was used to feed the flume at a feed rate of 10.3 ± 0.5 grains/s. The Shields number was $\Theta = \rho g R_b \tan\overline{\psi}/((\rho_p - \rho)g d_{50}) = 0.057$—$R_b = 9.4$ mm estimated by using the Einstein-Johnson's sidewall correction (Einstein, 1942; Johnson, 1942). The critical Shields number estimate was $\Theta_c = 0.056$, according to Recking et al. (2008). We designed a specific system to feed the flume with sediment (see Supporting Information for photographs), bounded by two constraints: the feed rate had to be low (a few grains per second) and the particle flux had to be as close to a Poisson process as possible. Gravel was initially contained in a hopper whose opening controlled the inflow rate. The particles fell onto a slowly rotating cylinder ($\Omega = 0.4$ rad/s) whose surface was covered with sandpaper. A vertical brush prevented grains from stacking and generating avalanches. After the cylinder had rotated by a certain angle, any grain stuck to the rough cylinder exterior was dislodged and fell into the flume. The grains fell onto a smooth white board, slipped down it while being filmed by a high-speed camera, and then arrived at the flume inlet, where they were entrained by the flow. Although the match was not perfect, the particle flux at the flume inlet was very close to a Poisson process.

2.3.2 Image Processing and Tracking

Particle motion was monitored in control volumes over the erodible bed or over a fixed board (at the flume outlet). Concerning the monitoring over the mobile bed, images were collected at 250 frames per second using a high-speed Basler A504k camera equipped with a Nikkor-S 1:1.4 $f = 50$ mm lens, at a resolution of 624×300 pixels (with the scale 1 px = 0.133 mm). A 35-cm long transparent plastic plate was placed above the water surface to prevent reflections and image distortion created by free surface waves. Images were taken from vertically above this plate. The main disturbance introduced by the plate in the underlying flow region was likely the strong mitigation of the non-uniformities of flow depth and bed elevation along the streamwise direction. We presume that the presence of this plate also exacerbated antidunes in the downstream sector of the flume. Three LED spotlights illuminated the control window

homogeneously. The experimental run lasted 22 min, and initial images were removed to extract a sequence of 20 min.

The raw images were processed by subtracting their background image, defined as the median of the 20 previous frames. This preliminary step enabled us to highlight moving particles and discard jiggling particles which were not being transported by the flow. Particle tracking was based on a procedure available from the TrackMate-ImageJ numerical framework (Tinevez et al., 2017). First, spot detection was carried out using a Laplacian of the Gaussian detector and considering an estimate of the mean grain size in the images as the detector size parameter. Second, in the particle linking step, we modified and used the Linear Assignment Problem (LAP) tracker initially proposed by Jaqaman et al. (2008): we modified the linking cost function so that it accounted for the preferential direction of particle displacement (downstream in our case). The *gap closing* option was allowed over two time steps. Moreover, spots and trajectories were filtered to reduce tracking errors, mostly caused by moving bubbles trapped at the interface between the transparent plate and the water flow. After the spot detection step, we filtered spots by considering their properties, which enabled us to identify spots associated with moving bubbles. We rejected spots characterized by an estimated diameter smaller than 7 px and/or by a maximum intensity higher than 160 (over 255). Among the trajectories reconstructed using the particle linking procedure, we discarded those composed of fewer than 4 spots in order to remove short tracklets caused by bubbles and improper particle linking. A validation test of this tracking method was conducted, and it is presented in the Supporting Information.

Finally, the resulting tracks were analyzed to calculate the variables of interest for the present study: we emphasized the time series $(t_i, N(t_i))$ of the number of moving particles, the distribution of the particle velocity u_p (averaged over all particle paths for each image), and the time series of the particle fluxes in the downstream section of the control window $\Phi_s(t)$. We considered three control windows of different streamwise lengths ($L = 17.5$ mm, 35 mm, and 70 mm), all located in the same section and starting 1.32 m from the flume inlet ($x = 0$). We present only results obtained with the longest window $L = 70$ mm. See the Supporting Information for further data on L's influence on the results (which was found to be small, on average).

2.4   Results

This section addresses the following points. First, we compare the various predictions of the Markovian theory developed in Sec. 2.2 against high-resolution experimental data. Second, we test the protocol proposed in Sec. 2.2.7. Third, to estimate whether this protocol has potential, we evaluate its performance under more complicated flow conditions: because bedforms developed downstream of the plate and thus influenced the bedload transport rate, we look more closely at the data acquired at the flume outlet. Before addressing each of these points, we adjust the model parameters λ, μ, σ, μ, ν_{out}, $\overline{u}_p$, and σ_u from the time series ($t_i = i\delta t$,

N_i, u_i), where $\delta t = 4$ ms is the time interval between two images, and N_i is the number of moving particles in the control volume. The inflow rate $\nu_{in} = 10.3$ grains/s was imposed experimentally at the flume inlet.

2.4.1   Parameter Estimation

Of five model parameters—entrainment parameters (λ and μ), deposition rate (σ), and flux parameters (ν_{out} and ν_{in})—four are unknown and $\nu_{in} = 9.98$ grains/s was set experimentally (taking the value measured in the control window rather than the one fixed at the flume inlet). We only need to select four relationships to determine the unknowns, but at least five equations are available:

1. Bed equilibrium

$$\sigma \langle N \rangle_{ss} = \mu \langle N \rangle_{ss} + \lambda. \tag{2.28}$$

2. Flux steadiness

$$\nu_{in} = \nu_{out} \langle N \rangle_{ss}. \tag{2.29}$$

3. Condition on the average N value

$$\langle N \rangle_{ss} = \frac{\beta}{\alpha} = \frac{\lambda + \nu_{in}}{\nu_{out} + \sigma - \mu}. \tag{2.30}$$

4. Condition on the N variance

$$\mathrm{var}_{ss} N = \frac{(\lambda + \nu_{in})(\nu_{out} + \sigma)}{(\nu_{out} + \sigma - \mu)^2}. \tag{2.31}$$

5. Condition on the autocorrelation time

$$\nu_{out} + \sigma - \mu = t_c^{-1}. \tag{2.32}$$

The autocorrelation time was $t_c = 221$ ms (see Fig. 2.6(b)). We set ν_{out} from Eq. (2.29): $\nu_{out} = \nu_{in}/\langle N \rangle_{ss} = 1.82$ 1/s. We solved Eqs. (2.30), (2.31), and (2.32) for λ, μ, and σ. We found $\lambda = 14.77$ grains/s, $\mu = 4.98$ 1/s, and $\sigma = 7.68$ 1/s. Furthermore, we inferred from the processed images that the mean particle velocity was $\overline{u}_p = 13.41$ cm/s and its standard deviation was $\sigma_u = 3.24$ cm/s. Note the value $\nu_{out} = 1.82$ 1/s was 5% below the theoretical value $\nu_{out} = \overline{u}_p/L = 1.91$ 1/s. Equation (2.28) was used to test whether the fitted values were consistent with the assumption of bed equilibrium.

2.4.2   Particle Flux

We begin our analysis with the particle flux across the control surface $\mathscr{S}$ located at the control volume's downstream end. Grains crossed the control surface at a mean rate $\widehat{\Lambda} = N_{tot}/T_{exp} =$

Table 2.1: Empirical and theoretical probabilities of observing k particles crossing the control surface $\mathscr{S}$ within the time interval $\delta t = 4$ ms.

k	Empirical value	Poisson prediction	Relative error
$k = 0$	0.959587	0.959567	0.002%
$k = 1$	0.039559	0.039604	−0.112%
$k = 2$	8.4×10^{-4}	0.00081	3.59%
$k = 3$	6.7×10^{-6}	11.1×10^{-6}	−40.71%

$\nu_{in} = 9.98$ grains/s ($N_{tot} = 11{,}974$ was the total number of grains to have crossed $\mathscr{S}$ over the run duration $T_{exp} = 1200$ s). As shown by Fig. 2.4(a), the particle flux was almost stationary, even though the time variations in Φ_s exhibited wide fluctuations over short timescales (see Fig. 2.8). The mean number of particles crossing the control surface $\mathscr{S}$ within $\delta t = 4$ ms was $\overline{N} = 0.04127$, whereas the variance was $\text{var} N = 0.04130$. The 0.07% deviation between these two values shows that the assumption of a Poisson process was realistic. Table 2.1 shows that the Poisson model properly predicts the number of particles crossing the window per time interval δt. The error for $k = 3$ particles is likely to have resulted from the sample's finite size (only three occurrences in 1200 s). The partial autocorrelation function was close to 1 for a lag of 1, then vanishingly small for lags larger than 1, as expected for a Poisson process.

Stationary jump processes are fully characterized by the probability of observing the process in a given state and by the waiting times τ between two jumps (Gillespie, 1992). Although Table 2.1 and Fig. 2.4(a) support the idea of a Poisson process, examining the waiting-time distribution tells us a different story: Fig. 2.4(b) shows the empirical probability density function of waiting times and their exponential distribution (2.6) (with rate $\widetilde{\Lambda} = 9.77$ s^{-1} adjusted on the waiting time sample using the method of moments). Over short periods, there was a fairly good match between the empirical and theoretical distributions, but for periods longer than 400 ms, deviation from the exponential distribution was marked. The sample's coefficient of variation was $\sigma_\tau / \overline{\tau} = 1.21$ (standard deviation $\sigma_\tau = \sqrt{\text{var}\tau} = 124$ ms, mean $\overline{\tau} = 102$ ms), thus higher than unity. This confirmed that waiting times were not strictly exponentially distributed. To better describe the probability distribution of waiting times, we can adjust a two-parameter hyper-exponential distribution, whose density function is:

$$p(\tau) = \alpha_1 \lambda_1 \exp(-\lambda_1 \tau) + \alpha_2 \lambda_2 \exp(-\lambda_2 \tau), \tag{2.33}$$

where α_1 and α_2 are mixture parameters satisfying $\alpha_1 + \alpha_2 = 1$, whereas λ_1 and λ_2 are two rates. Using the method of maximum likelihood, we found:

$$\alpha_1 = 0.13, \ \lambda_1 = 4.33 \text{ s}^{-1}, \ \alpha_2 = 0.87, \text{ and } \lambda_2 = 12.04 \text{ s}^{-1}, \tag{2.34}$$
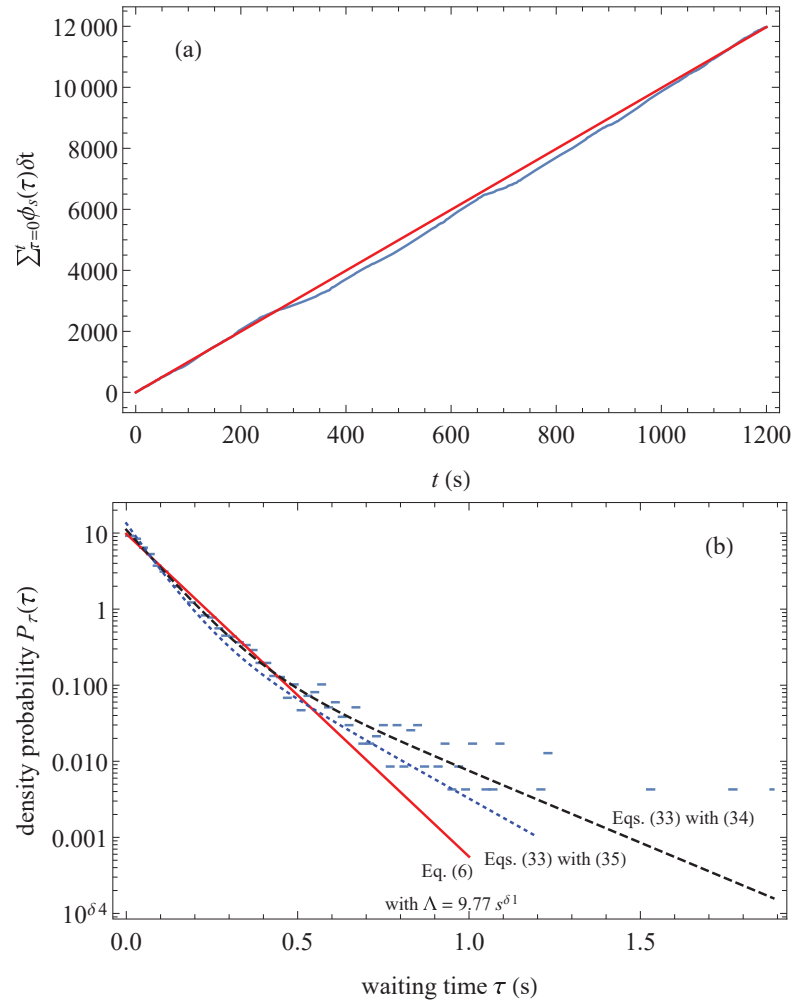
Figure 2.4: (a) Variation over time of the total number of particles crossing the control surface $\sum_0^t \delta_k(\tau)$. The red line represents the mean behavior $\Phi_s = \widehat{\Lambda} t$ with $\widehat{\Lambda} = v_{in} = 9.98$ grains/s. (b) Waiting times for the flux at the control window's downstream end $\mathscr{S}$. The solid red line represents the exponential distribution (2.6) with rate $\widetilde{\Lambda} = 9.77$ s^{-1} adjusted on the waiting time sample using the method of moments. The dashed black line represents the hyper-exponential distribution (2.33) fitted to the data using the method of moments. The dotted blue line represents the hyper-exponential distribution (2.35) adjusted on the flume inlet's data. The light blue dots show the empirical probabilities.

which was associated with slightly (20%) higher rates than those fitted at the flume inlet:

$$\alpha_1 = 0.19, \ \lambda_1 = 5.8 \ \text{s}^{-1}, \ \alpha_2 = 0.81, \ \text{and} \ \lambda_2 = 15.2 \ \text{s}^{-1}. \tag{2.35}$$

To compute the sample mean and variance for the time series (t_i, n_i), we used the bootstrap method and generated $M = 100$ samples from the experimental dataset (see Sec. 2.2.7). If the process was stationary and Poissonian with rate Λ, then we would expect that

$$\langle \overline{\Phi}_s \rangle \to \Lambda \ \text{and} \ \text{var}\overline{\Phi}_s(\Delta t) \to \frac{\Lambda}{\Delta t}, \tag{2.36}$$

as seen in Sec. 2.2.3. The parameter Λ was estimated by fitting an exponential distribution to the waiting times between two positive jumps (that is, events for which $n_i > 0$) in the time series (t_i, n_i). We found $\widetilde{\Lambda} = 9.77 \ \text{s}^{-1}$. Note the slight difference (2%) in the mean transport rate calculated using the assumption of a Poisson process ($\overline{\Phi}_{ss} = \Lambda = 9.77$ grains/s) and the one obtained empirically by setting $\overline{\Phi}_{ss} = \widehat{\Lambda} = N_{tot}/T_{exp} = 9.98$ grains/s. As shown in Fig. 2.4(b), the process was not a genuine Poisson process, and this led to small errors. As shown by Fig. 2.5(a), the empirical means computed using the bootstrap method were close to the mean flux value $\overline{\Phi}_{ss} = \widehat{\Lambda} = 9.98$ grains/s, and 2% higher than the rate $\widetilde{\Lambda}$ deduced from the waiting-time distribution. For the variance $\text{var}\overline{\Phi}_s(\Delta t)$, Fig. 2.5(b) shows the excellent agreement between the variances computed using the bootstrap method and the theoretical prediction (2.36).

We also used renewal theory for computing the particle flux (see Appendix B). Here, we used the hyper-exponential distribution to estimate the waiting time between two events. The number of particles which could arrive at the same time was estimated using the binomial-like distribution (2.60). From the experimental data, we deduced that there was a probability of $p = 11,473/11,989 = 0.979$ that a single particle crossed $\mathscr{S}$ within δt, and of $1 - p$ that two particles crossed it at the same time. This resulted in a flux average (2.70) that closely matched the feed rate $\widehat{\Lambda} = 9.98$ grains/s, as shown in Fig. 2.5(a). This confirmed that the slight discrepancy between theory and experiment was likely due to the existence of much longer waiting times than predicted by the exponential distribution. For the variance, our renewal model provided only the asymptotic scaling (2.71): $\text{var}\overline{\Phi}_s \approx 15.2/\Delta t$ grains^2/s^2, which resulted in the right trend ($\text{var}\overline{\Phi}_s \propto (\Delta t)^{-1}$, but overpredicted variance by 50%. This may seem surprising—because the renewal model performed better than the Markovian model at predicting the sample mean in Fig. 2.5(a)—but it should be remembered that Eq. (2.71) is an asymptotic expression that holds for sufficiently long times Δt. Further simulations (not shown here) of the renewal process, presented in Appendix B, confirmed the sample variance's sensitivity to sample size.
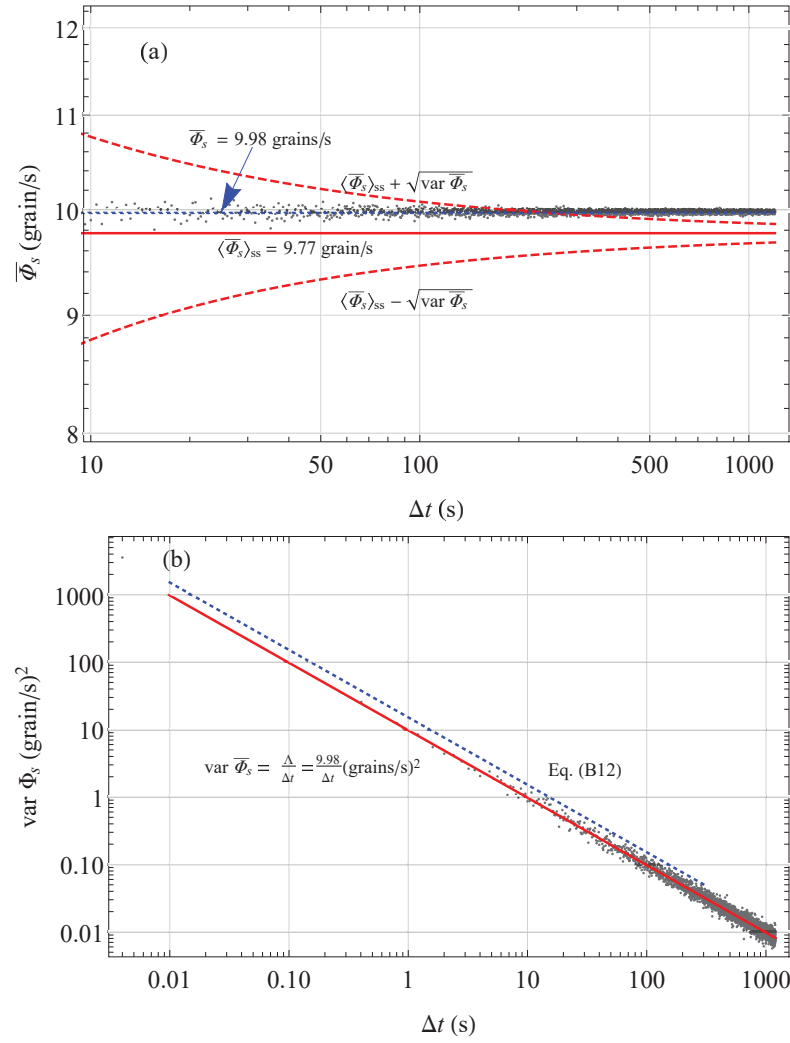
Figure 2.5: (a) Influence of the sampling duration on the computation of the sample mean. The solid red line is the theoretical mean value given by Eq. (2.36), while the dashed red lines show the uncertainty domain $\langle \overline{\Phi}_{ss} \rangle_{ss} \pm \mathrm{var}\Phi_{ss}$. The dotted blue line is the empirical mean flux $\overline{\Phi}_{ss} = \widehat{\Lambda} = N_{tot}/T_{exp} = 11,974/1200 = 9.98$ grains/s. (b) Influence of sampling duration on the sample variance. For both plots, the black dots were obtained using the bootstrap method. The solid red line shows the theoretical variance (2.9) with $\Lambda = \widehat{\Lambda} = 9.98$ grains/s, whereas the dashed blue curve shows the variance (2.71) derived from the renewal model.
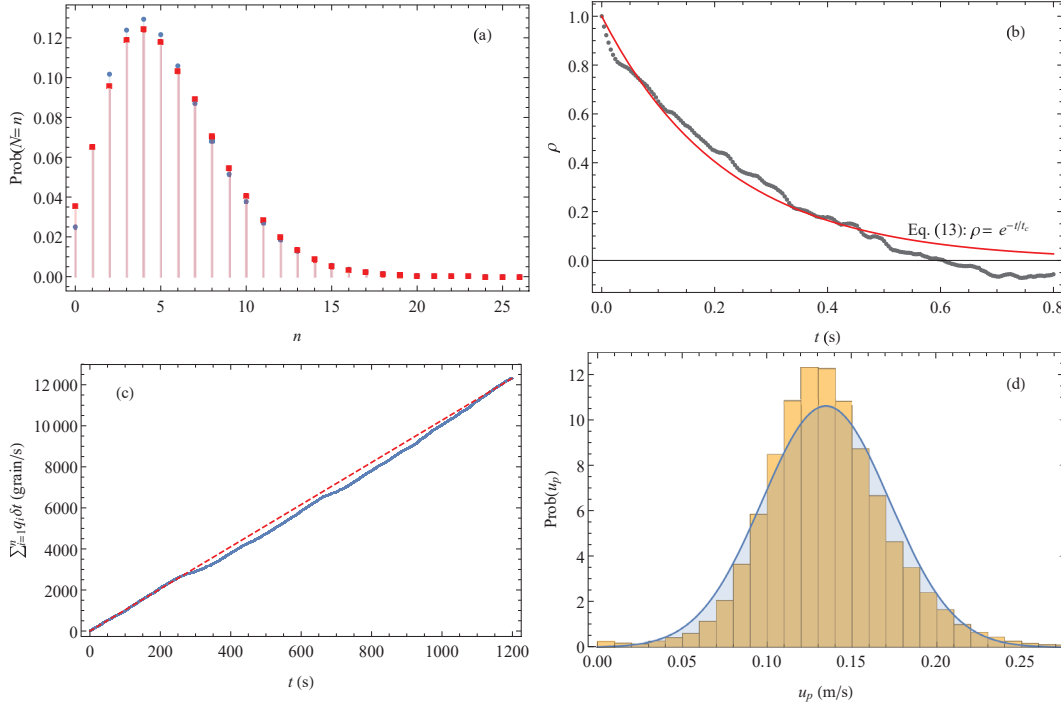
Figure 2.6: (a) Comparison between the empirical (blue dots) and theoretical (red squares, negative binomial distribution Eq. (2.11)) probability density functions of $N(t)$. (b) Autocorrelation function of $N(t)$: the black dots are the empirical function, and the solid red line shows the theoretical exponential function (2.13) with $t_c = 221$ ms. (c) Stationarity tests on the (t_i, q_i) time series: the solid line shows $\sum_i q_i \delta t$, whereas the dashed line is $\widehat{q}_{ss} t$ with $\widehat{q}_{ss} = 10.27$ grains/s the bedload transport rate averaged over the run duration. (d) Particle velocity distribution: in addition to the histogram, we have plotted the Gauss–Laplace distribution (2.5) fitted to the data (solid blue line).

2.4.3 Volume-Averaged Transport Rate

We recorded the number N of moving particles in each frame. The time-averaged number of moving particles was $\overline{N} = 5.47$, whereas the variance was $\text{var} N = 11.5$. Figure 2.6(a) shows that the negative binomial model closely matched the statistical distribution of the number of particles moving in the window during time interval δt. The error was usually less than 6%, except at $n = 0$ where it reached 30%. The time series shows large fluctuations in N, with peaks as large as $5\overline{N}$. Figure 2.6(b) shows that the exponential autocorrelation function (2.13) fitted the empirical autocorrelation function if we set $t_c = 221$ ms. The particles moved at a mean velocity $\overline{u}_p = 13.45$ cm/s (standard deviation $\sigma_u = 3.76$ cm/s). The Gauss–Laplace distribution offered a rough description of particle velocity fluctuations (see Fig. 2.6(d)). The stationarity test confirmed that the (t_i, q_i) was a stationary process, with a mean rate $\widehat{q}_{ss} = 10.27$ grains/s.

We used the bootstrap method to evaluate how the sample mean $\langle \overline{q}_s \rangle$ and variance $\text{var} \overline{q}_s$ were dependent on sampling duration Δt. As the autocorrelation time $t_c = 221$ ms was fairly long compared to the acquisition time $\delta t = 4$ ms ($t_c / \delta t \sim 50$), we had to resample the raw data series

(t_i, N_i) at a frequency of $1/(50\delta t) = 5$ Hz to obtain a sample of independent and identically distributed data. Figure 2.7(a) shows that the mean computed using the bootstrap method was close to 10.25 grains/s, a slightly (2%) higher value than the time-averaged flux $\langle \overline{\Phi}_s \rangle_{ss} = 9.98$ grains/s. Figure 2.7(b) shows the excellent agreement between the sample variances and their theoretical prediction (2.18). Because the velocity fluctuations here were small compared to their mean, taking velocity fluctuations into account did not lead to better results. This confirmed the observation, made by a number of authors (Cudden and Hoey, 2003; Ancey et al., 2008; Singh et al., 2009; Campagnol et al., 2012), that bedload transport fluctuations originate primarily from variations in the number of moving particles rather than from their velocities.

2.4.4 Influence of the Sampling Duration on the Time Series

When comparing the means and variances of the particle flux (Sec. 2.4.2) and volume-averaged transport rate (Sec. 2.4.3), we found that the two definitions led to similar values (to within a few percent) and the same dependence on the sampling duration Δt. Although this finding made sense intuitively, it was not easy to anticipate it from the theoretical results in Sec. 2.2.

This similarity holds only on average. As shown by Fig. 2.8, time series aspects depend a great deal on the definition of q_s and the sampling duration. Using short sampling durations, the particle flux showed wide fluctuations as there was no time correlation between the two measurements. On the contrary, the bedload transport rates were correlated because the acquisition frequency was much higher than $1/t_c \sim 5$ Hz. Using longer sampling durations (typically for $\Delta t \geq 1$ s), the two time-averaged time series look generally similar. For $\Delta t = 1$ s, instantaneous differences $\epsilon = \overline{q}_s/\overline{\Phi}_s - 1$ exceeding 100% were observed (see Fig. 2.8(b)), and, on average, the mean difference $\overline{\epsilon}$ reached 7%. For $\Delta t = 10$ s, the relative differences were usually less than 20%, whereas the mean difference between the two time-series dropped below 3%.

2.4.5 The Influence of Bedforms

Bedforms developed along the bed downstream of the observation plate covering the free surface. Forms were likely exacerbated by the plate as we observed a clear difference in behavior upstream and downstream of it:

- Downstream of the plate, we observed upstream-migrating antidunes. Their wavelength ranged from approximately 8 cm to 15 cm, and their amplitude was close to $2d_{50}$. Their celerity was in the 1–1.5-mm/s range, but they moved intermittently.

- Upstream of the plate, behavior was more complicated. Bed undulations were observed, but their origin and nature remained uncertain (perhaps they were sediment waves). Their wavelength fluctuated widely from 4 cm to 8 cm, and their amplitude was approximately one grain diameter. These forms experienced cycles of growth and decay over
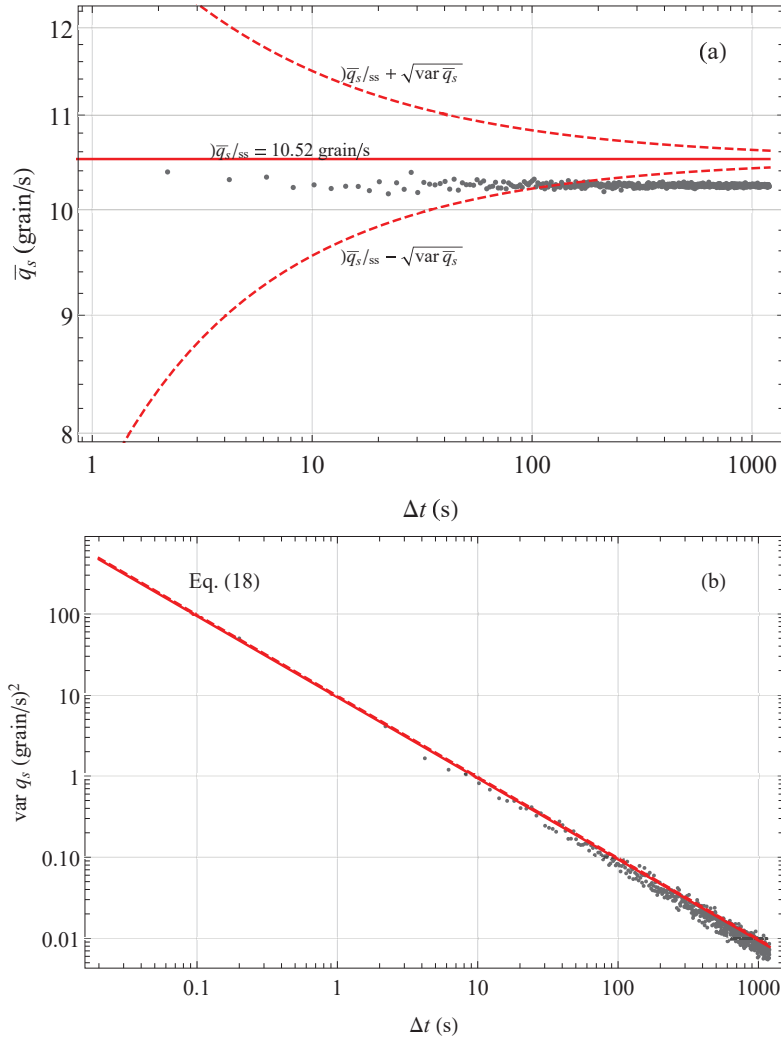
Figure 2.7: Case of the control volume at flume mid-length with erodible bed. (a) Influence of the sampling duration Δt on the computation of the sample mean: the black dots show the values generated using the bootstrap method. The solid red line shows the theoretical value (2.15). (b) Influence of the sampling duration on the computation of the sample variance. The solid red line shows the theoretical prediction (2.18) when assuming $\sigma_u = 0$ (i.e., velocity fluctuations are negligible), whereas the dashed red curve shows the theoretical prediction (2.25) when $\sigma_u > 0$. The latter curve is hardly discernible from the former as $\sigma_u \sim 0.07\overline{u}_p^2$.
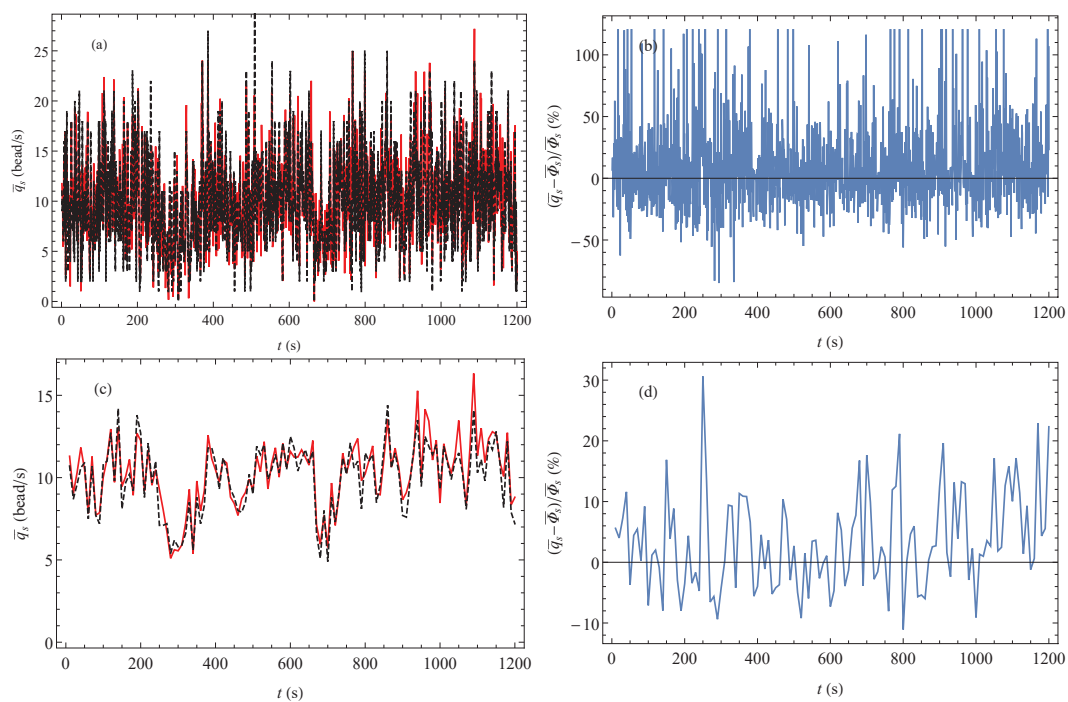
Figure 2.8: Case of the control volume at flume mid-length with erodible bed. (a) Time variations in the time-averaged transport rate $\overline{q}_s$ (solid red line) and particle flux (dashed black line) $\overline{\Phi}_s$ for a sampling duration $\Delta t = 250\delta t = 1$ s. (b) Relative difference between $\overline{q}_s$ and $\overline{\Phi}_s$ as a function of time t for $\Delta t = 1$ s. (c) Time variations in the time-averaged transport rate $\overline{q}_s$ (solid red line) and particle flux (dashed black line) $\overline{\Phi}_s$ for a sampling duration $\Delta t = 2500\delta t = 10$ s. Relative difference between $\overline{q}_s$ and $\overline{\Phi}_s$ as a function of time for $\Delta t = 10$ s.

timescales of a few minutes, with no evidence of migration (see movie S2).

We also measured an 11% increase in the bedload transport rate: over 20 min, a total of 13,271 particles left the flume, whereas 11,974 crossed the control surface $\mathscr{S}$ located in the middle of the flume. The Φ_s time series at the flume outlet was more intermittent: pulses of intense activity were separated by periods of lower activity, which was also reflected in longer waiting times between particle arrivals (waiting times as long as 6 s were measured) as shown by Fig. 2.9(a). Examining time variations in the cumulative amount of sediment shows that during the first 6 min, the particle flux was much higher than the feed rate (16.3 grains/s versus 10.3 grains/s, on average, at the flume inlet) (see Fig. 2.9(b)). After a phase that lasted about 100 s (between $t = 340$ s and 440 s) and during which the mean particle flux dropped to 2.7 grains/s, there was a period $440 \le t \le 1080$ s during which the particle flux remained almost constant ($\overline{\Phi}_s = 10.2$ grains/s) and close to the feed rate. We thus extracted a reduced sample between the timepoints $440 \le t \le 1080$ s.

Figure 2.9(c) shows that the double-averaged means (estimated using the bootstrap method) tended towards the mean particle flux $\widehat{\Lambda}_r = N_r/640 = 10.77$ grains/s obtained by dividing the number of particles $N_r = 6896$ leaving the flume between timepoints $t = 440$ s and $t = 1080$ s, by the length of time $1080 - 440 = 640$ s. As expected, the bootstrap method provided a correct estimate of the mean particle flux for this period. As the waiting-time distribution deviated from the exponential distribution, the particle rate deduced from the mean waiting time, $\widetilde{\Lambda}_r = 9.87$ grains/s, underestimated the actual transport rate by 8%. Applying the renewal model (2.70) led to a mean transport rate $\overline{\Phi}_s = 10.66$ grains/s, which was 1% below the actual rate. The main effect of bedforms was thus to alter the temporal distribution in the number of particles: the temporal distribution deviated gradually from the Poisson distribution as a result of increased intermittency, that is, alternating between periods during which no transport occurred and periods during which more intense sediment transport took place. Figure 2.9(d) shows that the double-averaged variance varied as $\widehat{\Lambda}_r/\Delta t$, as expected.

The forms observed upstream of the plate were likely driven by alternate phases of sediment storage (over periods spanning tens of seconds) and fast release of particle clusters. It is probable that this alternation changed the waiting-time distribution in the control window and created the hyper-exponential tail shown in Fig. 2.4(b). Downstream of the plate, the antidune migration period (in the 80–150-s range) was consistent with the time intervals between the bedload flux pulses recorded at the flume outlet (Fig. 2.1). We believe that the hyper-exponential waiting-time distribution at the flume outlet (Fig. 2.9) was due to the antidunes.
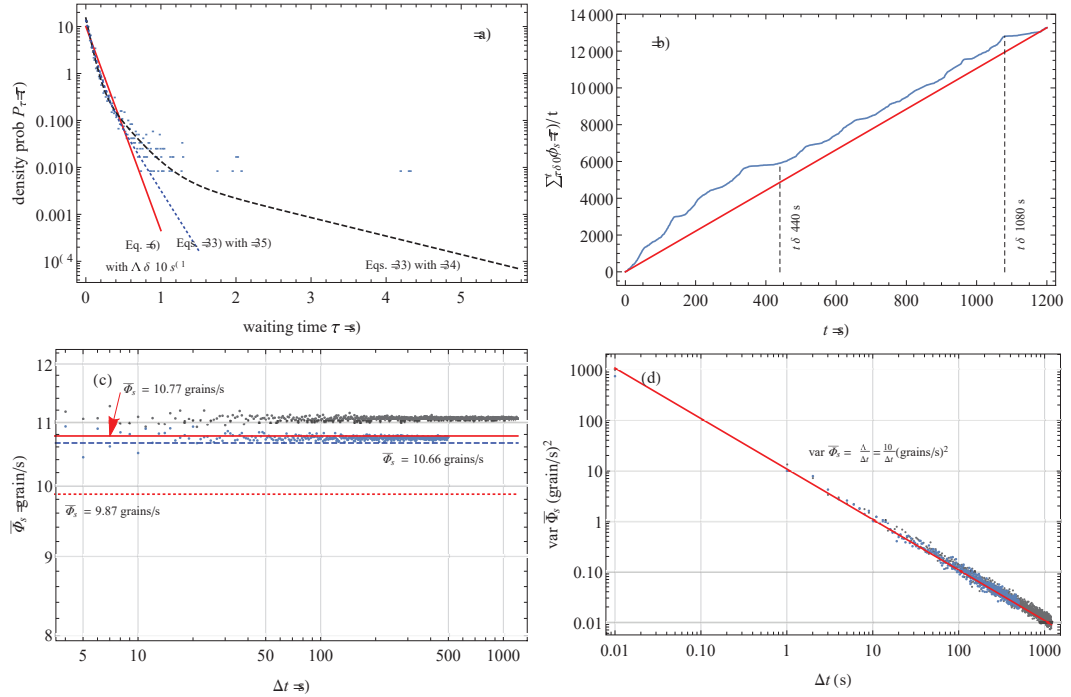
Figure 2.9: (a) Waiting-time distribution at the flume outlet: dots show the empirical probabilities. The solid red line is the exponential distribution (2.6) with rate $\widetilde{\Lambda} = 10.0$ grains/s. The dashed black line shows the hyper-exponential distribution (2.33) fitted to the data. The dotted blue line shows the hyper-exponential distribution (2.35) adjusted to the flume inlet data. (b) Stationary test: time variation in the total number of particles crossing the control surface $\sum_0^t \delta_k(\tau)$. The red line is the mean behavior $\Phi_s = \widehat{\Lambda}\delta t$ with $\widehat{\Lambda} = 13,271/1200 = 11.06$ grains/s. The dashed vertical lines show the period (from 440 s to 1080 s) over which the particle flux could be considered stationary. (c) Variations in the double-averaged particle flux with the sampling duration Δt. The solid red line shows the mean particle flux $\widehat{\Lambda}_r = N_r/640 = 10.77$ grains/s obtained by dividing the number of particles $N_r = 6896$ leaving the flume between times $t = 440$ s and $t = 1080$ s. The red line shows the mean particle flux defined from the waiting-time distribution by adjusting the exponential distribution (2.6) using the reduced sample, with $\widetilde{\Lambda}_r = 9.87$ grains/s. The dashed blue line shows the mean $\overline{\Phi}_s = 10.66$ grains/s, computed using the renewal model (2.70), with $p = 0.92$, $\lambda_1 = 3.59$ 1/s, $\lambda_2 = 14.69$ 1/s, $\alpha_1 = 0.16$, and $\alpha_2 = 0.84$. The blue points show the sample averages computed using the bootstrap method and the reduced sample as the training sample. The grey points show the sample averages when the entire time series is used as the bootstrap method's training sample. (d) Variation in the double-averaged variance var$\overline{\Phi}_s$ with the sampling interval Δt. The solid red line shows the theoretical variance (2.9) with $\Lambda = \widetilde{\Lambda} = 10.0$ grains/s.

2.5 Applications

We finish the paper by describing two potential applications for the measurement protocol outlined in Sec. 2.2.7:

- We ran long-duration experiments under steady-state conditions in a laboratory flume

(see Sec. 2.5.1). As gravel bars and pools developed and migrated along the flume bed, the bedload transport measured at the flume outlet exhibited wide fluctuations resulting from alternating phases of low and intense transport. Bedload transport pulses were often associated with the destruction of bars, which released large amounts of gravel (Dhont and Ancey, 2018).

- We have been monitoring a gravel-bed river in the Swiss Alps since 2011 (see Sec. 2.5.2). Contrary to other applications in this paper, this was not a steady-state system, but there were periods during which it approached a steady state, which made it possible to apply our measurement protocol.

These two applications illustrate the sampling duration's significance to the estimation of bedload transport rates. To obtain fairly high precision (10% variance or lower), one has to carefully study how the Q_s variance changes with the sampling duration Δt.

2.5.1 Laboratory Flume

Here, we show how the measurement protocol performed with a time series of bedload transport rates measured at the outlet of a flume 19 m long, 60 cm wide, and inclined at 1.6% to the horizontal. We used gravel whose median diameter was $d_{50} = 5.5$ mm. The water discharge was constant $Q_w = 15$ L/s. Transport rates were measured using impact plates and accelerometers operated at 100 Hz for a long period ($T_{exp} = 155$ h). Raw data were aggregated by averaging them over time steps of $\delta t = 1$ min. The reader is referred to Dhont (2017) and Dhont and Ancey (2018) for details of this experiment.

Figure 2.10(a) shows the bedload transport rate recorded at the flume outlet: periods of intense bedload transport were usually associated with the destruction of gravel bars or the scouring of pools. Despite these pulses, the overall bedload transport rate behaved like a quasi-stationary process, as shown by Fig. 2.10(b). Applying the central limit theorem enabled us to estimate how the time-averaged mean and variance varied with sampling duration Δt, whereas the bootstrap method enabled us to generate double-averaged means and variances for different Δt values (see Figs. 2.10(c) and (d)). Although the central limit theorem provides only an asymptotic expression for $\mathrm{var}\overline{Q}_s$ ($\mathrm{var}\overline{Q}_s = \sigma_q^2 \delta t / \Delta t$), we found that for all Δt values, this asymptotic relation closely matched the sample generated using the bootstrap method. Figure 2.10(d) shows that for a sampling duration $\Delta t = 1$ min, the variance was 4.3 grains^2/s^2, and thus we could only determine the mean bedload transport rate to within $\sqrt{4.3}/4.07 \sim 50\%$. If we wanted greater precision in the determination of Q_s—say 10% greater precision—we had to increase the sampling duration to 30 min, as per Fig. 2.10(d).

2.5.2 Gravel-Bed River

Here, we present an application to the River Navisence (canton Valais, Switzerland), a gravel-bed river near Zinal monitored since 2011. Bedload transport rates are measured using
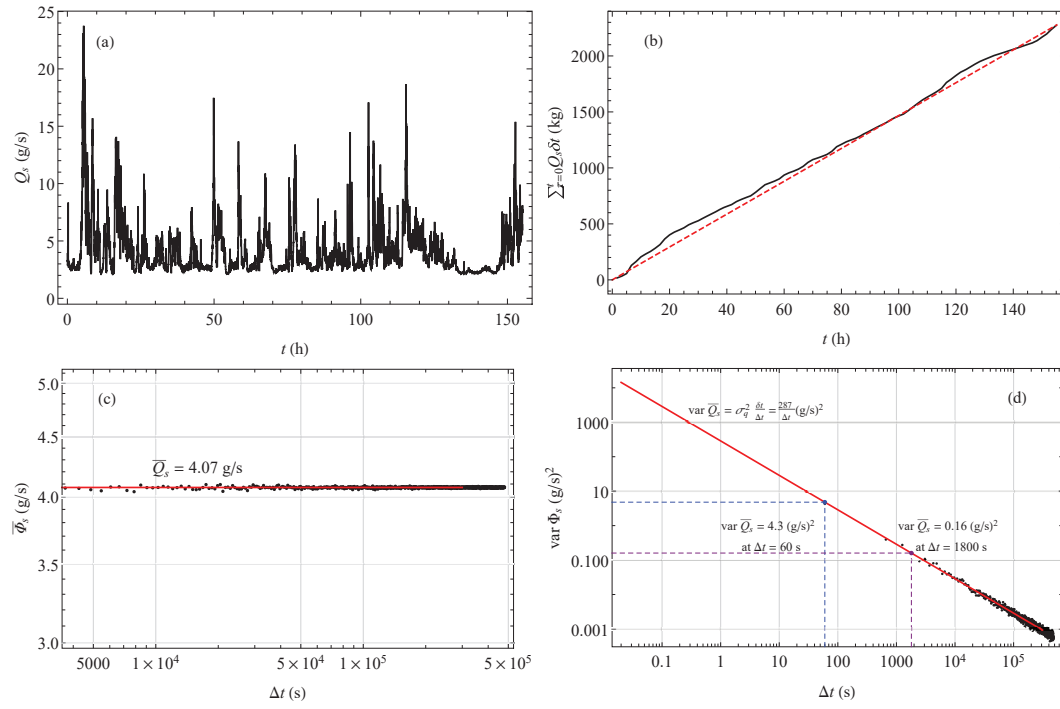
Figure 2.10: Application to a 19-m flume. (a) Time series of $\overline{\Phi}_s$. (b) Stationary test. The dashed red line is $Q_s = \widehat{\Lambda} t$ with $\widehat{\Lambda} = 4.07$ g/s. (c) Variation in the double-averaged mean with the sampling duration Δt. The solid red line shows the mean flux $\overline{Q}_{ss} = \widehat{\Lambda} = 4.07$ g/s, whereas the black dots show the means generated using the bootstrap method. (d) Variation in the double-averaged variance with sampling duration Δt. The black dots show the variances generated using the bootstrap method. The solid red line is the theoretical variance $\overline{Q}_s = \sigma_q^2 \delta t / \Delta t$ with $\sigma_q^2 = 4.8$ g^2/s^2.

geophones placed across a concrete sill of width $W = 9$ m (Ancey et al., 2014; Wyss et al., 2016). The mean bed slope upstream of the sill is $i = 3.2\%$. The median particle diameter of transported bedload was $d_{50} = 8$ cm.

Figure 2.11(a) shows the time series of bedload transport rates Q_s and water discharge Q_w for 8 July 2012 (a day picked randomly). Water discharge varied throughout the day under the effect of sunshine. Overnight and in the morning, bedload transport rates were negligibly low. In the afternoon, ice- and snow-melt increased water discharge and thus the transport rate went up. We isolated a sequence of transport rates from 17:00 to 18:00, for which bedload transport could be considered stationary, as shown by Fig. 2.11(b).
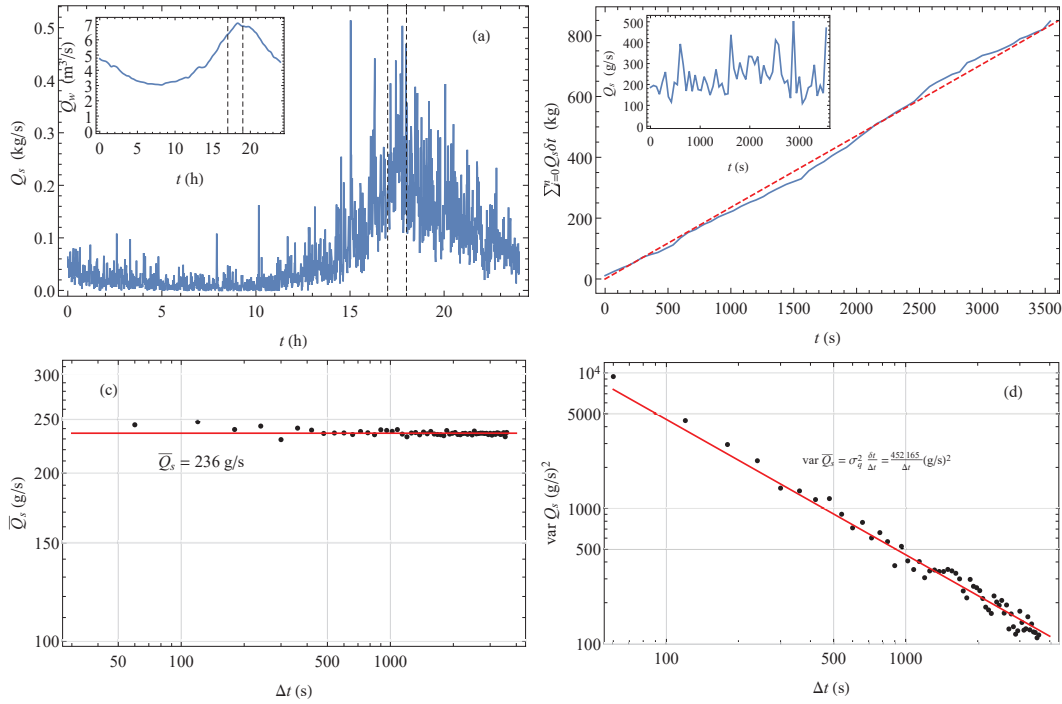
Figure 2.11: Application to the River Navisence. (a) Time series for 8 July 2012. (b) Stationary test. The dashed red line is $Q_s = \widehat{\Lambda} t$ with $\widehat{\Lambda} = 236$ g/s. (c) Variation in the double-averaged mean with the sampling duration Δt. The solid red line shows the mean flux $\overline{Q}_{ss} = \widehat{\Lambda} = 236$ g/s, whereas the black dots show the means generated using the bootstrap method. (d) Variation in the double-averaged variance with sampling duration Δt. The black dots show the variances generated using the bootstrap method. The solid red line is the theoretical variance $\mathrm{var}\overline{Q}_s = \sigma_q^2 \delta t / \Delta t$ with $\sigma_q^2 = 7536$ g^2/s^2.

Figures 2.11(c) and (d) show the double-averaged means and variances computed using the bootstrap method. As the bedload transport was stationary during the period considered, the double-averaged means were close to the mean rate $\overline{Q}_{ss} = \widehat{\Lambda} = 236$ grains/s estimated using the stationary test (see Fig. 2.11(b)). The variance curve in Fig. 2.11(d) enabled us to estimate that for $\Delta t = \delta t = 60$ s, the mean transport rate was accurate to within $\sigma_q / \overline{Q}_s = 36\%$. Increasing Δt by a factor of 10 ($\Delta t = 10$ min) decreased the uncertainty to 3.6%. As the 17:00

to 18:00 time slot corresponded to the day's peak bedload transport activity, it is tempting to consider that a convenient sampling duration for 8 July 2012 was $\Delta t = 10$ min—sufficiently long to obtain low var$\overline{Q}_s$ values and sufficiently short to capture the slow variations in the bedload transport rate with water discharge.

2.6 Conclusion

Bedload transport rates usually exhibit wide fluctuations, even under steady flow conditions. Measurements of time-averaged transport rates $\mathcal{Q}_s$ representative of bedload transport at given times can thus be biased to varying degrees, as illustrated by Fig. 2.1, where errors exceeding 100% can be observed at certain sampling durations.

The present paper examines how we can assess the uncertainties associated with estimating a time-averaged transport rate $\overline{\mathcal{Q}}_s$. We used the birth–death immigration–emigration model developed by Ancey et al. (2008). We arrive at an experimental protocol for measuring the mean particle flux $\mathcal{Q}_s = \overline{\Phi}_s$ or bedload transport rate $\mathcal{Q}_s = \overline{q}_s$ (see Sec. 2.2.7) and estimating the uncertainties associated with that measurement. The first step is to define a time interval over which $\mathcal{Q}_s(t)$ behaves like a stationary process. Depending on the data acquisition frequency and the relevance of the Markovian assumption (waiting times distributed exponentially or exhibiting a thicker tail), different models can be used to define the double-averaged mean and variance. When data-acquisition frequencies are sufficiently high (typically, higher than 1 Hz) and the Markovian assumption is realistic, then the Markovian model developed by Ancey et al. (2008) can be applied. When the Markovian assumption fails, a renewal model can be used. At low data acquisition frequencies, the central limit theorem can be employed to find the double-averaged variance's dependence on the sampling duration Δt.

Markovian theory provides valuable insights into the behavior of $\mathcal{Q}_s$ fluctuations. One remarkable result is that the ensemble variance of $\mathcal{Q}_s$ is controlled solely by the sampling duration Δt and mean rate $\overline{\mathcal{Q}}_s$. As exemplified by the toy model in Section 2.1.3, this ensemble variance offers a better estimate of the uncertainties associated with the measurement of $\overline{\mathcal{Q}}_s$ than does sample variance.

Appendices

2.7 Appendix A - Integral of a Markov Process

2.7.1 Theoretical Reminder: Master Equations and Other Definitions

We assume that the time variations in N can be described using Markov process theory Gillespie (1992). Between times t and $t + \mathrm{d}t$, the N variation (called the *propagator*)

$$\Theta(\mathrm{d}t; n, t) = N(t + \mathrm{d}t) - N(t) \text{ given that } N(t) = n, \tag{2.37}$$

has the following probability density function (strictly speaking, the probability mass function as N is a discrete random variable):

$$\Pi(m \mid dt; n, t) = \text{prob}(\Theta(dt; n, t) = m),\qquad(2.38)$$

with $m = 0$, 1, or -1 for a birth–death Markov process. The process can be also described by introducing the jump probability $q(n, t; \tau)$, which is the probability that N varies by ± 1 at some instant between t and $t + \tau$. The Markovian assumption imposes that for infinitesimal time intervals, $q(n, t; dt) = a(n, t)dt$, where a is a positive function of n and t. The state probability $w(m \mid n, t)$ is the probability that upon jumping at time t, N takes the new value $n + m$. The propagator density Π and the functions a and w are related:

$$\Pi(m \mid dt; n, t) = a(n, t)dt\, w(m \mid n, t) + (1 - a(n, t)dt)\delta_k(m, 0),\qquad(2.39)$$

where δ_k is the Kronecker delta function.

We also define the *consolidated characterizing function*:

$$W(m \mid n, t) = a(n, t) w(m \mid n, t),\qquad(2.40)$$

which can be interpreted as follows: $W dt$ is the probability that the number of particles $N(t) = n$ jumps from n to $n + m$ in the time interval dt. This function can be used in the *master equation*, that is, the governing equation for the probability of observing $N(t)$:

$$\frac{\partial}{\partial t} P(n, t \mid n_0, t_0) = \sum_{m=-1}^{m=+1} W(m \mid n - m, t) P(n - m, t \mid n_0, t_0) - W(-m \mid n, t) P(n, t \mid n_0, t_0),\quad(2.41)$$

and if we define

$$W_+(n) = W(1 \mid n, t) \text{ and } W_-(n) = W(-1 \mid n, t),\qquad(2.42)$$

which are the probabilities of gain or loss, respectively, then the master equation (2.41) can also be written

$$\frac{\partial}{\partial t} P(n, t \mid n_0, t_0) = W_-(n+1) P(n+1, t \mid n_0, t_0) - W_+(n) P(n, t \mid n_0, t_0) +\qquad(2.43)$$
$$W_+(n-1) P(n-1, t \mid n_0, t_0) - W_-(n) P(n, t \mid n_0, t_0).$$

It can be shown that the process is entirely determined by the functions Gillespie (1992):

$$a(n) = W_+ + W_- = \nu_{in} + \lambda + (\nu_{out} + \mu + \sigma)n\qquad(2.44)$$

where $a(n)dt$ represents the probability that N varies within the time period dt, and

$$\nu(n) = W_+ - W_- = \nu_{in} + \lambda + (\mu - \sigma - \nu_{out})n.\qquad(2.45)$$

Equivalently, we can work with the pairs of functions (W_+, W_-) or (a, ν).

2.7.2 Mean, variance and covariance of $N(t)$

It can be shown that the mean number of moving particles $\langle N \rangle$ satisfies the differential equation (see Chap. 6 in Gillespie (1992)):

$$\frac{\mathrm{d}}{\mathrm{d}t}\langle N \rangle = v(\langle N \rangle) = W_+(\langle N \rangle) - W_-(\langle N \rangle), \tag{2.46}$$

subject to the initial condition $\langle N \rangle(t_0) = N_0$. The variance of N is governed by

$$\frac{\mathrm{d}}{\mathrm{d}t}\mathrm{var}N = 2\left(\langle N v(N) \rangle - \langle N \rangle \langle v(N) \rangle\right) + (\langle a(N) \rangle), \tag{2.47}$$

subject to $\mathrm{var}N(t_0) = 0$. The time covariance is

$$\frac{\mathrm{d}}{\mathrm{d}t_2}\mathrm{cov}(N(t_1), N(t_2)) = \langle N(t_1) v(N(t_2)) \rangle - \langle N(t_1) \rangle \langle v(N(t_2)) \rangle, \tag{2.48}$$

for $t_0 \le t_1 \le t_2$ and subject to the the initial condition $\mathrm{cov}(N(t_1), N(t_1)) = \mathrm{var}N(t_1)$.

2.7.3 Integral S of $N(t)$

The time integral S of N is defined as

$$S(t) = \int_{t_0}^{t} N(t)\mathrm{d}t. \tag{2.49}$$

Its mean value is given by

$$\frac{\mathrm{d}}{\mathrm{d}t}\langle S \rangle = \langle N \rangle, \tag{2.50}$$

whereas the time variations in the covariance $\mathrm{cov}(S, N) = \langle SN \rangle - \langle S \rangle \langle N \rangle$ obey the equation

$$\frac{\mathrm{d}}{\mathrm{d}t}\mathrm{cov}(S, N) = \mathrm{var}N + \langle S v(N) \rangle - \langle S \rangle \langle v(N) \rangle, \tag{2.51}$$

subject to $\mathrm{cov}(S, N) = 0$ at time $t = t_0$. The S variance is

$$\frac{\mathrm{d}}{\mathrm{d}t}\mathrm{var}S = 2\mathrm{cov}(S, N), \tag{2.52}$$

subject to $\mathrm{var}S(t_0) = 0$. The covariance of S is the solution to

$$\mathrm{cov}(S(t_1), S(t_2)) = \mathrm{var}S(t_1) + 2\int_{t_1}^{t_2} \mathrm{cov}(S(t_1), N(\tau))\mathrm{d}\tau \tag{2.53}$$

for $t_0 \le t_1 \le t_2$ and where the integrand is the solution to the differential equation

$$\frac{\mathrm{d}}{\mathrm{d}t_2}\mathrm{cov}(S(t_1), N(t_2)) = \langle S(t_1) v(N(t_2)) \rangle - \langle S(t_1) \rangle \langle v(N(t_2)) \rangle, \tag{2.54}$$

for $t_0 \leq t_1 \leq t_2$. We refer the reader to Chapter 6 in Gillespie (1992) for the proofs.

2.7.4 Moments of S

The mean time integral S is the solution to Eq. (2.50)

$$\langle S(t) \rangle = N_0 t_c (1 - e^{-t/t_c}) + \langle N \rangle_{ss} \left(t - t_c (1 - e^{-t/t_c}) \right). \tag{2.55}$$

The solution to the covariance equation (2.51)

$$\frac{\mathrm{d}}{\mathrm{d}t} \mathrm{cov}(S, N) = \mathrm{var} N - \alpha \, \mathrm{cov}(S, N),$$

takes the form

$$\mathrm{cov}(S, N) = \frac{N_0 \gamma}{\alpha^2} \left(e^{-2t/t_c} + e^{-t/t_c} (\alpha t - 1) \right) + \frac{\beta (1 - e^{-t/t_c})^2 + \gamma \langle N \rangle_{ss} (1 - 2\alpha t e^{-t/t_c} - e^{-2t/t_c})}{2\alpha^2}, \tag{2.56}$$

where $\gamma = \nu_{out} + \sigma + \mu$ and $\alpha = \nu_{out} + \sigma - \mu$. We find that the covariance tends to the limit

$$\mathrm{cov}_{ss}(S, N) = \frac{\beta + \gamma \langle N \rangle_{ss}}{2\alpha^2} = \frac{(\lambda + \nu_{in})(\nu_{out} + \sigma)}{(\nu_{out} + \sigma - \mu)^3}. \tag{2.57}$$

Using Eq. (2.52), we deduce the variance of S by integrating the covariance $\mathrm{covcov}(S, N)$. Asymptotically, this scales as

$$\mathrm{var} S \propto \frac{\beta + \gamma \langle N \rangle_{ss}}{\alpha^2} t = \frac{(\lambda + \nu_{in})(\nu_{out} + \sigma) t}{(\nu_{out} + \sigma - \mu)^3}. \tag{2.58}$$

By solving Eq. (2.53), we find that the autocorrelation function of S is

$$\rho_s(\tau) = 1 + \frac{t_c}{\tau} \frac{(\nu_{out} + \sigma - \mu)^3}{(\lambda + \nu_{in})(\nu_{out} + \sigma)} (1 - e^{-\tau/t_c}). \tag{2.59}$$

2.8 Appendix B - Time-Averaged Particle Flux: Renewal Theory

The Markovian assumption imposes strict conditions on the applicability of Eq. (2.8). These are either an exponential distribution for the waiting times or, equivalently, a Poisson process for the number of particles crossing the control surface. We can relax these assumptions by considering other probability distributions and using renewal theory to compute the number of particles crossing the control surface $\mathscr{S}$. Let us consider that one or two particles can arrive at the same time:

$$\mathrm{prob}(N = 1) \quad = \quad p, \tag{2.60}$$

$$\mathrm{prob}(N = 2) \quad = \quad 1 - p, \tag{2.61}$$

$$\mathrm{prob}(N > 2) \quad = \quad 0, \tag{2.62}$$

and that the waiting-time distribution is the two-parameter hyper-exponential distribution, whose density function is

$$P_\tau(\tau) = \alpha_1 \lambda_1 \exp(-\lambda_1 \tau) + \alpha_2 \lambda_2 \exp(-\lambda_2 \tau), \tag{2.63}$$

where α_1 and α_2 are mixture parameters satisfying $\alpha_1 + \alpha_2 = 1$, whereas λ_1 and λ_2 are two rates. At time t, M jumps have occurred (with one or two arrivals). Let us call S the sum of particles that have crossed the control surface up to time t

$$S(t) = \sum_{i=1}^{M(t)} N_i \tag{2.64}$$

where $M(t) = \max\{n : T_n \le t\}$, and $T_n = \tau_1 + \tau_2 + \cdots + \tau_n$ for $n \ge 1$ ($T_0 = 0$), and τ_i is a sequence of waiting times distributed from (2.63). There is no analytical expression of S in (2.64), but we can derive approximations in the limit of $t \to \infty$. Using Wald's equation Grimmett and Stirzaker (2008), we can deduce the expectation of the sum S:

$$\mathbb{E}(S) = \mathbb{E}(N)\mathbb{E}(M), \tag{2.65}$$

and using the law of total variance, we get its variance:

$$\mathrm{var}S = \mathrm{var}N\mathbb{E}(M) + \mathbb{E}(N)^2 \mathrm{var}M. \tag{2.66}$$

Here we have: $\mathrm{var}N = p(1-p)$ and $\mathbb{E}(N) = 2 - p$. The number of jumps can be approximated as follows:

$$\mathbb{E}(M) = \frac{t}{\overline{\tau}} + o(t), \tag{2.67}$$

$$\mathrm{var}M = \frac{t\sigma_\tau^2}{\overline{\tau}^3} + o(t), \tag{2.68}$$

with

$$\overline{\tau} = \frac{\alpha_1}{\lambda_1} + \frac{\alpha_2}{\lambda_2} \text{ and } \sigma_\tau^2 = 2\left(\frac{\alpha_1}{\lambda_1^2} + \frac{\alpha_2}{\lambda_2^2}\right) - \left(\frac{\alpha_1}{\lambda_1} + \frac{\alpha_2}{\lambda_2}\right)^2. \tag{2.69}$$

We then deduce:

$$\overline{\Phi}_s(t) = \mathbb{E}\left(\frac{S}{t}\right) = (2 - p)\frac{\lambda_1 \lambda_2}{\lambda_2 \alpha_1 + \lambda_1 \alpha_2}, \tag{2.70}$$

and

$$\mathrm{var}\Phi_s(t) = \mathrm{var}\left(\frac{S}{t}\right) = \left(\frac{p(1-p)}{\overline{\tau}} + \frac{(2-p)^2 \mathrm{var}\tau}{\overline{\tau}^3}\right)\frac{1}{t}. \tag{2.71}$$

2.9 Appendix C - Exponential Velocity Distribution

Let us consider that the particle velocity is distributed exponentially. We then replace the Gaussian distribution (2.5) with the exponential law with mean $\overline{u}_p$

$$P_u(w) = \text{prob}(u = w) = \frac{1}{\overline{u}_p} \exp(-w/\overline{u}_p). \tag{2.72}$$

Like in § 2.5, we introduce the sum of k particle velocities

$$U = \sum_{i=1}^{k} u_{p,i}. \tag{2.73}$$

If k is fixed, then the probability P_k of observing U is the Erlang distribution with shape k and rate $1/\overline{u}_p$. If k varies randomly, then the probability of observing U is

$$P_U = \sum_{k=1}^{\infty} P_n(k) P_k(U). \tag{2.74}$$

The volume-averaged transport rate is $q_s = U/L$. If we still assume that the probability of observing k particles is given by the negative binomial distribution with parameters p and q, the probability distribution of U becomes

$$P_{q_s} = L P_U(Lq_s) = L \sum_{k=1}^{\infty} \binom{q+n-1}{q-1} p^q (1-p)^n \frac{(Lq_s)^{k-1} e^{-Lq_s/\overline{u}_p}}{\overline{u}_p^k (k-1)!}. \tag{2.75}$$

There exists a closed-form expression for P_{q_s}, but we just need the first two moments:

$$\langle q_s \rangle = \int_{\mathbb{R}_+} q_s P_{q_s} \mathrm{d}q_s = \frac{N_{ss}}{L} \overline{u}_p, \tag{2.76}$$

$$\text{var}\, q_s = \int_{\mathbb{R}_+} (q_s - \langle q_s \rangle)^2 P_{q_s} \mathrm{d}q_s = \frac{\text{var}_{ss} N}{L^2} (1+p) \overline{u}_p^2. \tag{2.77}$$

Assuming that particle velocity and particle number are independent variables, we can generalize the variance equation (2.18) to take velocity fluctuations into account in the double-averaged variance by following the same reasoning as that used for deriving Eq. (2.18):

$$\text{var}\, \overline{q}_s(\Delta t \mid t) = \text{var}_{ss} N \frac{\overline{u}_p^2}{L^2} (1+p) \frac{t_c}{\Delta t}, \tag{2.78}$$

an expression that is close to Eq. (2.25) obtained for Gaussian velocity distributions.

3 The variability of antidune morphodynamics on steep slopes

Ivan Pascal[1], **Christophe Ancey**[1], **and Patricio Bohorquez**[2]

[1] Laboratory of Environmental Hydraulics, École Polytechnique Fédérale de Lausanne, Lausanne, Switzerland.
[2] Centro de Estudios Avanzados en Ciencias de la Tierra, Universidad de Jaén, Campus de las Lagunillas, Jaén, Spain.

Doctoral candidate's contribution

The candidate designed and conducted the experiments. Gaëtan Gindrat contributed to the experimental work during his semester project at LHE. The analyses of the image sequences to extract bed topography and compute bedload transport rate data were carried out by the candidate. The candidate interpreted the results, with constructive comments provided by Prof. Bohorquez. Prof. Bohorquez conducted the first application of 2D fast Fourier transform on the bed elevation perturbation data. The scaling framework and the resulting relationships were original contributions by the candidate, who received feedbacks from Prof. Bohorquez and an anonymous reviewer during the peer-review process. Dr. Matthieu Cartigny and the Associate Editor also provided constructive comments on the manuscript. This manuscript was written by the candidate, with general and editorial comments provided by Prof. Ancey and Prof. Bohorquez.

Abstract

Steep streams on rough beds are generally characterised by supercritical flow conditions under which antidunes can develop and migrate over time. In this paper, we present flume experiments that we conducted to investigate the variability of antidune geometry and migration celerity, a variability observed even under steady-state conditions. Quantifying this variability is important for river morphodynamics, hydraulics and paleohydraulics. We imposed moderate to intense bedload transport rates at the flume inlet in order to assess their effects on antidune morphodynamics for near-constant values of the mean bed slope. The bed elevation profile was monitored for each experiment with high spatial and temporal resolution. Upstream migrating antidunes were observed along most of the flume length. Considering single values for wavelength and celerity was not sufficient to describe the antidune behaviour in these experiments. By using spectral analysis, we identified the variability ranges of bedform shape and celerity. Interestingly, migration celerity increased with increasing antidune wavelength; the opposite trend was reported for dunes in other studies. Antidunes were more uniform and migrated faster for higher sediment feeding rates. Scaling the spectra made it possible to find a general dimensionless relationship between antidune wavelength and celerity. This framework provides a novel method for estimating the mean bedload transport rate in the presence of upstream migrating antidunes.

3.1   Introduction

In nature, riverbeds usually exhibit bedforms of various spatial and temporal scales, which can migrate over time. The occurrence of a given bed morphology depends on the hydrodynamical and sedimentary conditions (sediment properties, supply, etc.). Studying bedform dynamics is important to understand both the evolution of alluvial environments and the implications for flow resistance and sediment fluxes. Antidunes are bedforms typical of supercritical (or near critical) flows on steep slopes and can be observed also for upper-flow regimes on mild slopes. The term "antidune" was originally proposed by Gilbert and Murphy (1914) to identify two-dimensional bedforms that migrate upstream, contrary to dunes. Nowadays, antidunes are defined as sinusoidal shaped bedforms for which the water surface is in phase with the bed undulations, according to Kennedy (1961). This definition is adopted in the present paper. Antidunes are associated with step-pool morphologies (Whittaker and Jaeggi, 1982; Grant, 1994; Chin, 1999) and may co-exist with cyclic steps in transcritical flows (Alexander, 2008; Cartigny et al., 2014; Slootman and Cartigny, 2020). Since the pioneering work by Kennedy (1961, 1963, 1969), great efforts have been dedicated to studying antidune formation and their stability domains (e.g. Reynolds, 1965; Engelund, 1970; Hayashi, 1970; Parker, 1975; Coleman and Fenton, 2000; Huang and Chiang, 2001; Kubo and Yokokawa, 2001; Carling and Shvidchenko, 2002; Colombini, 2004; Colombini and Stocchino, 2005; Deigaard, 2006; Di Cristo et al., 2006; Colombini and Stocchino, 2008; Bose and Dey, 2009; Andreotti et al., 2012; Colombini and Stocchino, 2012; Vesipa et al., 2012; Greco et al., 2018; Bohorquez et al., 2019). In parallel, experimental studies on antidunes have been performed to test theoretical

and numerical frameworks and to investigate the main physical mechanisms governing these bed instabilities (e.g. Guy et al., 1966; Cao, 1985; Recking et al., 2009; Mettra, 2014). In paleohydraulic studies, antidunes receive special attention because they are important proxies of hydraulic and sedimentary conditions (e.g. Shaw and Kellerhals, 1977; Carling et al., 2009). Also, downstream migrating antidunes were early documented in experiments (e.g. Kennedy, 1961) but a criterion for antidune migration direction has been formalised only recently (Núñez-González and Martín-Vide, 2011). Experimental studies have mostly focused on downstream migrating bedforms (dunes and bars) than on antidunes. This likely reflects the high demand of methods to quantify dune geometry and contribution to the sediment fluxes for streams on gentle slopes. To the best of our knowledge, Simons et al. (1965) can be credited with the first framework for computing the contribution of downstream migrating dunes to the mean bedload discharge. The existence of bedload transport pulses has been related to bedform migration (Gomez et al., 1989), a relationship that has been investigated in gravel-bed flumes through experimental investigations into alternate bars (e.g. Dhont and Ancey, 2018; Palucis et al., 2018). When alternate bars are associated with near-critical flows, antidunes may develop locally and participate to sediment transport (see Movie S3 in Dhont and Ancey, 2018).

For steep slopes, Recking et al. (2009) considered data regarding antidunes occurrence and proposed new specific relationships for predicting the dominant wave geometry. Migrating antidunes of variable wavelength have been observed in gravel-bed rivers (see Video Clip S2 in Froude et al., 2017). In his flume experiments on steep slopes, Mettra (2014) observed antidunes characterised by varying shapes and migration celerities and investigated the contribution of upstream migrating antidunes to the bedload flux. Based on the model proposed by Simons et al. (1965), he proposed two expressions for estimating the mean and maximum local bedload transport rates (involving mean and maximum values of antidune amplitude and celerity). Ancey and Pascal (2020) monitored bedload transport in a narrow flume in presence of upstream migrating antidunes and reported bedload pulses whose period was consistent with the antidune migration period. As far as we know, an integral relationship for computing the sediment flux associated to upstream migrating antidunes is not yet available. This expression should also include the potential scale dependencies between wave geometry and migration celerity. Upstream migrating antidunes travel in the opposite direction of the bedload flux which cannot be decomposed straightforwardly in a fraction that participates to the migration of a given antidune and in a passive fraction. This peculiarity prevents the direct application of the integration frameworks already defined for downstream migrating dunes by Nikora (1984) and Guala et al. (2014).

Running well-controlled flume experiments provides useful insights into the bedform dynamics under steady-state conditions. We performed experiments in a steep flume in which we monitored the bed topography with high spatial and temporal resolution. We used spectral analysis to quantify the variability of antidune geometry and celerity. We analysed how sediment transport rates depended on antidune migration celerity, and how antidune variability affected in turn bedload transport. We present the outcomes of this analysis with an emphasis

given to antidune wavelength and migration celerity. We provide tentative answers to the two following questions: (i) Does the variability of antidune geometry and migration celerity follow a general trend? (ii) Is it possible to define a method for estimating the mean bedload transport rate associated with upstream migrating antidunes on steep slopes? The findings are discussed and their potential implications for river morphodynamics, steep-stream hydraulics and paleohydraulics are outlined.

3.2 Methods

3.2.1 Experimental arrangement

To investigate antidune morphodynamics, we carried out experiments in a 2.5–m-long 4–cm-wide flume with transparent sidewalls. We used natural gravel with median particle diameter d_{50} = 2.9 mm (d_{16} = 2.5 mm, d_{84} = 3.3 mm) and sediment density ρ_s = 2550 kg m^{-3}. The bed layer thickness was 4 cm on average. We chose well-sorted natural gravel to avoid grain sorting. This choice also had the advantage of simplifying the protocol of bedload transport rate measurement. The flume (see Figure 3.1) was equipped with a sediment feeder, whose supply rate was controlled by a hopper and a rotating wheel. A high-speed camera was mounted over the flume outlet to monitor the sediment discharge. Another camera was used to film bed evolution from the side. We set the flume width at 4 cm to ensure a reasonable trade-off between ease of data acquisition and representativeness of flow and morphodynamic conditions (relative to those observed in real-world scenarios). This configuration enables the accurate assessment of the quasi-equilibrium state before starting topography data collection and after the run. This condition is fundamental to guarantee that the time series of the bed topography is not significantly influenced from processes related to bed disequilibrium at the flume scale. On the other hand, running experiments in small flumes requires particular attention and accurate systems to control and assess sediment and water supply (see the last part of the next section for details). As the flow conditions and associated bedforms (antidunes in our case) were nearly two-dimensional, we could use simple imaging techniques for extracting bed topography data from side images. The d_{50}/W ratio was kept under 0.1 to mitigate lateral confinement effects.

3.2.2 Experimental conditions

The experiments were carried out under steady-state conditions in terms of both water discharge and sediment supply. We ran four experiments with different transport intensities and similar values of mean slope angle, $\overline{\psi} \approx 3°$ (Table 3.1).

For each run, we imposed a constant sediment feed rate and set the flow discharge per unit width q_w which ensured balance between erosion and deposition at the flume scale. The sediment feed rates $q_{s,in}$ corresponded to different values of the ratio Θ/Θ_c, where Θ is the Shields number and Θ_c is the critical Shields number (see Table 3.2). We estimated Θ using
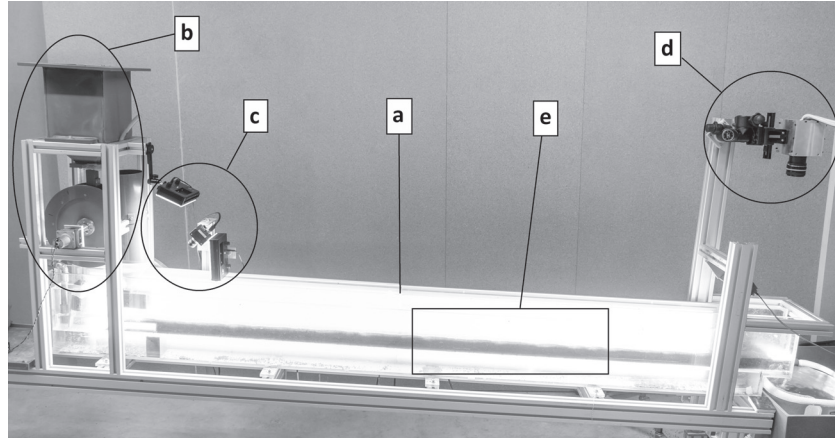
Figure 3.1: Experimental setup: (a) transparent tilting flume for quasi 2D flow, (b) sediment feeding system, (c) camera for monitoring sediment supply at the inlet, (d) camera for monitoring bedload discharge at the outlet, (e) window captured by the side camera (length $L_w = 0.75$ m).

Table 3.1: Main parameters for the experimental runs E1–E4.

Run	Dur. [min]	$\overline{\psi}$ [°]	$q_{s,in}$ [m² s⁻¹]	q_w [m² s⁻¹]	$h_0 \simeq \left\langle \overline{h} \right\rangle$ [m]	h (range) [mm]
E1	77	2.9	$2.0 \cdot 10^{-5}$	$3.1 \cdot 10^{-3}$	0.0083	6.5–9.5
E2	37	3.0	$3.5 \cdot 10^{-5}$	$3.8 \cdot 10^{-3}$	0.0092	7.5–10.7
E3	36	3.1	$4.8 \cdot 10^{-5}$	$4.2 \cdot 10^{-3}$	0.0095	8.0–11.0
E4	47	3.0	$6.1 \cdot 10^{-5}$	$4.8 \cdot 10^{-3}$	0.0104	8.5–12.0

the relationship:

$$\Theta = \frac{g \rho R_b \tan \overline{\psi}}{g(\rho_s - \rho) d_{50}} = \frac{R_b}{d_{50}} \frac{\tan \overline{\psi}}{s - 1}, \tag{3.1}$$

where g is the gravitational acceleration, ρ is the water density, $s = \rho_s / \rho$ is the sediment-to-water density ratio and R_b is the bed hydraulic radius calculated using the Einstein-Johnson sidewall correction method.

The Einstein-Johnson method (Einstein, 1942; Johnson, 1942) is based on the division of the real flow cross-section ($h_0 \times W$) in one area A_{sw} dominated by the sidewall friction and one area A_b dominated by the bed friction. Two virtual parallel flumes (flow surfaces equal to A_{sw} and A_b, and rough interface lengths of $2 h_0$ and W, respectively) with the same mean flow velocity U and mean energy slope ($\approx \overline{\psi}$) are then considered to compute the hydraulic radii R_{sw} and R_b. This method has proven to give a good approximation of the hydraulic features in supercritical flows in experimental flumes, also compared to more refined methods (Guo, 2015).

The hydraulic radius associated to sidewall friction R_{sw} was calculated by numerically iterating

Eq. (3.2) and Eq. (3.3).

$$\frac{\tau_{sw}}{\rho} = \frac{f_{sw}}{8} U^2 = gR_{sw}\overline{\psi}. \tag{3.2}$$

Equation (3.2) is a Darcy-Weisbach-type law for the flow shearing the sidewalls where τ_{sw} is the sidewall-related shear stress and f_{sw} is the wall friction coefficient. The latter was determined by the von-Kármán-Prandtl law as:

$$\left(f_{sw}\right)^{-1/2} = 2\log\left[Re_{sw}\left(f_{sw}\right)^{1/2}\right] - 0.8, \tag{3.3}$$

where $Re_{sw} = (4\,UR_{sw})/\nu$ is the sidewall-related Reynolds number and ν is the kinematic viscosity of the fluid phase.

We then computed the corresponding R_b value, according to its geometrical relationship with R_{sw}, as:

$$R_b = \frac{A_b}{W} = h_0\left(1 - \frac{2\,R_{sw}}{W}\right). \tag{3.4}$$

We estimated the reference flow depth h_0 for the application of the Einstein-Johnson method (note that the mean flow velocity was calculated as $U = q_w/h_0$) using the following Colebrook-type formula for rough fully-turbulent flows:

$$\left(f\right)^{-1/2} = -2\log\left(\frac{d_{50}}{3.71\,h_0}\right). \tag{3.5}$$

We decided to use a friction law to indirectly compute the reference values of h_0 because determining a single representative h value in these very shallow flows requires an insidious arbitrary definition of the bed and water surfaces. The estimated h_0 values showed good consistency with the flow depth h ranges measured for each experiment using image analysis (see Table 3.1). Notably, the reference h_0 value for each experiment was very close to the flow depth double-averaged over the control window and the entire run duration (maximum difference observed for E1, with $\langle\overline{h}\rangle = 8.1$ mm and $h_0 = 8.3$ mm).

Table 3.2 reports the critical Shields values Θ_c estimated from the following equation proposed by Recking et al. (2008):

$$\Theta_c = 0.15(\tan\overline{\psi})^{0.275}. \tag{3.6}$$

Table 3.2: Summary of mean flow velocity, bed hydraulic radius, Shields numbers and Froude number for the experimental runs E1–E4.

Run	$U = q_w/h_0$ [m s^{-1}]	R_b [m]	Θ [-]	Θ_c [-]	Θ/Θ_c [-]	$Fr = U/\left(gh_0\right)^{1/2}$ [-]
E1	0.37	0.0074	0.085	0.066	1.28	1.31
E2	0.41	0.0083	0.095	0.067	1.43	1.38
E3	0.44	0.0086	0.105	0.068	1.55	1.44
E4	0.46	0.0093	0.108	0.067	1.62	1.45

Flow conditions were supercritical (see Table 3.2) and turbulent ($Re = 3100 - 4800$) for the experiments presented here. Flows were shallow, with a relative roughness d_{50}/h in the 0.3–0.4 range. For the sake of obtaining a dataset representative of the morphodynamic variability of the system, the duration of each experiment was planned to be longer than 10 times the minimum temporal interval approximately required for one antidune to travel from the flume outlet to the flume inlet. This operational requirement corresponded to a minimum duration of $\approx$50 minutes for E1 and $\approx$30 minutes for E2.

Sediment and water supply: control and monitoring

Since this study focused on the interplay between antidune dynamics and sediment transport conditions, particular attention was dedicated to the systems (i.e. methods and devices) used to control the sediment feeding rate and the water flow rate, and assess their stability in time.

The main components of the sediment feeder (see Figure 3.1) were: a sediment tank, a hopper, and a motorised wheel. The grains contained in the sediment tank sank through the hopper aperture and deposited over the wheel surface, which was covered by sandpaper. Subsequently, they were driven to falling by the wheel rotation and the coupled action of a rubber scraper, which prevented periodical avalanches. The hopper aperture was maintained constant for this experimental campaign whereas the sediment feeding rate was adjusted by selecting the wheel angular velocity. The wheel electric motor (Nidec-Servo DMN37B6HPA motor + 6DG900 gearbox) was chosen during preliminary tests to ensure the desired sediment supply rates. The motor had a torque sufficient to unjam particles stuck between the hopper gate and the wheel. Unjamming was reinforced by adding a 5-mm-thick layer of soft foam between the cylindrical wheel and the sandpaper cover. Particular attention was given to ensuring a minimum filling level of the sediment tank (i.e. a minimum confining pressure) during each run to avoid irregularities in the granular flux inside the hopper. During their fall and before entering into the water flow, the sediments were forced to pass over an inclined white plate (illuminated by two LED spotlights) where they were filmed by a Basler acA2000-165um camera (operated at a frame rate of 100 frames per second). The videos collected during the calibration tests allowed us to compute the sediment feeding rates by using the same method presented in this paper for the bedload transport rate monitoring at the flume outlet. The feeding rate series were compared to the sediment samples collected for different sampling durations. These tests made it possible to assess the feeder performances and identify a possible source of fluctuations in the sediment supply: the periodical grain avalanche release over the rotating wheel. This issue was fixed by installing the rubber scraper. The maximum single file size possible with this inlet monitoring setup was sufficient to collect images only for an interval of 750 s, thus the continuous monitoring of the sediment feeding during the experiments was impossible. Others possible sources of fluctuations with this sediment supply system were the misalignment of the wheel axle and the irregularities in the wheel cylindrical shape—especially in the foam coating. Therefore, these sources were carefully inspected before and after each experiment. Moreover, the sediment supply rate steadiness was assessed before and after

each run by collecting dry sediment samples at the sediment feeder during 120–180 s. The maximum difference between the weight of the samples collected before and after each run was found for E1 ($\approx$ 2–3 % increase, sampling time $\Delta t = 180$ s).

The water recirculation was controlled with a Pedrollo CP 132A pump. The flow rate was monitored using an Endress+Hauser Proline Promag 50D (DN25) electromagnetic flow-meter mounted on the delivery line (flow velocity measure range 0.01–10 m s^{-1}). The flow-meter relative uncertainty on Q_w was lower than 1.5 % for a total flow rate $Q_w \geq 1.3 \cdot 10^{-4}$ m^3 s^{-1} (that is the Q_w value for E1). The flow discharge values of the runs were lower than the nominal specifications of the recirculating pump. The flow rate was stabilised by ensuring a sufficient pressure head on the pump delivery line with a valve mounted on the piping. During the experimental runs, we also maintained a constant pressure head on the pump suction line by keeping stable the water level in the outlet reservoir. The water discharge varied smoothly (with a period lower than 5 s) around its mean value (to within 3 %). The water discharge per unit width q_w in the surface flow layer was estimated by subtracting the hyporheic flow discharge from Q_w. The q_w values reported in Table 3.1 refer to these estimates. We measured the hyporheic flow discharge before and after each experiment by collecting manual samples at the flume outlet.

Boundary conditions: specific settings

Specific arrangements were used to set the inlet and outlet boundary conditions. The granular bed was bounded by a vertical perforated plate at the flume outlet. Similarly, a 15–cm-long plastic septum with perforated vertical walls was installed at the upstream bed boundary. Its upper face was covered by artificial roughness elements (transversal rectangular ridges 4 × 40 × 2 mm, streamwise spacing of 4 mm), whose purpose was to limit the flow velocity and thus to avoid triggering an artificial hydraulic jump at the flume inlet. The sediments were fed over this rough fixed surface in order to mitigate the sediment bursts that would have been caused by the impact of the grains over a fully mobile bed. This arrangement allowed the onset of the hyporheic flow inside the bed layer without sharp vertical deviations of the streamlines over the full bed layer. A honeycomb grid was installed upstream of both the septum and the sediment entrance to stabilise the flow free surface and mitigate the propagation of waves caused by the water inflow.

3.2.3   Data collection and image processing for bed topography detection

We monitored the bed topography by filming a 75–cm-long section of the flume from the side. The acquisition window was set at mid-length of the flume, with the upstream side located at $x = 1$ m from the flume inlet ($x = 0$ m). This central position reduced the possible influence of the boundary conditions on antidune dynamics. We collected the images of the bed profile using a Basler A504k camera (operated at a frame rate of 60 or 100 frames per second) equipped with a E Nikon lens (focal length $f = 28$ mm, aperture in the 1–2.8 range).

We processed the images (size 1280×200 pixels, resolution 1 px = 0.6 mm) by applying a binarisation filter with a threshold level adjusted to detect the bed-water interface. We then applied a moving average filter (horizontal window of 5 px = 3 mm $\simeq d_{50}$) to smooth small perturbations in the resulting topography caused by particles moving in the bed vicinity. The bed profile sequences were characterised by a temporal resolution of 1 s. The raw images were slightly affected by lens distortion; we decided not to correct it because the opposite effect of perspective distortion of the bed profile was intrinsic to the setup and irreparable in the present context. Therefore, the wavelength measurement accuracy on the bed profiles exceeded the camera nominal resolution and was of the order of d_{50}. To assess the wavelength accuracy, we filmed with a lateral view two thin vertical lines drawn on the opposite inner sides of each flume wall at the same cross-section (near the edge of the control window where the distortion effects are maximal) and we measured the virtual distance between these lines on the image. The maximum wavelength error estimate was approximately 2.5 d_{50}.

3.2.4 Bedload transport monitoring at the flume outlet

We started to collect bed topography data after the system reached quasi-equilibrium between the sediment supply and the sediment discharge. To check this operational requirement, we monitored the sediment flux at the flume outlet using a basket sampler (with a sampling time in the 60–120-s range). The run that required the longest stabilisation period before reaching quasi-equilibrium was E1 (more than 5 hours). In addition, we filmed the particles transported by the flow over a white board placed at the flume outlet. For this monitoring system, we used the same models of camera and lens as those used for monitoring the bed topography. The 0.055×0.040 m control window was covered by a 190×126-pixel frame. The frame rate was set at 60 or 100 frames per second. To estimate the bedload transport rates at the flume outlet, we used a definition based on particle activity, that is, the number of moving particles per streambed area (e.g. Furbish et al., 2012). Assuming that the mean grain velocity in the control window was constant for a given water discharge, we expressed the sediment transport rate $q_{s,out}$ as:

$$q_{s,out}(t) = \frac{N V_b}{L W} \overline{u}_p, \tag{3.7}$$

where $N(t)$ is the number of particles in the control window $L \times W$ (L is the size in streamwise direction and W corresponds to the flume width), $\overline{u}_p$ is the mean particle velocity in streamwise direction and V_b is the mean particle volume. It is worth noting that this equation provides the averaged transport rate over the window length L. The time resolution of the $q_{s,out}$ series was bounded by the characteristic time that the particles took to cross the window: $t_{tw} = L / \overline{u}_p$. The parameters to be calculated are $N(t)$ and $\overline{u}_p$. The particle activity $N(t)$ was estimated indirectly for each image: we applied a binarisation filter to each image, and we counted the number of pixels characterised by an intensity value over a calibrated threshold. We then considered a calibration factor to convert the pixel number into the particle number $N(t)$. The mean velocity $\overline{u}_p$ was estimated by tracking a set of particles (100 to 200 grains) in the control window for each experiment. During preliminary tests, we assessed that this

measurement technique led to relative error in the average sediment transport rate of less than 10 % when the sampling times were in the 60–120-s range.

3.2.5   Bed topography analysis

For each experiment, a bed elevation matrix $Z_0(x, t)$ was computed from the bed profiles collected in the control window. The preliminary step towards the analysis of the bed morphodynamics involved assessing how stable the bed slope was over time. The following step consisted in the subtraction of the mean bed elevation profile from the bed elevation matrix to obtain the bed elevation perturbation matrix $Z(x, t)$. Each matrix $Z(x, t)$ contained the information on the morphology and kinematics of the bedform patterns that developed and migrated during the respective run. The typical modes of the perturbations were estimated by applying a 2D Fast Fourier Transform (FFT) in the wavenumber and frequency domains to the matrix $Z(x, t)$. This operation was equivalent to the application of two consecutive 1D FFT in opposite domain directions. The resulting 2D spectra were analysed to assess the variability of bedform shapes and celerities. Moreover, we tested different scaling schemes to identify general trends in these spectra.

3.3   Results

3.3.1   Bed elevation perturbations

During the experiments, antidunes developed and migrated upstream along most of the flume length. The bed topography exhibited a nearly constant mean slope over time (Figure 3.2).

Figure 3.3 shows one sample of the bed elevation perturbation matrices for each experiment. Antidune behaviour depended on the transport conditions. For example, the antidune patterns migrated more steadily during runs E2 and E3 than during E1. Generally, we observed that antidunes were more uniform and migrated faster for higher sediment feeding rates $q_{s,in}$ (see Figure 3.3). During E1 and E2, antidunes were often observed to develop and migrate as groups of bedforms, also called *trains*. The number of antidunes composing each train was variable for E1 and E2. These antidune trains were occasionally disturbed or interrupted by local perturbations that propagated downstream. These downstream migrating perturbations were especially visible during E2 (Figure 3.3 (b)) in which they were characterised by typical spacing and period values in the ranges 0.4–0.5 m and 40–50 s respectively (perturbation velocities around 1 cm s^{-1}). We did not observe any evidence of hydraulic jumps associated with degradation waves. The antidune sequences appeared to be mostly continuous in E3. It is interesting to note that for E4, during which it was difficult to detect antidunes in real time by simple observation, the bed patterns were visible in the corresponding $Z(x, t)$ matrix during most of the run. The $Z(x, t)$ matrix of E4 was characterised by a lower signal-to-noise ratio for the bed profile detection when compared to the other experiments. This signal disturbance was caused by the high particle activity in this run. For all runs, the typical antidune amplitude
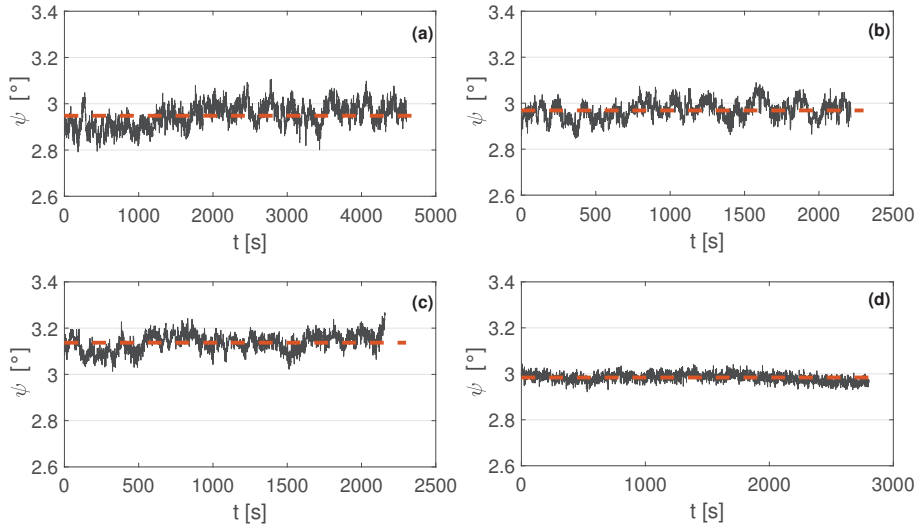
Figure 3.2: Time series of the mean bed slope in the control window for each experiment (black solid lines). Sub-plots from (a) to (d) refer to experiments from E1 to E4, respectively. The red dashed line indicates the mean bed slope over the entire duration of the experiment.

H_{AD} ranged from the median grain size d_{50} to the mean flow depth $\overline{h}$. The typical antidune wavelengths λ were approximately in the 5–15-cm range. By tracking the bedforms manually, we estimated the migration celerity c for each experiment. Due to the non-uniform migration speed, in particular for E1, the definition of a dominant celerity was considered inappropriate.

3.3.2 Bedload transport rate series and fluctuations

The bedload transport rate was measured at the flume outlet throughout the time of the experiment. The resulting time series were characterised by relatively large fluctuations relative to the mean transport rates (Figure 3.4). Considering the transport rate series averaged over 0.2 s, the highest pulses exceeded the average transport rates by 200 % and 100 % for E1 and E4, respectively. For E1 and E2, episodes of low bedload transport ($q_{s,out} < 10\% \, \overline{q}_{s,out}$) at the flume outlet were also recorded. Similar episodes were not observed for E3 and E4. The overall variability of the bedload transport rates, reflected by the coefficient of variation C_v, decreased almost linearly with increasing sediment transport rates (from $C_{v,\,E1} = 0.5$ to $C_{v,\,E4} = 0.19$).

Bedload transport fluctuations at the flume outlet were likely connected with the antidune morphodynamics. For E1, the antidunes were geometrically well-developed but their migration was particularly unsteady (Figure 3.3 (a)). Consequently, the bedload transport rate at the flume outlet during this run exhibited high variability, reflected by the most remarkable episodes alternating intense and weak sediment transport (Figure 3.5). At intermediate transport stages (E2 and E3) the antidune migration was more regular (Figure 3.3 (b) and (c))
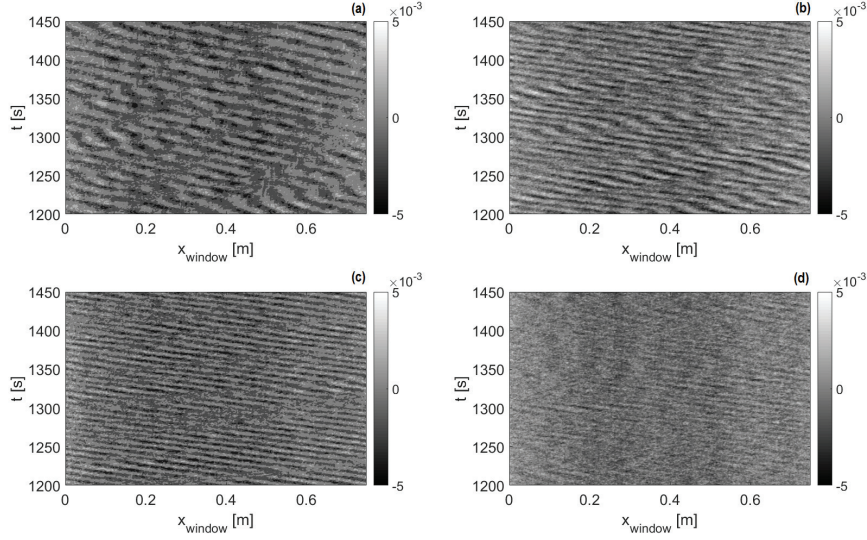
Figure 3.3: Contour plots of the bed elevation perturbation for time intervals of 250 s (from $t_1 = 1200$ s to $t_2 = 1450$ s). Sub-plots from (a) to (d) refer to experiments from E1 to E4, respectively. The colorbars refer to the z perturbations expressed as [m]. Sediment feeding rates $q_{s,in}$ were: (E1) $2.0 \cdot 10^{-5}$ m^2 s^{-1}, (E2) $3.5 \cdot 10^{-5}$ m^2 s^{-1}, (E3) $4.8 \cdot 10^{-5}$ m^2 s^{-1}, (E4) $6.1 \cdot 10^{-5}$ m^2 s^{-1}.
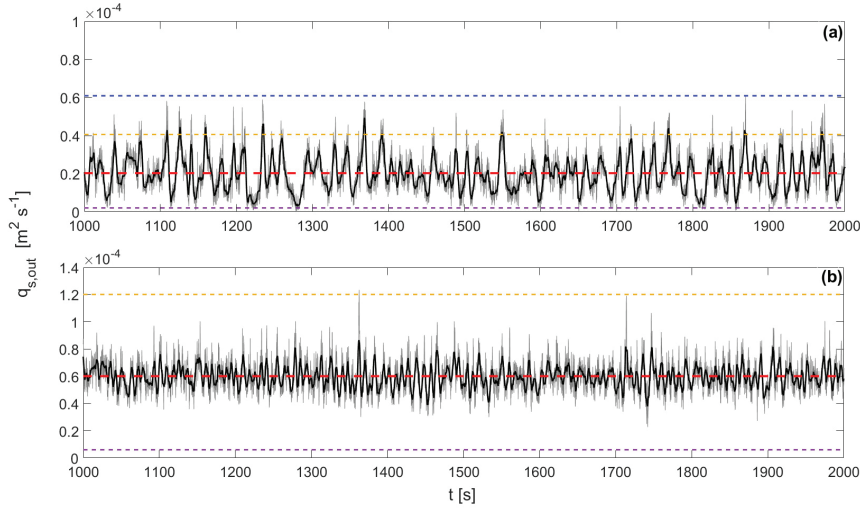
Figure 3.4: Time series of the bedload transport rate at the flume outlet during 1000 s for experiments E1 (a) and E4 (b). The grey solid line indicates the bedload transport rate series averaged over 0.2 s. The black solid line refers to the bedload transport rate averaged over 3 s. The red dashed line indicates the bedload transport rate averaged over the entire duration of the experiment, $\overline{q}_{s,out} \simeq q_{s,in}$. The additional dashed lines represent: 2 $q_{s,in}$ (yellow), 3 $q_{s,in}$ (blue), 0.10 $q_{s,in}$ (purple).

and the fluctuations of $q_{s,out}(t)$ were less intermittent and less strong (Figure 3.5) than for E1. The bedload transport rates measured in E4 (which is the run with the highest transport

intensity) showed the lowest variability, in line with earlier studies (e.g. Singh et al., 2009). The antidune signature was still noticeable in the bed elevation perturbation matrix $Z(x, t)$ for E4 (Figure 3.3 (d)).
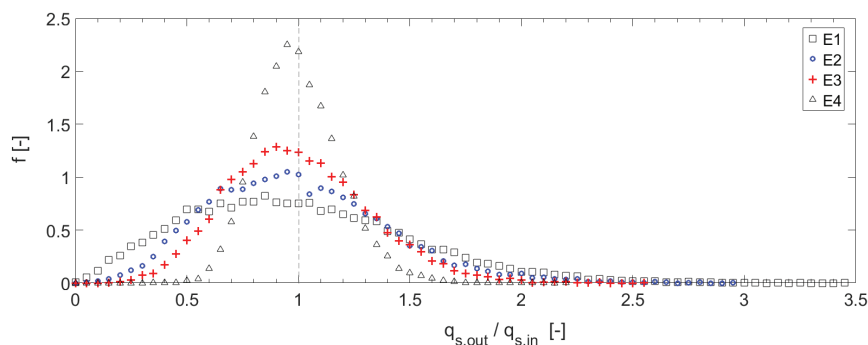
Figure 3.5: Empirical probability density functions for $q_{s,out}/q_{s,in}$ for all the experiments. These distributions refer to the bedload transport rates $q_{s,out}$ averaged over 0.2 s.

3.3.3 Spectral analysis of bed morphologies

By applying the 2D Fast Fourier Transform to the $Z(x, t)$ matrix for each experiment, we obtained the spectra shown in Figure 3.6 in the λ-T domain. These spectra outlined the multiscale nature of the bed morphologies and confirmed the observations made by considering only the bed elevation perturbation 2D plots. The FFT technique used did not allow us to determine the migration direction explicitly. In our experiments, antidunes were observed travelling upstream with non-constant geometry and migration celerity. The downstream migrating perturbations (visible in Figure 3.3 (b)) did not appear in these FFT spectra owing to their relatively low energy compared to those associated with the upstream migrating antidunes and their longer migration periods. Additional information regarding the downstream migrating perturbations can be found at the end of the Results section.

In order to explore and quantify variability in the antidune morphodynamics, we repeated our analysis by considering different domains in the perturbation spectrum. In Figure 3.6, the Power Spectral Density (PSD) of the bed elevation perturbations in the λ-T domain reveals wavelength variability for each experiment. The wavelength ranged from 0.05 to 0.18 cm for E1, and from 0.09 to 0.15 cm for E3. Although it was less pronounced than in similar studies on dunes (e.g. Guala et al., 2014), the wavelength variability was nonetheless noticeable in our experiments. This significant variability became less marked with increasing bedload transport intensities.

We also considered the spectra in c-λ plane (Figure 3.7) in order to highlight possible trends of migration celerity. Antidune celerity was assumed to take positive values. We transformed the
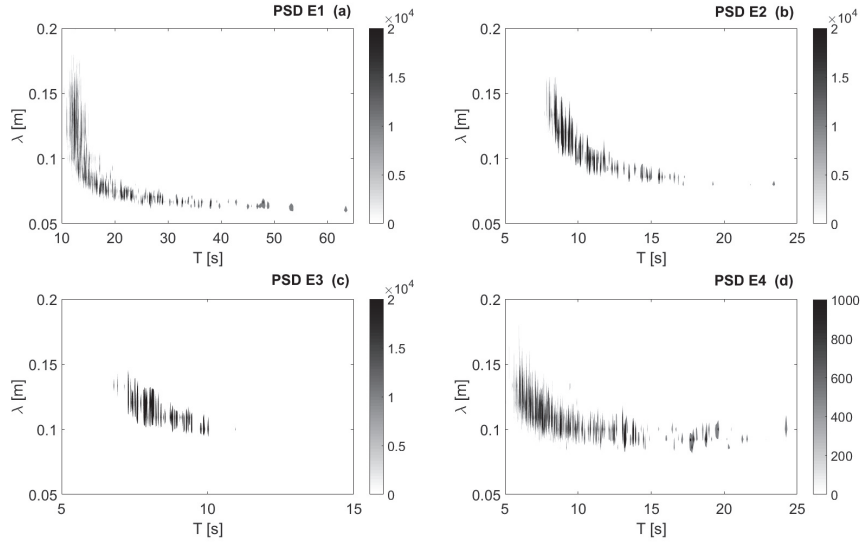
Figure 3.6: Spectra displayed in λ-T domain for experiments E1–E4 (a–d).
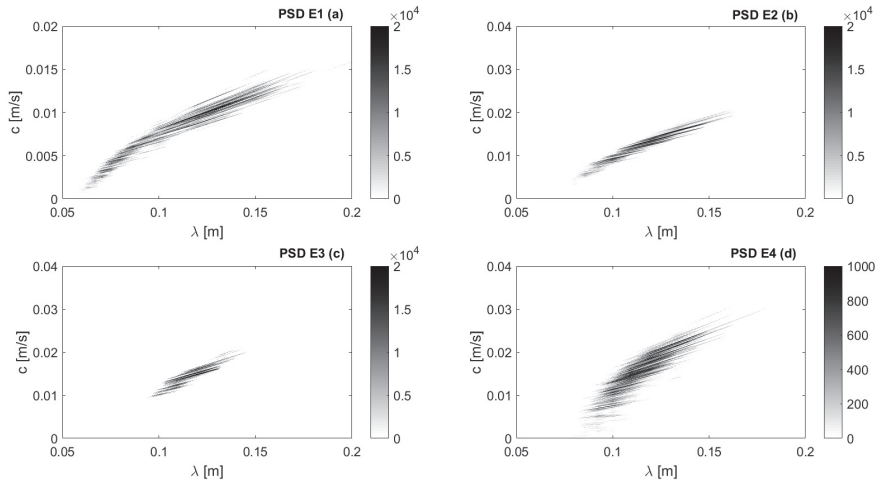
Figure 3.7: Spectra displayed in c-λ domain for experiments E1–E4 (a–d).

period values T into the corresponding migration celerity values c using the equation

$$c = \frac{\lambda}{T}. \tag{3.8}$$

Figure 3.7 shows that migration celerity increased with increasing antidune wavelength for all experiments. Otherwise stated, longer antidunes (high λ) generally migrated upstream faster than shorter ones (low λ). This result appeared consistent with visual analyses of the bed elevation perturbation matrices $Z(x,t)$. The relevance of these observations led us to analyse the spectra in dimensionless domains in order to determine how the antidune celerity depended on the problem variables. The dimensionless variables (T^*, λ^*, c^*) were obtained by scaling the physical variables (T, λ, c) with the reference flow depth h_0 and the convective

time λ/U as characteristic length and time, respectively:

$$T^* = T\frac{U}{\lambda};$$

(3.9)

$$\lambda^* = \frac{\lambda}{h_0};$$

(3.10)

$$c^* = \frac{c}{U}.$$

(3.11)

Figure 3.8 shows the contour plots of the spectral densities in c^*-λ^* domain. Note the different criterion used to visualise the E4 PSD contour because this spectrum was characterised by particularly low densities. Interestingly, $c^* \approx f(\lambda^*)$ increased with increasing λ^*, and the higher the transport stage, the steeper the curve $c^* \approx f(\lambda^*)$. Figure 3.8 also indicates that experiments with the highest transport intensities were characterised by the narrowest ranges of dimensionless wavelength.
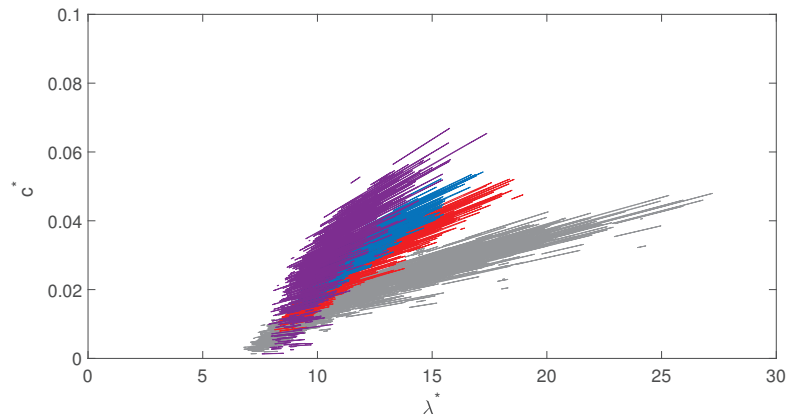
Figure 3.8: PSD contour plots in c^*-λ^* domain. The colours refer to: E1 (black), E2 (red), E3 (blue), E4 (purple). Contours are defined considering a single density level of 5000 for E1–E3. The E4 contour is defined with a density level of 500.

The dimensionless spectra of the various experiments did not overlap in Figure 3.8. We believed that the scaling based on the water phase features (see Equations (3.9)–(3.11)) did not allow us to capture the bedform dynamics in terms of dimensionless celerity and wavelength. In Figure 3.8, we observed that the mean sediment transport rate likely played a significant role in determining the antidune migration celerity. Based on this observation, we proposed an alternative normalisation scheme. To scale antidune celerity, we defined a characteristic sediment phase velocity U_N:

$$U_\mathrm{N} = \frac{\overline{q}_\mathrm{s}}{d_{\mathrm{V},50}\,(1-p)}.$$

(3.12)

where p is the porosity of the sediment mixture and $d_{\mathrm{V},50}$ is a characteristic length scale for the mean particle volume V_b (i.e. the diameter of an equivalent sphere of volume V_b). For

the sediment mixture used in E1–E4, we measured $p \simeq 0.38$ and $d_{V,50} = (6\,V_b/\pi)^{1/3} \simeq 2.7$ mm. U_N is proportional to the virtual convective velocity of the sediment volume in the bed active layer—whose mean thickness was assumed proportional to the characteristic grain size. This assumption is in agreement with the typical antidune amplitude observed in our experiments. We calculated the scaled dimensionless migration celerity c_N^* as:

$$c_N^* = \frac{c}{U_N} = \frac{c\,d_{V,50}\,(1-p)}{\overline{q}_s}. \tag{3.13}$$

Regarding the wavelength scaling, we considered the relationship proposed by Recking et al. (2009) to predict the dominant antidune wavelength on steep slopes:

$$\lambda_{R09} = d_{50}\,f(\Theta,\Theta_c,Fr) = d_{50}\,\xi(\Theta^\alpha\,\Theta_c^\beta\,Fr^\gamma) = 0.093\,\Theta\,\Theta_c^{-3}\,Fr\,d_{50}. \tag{3.14}$$

The combination of parameters in Eq. (3.14) was the result of detailed dimensional analysis conducted using Buckingham's Pi theorem; the coefficients $(\xi,\alpha,\beta,\gamma)$ were determined by fitting the relationship to data derived from 19 flume experiments (Recking et al., 2009). This validated relationship appeared well-suited to be tested as the wavelength reference scale for antidunes on steep slopes. We defined the dimensionless wavelength values λ_N^* as:

$$\lambda_N^* = \frac{\lambda}{\xi\,\Theta\,\Theta_c^{-3}\,Fr\,d_{50}} = \frac{\lambda}{\lambda_{R09}}. \tag{3.15}$$

The coefficient $\xi = 0.093$ was not strictly required for the wavelength scaling but maintaining it eased the interpretation of the λ_N^* values in proportion to λ_{R09}. Figure 3.9 shows the resulting contour plots for the spectra in the c_N^*-λ_N^* domain.
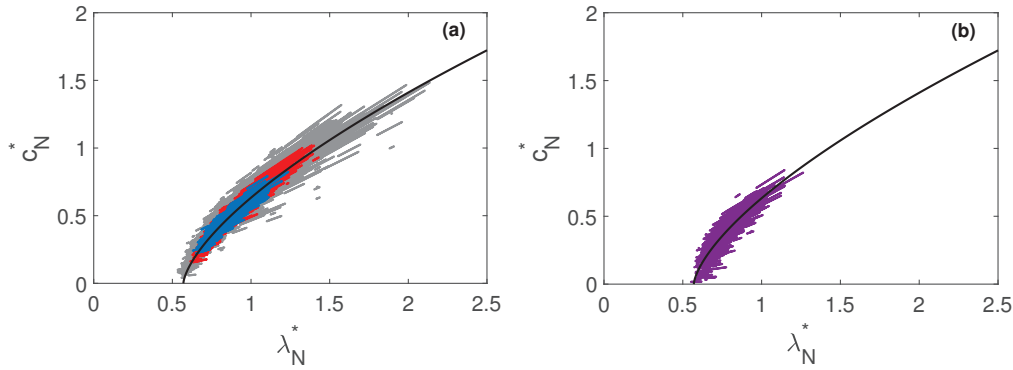
Figure 3.9: PSD contour plots in c_N^*-λ_N^* domain. The black lines represent the master curve of Eq. (3.16). (a) The colours refer to: E1 (grey), E2 (red), E3 (blue). Contours are defined considering a single density level of 5000 for E1–E3. (b) The E4 contour (purple) is defined with a density level of 500.

This scaling based on the parameters U_N and λ_{R09} allowed us to collapse all the spectral distributions onto a master curve $c_N^* \approx f(\lambda_N^*)$. The spectrum obtained for E4 followed the

same trend; we plotted it separately in Figure 3.9b for the sake of readability. Based on the trend of the spectral distributions in Figure 3.9, we expressed the relationship between scaled dimensionless celerity c_N^* and dimensionless wavelength λ_N^* as:

$$c_N^* \approx f(\lambda_N^*) = \frac{(\lambda_N^* - \lambda_A^*)^\zeta}{k},$$
(3.16)

where $\lambda_A^* \simeq 0.57$ [-], $\zeta \simeq 2/3$ [-] and $k \simeq 0.9$ [-] are regression coefficients.

By combining Eq. (3.16) and Eq. (3.13), we obtained an explicit formula to estimate the mean bedload transport rate associated with upstream migrating antidunes:

$$\overline{q}_{s,est} = c\, d_{V,50}\, (1-p)\, f_q(\lambda_N^*) = c\, d_{V,50}\, (1-p) \left[\frac{0.9}{(\lambda_N^* - 0.57)^{2/3}} \right],$$
(3.17)

where $f_q(\lambda_N^*) = [f(\lambda_N^*)]^{-1}$. Equation (3.17) shares some similarity with the frameworks proposed for downstream migrating dunes (e.g. Simons et al., 1965; Nikora, 1984; Guala et al., 2014) and differs in other aspects. These features are discussed in the Discussion section.

Performance assessment of Equation (3.17) with data available in literature

Although Eq. (3.17) is based on the approximation underpinning Eq. (3.16), it can be used to estimate the mean bedload transport rate by measuring the typical wavelength and associated celerity values for antidunes migrating upstream along steep slopes. We first assessed the performance of this approach to estimate the average bedload discharge. To that end, we used data from an experiment on antidunes obtained by Mettra (2014), who set the values listed in Table 3.3 for the mean bed slope $\overline{\psi}$, the flume width W, and the sediment size d_{50}. Mettra (2014) observed upstream migrating antidunes and applied a tracking criterion based on longitudinal bed profiles to collect wavelength and celerity data.

Table 3.3: Main experimental parameters of the run *2deg15v* (Mettra, 2014) and pairs (c, λ) based on data of the same experiment. The pairs (c, λ) were extracted from Figure 6.6 and Figure 6.8 (a) in Mettra (2014).

W [m]	$\overline{\psi}$ [°]	d_{50} [mm]	ρ_s [kg m^{-3}]	h [m]	Fr [-]	R_b [m]	Θ [-]	c [mm s^{-1}]	λ [m]
								0.8	0.20
0.08	2.0	6.25	2690	0.027	1.17	0.024	0.08	1.8	0.30
								2.5	0.40

To run this test, we first estimated the corresponding λ_N^* values from the λ values reported in Table 3.3 ($\lambda_{R09} = 0.257$ m for this experiment). The Shields number Θ was calculated using Eq. (3.1) with R_b estimated according to the Einstein-Johnson method as for the experiments presented here. The critical Shields number Θ_c was calculated using Eq. (3.6). We calculated the U_N and c_N^* values according to Eq. (3.12) and Eq. (3.13). Since the information about the
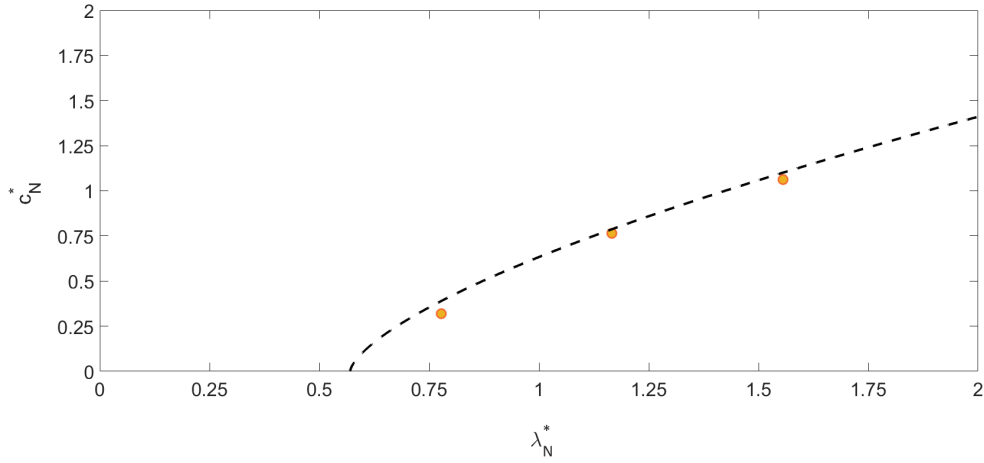
Figure 3.10: Master curve of Eq. (3.16) (dashed black line). The orange circles display the positions in c_N^*-λ_N^* domain of the data pairs reported in Table 3.3 for the run $2deg15v$ (Mettra, 2014). The pairs (c_N^*, λ_N^*) were calculated considering the $\overline{q}_{s,meas}$ value measured by Mettra (2014) and reported in Table 3.4.

mean particle volume was not available for the run *2deg15v*, we indirectly estimated $d_{V,50}$ assuming the same ratio $d_{V,50}/d_{50} = 0.92$ obtained for our experimental case. The porosity of the sediment mixture was $p = 0.42$ (Mettra, 2014). We then used Eq. (3.17) to calculate the corresponding $\overline{q}_{s,est}$ values (Table 3.4). Figure 3.10 shows the "true" positions of the pairs (c_N^*, λ_N^*) computed from the mean bedload transport rate $\overline{q}_{s,meas}$ (measured during the experiment). Since the maximum relative error for the mean bedload transport estimates was less than 20 %, the outcome of the test appeared satisfactory. This test highlighted the importance of having multiple pairs (c, λ) or better the $c - \lambda$ spectrum to assess and improve the reliability of the results. Unfortunately, we had to limit the comparison to a single experimental case due to the scarcity of experimental data available in the literature (in terms of associated values c and λ) for antidunes on steep streams with coarse sediments.

Table 3.4: Summary of the performance assessment of Equation (3.17) for the run *2deg15v* (Mettra, 2014).

c [mm s^{-1}]	λ [m]	λ_N^* [-]	$\overline{q}_{s,meas}$ [m^2 s^{-1}]	$\overline{q}_{s,est}$ [m^2 s^{-1}]	$(\overline{q}_{s,est} - \overline{q}_{s,meas})/\overline{q}_{s,meas}$ [%]
0.8	0.20	0.78		$6.43 \cdot 10^{-6}$	-18.0
1.8	0.30	1.17	$7.9 \cdot 10^{-6}$	$7.64 \cdot 10^{-6}$	-2.7
2.5	0.40	1.56		$7.60 \cdot 10^{-6}$	-3.3

Domain of application of Equation (3.16) and Equation (3.17)

We provide here further guidance on how to apply Equations (3.16) and (3.17). The data from which these relationships were derived came from experiments characterised by high relative roughnesses and steep slopes ($\overline{\psi} = 3°$). The scaling analysis presented above holds

for supercritical flows over well-sorted coarse natural sediments (i.e. $d_{50}/h \approx 0.1$–0.5 and $d_{50} \approx 2$–10 mm). Equation (3.16) is valid for mean slope angles $\overline{\psi}$ up to $\sim 4°$ provided the flow remains supercritical over most of the flume length and the bed shows no significant ψ fluctuations on the flume scale. Mettra (2014) observed degradation waves in one steep-slope experiment ($\psi \approx 4°$) and evoked the metastability of the bed profile as a potential cause. Concerning streams under near-critical flow conditions ($Fr \sim 1$), we recommend to carefully assess the continuity of the upstream migrating antidune pattern in the control window (recall Figure 3.3 and Figure 3.11). Equation (3.16) is not expected to hold in presence of extensive discontinuities in the antidune sequences (e.g. sediment waves or transitional bedforms). During an experimental run conducted with the same flume and sediments of the present study (with $\overline{\psi} = 1.55°$ and $Fr = 1.1$), Ancey and Pascal (2020) observed bed waves—characterised by "cycles of growth and decay over time scales of a few minutes, with no evidence of migration"—in the upstream part of the flume (see Movie S2 in the same paper) whilst upstream migrating antidunes were well developed in the downstream part. A plastic plate was installed over the flow surface in the middle part of the flume to facilitate particle tracking; this disturbance probably influenced the bedforms (Ancey and Pascal, 2020). In that specific configuration, the bed morphodynamics in the upstream sector was not consistent with the domain of application of Equation (3.16). With regards to bedload transport intensity, the experimental conditions of E4 likely represent the upper boundary when applying Eq. (3.17) to estimate the mean bedload transport rate. The cases characterised by very low bedload transport rates require special attention because in such circumstances, bedload transport is intermittent, and this intermittency affects antidune migration.

3.3.4 About the downstream travelling perturbations

We provide here additional information regarding the downstream travelling perturbations of the antidune sequences observed in our experiments. These observations might be useful for researchers who study morphodynamic instabilities in supercritical flows. The perturbations on which we focus here (also called "disturbances" in the previous sections) were downstream travelling discontinuities or non-uniformities in the wave geometry and celerity that affected the antidune sequences in our experiments. Looking at the E2 contour plot in Figure 3.11, one can identify perturbations which interrupt or not the antidune pattern continuity. For instance, we observed downstream travelling perturbations which propagated from accelerating antidunes. These perturbations were often associated with the splitting of one accelerating antidune or the appearance of a transition zone—likely an area with high particle activity—in which one could not distinguish the bedform crests and troughs that were previously evident (see Figure 3.11). In other cases, we observed occurrences of a local slow down of one antidune that subsequently propagated downstream affecting other antidunes. The perturbations travelled with typical celerity values of the same order of magnitude of the antidune celerity. This observation suggests a strong link with the bedload transport intensity. The travelling perturbations can also be interpreted as boundaries between the antidune trains when they were long-lasting. These type of perturbations and trains were mostly evident and frequent

during the experiments characterised by the lowest mean bedload transport rates (E1 and E2). Note that these trains did not vanish (or break suddenly) and apparently the flow remained supercritical over the entire flume length.
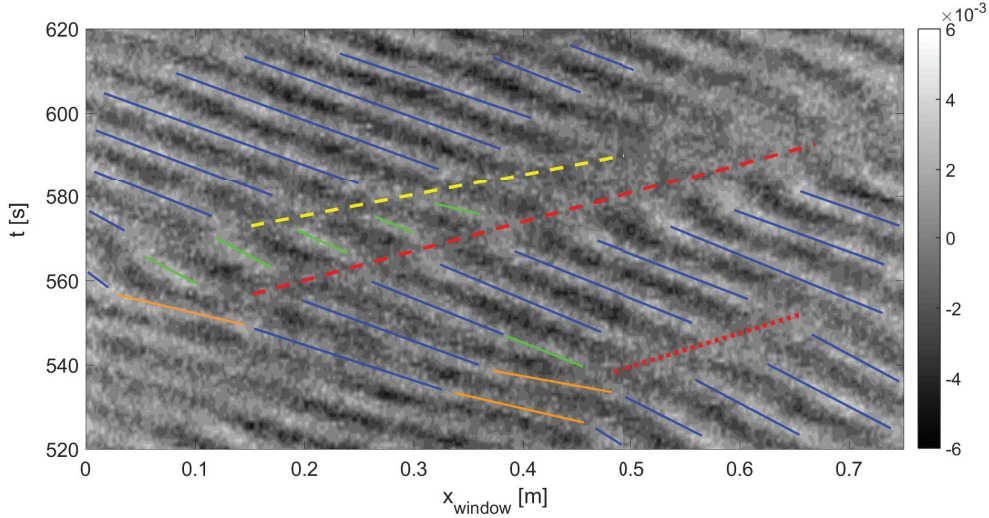
Figure 3.11: Contour plot of the bed elevation perturbation $Z(x, t)$ during E2 (100 s). The solid blue lines represent the approximated crest trajectory of undisturbed antidunes. The solid orange lines indicate the accelerating antidunes whereas the green lines indicate new antidune crests resulting from splitting events or disturbance-related discontinuities. The other thick lines represent: a travelling disturbance with discontinuity of the antidune pattern (long-dashed red), a splitting-related disturbance without persistent discontinuity (short-dashed red) and a secondary discontinuity/rearrangement of the antidune pattern (long-dashed yellow) associated with a previous discontinuity. The colorbar refers to the z perturbation expressed as [m].

Although the width of the control window in our experiments prevented the systematic analysis of the length and time scales of these downstream travelling perturbations, our experimental setup allowed us to make some interesting observation regarding the persistence of these perturbations in the time and space domains. Sometimes, these perturbations came from upstream and travelled across the entire control window. In other cases, they seemed to be originated from a local event in the antidune sequence (e.g. the sudden acceleration of a single antidune or an antidune splitting) and they propagated downstream. We also observed travelling disturbances, which caused a marked discontinuity in the antidune pattern (i.e. the transition zones mentioned above), and that were apparently damped (diffused?) over distances of few tens of centimetres (see Figure 3.11).

3.4 Discussion

As presented in the previous sections, the antidunes observed during the experimental runs exhibited significant variability of their wavelength and migration celerity. The wavelength

variability was found to be less pronounced for the experiments characterised by higher mean sediment transport rate. To the best of our knowledge, the range of variability for the antidune wavelength on a steep slope under moderate and intense bedload transport conditions has so far never been specified. This result was made possible by the application of spectral analysis on high resolution data. Looking at the bed elevation perturbation profiles, the antidunes were less prone to amplitude variability. The typical antidune amplitudes were observed to be slightly smaller than the mean flow depth. Regarding the antidune migration celerity, its variability was also noticeable and antidune celerity increased with increasing wavelength. Overall, antidunes characterized by similar wavelength values migrated faster for higher mean bedload transport rate.

In the next section we discuss the factors that could cause the variability of antidune morphodynamics observed in our experiments. We then explore the potential implications for related topics such as the estimation of a friction term associated with antidunes in flows characterised by high relative roughness and the links between antidune morphodynamics and sediment transport regimes.

3.4.1 Antidune morphodynamics and implications

We summarised the λ ranges for the experimental runs E1 to E3 in Table 3.5. To add an element of comparison in Table 3.5, we reported the wavelength $\lambda_{\min K63}$ and λ_{R09} computed for each experiment. $\lambda_{\min K63}$ is the theoretical minimum wavelength for 2D antidunes, according to Kennedy (1963), as:

$$\lambda_{\min K63} = 2\pi Fr^2 \overline{h} \tag{3.18}$$

Table 3.5: Summary of the ranges for the antidune wavelength λ (extracted from the spectral distributions) and estimated values for $\lambda_{\min K63}$ (Eq. (3.18) considering $\overline{h} = h_0$) and λ_{R09} (Eq. (3.14)) (runs E1–E3).

Run	λ [m]	$\lambda_{\min K63}$ [m]	λ_{R09} [m]
E1	0.06–0.20	0.09	0.106
E2	0.08–0.16	0.11	0.122
E3	0.09–0.15	0.124	0.133

As shown by Table 3.5, Equation (3.14) might provide good estimates of the mean antidune wavelength for E1 and E2. The λ_{R09} value estimated for E3 is closer to the maximum wavelength value. However, it is important to recall that this empirical equation was formulated to estimate the dominant antidune wavelength and its fitting was based on flume data for which the wavelength values were determined by dividing the length of the observation window by the number of antidunes detected (Recking et al., 2009).

Interestingly, the comparison of the values of $\lambda_{\min K63}$ with the ranges of λ determined from the spectra indicates that the shortest waves detected using the 2D FFT were located in

the region of existence of 3D antidunes according to Kennedy's stability diagram (Kennedy, 1963). This observation indicates that upstream migrating 2D (also named *long-crested*) antidunes and 3D antidunes might co-exist and interact in supercritical flows over steep slopes contributing to the variability of antidune shapes and celerities. This speculation could be a possible interpretation for the non-linear trends of the relationship between dimensionless migration celerity and dimensionless wavelength in Figure 3.8 and Figure 3.9. The real-time observation of the flow free surface over short antidunes in our experiments revealed transversal wavelets but without evidence of rooster tails. The wave amplitude of these wavelets was noticeably smaller than that of the water surface undulations caused by the sinusoidal bedforms. Regarding the bed shape for the short antidunes in our experiments, we sporadically observed antidune troughs that were more pronounced on the flume centerline than close to the flume walls but the crests appeared 2D. These kind of short bedforms might thus be typical of very shallow supercritical flows in which the particular conditions—notably the high relative roughness—might influence their form, shaping them differently from the 3D *short-crested* antidunes reported by other authors for flows characterised by lower relative roughness values (e.g. Kennedy, 1963). The small flume width values in our study, in the experiments conducted by Mettra (2014) and in some of the runs presented by Recking et al. (2009) might also play a role on the morphodydynamics of these short antidunes in terms of lateral confinement. Inoue et al. (2020) recently investigated the coexistence of 3D antidunes with alternate bars. Additional experimental studies considering different relative roughness d_{50}/h and aspect ratio h/W values—with systematic monitoring of the sediment transport and flow conditions—would be useful to further clarify the mechanisms that control the coexistence of different bedforms in supercritical flows over coarse-bedded streams.

At the meso-scale, a possible mechanism that may exacerbate variability in antidune geometry and celerity is related to the interactions within antidune trains which can involve antidunes of various wavelengths, but with similar amplitudes. These non-linear interactions often have the capacity to cause neighbouring antidunes to rearrange. Examples of this phenomenon can be observed in the contour plots of the bed elevation perturbation for E1 (see Figure 3.3 (a)) and E2 (see Figure 3.11), and in Movie V1 (see Supporting Information). Antidune interactions can be phenomenologically interpreted using the *lag distance* concept (Kennedy, 1963). Even small particle clusters eroded or deposited within a short time interval can have strong impacts on local flow and transport conditions. The effects of these perturbations are likely accentuated by the high relative roughness of the flows under study. In particular, in steep streams, an increase in the particle activity can trigger collective entrainment, that is, the dislodgement of several particles at the same time (Heyman et al., 2016). Consequently, the local lag between sediment flux and shear stress can be impacted non-uniformly by these bedload bursts along the stream. As a result, antidunes exhibiting similar geometries can be perturbed, undergo a non-uniform change in their migration celerity, and coalesce (or split), producing longer (or shorter) antidunes, as was observed for instance in run E1 (see Figure 3.3 (a) and Movie V1) and run E2 (see Figure 3.11). Interestingly, these events were observed mainly during E1, less frequently during E2 and were less clearly identifiable during E3 and E4. This is consistent

with the fact that local bedload transport pulses (or, conversely, phases of weak transport) are more frequently observed under low bedload transport conditions than under intense transport (Singh et al., 2009).

The formation, development and evolution of trains composed by a number of well-developed antidunes was likely caused by the above-mentioned interactions. Similar morphological patterns have been observed in experiments and the field (e.g. Recking et al., 2009; Froude et al., 2017) and their appearance likely represents a distinctive feature of the variability of antidune morphodynamics on steep slopes. According to Grant (1994), antidune interaction within these trains promotes an increase in the antidune wavelength, which could explain step-pool formation. Similar antidune trains have also been reproduced in numerical simulations by Bohorquez and Ancey (2016), who regarded "nonlinear coarsening" as a possible cause of the antidune wavelength increase observed in the upstream migration process.

The downstream travelling perturbations already described in the Results section can be interpreted as a complementary feature of the antidune trains. These disturbances either appear as the transient signature of local interactions (e.g. bedform merging and splitting events) or they mark a more persistent discontinuity in the antidune pattern and thus can be considered as boundaries between the antidune trains. We also tried to investigate the possible influences of these disturbances on the bedload transport rate series measured at the flume outlet. Assuming a constant perturbation celerity, we inferred the arrival times at the flume outlet of the perturbations that travelled across the control window. Unfortunately, we did not succeed in identifying a clear correlation between the estimated arrival times of these downstream migrating perturbations at the outlet and the occurrences of bedload pulses or phases of weak transport. The simple assumption of a constant perturbation celerity in the downstream part of the flume in which the antidunes are close to the outlet discontinuity is probably not sufficient to extrapolate a correspondence between perturbations and bedload pulses.

In our experiments of bedload transport over steep slope, antidune train morphodynamics likely depends on how particle diffusivity and deposition (governed by local flow conditions), and entrainment (strictly related to particle activity) are interrelated (Ancey and Heyman, 2014; Bohorquez and Ancey, 2016; Heyman et al., 2016). The parts played by the absolute nature of the antidune instability (Vesipa et al., 2014) and by turbulence (Breakspear, 2008) may be crucial as well. In steep stream flows under moderately intense transport conditions (as in E1 and E2), investigating these interrelations remains a great challenge because we need to: (i) track not only isolated particles, but also particle clusters when measuring particle diffusivity, (ii) run Particle Image Velocimetry (PIV) in difficult conditions, and (iii) monitor antidune evolution at high temporal and spatial resolution. Further studies on these interrelated processes are needed to confirm or infirm the possible influence of processes located far upstream (such as the sediment supply irregularities) on bedload transport in steep streams (Tucker and Bradley, 2010; Furbish and Roering, 2013; Ancey et al., 2015; Heyman et al., 2016), and their impact on bed instabilities.

Variability in the antidune morphodynamic features may affect flow resistance induced by antidunes. For flows on rough beds (that is, under low submergence conditions), the relative importance of grain- and form-induced flow resistance depends a great deal on antidune shape variability, in particular on the non-uniform and abrupt changes in bed curvature that may be caused by erosion or deposition of a relatively small number of grains. Bed curvature alters the momentum distribution within the flow (Dressler and Yevjevich, 1984). It has been taken into account for a sinusoidal bed surface by Vesipa et al. (2012), who used the Dressler equations (Dressler, 1978)—rather than the common form of the Saint-Venant equations—and a mechanistic model for sediment transport. Our experimental results and analyses prove that form-induced flow resistance may be neglected to estimate the double-averaged flow depth $\langle \overline{h} \rangle$ and to describe the typical bedform dynamics when considering relatively continuous antidune trains. However, the experimental observation of transient local non-uniformities (e.g. antidune merging and splitting events) and of downstream travelling perturbations which propagated from one or two accelerating antidunes (see Figure 3.11) should spur further research on the interplay between curvature-induced flow resistance and antidune morphodynamics variability by taking a closer look at factors such as interaction between bedforms, the influence of the bedload transport stochastic nature, and the perturbations caused by turbulence and unsteady sediment supply.

The present study explains why antidunes are seldom directly observed in the field and possibly why geomorphological records of natural gravel-bed streams may be difficult to interpret even when antidunes were not strongly reworked by later events. Direct observation is made difficult by the antidune geometry and celerity variability, which can thus "hide" their presence during flood events. Even in field sites for which disturbing factors such as grain sorting play a minor role, antidune trains are less visible than expected because of variability. In this respect, with the advent of cost-effective drone-based technologies (e.g. UAV-carried multi-beam sonar and ground penetrating radar) we expect a revival of interest in the field investigations on antidunes. Our experimental work is a first step towards determining the variability ranges in the antidune geometry and celerity.

3.4.2 The interplay between transport intensity and upstream migration celerity

In the Results section, we demonstrated that the celerity scaling based on U_N is useful to model how the sediment flux affects the antidune migration. As expected, the larger the mean sediment flux, the higher the migration celerity c. The intense particle activity promotes deposition on the antidune stoss side, and erosion on its lee side. We now compare the structure of Eq. (3.17) to that of the formula (see Eq. (3.20)) originally proposed by Simons et al. (1965) to model the contribution of downstream migrating dunes to the bedload flux.

$$\overline{q}_s = \left(1 - p\right) d_{V,50}\, f_q(\lambda_N^*)\, c = \frac{1}{2}\left(1 - p\right)\left(2\, d_{V,50}\right) f_q(\lambda_N^*)\, c \qquad \text{Eq. (3.17)} \qquad (3.19)$$

$$\overline{q}_s = \frac{1}{2}\left(1-p\right)H_{dune}\,c_{dune} + C_{q,1} \tag{3.20}$$

As one can see in the two equations reported above, Equation (3.17) might also be interpreted as a "contribution" to the mean bedload flux of a triangular antidune with the same shape coefficient ($\frac{1}{2}\left(1-p\right)$) of the Simons' formula. Analogously, the term $2\,d_{V,50}$ is proportional to the bedform amplitude (H_{dune} is the dune amplitude). The migration celerities also appear in both Eq. (3.17) and Eq. (3.20). It is worth noting that the celerity of upstream migrating antidunes takes positive values in our framework whereas the sign convention is different in Eq. (3.20) (celerity $c_{dune} > 0$ for downstream migrating dunes). The term $C_{q,1}$ in Eq. (3.20) is a constant of integration that stands for the "part of the bedload which does not enter into propagation of dunes and ripples" (with $C_{q,1} = 0$ at the threshold of motion and as long as the bed is covered by dunes, and $C_{q,1} = \overline{q}_s$ in case of transport in plane bed configuration) (Simons et al., 1965). Some hypotheses concerning the possible values taken by the "shape factor" (not formally defined) were already formulated by Mettra (2014) for the bedload flux contribution of a single antidune. The main difference between the relationships proposed for uni- and multi-modal dune fields (e.g. Simons et al., 1965; Nikora, 1984; Guala et al., 2014) and Eq. (3.17) is that the latter should not be intended as the integral of the bedload flux contributions resulting from multiple migrating bedforms of different geometry. This semi-empirical multi-scale relationship for estimating the mean bedload transport rate is based on Eq. (3.16), which can be interpreted as: an upstream migrating antidune within an antidune sequence under quasi-equilibrium transport conditions typically responds to the forcing imposed by the mean bedload transport rate $\overline{q}_s$ by migrating with celerity proportional to U_N and to $f(\lambda_N^*)$. According to our results, antidune upstream migration may be formally interpreted as a response to the mean bedload flux and not as a contribution to it. The functional form of the dimensionless wavelength $f(\lambda_N^*) = [f_q(\lambda_N^*)]^{-1}$ in Eq. (3.16) embeds the effects on the migration celerity of both antidune shape and mean flow conditions (see Eq. (3.14)). The term $f(\lambda_N^*)$ (see Eq. (3.16)) can be interpreted as an empirical conversion factor that expresses the typical ratio of the mean bedload flux that actively participates in determining the migration celerity of antidunes characterised by a dimensionless wavelength λ_N^* (depositing on their stoss side and being eroded by their lee side). The positive trend for $f(\lambda_N^*)$ likely reflects the signature of the damping effect induced by the bedload layer inertia on antidune migration. In fact, inertial effect can increase the lag between sediment flux and shear stress, slowing antidune migration. The negative impact of inertia on the antidune migration celerity has been demonstrated theoretically by Vesipa et al. (2012). It seems coherent that this damping effect impacts relatively more the migration celerity of the short antidunes than that of the long ones because of their different size, thus causing the non-linearity in $f(\lambda_N^*)$. According to our observations, the interplay between sediment flux and inertia may hold at relatively high transport rates (E4) until to the situation in which the antidunes are levelled out (bedload-laden flow with not clearly identifiable bed-flow interface). Considering the PSD countour for E1 in Fig. 3.9a, $f(\lambda_N^*)$ may take values higher than the unity. This somewhat unexpected outcome might suggest that the longest antidunes during

E1 migrated under sustained bedload transport rate higher than the mean feeding rate (i.e. during long-lasting bedload pulses) and/or that their actual wave amplitude was lower than $2\,d_{V,50}$. However, in our experiments we did not find any clear proportionality between the antidune amplitude and wavelength. It is worth underlining that the scaling method presented in this paper is based on parameters that have been estimated by considering relationships holding for uniform flows. This method has proven to be successful for describing the typical morphodynamic features observed in our experiments; alternative approaches, which take flow non-uniformity into account, could reveal interesting information concerning particular local events such as bedload pulses associated to the migration of a single antidune or to the transit of a downstream travelling perturbation.

3.5 Conclusions

The experimental study presented in this paper shows that antidunes on steep slopes exhibit significant variability of shapes and celerity, even under steady-state conditions. The wavelength variability range increased with decreasing mean sediment transport rate. Overall, we observed that the larger the antidune wavelength, the higher its migration celerity. One strength of this paper is to show how to infer information on this variability from high resolution data by applying spectral analysis. By using a scaling technique, we collapsed all the bed elevation perturbation spectra onto a single curve that captured the bedform dynamics in terms of dimensionless celerity c_N^* and wavelength λ_N^*. The resulting trend $c_N^* \approx f(\lambda_N^*)$ was described by a functional relationship. This multi-scale relationship embedded the interplay between the sediment flux and antidune migration. We proposed a new method for estimating the mean bedload transport rate by monitoring antidune morphodynamics. Although our first test gave satisfactory results, additional data are needed to confirm our results. We are currently conducting a new experimental campaign using a longer flume.

Accounting for variability in the antidune morphodynamic features is key to estimating sediment fluxes and form-induced flow resistance on steep slopes. This variability likely explains the elusiveness of antidunes in direct field observations. The findings may help paleohydraulics studies regarding coarse-bedded streams.

4 On antidune trains and bedload pulses under steady- and quasi-steady-state conditions

Ivan Pascal[1]**, Patricio Bohorquez**[2] **and Christophe Ancey**[1]

[1] Laboratory of Environmental Hydraulics, École Polytechnique Fédérale de Lausanne, Lausanne, Switzerland.

[2] Centro de Estudios Avanzados en Ciencias de la Tierra, Universidad de Jaén, Campus de las Lagunillas, Jaén, 23071 Spain.

Doctoral candidate's contribution

The candidate designed and conducted the experiments. The data were analysed and interpreted by the candidate, who wrote the manuscript. Further discussions on results and manuscript structure with Prof. Ancey and Prof. Bohorquez are foreseen.

4.1   Introduction

In this chapter, we present the first results of an experimental campaign conducted in a new flume, which was specifically designed and built to improve the imaging conditions for the monitoring of bedload fluxes and bed topography and to investigate possible influences related to the channel length on the variabilities of the bedload transport rates and of the antidune morphodynamics. This third study is important for three main reasons. First, it represents a valuable test of the methods and findings presented in Chapter 2 and Chapter 3. Second, this new 5.8–m-long flume makes it possible to better assess and quantify the non-uniformities in the antidune patterns (compared to the 2.5–m-long setup). Third, the frameworks proposed in Chapter 2 and Chapter 3 are combined with wavelet transform analyses to take a closer look at how the periodicity of the bedload pulses observed at the flume outlet is linked with the migration period of the antidunes located close to the bedload monitoring cross-section.

An experiment under steady-state conditions (ES1) was carried out to study the behaviour of the bedload pulses observed at the flume outlet and the relationship between their periodicity and the migration periods experienced by the antidunes under steady-state conditions. We analysed the uncertainty of the time-averaged bedload transport rates for different sampling intervals by using the protocol presented in Chapter 2. Moreover, we studied the convergence of the time-averaged bedload transport rates towards the sediment supply rate. The underlying question was: how long should the time-averaging interval be (compared to the antidune migration period) to approximate the steady-state bedload transport rate within a certain error range?

Concerning antidune morphology, we wanted to assess the occurrence and magnitude of systematic changes of bedform wavelength that may occur as the antidunes migrate upstream. Bohorquez and Ancey (2016) reported a systematic increase of antidune wavelength in their numerical simulation (under conditions similar to those of the ES1 run). In the experimental runs conducted in the 2.5–m-long flume (Chap. 3), we did not identify this phenomenon. We wondered if its manifestation could have been hindered by the limited flume length. During the ES1 experiment, we monitored the bed topography in two control windows (as long as 1.7 m) in a 5.8–m-long flume. We conducted 2D spectral analysis of the bed elevation perturbation to accurately quantify λ and c ranges and clarify whether the antidune wavelength systematically increased or not. This analysis also made it possible to carry out an additional test of the relationship proposed by Pascal et al. (2021) for predicting the trend $c_N^* \approx f(\lambda_N^*)$ (Eq. 3.16, Chap. 3). Furthermore, we performed continuous wavelet transform analysis of the antidune pattern to investigate the behaviour of transient and localised non-uniformities that may affect the antidune sequences. In particular, we focused our attention on the disturbance caused by the bed discontinuity at the flume outlet.

We also conducted an experiment with no sediment supply at the flume inlet. This run (ED1) started at the end of the ES1 run, when the sediment feeding was interrupted. The progressive

erosion of sediment from the bed in the upstream sector of the flume led to a temporary increase of the mean bedload transport rate at the flume outlet. We identified a period during which the behaviour of the bedload transport rate series was close to a stationary process and we tested the protocol for estimating the variance of double-averaged bedload transport rates. Spectral analysis of the bed elevation perturbation data was performed to understand how the antidune sequences behaved under conditions of increased sediment supply rate.

4.2 Methods

4.2.1 The long-flume setup

We conducted the main experimental run using a narrow flume (Figure 1) whose active length was equal to $L_f = 5.80$ m (total length of 6.5 m). Its cross-sectional width ($W = 4$ cm) is the same as that of the flume used in previous studies conducted by Ancey and Pascal (2020) and Pascal et al. (2021) but the flume length was more than doubled. One advantage of this long flume was the possibility to explore potential morphological changes in the bedform sequences as they migrated far upstream under steady-state conditions (ES1, i.e. with active sediment feeding). During the bed degradation phase of the experiment (ED1, see Section 4.3) the large flume length was required to investigate the feedback between bedload transport and antidune morphodynamics in the downstream sector of the flume while the upstream part of the bed was experiencing gradual erosion due to the absence of sediment feeding at the flume inlet.
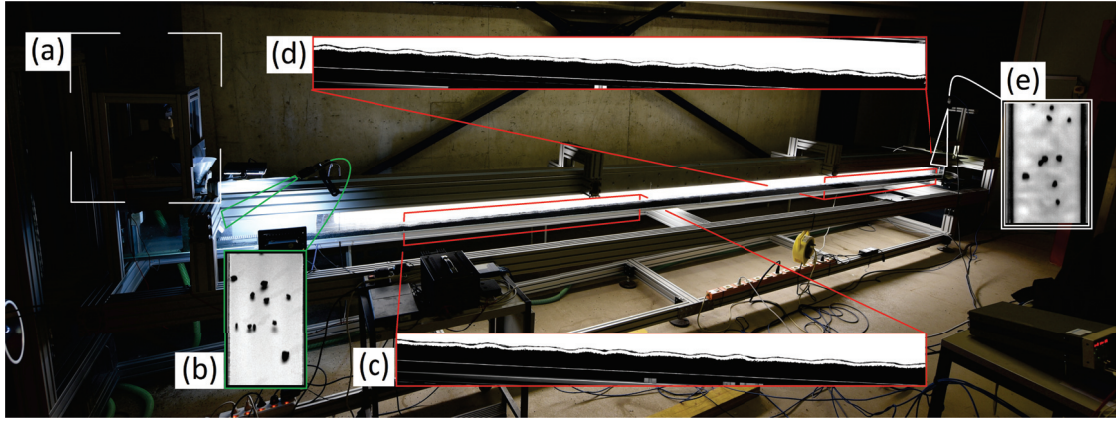
Figure 4.1: Setup 5.8–m-long tilting flume: (a) sediment feeding system, (b) high-speed camera for monitoring sediment supply rate at the inlet, (c) upstream topography control window $L_{TCW1} = 1.52$ m, (d) downstream topography control window $L_{TCW2} = 1.74$ m, (e) high-speed camera for monitoring bedload transport rate at the outlet. Flow from left to right.

The sediment used for this study was well-sorted dark gravel characterised by median particle diameter $d_{50} = 2.5$ mm ($d_{16} = 2.1$ mm, $d_{84} = 3$ mm), mean particle volume $V_p = 8.5 \cdot 10^{-9}$ m^3 and sediment density $\rho_s = 2550$ kg m^{-3}. This gravel was slightly finer than that used in the

experimental campaign conducted by Pascal et al. (2021). The mean bed thickness under bed equilibrium conditions was approximately equal to 4.5 cm. The dry sediment was supplied at the flume inlet by a feeding system whose functioning and features were very similar to those of the feeders used by Ancey and Pascal (2020) and Pascal et al. (2021). The feeder wheel was operated by a 12VDC 2rpm electrical motor. The water flow-rate Q_w was controlled using a GYSI EH 5/2 recirculating pump. The flow discharge during the experiment was continuously monitored using an Endress+Hauser Proline Promag 50D (DN25) flow-meter. The hyporheic flow discharge $Q_{w,hyp}$ was sampled manually at the flume outlet before and after the experiment. The flume inlet and outlet were designed with the purpose to ensuring boundary conditions as similar as possible to those imposed for the experimental campaign conducted by Pascal et al. (2021). Two 15–cm-long perforated boxes bounded both the upstream and the downstream ends of the granular bed ($x_{inlet} = 0$ m $x_{outlet} = 5.80$ m). These boxes were installed to stabilise the boundary conditions. In particular, the box located at the flume outlet was filled with gravel to minimize sharp deviations of the hyporheic flow. In the following sections, we refer to its upstream perforated wall (in contact with the downstream edge of the erodible bed) as the 'septum'. The white-coloured upper face of the outlet box acted as neutral background for the image-based tracking of the particles transported by the water flow. At the flume inlet the sediments were fed over a white tilted plate—where they slided and were filmed—before falling onto the rough surface of the upstream box and being transported by the water flow. Refer to the Monitoring systems section (4.2.3) for details regarding bedload transport and sediment feeding monitoring.

4.2.2 Experimental procedure and conditions

We ran one experiment (ESD1) that lasted 120 minutes. The first part of the experiment (referred to as ES1) was carried out under steady-state conditions with active sediment feeding at the flume inlet ($q_{s,in} = 1.79 \cdot 10^{-5}$ m^2 s^{-1}). After 60 minutes the sediment feeder was stopped whereas the water discharge was maintained unchanged. Therefore, a bed degrading phase (referred to as ED1) begun with a gradual bed erosion that propagated downstream from the flume inlet. We reported in Table 4.1 the main parameters values for the ES1 phase of the experimental run. The sediment feeding rate $q_{s,in}$ and the mean bed slope $\overline{\psi}$ were directly imposed whereas the water discharge value was selected to maintain the balance between erosion and deposition at the flume scale (i.e. near-constant overall mean bed slope over time).

$\overline{\psi}$ [°]	$q_{s,in}$ [m^2 s^{-1}]	$\overline{q}_{s,ES1}$ [m^2 s^{-1}]	q_w [m^2 s^{-1}]	R_b (h_0^*) [mm]	Fr [-]	Θ [-]	Θ_c [-]
2.7	$1.79 \cdot 10^{-5}$	$1.77 \cdot 10^{-5}$	$4.4 \cdot 10^{-3}$	9 (10)	1.42	0.107	0.065

Table 4.1: Main experimental parameters for the run ES1. * Reference flow depth $h_0 \simeq \left\langle \overline{h} \right\rangle$ calculated with a Colebrook-type relationship for rough fully-turbulent flows.

We estimated the Shields parameter Θ as

$$\Theta = \frac{g\rho R_b \tan\overline{\psi}}{g(\rho_s - \rho)d_{50}} = \frac{R_b}{d_{50}}\frac{\tan\overline{\psi}}{s-1}, \tag{4.1}$$

where g is the gravitational acceleration, ρ is the water density, $s = \frac{\rho_s}{\rho}$ is the sediment-to-water density ratio and R_b is the bed hydraulic radius. The Einstein–Johnson correction method Einstein (1942); Johnson (1942) was used to compute R_b. This choice was made to ensure consistency in the comparisons between findings of the present study and previous results obtained by Pascal et al. (2021) who calculated the Shields parameter Θ using the same sidewall correction method. The reader is invited to consult Guo´s works concerning the Einstein–Johnson correction procedure for further useful information and considerations (see Guo, 2015, 2017). The mean critical Shields value for ES1 was estimated as $\Theta_c = 0.15(\tan\overline{\psi})^{0.275}$ according to Recking et al. (2008).

4.2.3 Monitoring systems

Bedload transport monitoring at the flume outlet

We monitored the bedload transport rate at the flume outlet by filming the particles using a acA2000-165um Basler high-speed camera (lens: Fujinon TV 1:1.7 / 35 mm, f-stop = 5.6) as they left the flume passing over the outlet septum. The camera was operated at 100 frames per second. We selected an image window at the flume outlet with size 7.5 × 4 cm, which was captured with a 320 × 172-pixel frame. Since the uppermost face of the outlet septum was white, it acted as neutral background for the particle tracking procedure and we did not need to perform a background subtraction step. Regarding the image pre-processing, we simply inverted the image pixel values so that the particles appeared as bright patches over the dark background. The tracking procedure (composed by particle detection, filtering and linking steps) was conducted with a framework similar to that adopted by Ancey and Pascal (2020), which was mainly based on algorithms available in the TrackMate plugin (Tinevez et al., 2017) of the ImageJ platform (Schindelin et al., 2015). Specifically, the following sequence of operations was conducted:

- We detected the spots (i.e. the particles) using the Laplacian of Gaussian detector embedded in TrackMate. We set the spot size parameter according to the mean particle size on the images. The quality detection threshold was set arbitrarily (by checking on a small video sample) to minimise false detections caused by single particles detected as two spots and by light reflections on the wavy water surface;

- We filtered the spots whose intensity was lower than 210 over 255 (in the inverted image) to discard most of the remaining false spots due to the surface waves;

- The spots were then linked together to form the final trajectories by applying a modified

version of LAP tracker designed by Jaqaman et al. (2008). Our modification regards the linking cost function and allowed us to set a constraint on the motion direction (no upstream motion considered) which reflected the a-priori knowledge regarding the particle motion at the flume outlet (i.e. downstream). This modified LAP version improved the performance of the particle linking step when the spot density was high (more than 20 moving particles at the same time in the control window) and allowed us to keep a relatively low acquisition frequency (100 fps) in this fixed white background configuration;

- The resulting trajectories were filtered to remove those that were composed by less than 4 spots, which were often the result of single particles identified by two spots over short distances.

Since the spot detection performance was satisfactory—given the stable white background—we preferred not to use the gap closing option for the spot linking step. This option could be useful in case of low spot density and persistent local reflections caused by waves. As final step, the set of trajectories was analysed to compute the time series of the number of moving particles $N(t)$ in the outlet control window (OCW, streamwise length $L = 4$ cm), the $u_p(t) = \sum_{tr=1}^{N} u_{p,tr}$ volume-averaged velocities (where $u_{p,tr}$ is the track-averaged velocity for each moving particle within the OCW at time t), and the times series of $\overline{\Phi}_s(\Delta t \mid t)$ (see Eq. 2.1 in Chapter 2). The particle flux $\overline{\Phi}_s(t)$ was calculated at the middle cross-section of OCW ($\mathscr{S}_{OCW}$) to ensure the maximum accuracy achievable with our setup. The $N(t)$ and $u_p(t)$ data were required to calculate the volume-averaged bedload transport rates $\overline{q}_s(\Delta t \mid t)$ according to the relationships Eq. 2.2 and Eq. 2.3 presented in Chapter 2 (2.4) (Ancey and Pascal, 2020). Note that we neglected the instantaneous velocity variations of the particles around their track-averaged velocities $u_{p,tr}$ for the calculation of $u_p(t)$ (the relative magnitude of these variations was very small in the OCW volume). The methods used for analysing the bedload transport rate data are described in the next Data analysis section.

Sediment feeding monitoring

The continuous monitoring of the sediment feeding rate at the flume inlet was ensured by a acA2000-165um Basler high-speed camera (lens: Fujinon CF16ZA-15 1:1.8 / 16 mm f-stop = 4) which was operated at a frequency of 100 fps. The image window on the white tilted plate (7.5 × 4 cm) was captured with a 500 × 272-pixel frame. This monitoring system remained active during the entire duration of ES1. The particle tracking technique is the same used for the outlet bedload transport monitoring. We computed the sediment feeding rate in terms of particle flux across a reference section $\mathscr{S}_{inlet}$ located at mid-length of the tilted plate. We used a signal generator to set the same frame trigger for both cameras—at the flume inlet and outlet—to ensure time synchronisation of the bedload transport rate series.

Bed topography monitoring with lateral cameras

The bed topography monitoring was based on the same method used by Pascal et al. (2021). The main difference lied in our consideration of two topography control windows (respectively, TCW1 and TCW2). Each TCW was filmed by a dedicated acA4112-30um Basler camera (operated at 1 fps) equipped with a Computar 1:2.8 / 25 mm C-mount 1.1" lens. On the side of the flume opposite to the cameras a series of backlight panels ensured a uniform bright background. Setting two control windows instead of one was required to ensure high-quality images and highly accurate topography profiles in the laboratory conditions (the maximum distance between cameras and flume was constrained). Capturing the bed profile over the entire flume length in a single control window would have been possible by composing frames from three cameras but in any case the joint between the two 3.25–m-long sectors of the flume walls would have disturbed the bed-detection step. Therefore, we preferred to work with two separated control windows and to privilege image accuracy. Details regarding the position of the control windows and image resolution are reported in Table 4.2.

CW	x_{ups} [m]	x_{dws} [m]	Δx_{CW} [m]	Nominal res. [mm/px]
TCW1	0.66	2.18	1.52	0.43
TCW2	4.06	5.80	1.74	0.43

Table 4.2: Main geometrical parameters for the topography control windows (TCW1 and TCW2) as they were set during ES1.

The bed profile was detected by applying a binarization filter to the raw image. The detected bed elevation at each flume cross-section represented the highest z-coordinate of the bed interface over the cross-section. Since the bedforms were nearly two-dimensional (2D), the detected profile was a close approximation of the centreline bed topography. A running average filter (horizontal span equal to d_{50}) applied to the resulting topographical made it possible to smooth the very short perturbations caused by moving particles that were in contact with the bed. For each TCW, we obtained a $Z_{0,TCWj}(x, t)$ matrix containing the bed elevation z for each $\{x, t\}$ pair. As in the previous study by Pascal et al. (2021), the lens distortion effect on the raw images was not corrected as it partially counterbalanced the perspective distortion of the bed profile (not recoverable with the current setup). To assess the magnitude of the wavelength accuracy error (larger than the nominal image resolution), we used the same indirect method already adopted by Pascal et al. (2021), which is based on the lateral imaging of two thin vertical wires (each one placed in contact with one of the two glass side-walls) at the same x-coordinate near the edge of the control window (where the distortion effects are maximal). We estimated a maximum wavelength error of approximately $3d_{50}$ for both TCW1 and TCW2.

It is important to underline that in this experimental study the downstream end of the downstream control window TCW2 coincided with the upstream edge of the flume outlet plate.

This configuration of TCW2 was selected to follow—in the close vicinity of the flume outlet—eventual downstream travelling disturbances, which might interrupt or perturb the antidune sequence continuity. These features were already observed experimentally by Pascal et al. (2021) (see Sec. 3.4 and 3.6) but open questions remain about their potential impact on bedload transport pulses.

4.2.4   Data analysis

Bedload data analysis

As a first step in the bedload data inspection, the $q_s(t)$ series for the flume outlet was analysed by considering the entire experimental dataset of ES1 and ED1 (total duration of 7200 s). We integrated the bedload transport rate $q_s(t)$ over time using the following relationship to obtain the cumulative volume of sediments $V_{cum}(t_D \mid t_{D0})$ that left the flume between a reference starting time t_{D0} and t_D.

$$V_{cum}(t_D \mid t_{D0}) = \int_{t_{D0}}^{t_D} q_s(t) W \, dt, \tag{4.2}$$

where the time reference t_{D0} was usually set equal to the starting time of ES1 ($t = 0$ s). The analysis of the $V_{cum}(t_D \mid t_{D0})$ plot from the entire dataset was required to assess the steadiness of the bedload transport rate during ES1 and to identify the main trends for the bedload flux at the flume outlet during ED1. In the following part of the analysis different initial reference times were used to compute $V_{cum}(t_D \mid t_{D0})$. When this was the case, the corresponding time reference is explicitly indicated. A primary step in this study was to analyse the trends of the averaged bedload transport rates and their variance in presence of upstream migrating antidunes under moderately intense transport by using the approach proposed by Ancey and Pascal (2020). The procedure for estimating the mean bedload transport rate and the associated variance during the quasi-steady ES1 run was thus based on the protocol presented in Chapter 2 (2.2.7) (Ancey and Pascal, 2020). It is important to recall that this protocol may be applied even when the behaviour of the moving particles does not follow that of a Markovian process (when the Poisson law is not suitable to describe the number of moving particles that crossed a control section $\mathscr{S}$ during the δt interval) because it is possible to use the renewal theory (Ancey and Pascal, 2020). For the sake of clarity, the specific choices that were made to apply the protocol to the experimental data of ES1 and ED1 are described in the Results section.

Bed topography data analysis

Regarding the analysis of the bedform morphodynamics, we followed the framework already used in Chapter 3 (Pascal et al., 2021). We briefly recall the fundamental concepts and steps of this spectral analysis, which was based on the application of the 2D fast Fourier trans-

form (FFT)—already used for 2D spectral descriptions of migrating dunes (Guala et al., 2014). First, we selected the submatrix of interest $Z_{0,TCWj}([x_a x_b], [t_a t_b])$ in the bed elevation matrix $Z_{0,TCWj}(x, t)$ (e.g. the part of the matrix corresponding to the full TCW1 length during ES1). Second, we inspected the bed slope time series to assess its steadiness and to identify eventual signatures of marked degradation or aggradation processes. Third, the bed elevation perturbation matrix $Z_{TCWj}([x_a x_b], [t_a t_b])$ was obtained by subtracting the mean bed slope trend from the raw bed elevation $Z_{0,TCWj}([x_a x_b], [t_a t_b])$. Fourth, we applied the 2D-FFT in temporal and spatial frequency domain on the perturbation matrix $Z_{TCWj}([x_a x_b], [t_a t_b])$ and we computed the power spectral density for each λ, T pair by using the Fourier coefficients which resulted from the 2D-FFT application. This analysis was performed for different sub-matrices of interest depending on the behaviour of antidune patterns and bedload transport rate during ES1 and ED1 (details are given in the Results section 4.3). Each $\lambda - T$ spectrum was then converted in the dimensionless $\lambda_N^* - c_N^*$ spectrum by using the conversion expression $c = \lambda/T$ and the set of scaling relationships used in Chapter 3.2 (Pascal et al., 2021). The two relationships for computing the dimensionless wavelength and dimensionless celerity read:

$$c_N^* = \frac{c}{U_N} = c \frac{\overline{q}_s}{d_{V,50}\left(1-p\right)};$$ (4.3)

$$\lambda_N^* = \frac{\lambda}{\lambda_{R09}}; \quad \text{where} \quad \lambda_{R09} = 0.093 \frac{\Theta}{\Theta_c^3} Fr d_{50} \quad \text{(Recking et al., 2009).}$$ (4.4)

Concerning the celerity scaling of Eq. 4.3, U_N is a scale proportional to the virtual velocity of the sediment phase that composes the bed active layer (Pascal et al., 2021). According to Pascal et al. (2021), the thickness of such layer—which approximately corresponds to the antidune amplitude—was assumed constant and proportional to a characteristic grain size $d_{V,50} = (6 V_b/\pi)^{1/3} = 2.5$ mm (estimated from the characteristic particle volume). Almost equivalently, d_{50} can be considered as length scale for computing U_N when the sediment particles are rounded (as in the present case $d_{V,50} \simeq d_{50}$) or when an estimate of V_b is not available. In any case, before applying the celerity scaling based on U_N proposed by Pascal et al. (2021) (and the related relationships), it is advisable to check whether the observed antidune amplitudes H_{AD} were close to $2d_{V,50}$ or not. As presented in Sec. 4.3.2, this condition was satisfied by the antidunes observed during ES1 and approximately also by those observed during ED1. The spectral analysis for ES1 was conducted over both TCW1 and TCW2 in order to investigate possible non-uniformities in the antidunes sequences as the bedforms migrated upstream from TCW2 to TCW1. Regarding the ED1 run, we mainly analysed the topographic data collected in TCW2, whereas the TCW1 data were mainly used to study the evolution of the slope profile during the degrading phase. We tested the indirect method (based on antidune spectrum data) proposed by Pascal et al. (2021) to estimate the mean bedload transport rate for ES1. Other tests were conducted by considering a period of quasi-steady bedload discharge during ED1 and the $\lambda_N^* - c_N^*$ spectrum calculated from the corresponding sub-matrix of $Z_{0,TCW2}$.

Chapter 4. On antidune trains and bedload pulses under steady- and quasi-steady-state conditions

Wavelet transform analysis tools used in this study

Wavelet analysis is a useful tool to investigate local variability in an oscillating signal when the global perspective provided by Fourier transforms alone is not sufficient for the investigation purposes. Specifically, as synthesised by Grinsted et al. (2004), wavelet transforms "expand time series into time frequency space" and are therefore particularly suitable to highlight local non-uniformities which may occur in pulsating signals. Concerning the bed topography data in this study, we were interested in investigating both the temporal frequencies of the bed elevation perturbation (at a given location) and the spatial periodicity of the bed topographic profile (at a given time). Moreover, we wanted to study the temporal periodicity of the fluctuations in the bedload transport rate series. Therefore, we applied continuous wavelet transform (CWT) to our datasets to assess the presence of (i) non-uniformities in the bedform shape and migration celerity within the antidune sequences (CWT on space and time series) and of (ii) non-uniformities in the fluctuation period of the bedload transform rate at the flume outlet (CWT on time series).

Here, we provide only brief information regarding the wavelet function that we considered for this study and its CWT-based applications to our data series and we refer the interested reader to specific literature works (e.g. Farge, 1992; Foufoula-Georgiou and Kumar, 1994; Torrence and Compo, 1998; Grinsted et al., 2004) for extensive descriptions of theoretical aspects. The wavelets are real or complex valued functions with zero mean localised in both time and frequency domains—the terms 'time' and 'frequency' here are used for indicating reciprocal mathematical domains. The precise conditions (admissibility, similarity, invertibility and regularity) that a function should satisfy in order to be considered a proper mother wavelet have been summarised by Farge (1992). We chose the Morlet (with dimensionless frequency parameter $\omega_0 = 6$) as mother wavelet for our feature detection applications as it represents a good compromise between time and frequency localization (Grinsted et al., 2004). The Morlet wavelet is a complex valued function whose mathematical expression is:

$$\Psi_0(\eta) = \pi^{-1/4} e^{i\omega_0 \eta} e^{-\eta^2/2}, \tag{4.5}$$

where $\eta = t/s$ is the dimensionless 'time' (with the scale parameter $s = n_s \delta t$).

Applying a CWT involves performing the convolution of the signal obs_n (e.g. time series of observations with time step δt) with translated, stretched and normalised versions of Eq. 4.5. The stretching is done by varying s. In the CWT case, the convolution is conducted N_0 times with the function centred over all the localised 'time' indexes $n = 1, ..., N_0$ and the process is repeated for all the investigated scale values s. The operation is synthesised by the expression:

$$W_n(s) = \sqrt{\frac{\delta t}{s}} \sum_{n'=1}^{N_0} obs'_n \Psi_0 \left[(n' - n)\frac{\delta t}{s} \right] \tag{4.6}$$

where the $(\delta t/s)^{0.5}$ term in the right-hand side ensures the normalization. Numerically, the convolution series expressed in the 'time' domain by Eq. 4.6 is more efficiently implemented in the Fourier frequency domain (see Torrence and Compo, 1998). One can then compute the local wavelet power as $|W_n(s)|^2$ and interpret the complex part of $W_n(s)$ as the local phase of the signal. Analysing the power scalograms (i.e. the 2D plots of the $|W_n(s)|^2$ terms in 'time' and 'scale' domains, possibly with the local phase indication) and the 1D wavelet spectra computed from different portions of our data series allowed us to quantify the magnitude and extension of the non-uniformities that we identified in the antidune patterns and in the bedload fluctuations. For the CWT computations, we made extensive use of the 'wavelet-coherence' MATLAB package provided by Grinsted et al. (2004). We represented the results with partially modified codes to improve readability for this specific case. We defined the cone of influence (COI) that identifies the zones of the scalograms in which the edge artefacts are non-negligible as formulated by Grinsted et al. (2004). The local peaks in the wavelet power were compared against a background red noise spectrum—as defined by Grinsted et al. (2004) according to Torrence and Compo (1998)—to assess their statistical significance. Visual analyses of local portions of the signal were also conducted to ensure that the outcomes of the wavelet analyses were physically coherent.

4.3   Results

In this introduction to the Results section we present a global perspective on the experimental results in terms of bedload transport, bed topography and water flow features. Further specific results obtained by analysing the data according to the frameworks presented in the previous Methods section are reported in the following parts of this section.

We first outline the overall trends of the estimated cumulative volume of sediments $V_{cum}(t)$ that crossed the outlet section and of the mean bed slope in the control window TCW1 and TCW2 during the entire experiment (ESD1). Subsequently, we give some general information related to the water flow features that were observed. We then report the results of the analyses focused on sediment flux and bedforms dynamics (and on the feedbacks between them) both under quasi-equilibrium conditions and bed degrading conditions.

Figure 4.2 shows the trends of $V_{cum}(t)$, $V_{fed}(t)$, ψ_{TCW1} and ψ_{TCW2} during the entire duration of ESD1. Analogously to $V_{cum}(t)$, $V_{fed}(t)$ represents the estimated volume of sediments fed at the flume inlet until time t. As on can see, the sediment feeding rate (i.e. the slope of the $V_{fed}(t)$ curve) was remarkably stable during the first 16 minutes of ES1. Unfortunately, the feeder steadiness was not optimal during the entire ES1 part of the run. The feeding rate experienced a subtle increase and was about 5% higher than the nominal feeding rate between $t = 1000$ s and $t = 2300$ s. This phase was followed by a decrease of similar magnitude. Therefore, the feeding rate was approximately 5% lower than its nominal value during the
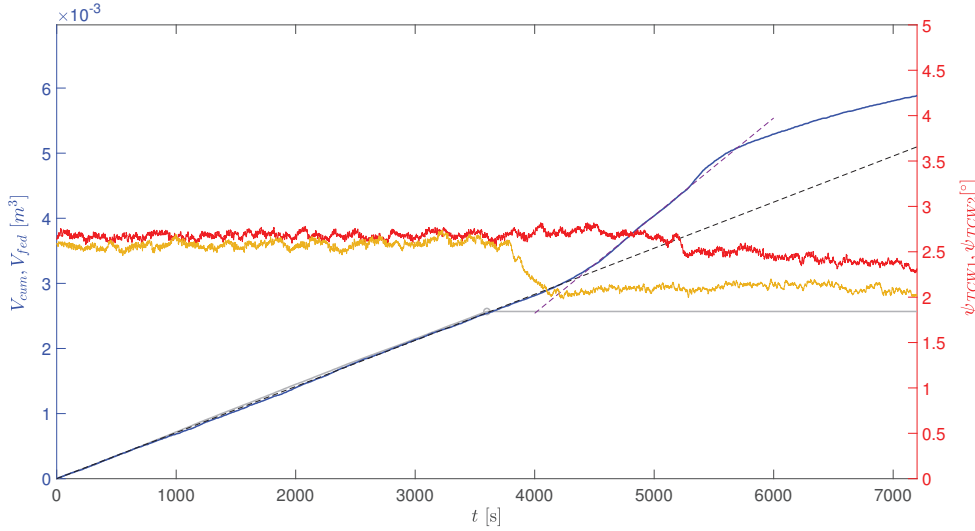
Figure 4.2: Trends of V_{cum} (solid blue line), V_{fed} (solid grey line), ψ_{TCW1} (solid orange line) and ψ_{TCW2} (solid red line) during the entire duration of ESD1. The grey circle marks the interruption of the sediment feeding at $t = 3600$ s. The dashed black line indicates the linear trend with constant slope equal to $\overline{q}_{s,ES1}W$. The dashed purple line indicates the linear trend of V_{cum} between $t = 4550$ s and $t = 5250$ s (approximately equal to $2\,\overline{q}_{s,ES1}W$).

last part of ES1. The slope of the cumulative volume curve $V_{cum}(t)$ was almost parallel to the nominal feeding rate slope during the first hour of the experiment and the response to the variations in the real feeding rate was relatively smooth. Therefore, we decided to consider the entire ES1 phase to analyse the interplay between antidune trains and bedload transport rates under quasi-steady transport conditions. In the following sections we specify whether the analyses of bedload transport and antidune morphodynamics gave significantly different outcomes or not when executed considering the full ES1 dataset or only the data referred to the first 700–s-long period of the experiment. Concerning the bed topography during ES1, the average slope angle values in the two control windows during ES1 were very close to each other, although not exactly equal. The slope angles oscillated around values of $\psi_{TCW1} = 2.55°$and $\psi_{TCW1} = 2.65°$and values of $\psi_{TCW2} = 2.65°$and $\psi_{TCW2} = 2.75°$for TCW1 and TCW2, respectively. This oscillating behaviour, which reflected a bed elevation difference of the order of d_{50} between the two edges of the same control window, was very similar to that observed by Pascal et al. (2021) in a 2.5–m-long flume. After the interruption of the sediment feeding (operated at $t = 3600$ s) the degradation phase ED1 began. A marked erosion process onset near the septum at the flume inlet and about 1 minute after the feeding interruption (i.e. $t \approx 3660$ s) the septum vertical step started to be exposed. This flow irregularity first evolved in a step-pool configuration and then in a small waterfall (transcritical to nappe flow, see Chanson, 2001), when the bed was completely eroded near the septum (around $t \approx 4200$ s). The bed topographic profile evolved over time and the upstream edge of the granular bed migrated downstream. For instance, this edge was located in $x \simeq 8$ cm at $t \simeq 5700$ s and in

$x \simeq 14$ cm at $t \simeq 6000$ s. The associated flow exhibited a complex configuration typically characterised by an undulated hydraulic jump downstream of the sector characterised by the high-velocity flow over the smooth glass bottom. The deviation from the quasi-steady regime profile was first noticeable in the trend of ψ_{TCW1} (around $t = 3800$ s). As expected, due to the lack of sediment feeding the erosive process, which was initially localised in the most upstream part of the flume, led to a decrease of the slope angle in TCW1. Most of this decrease in ψ_{TCW1} happened during the timeframe between $t = 3800$ s and $t = 4500$ s. During the same interval, the overall slope ψ_{TCW2} in the downstream control window experienced a slight increase ($\psi_{TCW2} > 2.7°$). Afterwards, the degradation wave travelled toward the downstream sector and the ψ_{TCW2} began to decrease as well. There was a sudden diminution of the ψ_{TCW2} value after $t = 5200$ s and then the decrease continued more gradually, as the degradation continued.

Observing the different time evolution of the variables in Figure 4.2 made it possible to identify coherent links that are clues of processes happening at the flume scale during ED1. The trend of the bedload transport rate (for time averages of the order of 50 s) experienced a marked growth as an indirect consequence of the sediment feeding interruption. In particular, the bedload transport rate trend at the outlet gradually rose between $t = 3800$ s and $t = 4550$ s, followed by a quasi-steady phase with $\overline{q}_s(t \mid \Delta t = 200 \text{ s}) \approx 2 q_{s,in}$ until $t = 5250$ s. Then the arrival of the degradation wave in the sector covered by the downstream control window TCW2 led to the most intense transport phase at the flume outlet that lasted around 250 s. The data acquisition was stopped few minutes later than the moment in which the most upstream part of the bed in TCW1 was completely eroded. During the last phase of ED1, after $t = 5500$ s, the bedload transport rate at the flume outlet gradually decreased to approach a value close to 75% $q_{s,in,ES1}$. Although the performances of the particle tracking method were satisfactory during the ES1 phase, they were less good during the ED1 phase. The mean particle activity in the OCW during the phase of highest bedload discharge (between $t = 4550$ s and $t = 5500$ s) was approximately doubled compared to the ES1 typical conditions and this fact made the spot detection and linking steps more difficult. The challenging conditions (together with the simplification of using a single value V_{50} to calculate the volumetric transport rates) probably contributed to the small discrepancies identified between the cumulated volume of sediment V_{cum} (estimated by integrating the outlet bedload transport rates over the ED1 duration) and its counter-proof values measured from basket sampling and image-based analysis of the bed profiles. We estimated $V_{cum}(t = 7200\text{s} \mid t_{D0} = 3600\text{s}) = 3.3 \cdot 10^{-3} \text{m}^3$ from integration of the q_s time series, whereas the volume estimates obtained from basket sampling and post-analysis of the bed profiles were 5% and 7% lower than this value, respectively. Given the challenging conditions, a difference of this order of magnitude between the estimates did not come as a surprise.

The flow during ES1 was turbulent, supercritical and characterised by high relative roughness d_{50}/h similarly to the conditions of the experiments reported by (Pascal et al., 2021). During the degradation phase ED1, the turbulent flow experienced unsteadiness and non-uniformities along the flume as previously mentioned. Downstream of the sector characterised

by the undulated hydraulic jump, the remaining stretch was still characterised by supercritical flow. Further details about the flow configuration (the typical values of h and Fr) observed for defined time and space intervals are reported in the sections 4.3.1 and 4.3.2 where we describe the analyses of the antidune dynamics based on different sub-matrices of interest $Z_{0,TCWj}([x_a x_b], [t_a t_b])$.

4.3.1   Steady phase ES1

ES1: Properties of the bedload transport series

In the first part of this section, we present the outcomes of the ES1 experimental run with a particular focus on bedload transport time series. Comparing this experimental dataset with others collected in the short flume (see the first two chapters of this thesis) is useful to set the context for presenting further results regarding the application of the mean bedload transport rate measurement protocol (Section 4.3.1). These comparisons and considerations are pertinent also in view of the performance assessment of the $\overline{q}_s$ estimation method based on the spectral analysis of the antidune patterns (Section 4.3.1).

ES1 was characterised by moderately intense bedload transport regime. Figure 4.3 (a) and 4.3 (b) show how the time series of the bedload transport rates at the flume outlet (q_s and $\overline{\Phi}_s(t)$) oscillated around the mean rate.

Figure 4.3 (c) shows the differences between the bedload transport rate expressed as local particle flux $\overline{\Phi}_s(t)$ or as volume-averaged $\overline{q}_s$ for 0.2-s time averages during ES1. Figure 4.3 (d) show the $\overline{q}_s(t \mid \Delta t) - \overline{\Phi}_s(t \mid \Delta t)$ differences for 2-s time averages. It is interesting to note that the $\overline{q}_s(t \mid \Delta t) - \overline{\Phi}_s(t)$ differences averaged over 2 s were relatively small and mainly reflected missed particle detections (in $\overline{\Phi}_s(t)$), whereas for the 0.2-s time-averaged signals the difference $\overline{q}_s(t \mid \Delta t) - \overline{\Phi}_s(t \mid \Delta t)$ took both positive and negative values, and was relatively high compared to $q_{s,in}$ at times. Similar plots were presented also in Chapter 2 for the P run. Concerning the influence of the missed particle detections on $\overline{\Phi}_s(t)$, we identified this discrepancy ($\overline{\Phi}_{s,ES1}(t) = 1.70 \cdot 10^{-5}$ m^2 s^{-1}, whereas $\overline{q}_{s,ES1} = 1.77 \cdot 10^{-5}$ m^2 s^{-1}) and we retained the $\overline{q}_{s,ES1}$ value (run average in Table 1) as reference mean bedload transport rate for ES1 since it corresponded to the average rate computed from the basket samples collected at the flume outlet during ES1. Noteworthy, in the present case it appears that the time averages $\overline{\Phi}_s(t \mid \Delta t)$ and the time-volume averages $\overline{q}_s(t \mid \Delta t)$ converged towards relatively similar values (valued net of the tracking errors) after only few seconds. This result is primarily linked to the fact that the monitoring was conducted over a fixed plate, which thus prevented erosion and deposition events in the control window. Such an information is important in perspective of considerations regarding the uncertainty and convergence of $\overline{\Phi}_s(t \mid \Delta t)$ and $\overline{q}_s(t \mid \Delta t)$ rates towards the run-averaged rates (for $\Delta t > 2$ s) reported in the Section R Protocol.
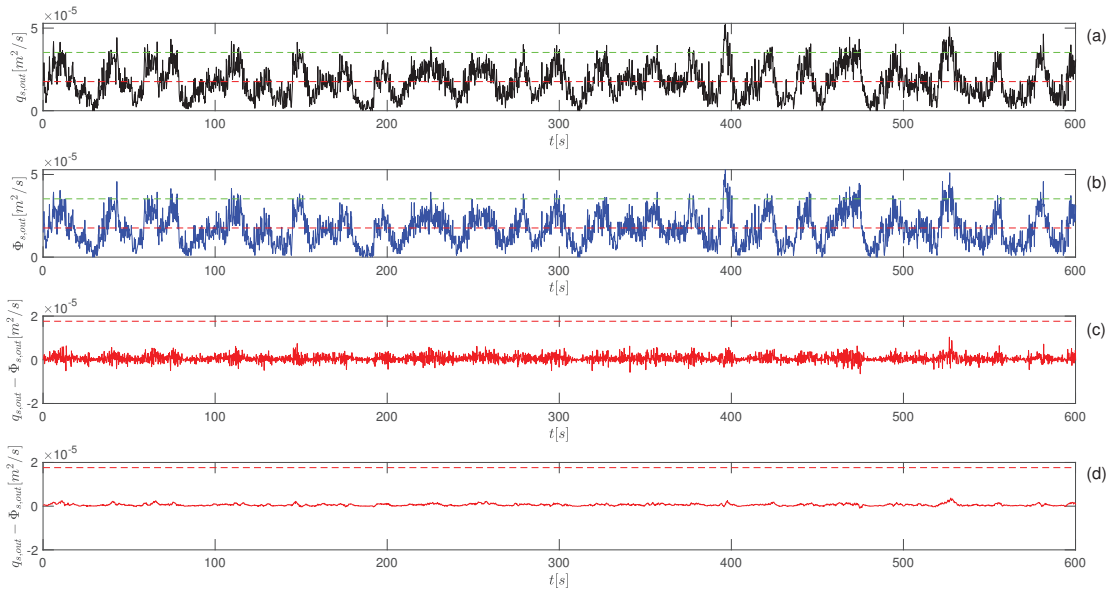
Figure 4.3: (a) Sample of $\overline{q}_s$ (0.2-s time average) collected during ES1 (from $t = 0$ s to $t = 600$ s). (b) Sample of $\overline{\Phi}_s$ (0.2-s time average) collected during ES1 (from $t = 0$ s to $t = 600$ s). (c) Series of $\overline{q}_s(t \mid \Delta t) - \overline{\Phi}_s(t \mid \Delta t)$ differences for the 0.2-s averaged rates in (a) and (b). (d) Series of $\overline{q}_s(t \mid \Delta t) - \overline{\Phi}_s(t \mid \Delta t)$ differences for 2-s averaged rates. The dashed red lines indicate the mean bedload transport rate $\overline{q}_{s,ES1}$ whereas the dashed green lines indicate a constant rate of $2\overline{q}_{s,ES1}$.

The mean bedload transport rate during ES1 was definitely higher than the mean rate imposed during the P experiment (e.g. Ancey and Pascal, 2020). The particle flux at the flume outlet during ES1 was not expected to follow a Markovian behaviour. In that case, the particle arrival intervals at a given cross-section $\mathscr{S}$ should follow an exponential distribution as this condition indicates that the particle arrival process behaves as a Poisson process.

We present in Fig. 4.4 the arrival times empirical distribution which outlines how the particle flux at the flume outlet during ES1 behaved differently from a Markovian process. One can see that the particle waiting times τ (also called arrival times or arrival intervals) at the $\mathscr{S}_{OCW}$ cross-section followed a marked hyper-exponential distribution, whose density function reads as:

$$P_\tau(\tau) = \alpha_1 \Lambda_1 \exp(-\Lambda_1 \tau) + \alpha_2 \Lambda_2 \exp(-\Lambda_2 \tau). \tag{4.7}$$

We conducted a distribution fitting based on the experimental data collected during the first 600-s-long period of ES1 and we found $\Lambda_1 = 9.48$, $\Lambda_2 = 52.58$, $\alpha_1 = 0.0093$, and $\alpha_2 = 0.9907$ (which satisfy the condition $\alpha_1 + \alpha_2 = 1$). This type of distribution was already retrieved for the arrival times distribution at the outlet cross-section during the P experiment (see Chapter
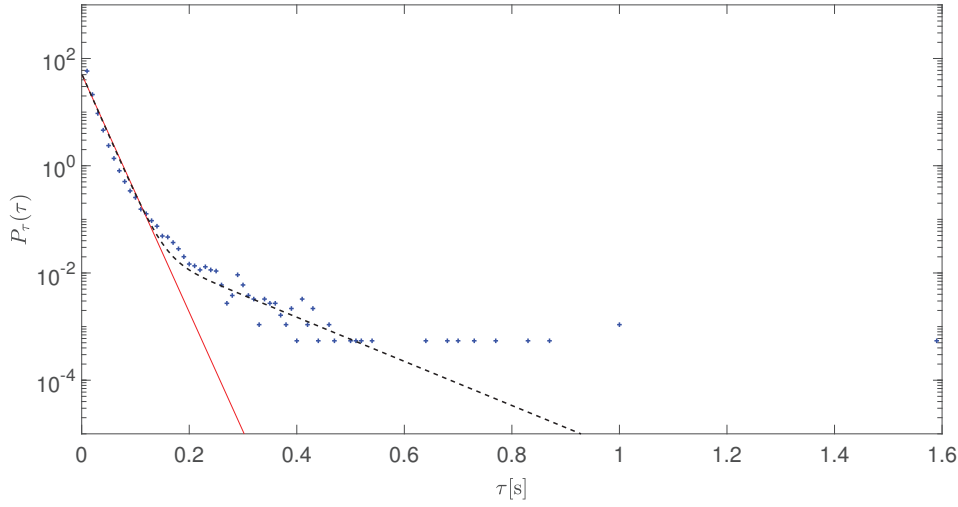
Figure 4.4: Arrival times empirical distribution at the middle cross-section of OCW ($\mathscr{S}_{OCW}$) during ES1 (blue crosses). The exponential and hyper-exponential distributions fitted on the experimental data are indicated by a solid red line and a dashed black line, respectively.

2, Ancey and Pascal, 2020) and it likely represents a typical consequence of the antidune migration process upstream of the outlet control section on the particle flux.
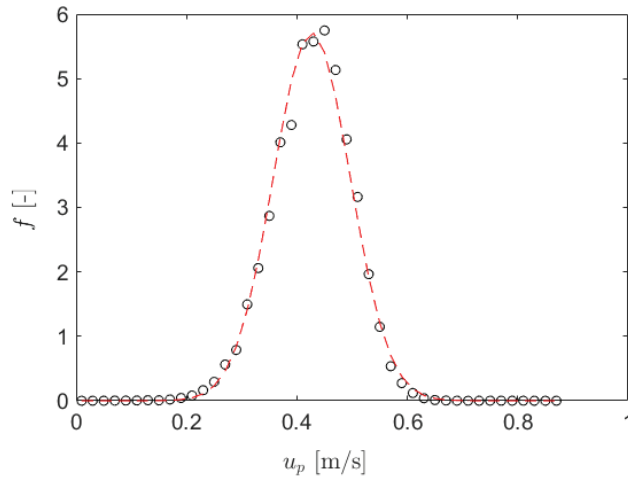
Figure 4.5: Empirical probability density function of the particle velocity u_p during ES1. The dashed red line indicate the Gaussian distribution fitted on the u_p data.

Figure 4.5, Fig. 4.6 and Fig. 4.7 show the observed probability density functions of particle velocity u_p, number of moving particles N in the control window, and particle crossings $\overline{\Phi}_s(t \mid \delta t)$ (for $\delta t = 0.01$) at the control cross-section. Curves corresponding to fitted theoretical
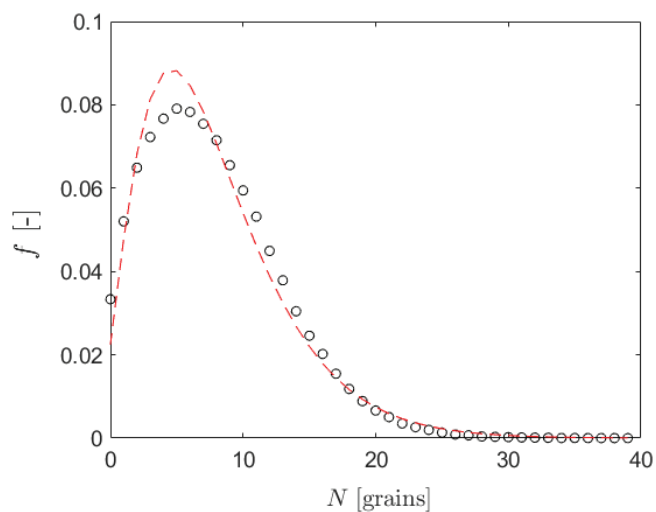
Figure 4.6: Empirical probability density function of the number of moving particles N in the control window during ES1. The dashed red line indicate the Negative Binomial distribution fitted on the N data.
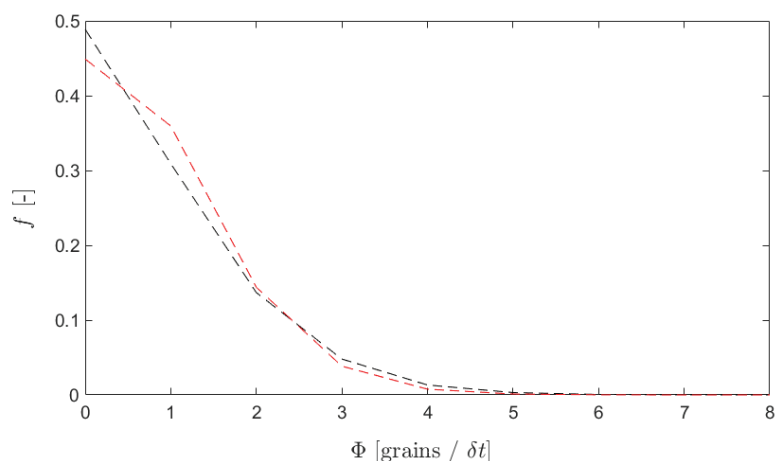
Figure 4.7: Empirical probability density function of the particle crossings $\overline{\Phi}_s(t \mid \delta t)$ (for $\delta t = 0.01$ s) at the control cross-section during ES1. The dashed red line indicate the Poisson distribution fitted on the $\overline{\Phi}_s(t \mid \delta t)$ data.

distributions (Gaussian, Negative Binomial, and Poisson distribution, respectively) were also displayed for comparison. The information summarised in Fig. 4.5, Fig. 4.6 and Fig. 4.7 was also useful for the application to the ES1 case of the protocol for estimating mean bedload transport rates and their variance (Section 4.3.1).

Chapter 4. On antidune trains and bedload pulses under steady- and quasi-steady-state conditions

ES1: Fluctuations in q_s and comparisons with runs in similar conditions

We compared the ES1 bedload transport data also with those collected during the E1 run (Pascal et al., 2021). This comparison was only possible in terms of volume-averaged transport rates q_s because during E1, E2, E3 and E4 the bedload transport monitoring was not based on particle tracking, thus it was not possible to compute $\overline{\Phi}_s(t)$ data. In agreement with the ES1 experiment design, the mean bedload transport rate was close to the one imposed for the E1 run by Pascal et al. (2021) ($\overline{q}_{s,E1} = 2 \cdot 10^{-5}$ m^2 s^{-1}, see Chap. 3). Since a supplementary run named ES2 ($\psi_{s,ES2} = 3°$ and $\overline{q}_{s,ES2} = 1.85 \cdot 10^{-5}$ m^2 s^{-1}) was conducted to test the reproducibility in the longer flume of the E1 run ($\psi \approx 3°$), we took advantage of the ES2 q_s dataset (measured at the flume outlet) and we included elaborations related to it in the next figures to give a more complete perspective of the ES1 results. It is important to recall here that the bedload transport monitoring technique and setup used during ES2 were exactly the same used for ES1.

In Fig. 4.8 one can observe that the overall behaviour of q_s fluctuations was qualitatively similar for ES1 and E1. At the sub-second time scale, the q_s series during ES1 was apparently characterised by a slightly higher frequency of intense and weak (or null) bedload transport occurrences than the E1 series (Fig. 4.8 and Fig. 4.9). Some differences in the measurement and post-processing technique (and in the accuracy of the q_s data) as well as the small differences between the physical parameters of the runs could have contributed to that small discrepancy. Among the physical factors, the different flume length (2.5 m for E1 against 5.8 m for ES1), the different mean slope angle ($\overline{\psi}$ of approximately 2.9° for E1 against 2.6° for ES1), the slightly different median grains sizes ($d_{50} = 3$ mm for E1 against $d_{50} = 2.5$ mm for ES1), and the non-linear response to small differences in the mean bedload transport rate (the mean transport rate during ES1 was approximately 10% lower than the one measured during E1) might have played a role in these small differences observed for the bedload transport behaviour at relatively short time scales. Since the discrepancy between the occurrence frequency distributions was barely detectable, we could consider that the $q_s(t \mid \Delta t = 0.2\text{s})$ time series explored the same range of relative $q_s/\overline{q}_{s,\,Ei}$ values with nearly equivalent occurrence density during ES1 and E1.

For time scales longer than 1 s, the ES1 q_s series in Fig. 4.8 (a) exhibited a fluctuation pattern similar to that recorded during E1 (Fig.4.8 (b)) in which the bedload pulses appeared well-rhythmed from time to time but their periodicity and amplitude were not uniform. Such a similarity in the q_s fluctuation pattern at mid temporal scales could provide a clue of analogous antidune dynamics—at least in the vicinity of the flume outlet—during these steady-state runs characterised by very similar boundary conditions and mean transport rates. It is worth underlining that, considering two experiments under very similar forcing conditions but different system size (i.e. length), relatively large autogenic fluctuations (at the flume scale) were likely expected in the larger system (see Hwa and Kardar, 1992; Jerolmack and Paola, 2010). The q_s data suggest that antidunes near the flume outlet might have behaved in similar ways during most of the E1 and ES1 runs, despite a higher potential for large fluctuations
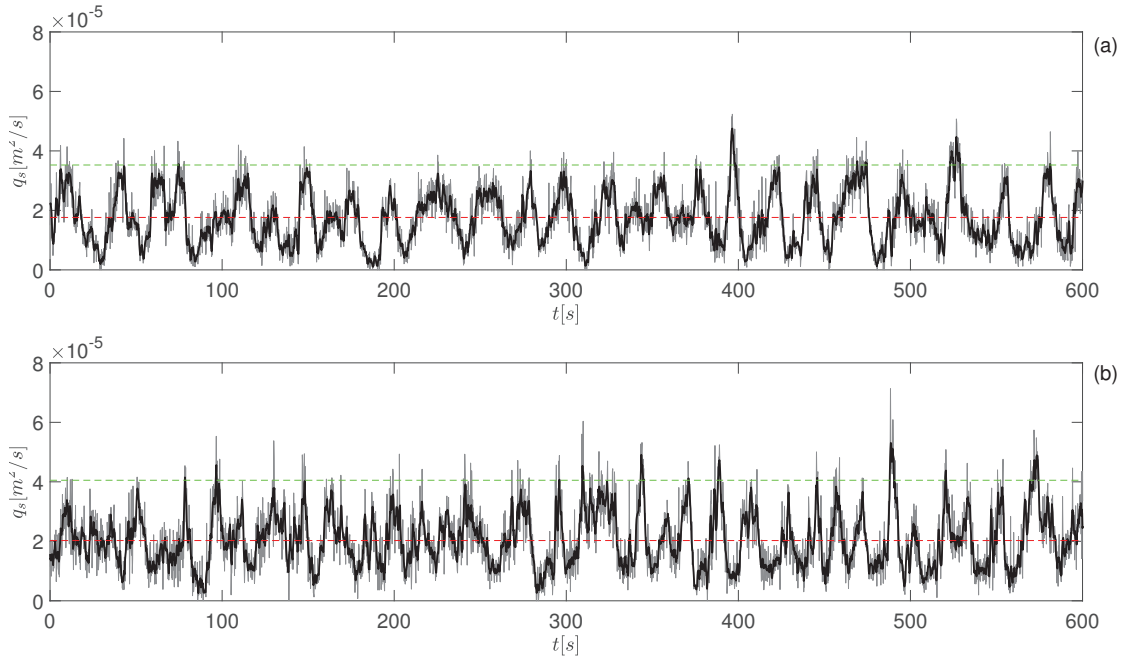
Figure 4.8: Example of q_s fluctuations during ES1 (a) and E1 (b). The grey lines indicate the 0.2-s time-averaged rates, whereas the black lines indicate the 1-s time-averaged rates. The dashed red lines indicate the mean bedload transport rate $\overline{q}_{s,Ei}$ (averaged over E_i run), whereas the dashed green lines indicate a constant rate of $2\overline{q}_{s,Ei}$.

of the ES1 system (5.8–m-long flume) compared to the E1 system. Perhaps, under bedload transport forcing as intense as those imposed during the runs ES1 and E1, the probability of observing bedload pulses generated by flume scale degradation events (as observed by Mettra, 2014) is so low that the duration of these experiments was not sufficient to observe a substantially different behaviour in the two systems.

As summarised later in this chapter (Section 4.3.1), we also investigated the presence, magnitude, typical frequency and temporal distribution of q_s pulses at the flume outlet by using wavelet transform analysis. This tool allowed us to efficiently access both overall and time-localised perspectives on the q_s fluctuations.

ES1: Uncertainty and convergence of time-averaged bedload transport rates towards the feeding rate

In the first part of this section we present an application to the ES1 data of the protocol described in Chapter 2 for estimating the uncertainty of bedload transport rates ($\overline{\Phi}_s(\Delta t \mid t)$ or $\overline{q}_s(\Delta t \mid t)$) computed from high-frequency data ($\delta t = 0.01$ s). The second part of the section is focused on the convergence of these time-averaged rates towards the run-averaged rate

113
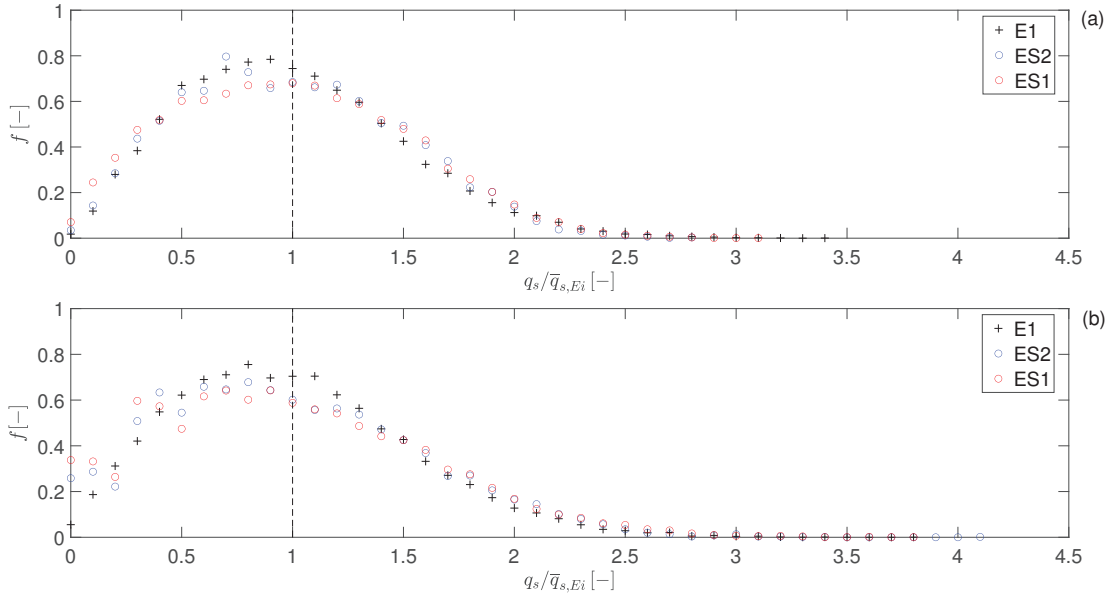
Figure 4.9: Empirical probability density functions of the normalised q_s rates for the experiments ES1, ES2 and E1. (a) Distributions for q_s data processed with 0.2-s time-averaging and 0.2-s subsampling. (b) Distributions for q_s data processed with 0.2-s subsampling only. The vertical dashed lines denote the $q_s/\overline{q}_{s,\,Ei}=1$ coordinate. The legends of the symbols for the frequencies associated with each dataset are specified in each sub-plot. Note: a single constant particle velocity U_p was considered for the E1 q_s series.

$(\overline{q}_{s,ES1} \simeq q_{s,in})$. In this section, we express the transport rates in terms of particle discharge (as [grains/s]) for the sake of clarity and coherence with the study presented in Chapter 2.

As one can see in Fig. 4.10, the bedload flux at the flume outlet during ES1 behaved as a steady-state process, since the cumulative amount of sediments collected in time $(V_{cum}(t)/V_p)$ followed relatively well a linear trend with constant slope. For the sake of simplicity and conciseness, we decided to present the application conducted on the $\overline{\Phi}_s(t)$ data only. The results of the application to the $q_s(t)$ data were qualitatively the same. Working with $\overline{\Phi}_s(t)$ samples was simpler in term of data manipulation (it was not necessary to re-sample the dataset for ensuring *iid* observations) and it also facilitated the computation of the theoretical approximations of mean and variance by using renewal theory. Using the renewal theory approach was required because the particle flux at the flume outlet did not behave as a Markovian process (see Section 4.3.1 and Fig. 4.4 arrival times). The analysis of the uncertainty dependence on the sampling duration was carried out for increasing Δt intervals going from 1 s up to 100 s. These Δt intervals were both large enough to ensure meaningfulness of the bootstrap application (for $\Delta t = 1$ s, $\Delta t/\delta t = 100$ observations) and small enough to neglect the influence of the dataset finite size on the analysis outcomes.
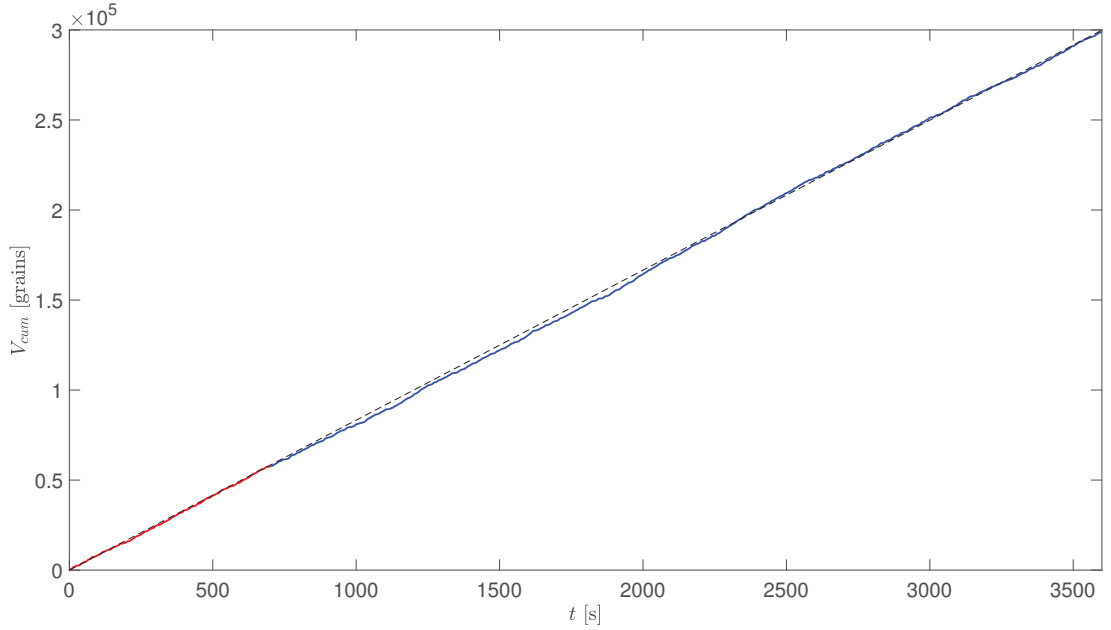
Figure 4.10: Trend of V_{cum} during ES1. The solid red line identifies the trend during the T_1 period whereas the solid blue line identifies the trend during T_2. The dashed black line indicates the linear trend with constant slope equal to $\overline{q}_{s,ES1} W$.

First of all, a reference time $t_{\mathrm{ref},i}$ was randomly chosen among the measurement times that were distant at least $(\Delta t)_{max} / (2\delta t) + 1$ steps from the initial and final observations of the $\overline{\Phi}_s(t)$ dataset corresponding to the ES1 duration. This choice was made to focus on the uncertainty of local $\overline{\Phi}_s(\Delta t \,|\, t)$ estimates (here 'local' should be interpreted in temporal sense). We then extracted one sample of duration Δt centred at $t_{\mathrm{ref},i}$ for each Δt value investigated. These samples represent the 'original samples' (one for each Δt). Each one of these samples contained $\Delta t / \delta t$ contiguous observations of $\overline{\Phi}_s(t)$ from the dataset of each period T_i. The subsequent steps were then conducted:

(a) Generation of $M = 100$ bootstrap samples (size $\Delta t / \delta t$) from each original sample corresponding to a Δt value;

(b) Computation of the $\overline{\Phi}_{s,m-boot}(\Delta t \,|\, t_{\mathrm{ref},i})$ rate associated to each bootstrap sample m;

(c) Computation of the double-averaged rate $\langle \overline{\Phi}_s \rangle_M(\Delta t \,|\, t_{\mathrm{ref},i})$ (ensemble-time mean) from the ensemble of M rates corresponding to each Δt;

(d) Computation of the variance of the M-sized ensemble of rates for each Δt.

Examples of results of this protocol application are displayed in Fig. 4.11 and Fig. 4.12 for cases in which the $\overline{\Phi}_s(\Delta t \,|\, t_{\mathrm{ref},i})$ rates for small sampling intervals Δt were significantly higher or lower than $\overline{q}_{s,ES1}$, respectively. As one can see, this Δt span (1–100 s) allowed us to
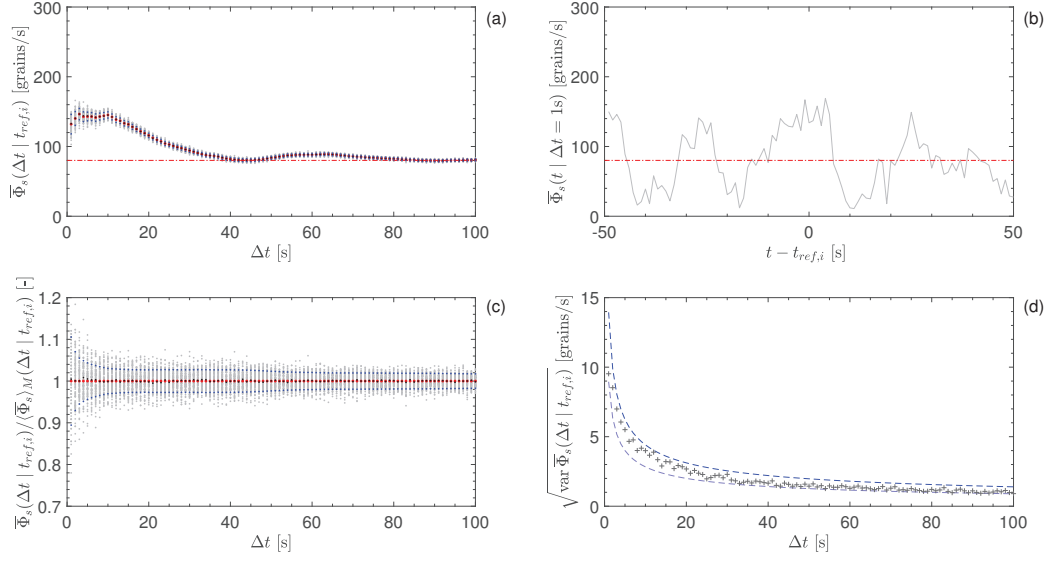
Figure 4.11: Results of the protocol application for $t_{\text{ref},i} = 470$ s with Δt intervals from 1 s up to 100 s. (a) Samples $\overline{\Phi}_{\text{s,m-boot}}(\Delta t \mid t_{\text{ref},i})$ from bootstrapping ($M = 100$) for each Δt value (grey dots), ensemble-time average $\langle\overline{\Phi}_s\rangle_M(\Delta t \mid t_{\text{ref},i})$ for each Δt value (red dots), values corresponding to $\langle\overline{\Phi}_s\rangle_M(\Delta t \mid t_{\text{ref},i}) \pm ((\text{var}\,\overline{\Phi}_s(\Delta t))_{Ren.Th.})^{0.5}$ (see Eq. B12) for each Δt value (blue dots), time-averaged rates $\overline{\Phi}_s(\Delta t \mid t_{\text{ref},i})$ from the original samples (black dots), run-averaged rate $\overline{q}_{s,\text{ES1}}$ (dash-dotted red line). (b) Series of $\overline{\Phi}_s(t \mid \Delta t = 1\text{s})$ rates for $t_{\text{ref},i} = 470$ s (grey line), run-averaged rate $\overline{q}_{s,\text{ES1}}$ (dash-dotted red line). (c) Normalised sample values $\overline{\Phi}_{\text{s,m-boot}}(\Delta t \mid t_{\text{ref},i})/\langle\overline{\Phi}_s\rangle_M(\Delta t \mid t_{\text{ref},i})$ for each Δt value (grey dots), values corresponding to $(\langle\overline{\Phi}_s\rangle_M(\Delta t \mid t_{\text{ref},i}) \pm ((\text{var}\,\overline{\Phi}_s(\Delta t))_{Ren.Th.})^{0.5}/\langle\overline{\Phi}_s\rangle_M(\Delta t \mid t_{\text{ref},i})$ (see Eq. B12) (blue dots), normalised time-averaged rates $\overline{\Phi}_s(\Delta t \mid t_{\text{ref},i})/\langle\overline{\Phi}_s\rangle_M(\Delta t \mid t_{\text{ref},i})$ from the original samples (black dots). The red dots identify the normalised ensemble-time averages $\langle\overline{\Phi}_s\rangle_M(\Delta t \mid t_{\text{ref},i})/\langle\overline{\Phi}_s\rangle_M(\Delta t \mid t_{\text{ref},i}) = 1$ (for definition) for each Δt value. (d) Empirical standard deviation values $(\text{var}\,\overline{\Phi}_s(\Delta t \mid t_{\text{ref},i}))^{0.5}$ (black crosses), theoretical trend $(\text{var}(S/\Delta t))^{0.5}$ from Eq. B12 (dashed blue line), theoretical trend in case of Markovian process for the standard deviation $(\Lambda_{s,\text{ES1}}/\Delta t)^{0.5}$ from Ancey and Pascal (2020) (dashed purple line).

investigate a relatively wide uncertainty range for the ES1 case—corresponding to standard deviation values from 14 grains/s down to less than 2 grains/s. This uncertainty (that we could call 'Δt-intrinsic') may be interpreted as the dispersion of the measured rates around the actual time-localised mean bedload transport rate. Its trend for increasing Δt values was well described by Eq. 4.8, which is based on the application of renewal theory (see Appendix B in Ancey and Pascal, 2020).

$$\text{var}\,\overline{\Phi}_s(\Delta t \mid t) = \text{var}\left(\frac{S}{\Delta t}\right) = \left(\frac{\text{var}\,N_\Phi}{\overline{\tau}} + \frac{(\mathbf{E}(N_\Phi))^2\sigma_\tau^2}{\overline{\tau}^3}\right)\frac{1}{\Delta t}, \tag{4.8}$$

where S is the sum of particles that have crossed the control surface from time $t - 0.5\Delta t$ up
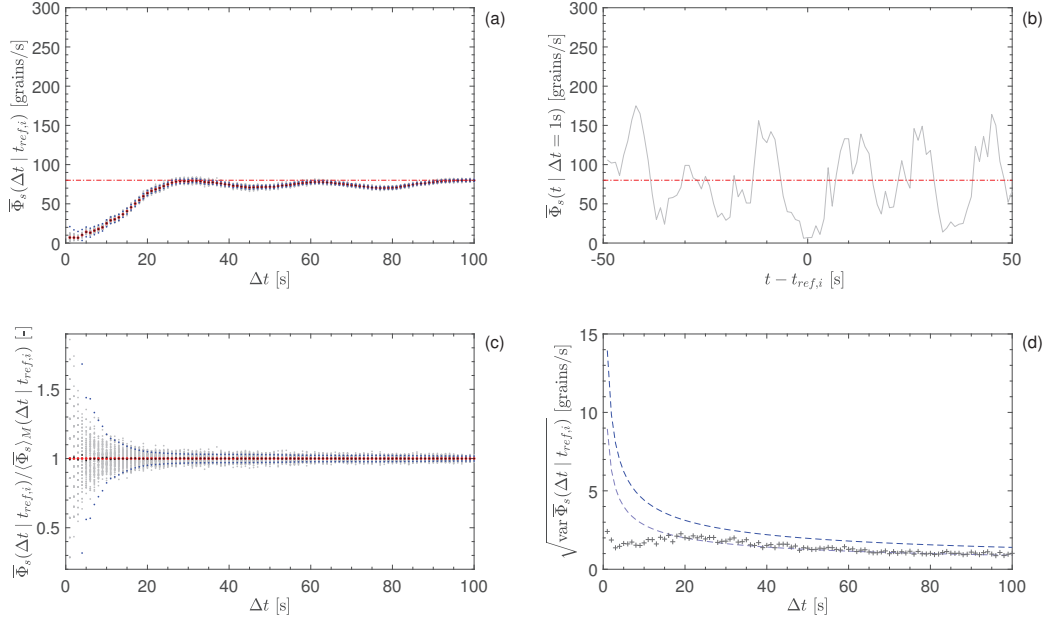
Figure 4.12: Results of the protocol application for $t_{\text{ref},i} = 2210$ s with Δt intervals from 1 s up to 100 s. (a) Samples $\overline{\Phi}_{\text{s,m-boot}}(\Delta t \mid t_{\text{ref},i})$ from bootstrapping ($M = 100$) for each Δt value (grey dots), ensemble-time average $\langle\overline{\Phi}_s\rangle_M(\Delta t \mid t_{\text{ref},i})$ for each Δt value (red dots), values corresponding to $\langle\overline{\Phi}_s\rangle_M(\Delta t \mid t_{\text{ref},i}) \pm ((\text{var}\,\overline{\Phi}_s(\Delta t))_{Ren.Th.})^{0.5}$ (see Eq. B12) for each Δt value (blue dots), time-averaged rates $\overline{\Phi}_{\text{s}}(\Delta t \mid t_{\text{ref},i})$ from the original samples (black dots), run-averaged rate $\overline{q}_{\text{s,ES1}}$ (dash-dotted red line). (b) Series of $\overline{\Phi}_s(t \mid \Delta t = 1\text{s})$ rates for $t_{\text{ref},i} = 2210$ s (grey line), run-averaged rate $\overline{q}_{\text{s,ES1}}$ (dash-dotted red line). (c) Normalised sample values $\overline{\Phi}_{\text{s,m-boot}}(\Delta t \mid t_{\text{ref},i})/\langle\overline{\Phi}_s\rangle_M(\Delta t \mid t_{\text{ref},i})$ for each Δt value (grey dots), values corresponding to $(\langle\overline{\Phi}_s\rangle_M(\Delta t \mid t_{\text{ref},i}) \pm ((\text{var}\,\overline{\Phi}_s(\Delta t))_{Ren.Th.})^{0.5}/\langle\overline{\Phi}_s\rangle_M(\Delta t \mid t_{\text{ref},i})$ (see Eq. B12) (blue dots), normalised time-averaged rates $\overline{\Phi}_{\text{s}}(\Delta t \mid t_{\text{ref},i})/\langle\overline{\Phi}_s\rangle_M(\Delta t \mid t_{\text{ref},i})$ from the original samples (black dots). The red dots identify the normalised ensemble-time averages $\langle\overline{\Phi}_s\rangle_M(\Delta t \mid t_{\text{ref},i})/\langle\overline{\Phi}_s\rangle_M(\Delta t \mid t_{\text{ref},i}) = 1$ (for definition) for each Δt value. (d) Empirical standard deviation values $(\text{var}\,\overline{\Phi}_s(\Delta t \mid t_{\text{ref},i}))^{0.5}$ (black crosses), theoretical trend $(\text{var}\,(S/\Delta t))^{0.5}$ from Eq. B12 (dashed blue line), theoretical trend in case of Markovian process for the standard deviation $(\Lambda_{\text{s,ES1}}/\Delta t)^{0.5}$ from Ancey and Pascal (2020) (dashed purple line).

to $t + 0.5\Delta t$, τ is the waiting time (mean value $\overline{\tau}$, see also Fig. 4.4 and Eq. 4.7), and N_Φ is the number of particles which have crossed the control surface during a given arrival event (i.e. a 'jump') whose distribution can be retrieved by the empirical distribution of the particle crossings (Fig. 4.7). It is worth recalling that Eq. 4.8 (Eq. B12 in Ancey and Pascal, 2020) is an approximated asymptotic relationship, which is expected to hold for long Δt intervals. Despite being an approximated expression, Eq. 4.8 proved suitable for a conservative assessment of the variance of $\overline{\Phi}_{\text{s}}(\Delta t \mid t_{\text{ref},i})$ rates for monitoring purposes (Fig. 4.11 and Fig. 4.12). The trend of the empirical standard deviation values was occasionally notably lower than the Eq. B12 trend, especially for small Δt values (see Fig. 4.12). This overestimation occurred when the particle

flux was low in the few seconds before and after $t_{\text{ref,i}}$. For instance, in the case presented in Fig. 4.12, the empirical standard deviation for $\Delta t = 5$ s was about 2 grains/s that corresponded to an actual relative uncertainty around 13% for the estimate $\langle \overline{\Phi}_s \rangle (\Delta t = 5\text{s} \mid t_{\text{ref},i} = 2010\text{s}) \simeq$ 15 grains/s. In the specific case, the variance predicted by Eq. 4.8 corresponded to a relative uncertainty around 40%.

The second aspect that we studied after the protocol application was the convergence of the time-averaged rates (already affected by their Δt-intrinsic uncertainty) towards the run-averaged rate. This uncertainty on the $\overline{\Phi}_s$ estimates of the run-averaged rate ($\overline{q}_{s,\text{ES1}} \simeq q_{s,in}$) was explored by computing $\overline{\Phi}_s(\Delta t, t_{samp,r})$ time-averaged rates from samples centred at times $t_{samp,r}$. The selected times $t_{samp,r}$ were equispaced of 10 seconds from $t = 180$ s up to $t = 3420$ s. This time grid was chosen to homogeneously cover the ES1 time span and to ensure that we could investigate the convergence up to Δt values of 360 s (i.e. 6 minutes) with relatively low influence of the ES1 time-series edges. Assessing the behaviour for Δt values up to 360 s appeared necessary, as the convergence of $\overline{\Phi}_s(\Delta t, t_{samp,r})$ towards the run-averaged rate ($\overline{q}_{s,\text{ES1}} \simeq q_{s,in}$) was expected to be slower than the decay in the Δt-intrinsic uncertainty (described by Eq. B12).

Considering the plot of the cumulative amount of sediments during ES1 ($V_{cum}(t)/V_p$) in Fig. 4.10, the first 700–s-long period of the run stands out as the interval during which the bedload transport was the closest to the linear trend of slope $\Lambda_{s,\text{ES1}}$. Despite a less linear behaviour, also the following part of the $\overline{\Phi}_s(t)$ series for ES1 can be approximately considered as the result of a stationary process. Therefore, one can identify a T_1 period (from $t = 0$ s to $t = 700$ s) and a T_2 period (from $t = 700$ s up to $t = 3600$ s) in ES1. In order to assess whether the little deviations from the steady trend (those occurred during T_2) significantly affected the rate convergence, we paid particular attention to distinguishing the $\overline{\Phi}_s(\Delta t, t_{samp,r})$ rates whose sampling interval (centred at $t_{samp,r}$) completely belonged to T_1 or T_2 in the next figures.

We studied the progressive convergence of $\overline{\Phi}_s(\Delta t, t_{samp,r})$ towards the run-averaged rate ($\overline{q}_{s,\text{ES1}} \simeq q_{s,in}$), which can be estimated as $\overline{\Phi}_s(\Delta t = 3600\text{s}, t_{\text{ref},i} = 1800\text{s})$. By analysing the dispersion of the $\overline{\Phi}_s(\Delta t, t_{samp,r})$ rates around $\overline{q}_{s,\text{ES1}}$ for increasing Δt (Fig. 4.13) and various sampling times $t_{samp,r}$, we had confirmation that approximating $\overline{q}_{s,\text{ES1}}$ within a certain error range required a Δt interval notably longer than the one required just to ensure a relatively similar accuracy on the estimation of the time-localised mean bedload transport rate. For instance, measuring $\overline{\Phi}_s(t \mid \Delta t)$ rates with $\Delta t = 45$ s was required to obtain an intrinsic accuracy under ± 2 grains/s (which would have meant a typical error around ± 5 % for a hypothetical local rate $\overline{\Phi}_s(t \mid \Delta t) \simeq 40$ grains/s) but sampling over intervals Δt as long as 240 s was required to approximate $\overline{q}_{s,\text{ES1}}$ within the $\pm 15\%$ deviation range. We also found that the convergent behaviour of $\overline{\Phi}_s(\Delta t, t_{samp,r})$ resulted different when the Δt-wide interval centred at $t_{samp,r}$ fell completely within T_1 (see red dots in Fig. 4.13). Since the bedload transport rate was the most steady during T_1, sampling $\overline{\Phi}_s(t \mid \Delta t)$ rates with interval $\Delta t = 90$ s during this period was sufficient to achieve $\overline{q}_{s,\text{ES1}}$ estimates within the $\pm 15\%$ deviation range ($\Delta t \geq 150$ s was
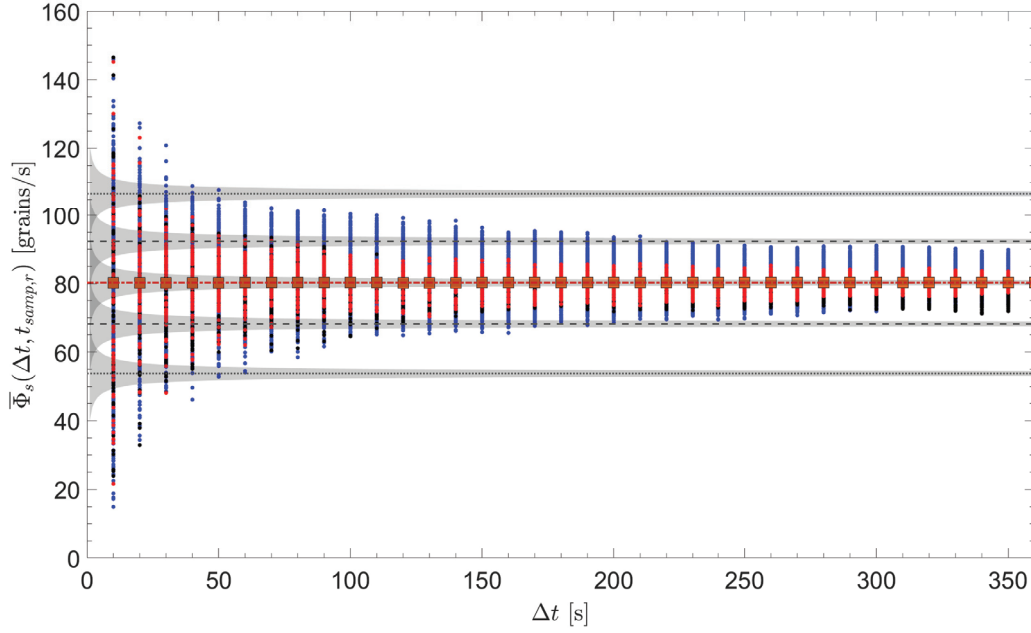
Figure 4.13: Series of $\overline{\Phi}_s(\Delta t, t_{samp,r})$ rates (dots) computed from the ES1 $\Phi_s(t)$ dataset for Δt-wide samples centred at times $t_{samp,r}$. The selected times $t_{samp,r}$ were equispaced of 10 seconds from $t = 180$ s up to $t = 3420$ s. The red dots identify time-averaged rates whose sampling interval (centred at $t_{samp,r}$) completely belonged to T_1, the blue dots indicate rates computed from samples which were collected during T_2, whereas the black dots identify rates computed from samples which partially belonged to both T_1 and T_2 datasets. The orange squares indicate $\langle\overline{\Phi}_s\rangle_R(\Delta t)$ double-averaged rates. The horizontal dash-dotted red line denotes the run-averaged rate $\overline{\Phi}_{s,ES1} = 80$ grains/s. The dashed black lines indicate the constant rates $1.15\overline{\Phi}_{s,ES1}$ and $0.85\overline{\Phi}_{s,ES1}$ corresponding to the $\pm15\%$ deviation range. The dashed black lines indicate the constant rates $1.33\overline{\Phi}_{s,ES1}$ and $0.67\overline{\Phi}_{s,ES1}$ corresponding to the $\pm33\%$ deviation range. The grey shaded areas identify the standard deviation limits associated to the Δt-intrinsic uncertainty (described by Eq. B12) around the constant rates indicated by the dashed and the dotted lines.

required for $\pm10\%$ estimate error). These findings suggest that non-uniform sequences of bedload pulses (in terms of amplitude and period)—likely associated to antidunes that exhibited notably different migration periods near the flume outlet (see Sec. 4.3.1)—played a significant role in the convergence of $\overline{\Phi}_s(\Delta t, t_{samp,r})$ rates during ES1. The bedload transport rate fluctuations observed during T_1 were probably associated to antidune trains composed of bedforms with relatively similar migration period near the flume outlet. Remarkably, the overall time-averaged rate $\overline{\Phi}_s(\Delta t = 3600$ s, $t_{ref,i} = 1800$ s) matched the trend of the ensemble-time-averaged $\langle\overline{\Phi}_s\rangle_R(\Delta t)$ rates (see in Fig. 4.13). This might seem a trivial equivalence but it was tightly related to the overall steadiness of the ES1 run. For instance, this was not the case with the run time-averaged rate ($\Delta t = 1200$ s) computed for the P experiment presented in Chapter 2.

Looking at figure Fig. 4.13, one can see that in order to obtain $\overline{\Phi}_s(t \mid \Delta t)$ estimates of the run-averaged bedload transport rate (or feeding rate) within the ±33% deviation range we should sample with $\Delta t \gtrsim 55$ s (an interval sufficient for achieving estimates close to the 20% deviation range during T_1). Remarkably, this time scale is approximately equal to $3T_{AD,fast}$ (where $T_{AD,fast}$ is the typical migration period expected for antidunes with $\lambda \gtrsim \lambda_{R09}$ according to Pascal et al. (2021)) and the scatter of the $\overline{\Phi}_s(t \mid \Delta t)$ rates around the run average displayed a marked narrowing for Δt approaching this time scale.

We may speculate that the $T_{AD,fast}$ estimate could represent the base of a semi-empirical criterion for determining the most suitable bedload sampling interval depending on the expected antidune dynamics. For instance, sampling bedload fluxes with intervals $\Delta t \gtrsim k_T T_{AD,fast}$ (with $k_T \gtrsim 3$) during ES1 could ensure $\overline{\Phi}_s$ estimates of the run-averaged rate within (or close) to the ±33% deviation range. This hypothetical criterion proved to approximately hold also for the datasets of the experiments E1–E4 (see Supporting Information C4 - S2). Therefore, it might be valid in presence of upstream migrating antidunes similar to those studied in this research work (i.e. low-amplitude antidunes and definitely supercritical flow conditions) under moderate bedload transport rates ($\overline{q}_s \gtrsim \overline{q}_{s,ES1}$).

However, linking the convergence behaviour of the $\overline{\Phi}_s(\Delta t, t_{samp,r})$ rates to a single timescale $k_T T_{AD,fast}$ might be an oversimplification. The potential shortcomings of such a criterion lie in the sporadic occurrence of time-localised bedload transport episodes (e.g. large bedload bursts, prolonged phases of weak transport), which can significantly affect the convergence of the $\overline{\Phi}_s(\Delta t, t_{samp,r})$ rates. These episodes are more probable when the antidune pattern is affected by non-uniformities in the close vicinity of the measurement cross-section (see Section 4.3.1) or when the trend of the cumulated sediment load at the control section deviates significantly from the steady-state (e.g. during the T_2 period). For instance, the criterion presented above is generally not expected to hold in cases characterised by weak and intermittent bedload transport (e.g. P run presented in Chapter 2) in which antidune dynamics may often deviate from the behaviour observed during the ES1 and E1–E4 experiments—in particular, close to bed discontinuities, where non-uniformities in the antidune sequences are more likely to appear (see outcomes presented in Section 4.3.1). In confirmation of this complexity, the longest migration periods $T_{AD,slow}$ observed in the 2D-FFT spectra for the slow-migrating shortest antidunes during E1, E2, E3 and E4 were longer for runs characterised by lower mean bedload transport rates (Pascal et al., 2021) but they did not seem to scale with the $T_{AD,fast}$ time scales in a straightforward manner.

ES1: Testing the q_s estimation framework based on the spectral analysis of the antidune pattern

In Chapter 3, we could test the $\overline{q}_s$ estimation framework based on the $c_N^* \approx f(\lambda_N^*)$ on a literature case in which $\{c, \lambda\}$ associated pairs were available (run *2deg15v*, Mettra, 2014).

In this section we present a performance assessment of Eq. (3.17) conducted on the ES1

data. For an unbiased test of the method we decided to first apply it to the 2D-FFT spectra computed considering the topographic datasets collected for TCW1 and TCW2 during the entire ES1 run. For the TCW2 window, we decided to analyse the data from the upstream edge ($x_a = x_{ups,TCW2} = 4.06$ m) to 50 cm upstream of the downstream edge $x_b = x_{dws,TCW2} - 0.50 = 5.30$ m in order to avoid including eventual non-uniformities in the vicinity of the flume outlet. According to this idea, we computed the $\lambda - c$ FFT spectra for the Z_{TCW1} ($[x_a = 0.66$ m $x_b = 2.18$ m], $[t_a = 0$ s $t_b = 3600$ s]) and the Z_{TCW2*} ($[x_a = 4.06$ m $x_b = 5.30$ m], $[t_a = 0$ s $t_b = 3600$ s]) matrices (Fig. 4.14 (a) and (b)).
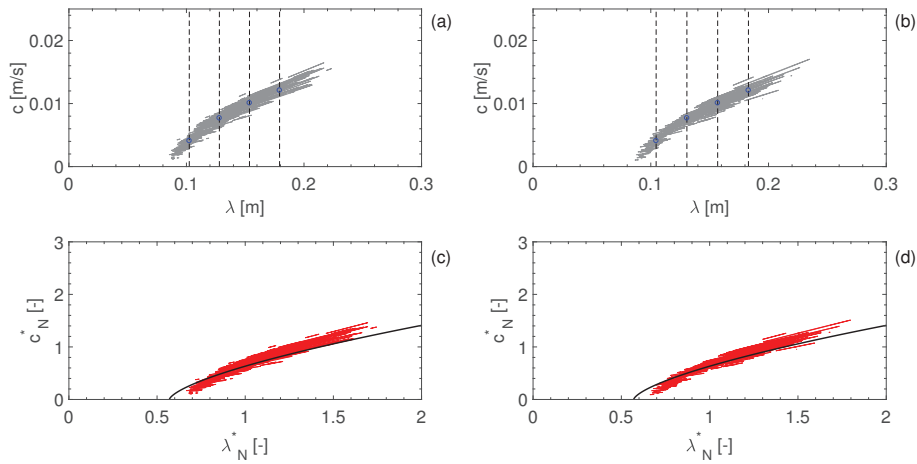
Figure 4.14: Sub-plots (a) and (b) contain the $\lambda - c$ spectra computed for Z_{TCW1} and Z_{TCW2*}, respectively (entire duration of ES1). The vertical dashed lines identify the λ coordinates corresponding to $[0.8, 1, 1.2, 1.4]\lambda_{R09}$. The blue circles indicate the $\{\lambda, c\}$ pairs (Tab. 4.3) used to compute the $\overline{q}_{s,est}$ values reported in Tab. 4.4. Sub-plots (c) and (d) contain the $\lambda_N^* - c_N^*$ dimensionless spectra computed for Z_{TCW1} and Z_{TCW2*}, respectively, considering the run-averaged transport rate $\overline{q}_{s,ES1}$. The solid black line in both (c) and (d) indicates the dimensionless trend $c_N^* \approx f(\lambda_N^*)$ found by Pascal et al. (2021).

As recommended by Pascal et al. (2021) (Chapter 3), we estimated $\overline{q}_{s,est}$ using multiple $\{\lambda, c\}$ pairs in order to detect possible irregularities (the trend is expected to follow $c_N^* \propto (\lambda_N^*)^{2/3}$) and thus to have a confirmation of the framework reliability for the case under examination. Therefore, we extracted the celerity values $c_{test,TCWj}$ corresponding to $\lambda = [0.8, 1, 1.2, 1.4]\lambda_{R09}$ from the spectrum calculated for each control window TCWj.

The formula used for the estimation (Eq. presented in Chapter 3) reads:

$$\overline{q}_{s,est} = c \, d_{V,50} \, (1-p) \, f_q(\lambda_N^*) = c \, d_{V,50} \, (1-p) \left[\frac{0.9}{\left(\lambda_N^* - 0.57\right)^{2/3}} \right]. \tag{4.9}$$

The physical parameters considered for the estimation are reported in Table 4.3 for each control window. We summarised the selected pairs $\{\lambda, c\}$ and the corresponding $\overline{q}_{s,est}$ estimates in Table 4.4.

CW	$\overline{\psi}$ [°]	$d_{50} \simeq d_{V,50}$ [m]	λ_{R09} [m]	Fr [-]	Θ [-]	Θ_c [-]	c [mm s^{-1}]	λ [m]
TCW1	2.6	0.0025	0.128	1.40	0.103	0.064	4.1	0.102
							7.7	0.128
							10.1	0.154
							12.1	0.179
TCW2	2.7	0.0025	0.131	1.43	0.108	0.065 [-]	4	0.105
							7.5	0.131
							10	0.157
							12	0.183

Table 4.3: Parameters considered for the estimation of $\overline{q}_{s,ES1}$ based on Eq.4.9. Slope-dependent parameters computed considering the run-averaged slope angle value in each control window. Pairs c, λ extracted from Fig. 4.14 (a) and (b).

CW	$\overline{q}_{s,ES1}$ [m^2 s^{-1}]	c [mm s^{-1}]	λ [m]	$\overline{q}_{s,est}$ [m^2 s^{-1}]	$(\overline{q}_{s,est} - \overline{q}_{s,ES1}) / \overline{q}_{s,ES1}$ [%]
TCW1	$1.77 \cdot 10^{-5}$	4.1	0.102	$1.54 \cdot 10^{-5}$	-13
		7.7	0.128	$1.91 \cdot 10^{-5}$	+8
		10.1	0.154	$1.94 \cdot 10^{-5}$	+9.5
		12.1	0.179	$1.94 \cdot 10^{-5}$	+9.5
TCW2	$1.77 \cdot 10^{-5}$	4	0.105	$1.51 \cdot 10^{-5}$	-15
		7.5	0.131	$1.86 \cdot 10^{-5}$	+5
		10	0.157	$1.92 \cdot 10^{-5}$	+8.5
		12	0.183	$1.92 \cdot 10^{-5}$	+8.5

Table 4.4: Results of the $\overline{q}_{s,ES1}$ estimation based on the $\lambda - c$ spectra and on Eq.4.9.

Considering the two intermediate $\overline{q}_{s,estES1}$ values for each control window one can realise that this framework provided consistent estimates affected by a relatively small but systematic overestimation—which means that antidunes with $\lambda \geq \lambda_{R09}$ migrated slightly faster than predicted by the dimensionless relationship. Such relative errors (in the 5–10 % range) might be acceptable or not depending on the purpose of the bedload transport estimation.

The two $\lambda - c$ FFT spectra computed for TCW1 and TCW2 (ES1) provided useful information also regarding the variability of the antidune morphodynamics. In Fig. 4.14 (c) and (d) one can see that the shortest antidunes during ES1 (minimum $\lambda \simeq 0.7\lambda_{R09} \simeq 9$ cm) were longer than the shortest antidunes observed during E1 ($\lambda \simeq 0.6\lambda_{R09} \simeq 6$ cm, Pascal et al. (2021)) and exhibited migration celerity values slightly lower than those predicted for similar λ_N^* values by Pascal et al. (2021) (see Eq. 3.16). The experimental conditions during ES1 and E1 were very

similar and the flume length did likely not play a major role on this difference. Interestingly, the sediments used for ES1 were similar in size to those used during E1 ($d_{50} = 2.5$ mm against $d_{50} = 2.9$ mm) but they were more rounded on average (as deductible by $d_{50} = d_{V,50} = 2.5$ mm for the ES1 case). These observations might suggest a non-negligible influence of the grain-grain interactions (reflected for instance by the sediment mixture stability angle) on the antidune slope stability, an aspect already explored by Mettra (2014) and whose effects on the antidune shape and celerity would deserve further investigation. Recking et al. (2009) took into account the dependence of Θ_c on the slope angle $\overline{\psi}$ for the dimensional analysis that resulted in the λ_{R09} relationship but the possible influence of the sediment stability angle was not included.

The difference between $\lambda_{R09,TCW1} = 0.128$ m and $\lambda_{R09,TCW2} = 0.131$ m was very small and depended on the slight differences in the local $\overline{\psi}$ values measured in TCW1 and TCW2. This difference should be considered as barely significant given that the measurement of these ψ angles is affected by the uncertainty in the vertical alignment of the cameras ($\approx 0.1°$) We did not observe any significant increase in the antidune wavelength between the portion of TCW2 considered and the TCW1 sector during ES1. This outcome is in contradiction with the numerical results by Bohorquez and Ancey (2016). The simulation conducted by Bohorquez and Ancey (2016) considered a case with $W = 0.08$ m and characterised by a mean bedload transport rate $\overline{q}_{s,B16} \simeq 6\overline{q}_{s,ES1}$, which corresponded to a dimensionless rate $\overline{\varphi}_{s,B16} \simeq 1.7\overline{\varphi}_{s,ES1}$ and to a particle flux $\overline{q}_{s,B16} = 86$ part. s^{-1}. If any 'coarsening mechanism' affected the bedforms during ES1 its effects on the antidune wavelength were probably damped by some counterbalancing process.

ES1: Insights on the antidune pattern non-uniformities from wavelet analysis

Monitoring the bed topography in the vicinity of the flume outlet (TCW2) during the ES1 experiment allowed us to capture in the detail the antidune growth and migration near the outlet discontinuity. As mentioned at the end of the previous section, we did not observe a systematic change in the antidune wavelength between the upstream sector of TCW2 (from $x_a = 4.06$m to $x_b = 5.30$m) and TCW1 (from $x_a = 0.66$m to $x_b = 2.18$m) for the ES1 case (Fig. 4.14 (a) and (b)). However, the sub-matrix Z_{TCW2*} considered to compute the FFT $\lambda - c$ spectrum presented in Fig. 4.14 (b) did not include the most downstream part of TCW2 because we were mostly focusing on the $\overline{q}_{s,ES1}$ estimation. Considering the entire TCW2 window was necessary to assess and quantify local non-uniformities in the antidune morphodynamics near the flume outlet discontinuity. Observing Fig. 4.15 is useful to understand how the bedforms typically behaved near the flume outlet. Interestingly, the incipient antidune located right upstream of the septum cyclically developed and migrated upstream—away from the discontinuity—in a process that may be often interpreted as an antidune splitting. This antidune 'detachment' process left behind (i.e. near the outlet discontinuity) a new incipient short antidune. The cycle intermittently repeated and antidunes of various λ detached and migrated upstream over time.
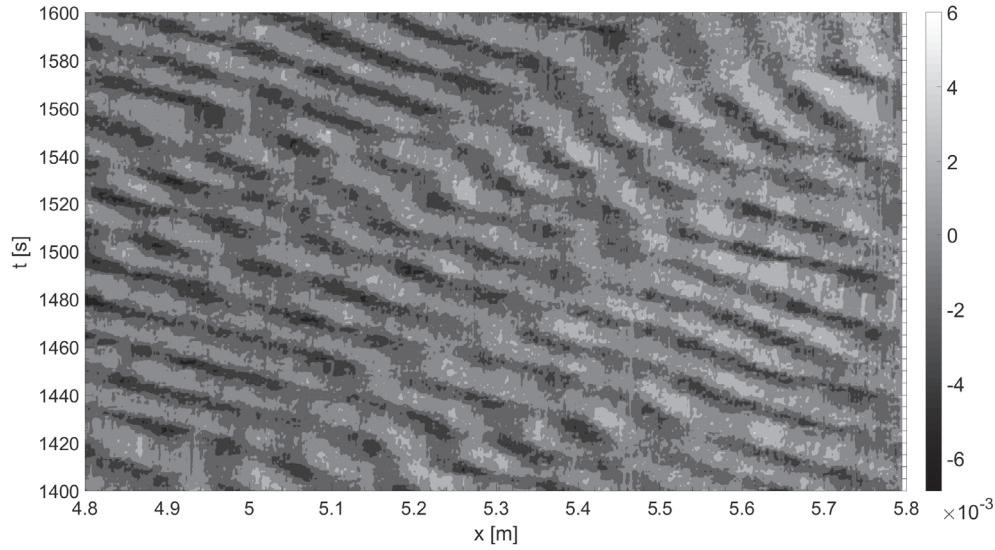
Figure 4.15: Contour plot of the bed elevation perturbation in TCW2 (from $x_a = 4.80$m to $x_b = 5.80$m and from $t_a = 1400$ s $t_b = 1600$ s). The colour bar refers to the z perturbation expressed as [m].

As already observed for the experiments presented by Pascal et al. (2021) (Chapter 3), down-stream travelling perturbations often affected the continuity of antidune trains in both control windows (see Fig. 4.16 for an example regarding TCW1). The disturbance of the antidune sequences introduced by the bed discontinuity at the flume outlet seemed to be dominant compared to that caused by downstream travelling perturbations (see Fig. 4.15). Visual anal-yses of the antidune patterns recorded during ES1 in both TCW1 and TCW2 confirmed that antidunes also experienced significant transient morphological changes during their up-stream migration without direct appearance of a discontinuity in the antidune sequence (e.g. a small temporary increase in the wavelength and/or amplitude of a single 'typical' antidune, which then recovered its former shape while the closest downstream antidune started to experience a similar transient evolution). However, these transient changes often triggered antidune merging and splitting events later and further downstream in the antidune train, which thus underwent a rearrangement or was divided by a consequent downstream travelling discontinuity.

Basically, we identified two families of antidune non-uniformities: (i) those related to the local bed discontinuity at the flume outlet, and (ii) those associated to antidune interactions and/or downstream travelling perturbations that locally affected the antidune morphology and occa-sionally interrupted the antidune sequences. To better characterise these non-uniformities in the antidune pattern we conducted a series of analyses based on wavelets transforms. Gen-eral indications regarding the mother wavelet considered, the Morlet, as well as the wavelet analysis tools employed in this study are available in the last part of the Methods section.
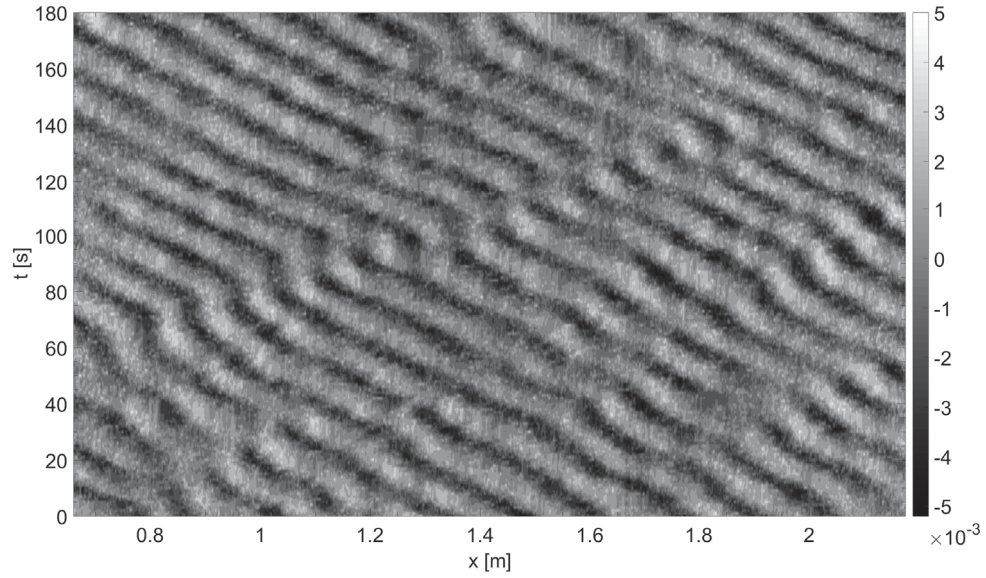
Figure 4.16: Contour plot of the bed elevation perturbation in TCW1 (entire control window from $t_a = 0$ s to $t_b = 180$ s). The colour bar refers to the z perturbation expressed as [m]. Well visible, a downstream travelling perturbation propagating from $x \approx 1.25$ m at $t \approx 100$ s.

Concerning the outlet-related non-uniformity, we qualitatively observed that the antidune wavelength in the first few decimetres upstream of the flume outlet varied noticeably (likely under the effect of the bed discontinuity) and that the antidunes approached a more uniform shape (with λ closer to λ_{R09}) as they travelled upstream. This local outlet-related variability was quantitatively confirmed by the analysis of the 1D wavelet spectra of the local perturbation $z(t \mid x_{fixed})$ computed for different locations x_{fixed} in TCW2 (Fig. 4.17). The spectrum computed for $z(x = 5.70\text{m}, t)$ displayed a wider bell shape and was richer than the other spectra in Fig. 4.17 for period values in the 20–30-s range. Since the estimate of the typical migration period for antidunes characterised by $\lambda \geq \lambda_{R09}$ was $T_{AD,\text{fast}} \approx 18$ s, this feature suggests a higher occurrence rate of slow-migrating antidunes close to the flume outlet.

Regarding the transient downstream travelling disturbances, we obtained useful information on their behaviour by analysing a series of CWT power scalograms of the bed profile for subsequent time steps. Essentially, we applied a Morlet wavelet transform over each spatial signal (e.g. the bed profile in TCW2 at time t) and we compared these scalograms (referred to subsequent times $t = 0$ s, 1 s, 2 s,...) to observe how the Fourier period of the signal (λ in this case) evolved in stream-wise direction and over time. Figure 4.18 shows a scalogram computed for the bed profile in TCW2 at time $t = 1970$ s.

Computing a series of averaged scalograms from n_S consecutive scalograms (see Fig. 4.19,
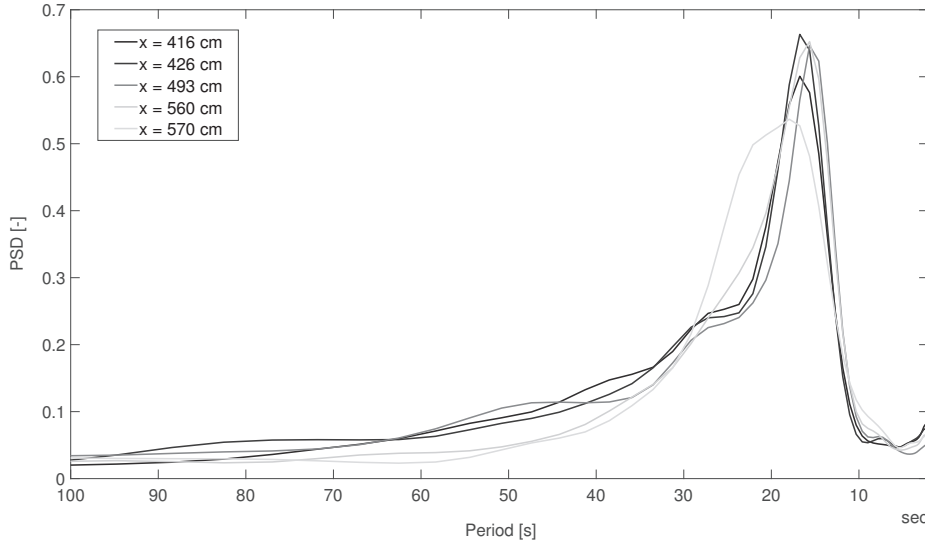
Figure 4.17: Wavelet spectra of the local perturbation $z(t \mid x_{fixed})$ computed for different cross-sections x_{fixed} in TCW2. The entire time series for ES1 were considered. Brighter grey shades indicate spectra computed for cross-sections located closer to the flume outlet.

with $n_S = 3$) made it possible to highlight the position and extent of the antidune trains and to better detect the discontinuities which bounded them. The averaged scalogram in Fig. 4.19 is part of the last frame of Movie V3, which includes the scalograms computed for TCW1 from $t = 106$ s to $t = 174$ s (see Movie V3: 10.5281/zenodo.6725988). By observing Movie V3 one can see that the longitudinal bed profiles were characterised by sectors with relatively high wavelet magnitude for values of Fourier period (λ) close to λ_{R09} and that the length and position of these sectors varied over time. These sectors represent trains composed by relatively similar antidunes, which migrated with the most constant celerity. The low-magnitude areas represent the more or less persistent disturbances that propagated downstream. Moreover, in a single scalogram, multiple peaks (or a wide peak) in the λ space for the same x coordinate mark the presence of antidunes with complex shapes, which likely anticipated (or resulted from) the occurrence of merging and splitting events. Although during ES1 antidunes often exhibited a shape with $\lambda \simeq \lambda_{R09}$ (and $\lambda > 0.5\lambda_{R09}$) and we did not observe a systematic increase or decrease in the antidune wavelength of the antidunes along their migration path. These figures highlight the complex ongoing interactions between adjacent antidunes within these sequences, as well as the extremely dynamic nature of these bedform systems (in a state which is commonly identified as steady).

ES1: Insights on $q_s(t)$ fluctuations from wavelet analysis

In this last part of the Results section dedicated to the ES1 run, we present preliminary outcomes of the CWT analysis conducted on the outlet q_s time series by using the Morlet
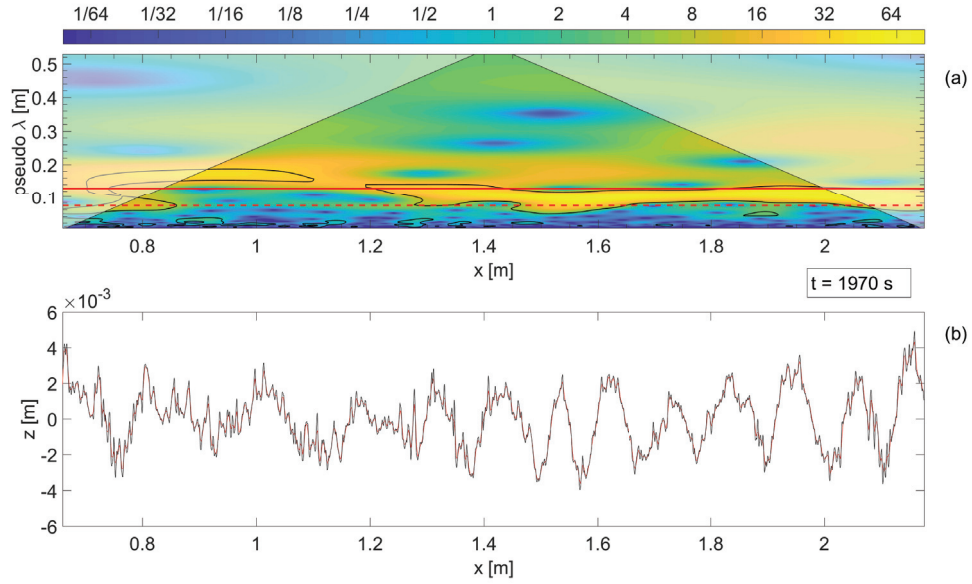
Figure 4.18: (a) Wavelet power scalogram of the $z(x, t_{fixed})$ perturbation computed for the entire TCW2 at time $t = 1970$ s. The thick solid red line indicates the constant wavelength coordinate corresponding to λ_{R09}. The dashed red line indicates the approximate minimum wavelength $0.57\lambda_{R09}$. The thin black lines identify the contour lines corresponding to the 5% significance level (95% confidence) against red noise. (b) Raw signal $z(x, t = 1970\,\text{s})$ in TCW2 (in black). The thin red line indicates the signal $z(x, t = 1970\,\text{s})$ smoothed with a gaussian filter (span of $3d_{50}$). The smoothed signal was considered for the wavelet transform application.

wavelet. The first and foremost purpose of this analysis was to assess how similar were the periodic fluctuation patterns in the q_s series during the T_1 and T_2 periods identified in 4.3.1. We recall that T_1 (from $t = 0$ s to $t = 700$ s) was the period during which the outlet bedload transport rates exhibited the most steady behaviour (i.e. the $V_{cum}(t)$ function was very close to a linear trend), whereas during T_2 (from $t = 700$ s up to $t = 3600$ s) the $V_{cum}(t)$ function slightly deviated from the run-averaged trend (especially between $t \sim 1000$ s and $t \sim 2250$ s, see Fig. 4.10). We expected to find peaks in the CWT scalogram around the dominant fluctuation period $T_{AD,fast}$ predicted accordingly to the findings by Pascal et al. (2021) (Chapter 3)—$T_{AD,fast}$ is the typical migration period expected for an antidune with $\lambda \gtrsim \lambda_{R09}$.

As one can see in the wavelet power scalogram in Fig. 4.20 this prediction was globally respected; the q_s CWT power was often concentrated in the period scale close to $T_{AD,fast}$. A typical oscillation period slightly longer than $T_{AD,fast}$ was consistent with the outcomes of the CWT analyses carried out on the bed elevations perturbations $z(t \mid x_{fixed})$ (see previous Section, 4.3.1). Indeed, we recall that we detected a relatively high occurrence of oscillation periods longer than $T_{AD,fast}$ for $z(t \mid x_{fixed})$ signals measured close to the flume outlet (see spectra in Fig. 4.17).

By observing the scalogram in Fig. 4.20, one can identify continuous 'patches' with significant
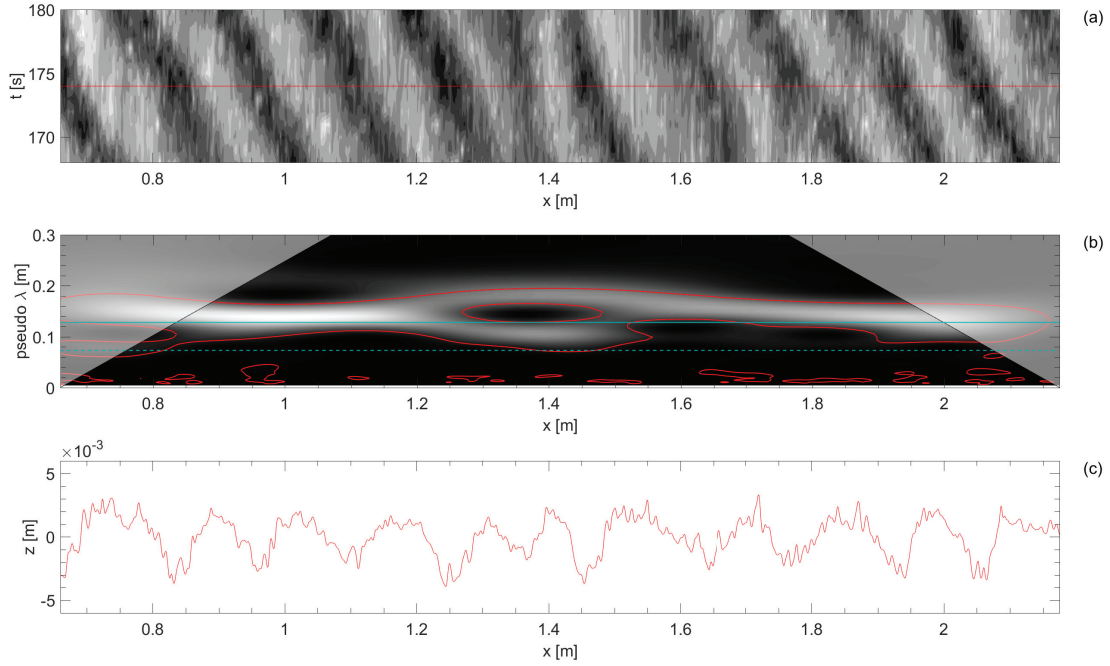
Figure 4.19: (a) Contour plot of the $z(x, t)$ perturbation in TCW1 (ES1) from $t = 168$ s to $t = 180$ s with the $t = 174$-s coordinate identified by the solid red line. (b) Averaged wavelet power scalogram (average of $n_S = 3$ scalograms from $t = 172$ s to $t = 174$ s). The solid green line indicates the constant wavelength coordinate corresponding to λ_{R09}, whereas the dashed green line corresponds to the approximate minimum wavelength $0.57\lambda_{R09}$. The thin red lines identify the contour lines corresponding to the 5% significance level (95% confidence) against red noise. (c) Signal of the $z(x, t_{fixed})$ perturbation for the entire TCW1 at $t = 174$ s after smoothing with gaussian filter (span of $3d_{50}$).

power density and similar period values, which correspond to time intervals during which the $\overline{\Phi}_s(t \mid \Delta t = 1\mathrm{s})$ series exhibited pulses with similar periodicity and high amplitudes. These patches were particularly evident and interconnected in the time span corresponding to the T_1 period of the ES1 run. The $\overline{\Phi}_s(t \mid \Delta t = 1\mathrm{s})$ fluctuations appeared less regular in time during the central part of the ES1 run, especially in the time interval from $t \sim 1000$ s and $t \sim 2250$ s. This outcome is in line with the results presented in Section 4.3.1, where we outline how the convergence of the $\overline{\Phi}_s(\Delta t, t_{samp,r})$ rates towards the run-averaged rate ($\simeq q_{s,in}$) was usually slower during T_2 than during T_1. The analysis of the global and time-localised wavelet spectra presented in Fig. 4.21 indicated that during T_1 the q_s oscillation power was particularly concentrated in the period range that corresponds to 1–$2\,T_{AD,fast}$. This observation indicates that the periodicity of most bedload pulses was tightly related to antidune migration close to the flume outlet and to the longer migration periods that were often observed there (see Sec. 4.3.1).
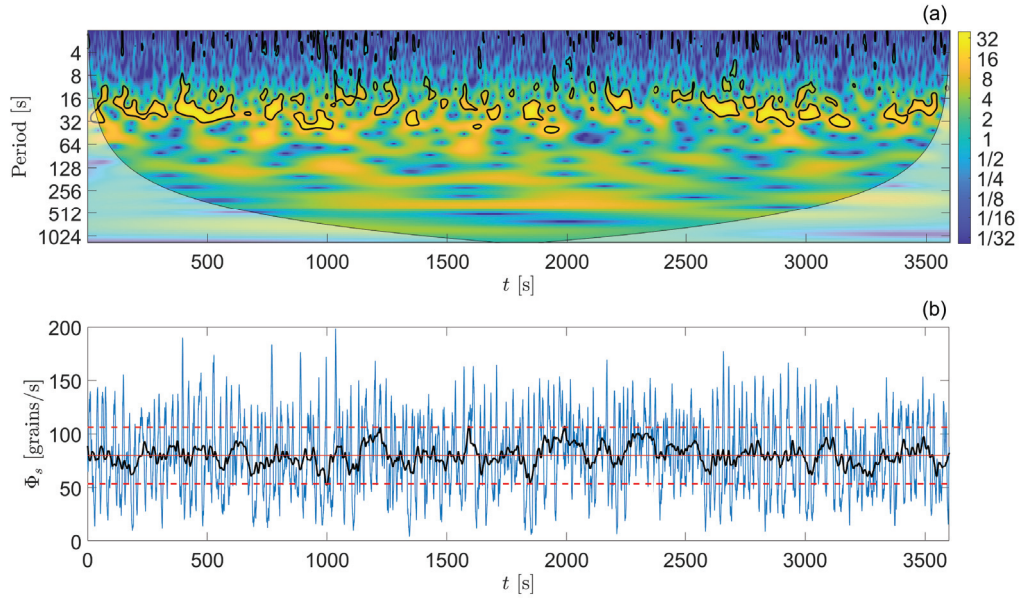
Figure 4.20: (a) Wavelet power scalogram (Morlet CWT) for the $\overline{\Phi}_s(t \mid \Delta t = 1\text{s})$ time series of the ES1 run. The black lines indicate the contours that correspond to the 5% significance level (95% confidence). (b) Time series of $\overline{\Phi}_s(t \mid \Delta t = 3\text{s})$ (blue line) and $\overline{\Phi}_s(t \mid \Delta t = 3T_{AD,fast} = 54\text{s})$ for the entire duration of the ES1 run. The solid red line indicates the run-averaged bedload flux $\overline{\Phi}_{s,ES1}$. The dashed red lines indicate the constant rates $1.33\overline{\Phi}_{s,ES1}$ and $0.67\overline{\Phi}_{s,ES1}$ which correspond to the $\pm 33\%$ deviation limits.

4.3.2 Bed-degrading phase ED1

ED1: Uncertainty and convergence of time-averaged bedload transport rates during a quasi-steady bedload transport phase

In this second part of the Results section, we present preliminary findings of our investigation regarding the influence of sediment pulses on the bedload transport rate estimations during the ED1 phase of the experimental run. This assessment was conducted considering bedload transport data collected during a 400–s-long period during which a limited sector of the system (approximately correspondent to TCW2) approached quasi-steady transport conditions, while the system was globally undergoing bed-degradation. We already anticipated (see Fig. 4.2) that between $t = 4550$ s and $t = 5250$ s the bedload flux at the flume outlet followed a quasi-steady phase with $\overline{q}_s(t \mid \Delta t = 200 \text{ s}) \approx 2q_{s,ES1}$. The bedload transport rate was particularly stable from $t = 4800$ s to $t = 5200$ s. We selected this time frame (that we called T_3) and we studied the uncertainty of the local bedload transport rate estimates as well as their convergence towards the mean bedload transport rate of this period (estimated from the slope of the $V_c um$ trend as $\overline{q}_{s,T3} = \overline{\Phi}_s(t = 5000 \text{ s}, \Delta t = 400 \text{ s}) \simeq 2.12\overline{q}_{s,ES1}$).

Regarding the Δt-intrinsic uncertainty, we applied the same framework proposed by Ancey and Pascal (2020) (Chapter 2) and already used for the ES1 case (Section 4.3.1). The period T_3
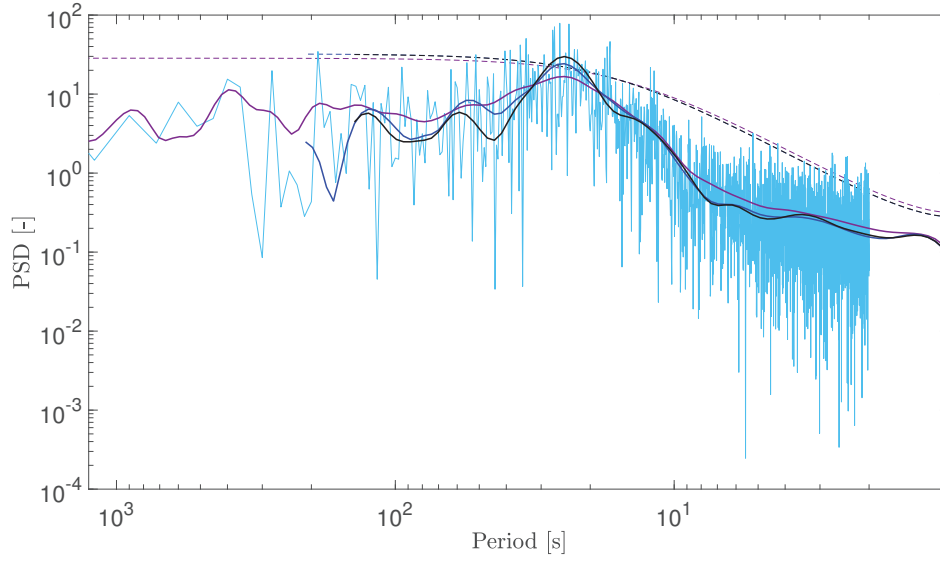
Figure 4.21: Wavelet power spectra (Morlet CWT) and FFT spectrum computed from the $\overline{\Phi}_s(t \mid \Delta t = 1\text{s})$ time series of the ES1 run. The different solid lines indicate, the ES1 FFT spectrum (light blue), the ES1 CWT spectrum (purple) and the spectra computed for the $\overline{\Phi}_s(t \mid \Delta t = 1\text{s})$ time series from $t = 0$ s to $t = 600$ s (dark blue) and that from $t = 400$ s to $t = 600$ s (black). Each dashed line indicates the background red noise spectrum that corresponds to the 5% significance level associated with each wavelet spectrum. In detail, the ES1 background spectrum (dashed purple), the $t = 0$–600 s background spectrum (dashed dark blue) and the $t = 400$–600 s background spectrum (dashed black).

was relatively short (400 s) compared to the period $T_1 + T_2$ studied for the ES1 run. Therefore, in order to avoid edge effects due to the limited time frame, we decided to consider random reference times $t_{\text{ref},i}$ in the 4850–5150-s range and 1–100 s Δt spans for our investigation on the $\overline{\Phi}_s(\Delta t \mid t_{\text{ref},i})$ uncertainty. Our intention was to study a range of uncertainty similar to that explored for the ES1 case. Since we were primarily interested in investigating the relative uncertainty of the bedload transport estimates (i.e. on $(\text{var}\,\overline{\Phi}_s(\Delta t \mid t_{\text{ref},i}))^{0.5}/\overline{q}_{s,\text{T3}}$), assuming that the uncertainty trend predicted by Eq. 4.8 approximately held also for the T_3 bedload transport rates, we expected that the higher mean bedload transport rate during T_3 counterbalanced the relatively small Δt span investigated. Interestingly, the empirical distribution of the waiting times τ computed for T_3 did not show a marked hyper-exponential trend and was relatively close to the exponential distribution with parameter $\Lambda_{s,T3} = 1/\overline{\tau} = 78.65 \text{ s}^{-1}$ (see Fig. 4.26). Therefore, we considered this exponential distribution for modelling the parameters $\overline{\tau}$ and σ_τ^2 in Eq. 4.8.

As one can see in the two examples reported in Fig. 4.22 and Fig. 4.23, our expectations were basically confirmed. The empirical standard deviation series in Fig. 4.22 (d) roughly followed

Figure 4.22: Results of the protocol application for $t_{\text{ref},i} = 5085$ s with Δt intervals from 1 s up to 100 s. (a) Samples $\overline{\Phi}_{\text{s,m-boot}}(\Delta t \mid t_{\text{ref},i})$ from bootstrapping ($M = 100$) for each Δt value (grey dots), ensemble-time average $\langle \overline{\Phi}_s \rangle_M (\Delta t \mid t_{\text{ref},i})$ for each Δt value (red dots), values corresponding to $\langle \overline{\Phi}_s \rangle_M (\Delta t \mid t_{\text{ref},i}) \pm ((\text{var} \overline{\Phi}_s(\Delta t))_{Ren.Th.})^{0.5}$ (see Eq. B12) for each Δt value (blue dots), time-averaged rates $\overline{\Phi}_s(\Delta t \mid t_{\text{ref},i})$ from the original samples (black dots), run-averaged rate $\overline{q}_{\text{s,T3}}$ (dash-dotted red line). (b) Series of $\overline{\Phi}_s(t \mid \Delta t = 1\text{s})$ rates for $t_{\text{ref},i} = 5085$ s (grey line), run-averaged rate $\overline{q}_{\text{s,T3}}$ (dash-dotted red line). (c) Normalised sample values $\overline{\Phi}_{\text{s,m-boot}}(\Delta t \mid t_{\text{ref},i})/\langle \overline{\Phi}_s \rangle_M (\Delta t \mid t_{\text{ref},i})$ for each Δt value (grey dots), values corresponding to $(\langle \overline{\Phi}_s \rangle_M (\Delta t \mid t_{\text{ref},i}) \pm ((\text{var} \overline{\Phi}_s(\Delta t))_{Ren.Th.})^{0.5}/\langle \overline{\Phi}_s \rangle_M (\Delta t \mid t_{\text{ref},i})$ (see Eq. B12) (blue dots), normalised time-averaged rates $\overline{\Phi}_s(\Delta t \mid t_{\text{ref},i})/\langle \overline{\Phi}_s \rangle_M (\Delta t \mid t_{\text{ref},i})$ from the original samples (black dots). The red dots identify the normalised ensemble-time averages $\langle \overline{\Phi}_s \rangle_M (\Delta t \mid t_{\text{ref},i})/\langle \overline{\Phi}_s \rangle_M (\Delta t \mid t_{\text{ref},i}) = 1$ (for definition) for each Δt value. (d) Empirical standard deviation values $(\text{var} \overline{\Phi}_s(\Delta t \mid t_{\text{ref},i}))^{0.5}$ (black crosses), theoretical trend $(\text{var}(S/\Delta t))^{0.5}$ from Eq. B12 (dashed blue line), theoretical trend in case of Markovian process for the standard deviation $(\Lambda_{\text{s,T3}}/\Delta t)^{0.5}$ from Ancey and Pascal (2020) (dashed purple line).

the trend predicted by the renewal theory application (Eq. 4.8) and was close to the theoretical trend $(\text{var} \overline{\Phi}_s(\Delta t \mid t_{\text{ref},i}))^{0.5} = (\Lambda_{\text{s,T3}}/\Delta t)^{0.5}$, even if the underlying process was not a random Markovian process. Indeed, the empirical waiting time distribution was slightly different from an exponential distribution (see Fig. 4.26). During T_3, the mean number of particles that crossed the control surface $\mathscr{S}_{OCW}$ within a time interval $\delta t = 0.01$ s ($\overline{N} = 1.681$) was 13% lower than the variance $\text{var} N = 1.905$.

When the local transport rates in the close vicinity of $t_{\text{ref},i}$ were relatively low, as for $t_{\text{ref},i} = 4950$ s in Fig. 4.23 (d), the Eq. 4.8 trend notably overestimated the empirical $(\text{var} \overline{\Phi}_s(\Delta t \mid t_{\text{ref},i}))^{0.5}$ series for small Δt values (as one may expect from an asymptotic approximation). Summarising, we managed to study the uncertainty in the local mean bedload transport rates for values of
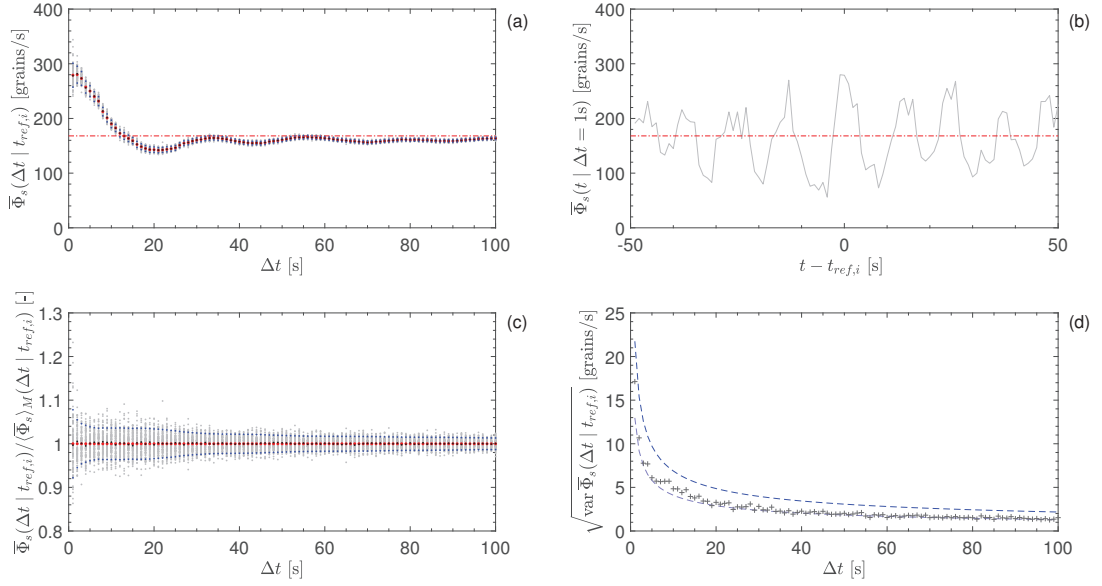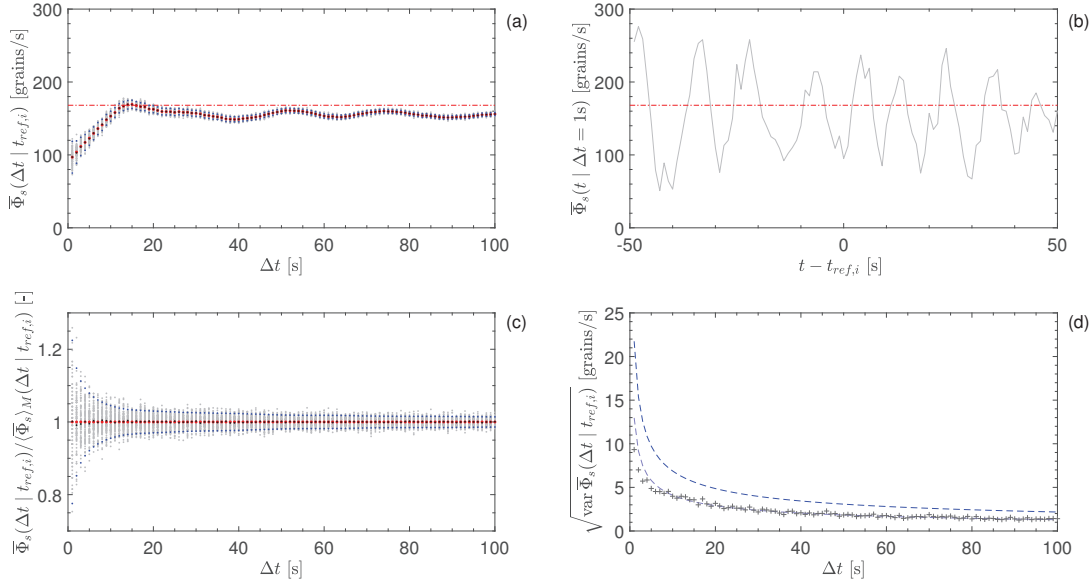
Figure 4.23: Results of the protocol application for $t_{\text{ref},i} = 4950$ s with Δt intervals from 1 s up to 100 s. (a) Samples $\overline{\Phi}_{\text{s,m-boot}}(\Delta t \mid t_{\text{ref},i})$ from bootstrapping ($M = 100$) for each Δt value (grey dots), ensemble-time average $\langle \overline{\Phi}_s \rangle_M(\Delta t \mid t_{\text{ref},i})$ for each Δt value (red dots), values corresponding to $\langle \overline{\Phi}_s \rangle_M(\Delta t \mid t_{\text{ref},i}) \pm ((\text{var}\,\overline{\Phi}_s(\Delta t))_{Ren.Th.})^{0.5}$ (see Eq. B12) for each Δt value (blue dots), time-averaged rates $\overline{\Phi}_s(\Delta t \mid t_{\text{ref},i})$ from the original samples (black dots), run-averaged rate $\overline{q}_{\text{s,T3}}$ (dash-dotted red line). (b) Series of $\overline{\Phi}_s(t \mid \Delta t = 1\text{s})$ rates for $t_{\text{ref},i} = 4950$ s (grey line), run-averaged rate $\overline{q}_{\text{s,T3}}$ (dash-dotted red line). (c) Normalised sample values $\overline{\Phi}_{\text{s,m-boot}}(\Delta t \mid t_{\text{ref},i})/\langle \overline{\Phi}_s \rangle_M(\Delta t \mid t_{\text{ref},i})$ for each Δt value (grey dots), values corresponding to $(\langle \overline{\Phi}_s \rangle_M(\Delta t \mid t_{\text{ref},i}) \pm ((\text{var}\,\overline{\Phi}_s(\Delta t))_{Ren.Th.})^{0.5}/\langle \overline{\Phi}_s \rangle_M(\Delta t \mid t_{\text{ref},i})$ (see Eq. B12) (blue dots), normalised time-averaged rates $\overline{\Phi}_s(\Delta t \mid t_{\text{ref},i})/\langle \overline{\Phi}_s \rangle_M(\Delta t \mid t_{\text{ref},i})$ from the original samples (black dots). The red dots identify the normalised ensemble-time averages $\langle \overline{\Phi}_s \rangle_M(\Delta t \mid t_{\text{ref},i})/\langle \overline{\Phi}_s \rangle_M(\Delta t \mid t_{\text{ref},i}) = 1$ (for definition) for each Δt value. (d) Empirical standard deviation values $(\text{var}\,\overline{\Phi}_s(\Delta t \mid t_{\text{ref},i}))^{0.5}$ (black crosses), theoretical trend $(\text{var}(S/\Delta t))^{0.5}$ from Eq. B12 (dashed blue line), theoretical trend in case of Markovian process for the standard deviation $(\Lambda_{\text{s,T3}}/\Delta t)^{0.5}$ from Ancey and Pascal (2020) (dashed purple line).

the variation coefficient $(\text{var}\,\overline{\Phi}_s(\Delta t \mid t_{\text{ref},i}))^{0.5}/\overline{q}_{\text{s,T3}}$ going from ~10 % to ~1 %. This outcome is important as this test represented the first validation attempt of the protocol proposed by Ancey and Pascal (2020) for bedload flux data collected with high-frequency monitoring in a well-controlled system which was out of the so-called equilibrium conditions but nevertheless behaved like a quasi-steady system during a specific period. The transport conditions of this system during T_3 were quite peculiar, as the quasi-steady state of the bedload flux was likely governed by the downstream-travelling erosional wave whose front was still located in the upstream sector of the flume. After the interruption of the automatic sediment feeding, the onset of this erosional front which was progressively associated with non-uniform flow conditions. Namely, a step-pool which evolved in a tumbling flow at the inlet and, most importantly,

a downstream migrating undular hydraulic jump. The erosive action of the flow at the upstream edge of the granular bed provided sustained bedload supply towards the downstream sector of the flume during T_3. An enhanced transport capacity manifestly characterised this sediment-laden flow in the TCW2 sector compared to the flow under "equilibrium conditions" (ES1). We speculate that this feature could be due to the augmented frequency of granular collisions between the sediment particles transported by the flow and those resting onto the bed surface—as well as between the transported particles—caused by the increased bedload concentration. These collisional interactions affect the momentum exchanges between flow, transported particles and particles at rest on the bed surface (Drake et al., 1988; Böhm et al., 2004). According to Ancey et al. (2008), the entrainment of bed particles may also be indirectly influenced by moving particles; their transit close to the bed causes "significant modifications in the velocity profile [...] which may increase the force exerted by the fluid" on the particles at rest. At the meso-scale, these direct and indirect influences on the bed particles stability may be phenomenologically interpreted as a transient contribution to the effective bed shear stress. Our experimental observations suggest that during T_3, a significant fraction of the moving particles could have travelled in the form of a bedload sheet along the sector that corresponds to TCW2. The bedload transport rate series during the T_3 period was less intermittent than during ES1 and could be compatible with the migration of a low-relief bedform, which could have ensured the base level of bedload transport rate with superimposed the pulses associated to the upstream-migrating antidunes. This process could be a tentative explanation for the roughly exponential trend of the empirical distribution of the waiting times τ computed for T_3. This tentative explanation seems in agreement with the outcomes of the 2D-FFT spectral analysis presented in the next section (4.3.2).

The convergence of the $\overline{\Phi}_s(\Delta t, t_{samp,r})$ rates towards $\overline{q}_{s,T3}$ was studied following the same framework used in Sec. 4.3.1. We considered times $t_{samp,r}$ equispaced of 3 seconds from $t = 4860$ s up to $t = 5140$ s. We investigated the convergence up to Δt values of 120 s. We knew that the transport was less intermittent during T_3 compared to the ES1 case. Therefore, we expected faster antidune migration and more rapid convergence $\overline{\Phi}_s(\Delta t, t_{samp,r}) \to \overline{q}_{s,T3}$ compared to the trend observed for the ES1 run. This expectation was confirmed by the outcomes of this analysis (presented in Fig. 4.24). It is interesting to note that the $\langle \overline{\Phi}_s \rangle_R (\Delta t)$ double-averaged rates did not converge exactly towards the T_3 time-averaged rate $\overline{q}_{s,ES1} = \overline{\Phi}_s(t = 5000 \text{ s}, \Delta t = 400 \text{ s}) = 168$ grains/s but towards a slightly lower rate ($\simeq 163$ grains/s, -3% deviation) which was closer to the rate $\overline{\Phi}_s(t = 5000 \text{ s}, \Delta t = 280 \text{ s}) \simeq 162$ grains/s. This difference can be justified by the relatively low influence of the rates sampled near the edges of the T_3 period on the above-mentioned double-averaged rates. For the conditions registered in the downstream sector of the flume during T_3 (see Tab. 4.5), the predicted value of the typical antidune migration period based on the $c_N^* \approx f(\lambda_N^*)$ relationship (Pascal et al., 2021) was $T_{AD,fast} \approx 9$ s. Since the $\overline{\Phi}_s(\Delta t, t_{samp,r})$ samples converged within the ± 15 % deviation levels for intervals $\Delta t \gtrsim 3T_{AD,fast}$, we can affirm that the convergence of this less intermittent series was faster compared to the ES1 case (see Fig. 4.13).
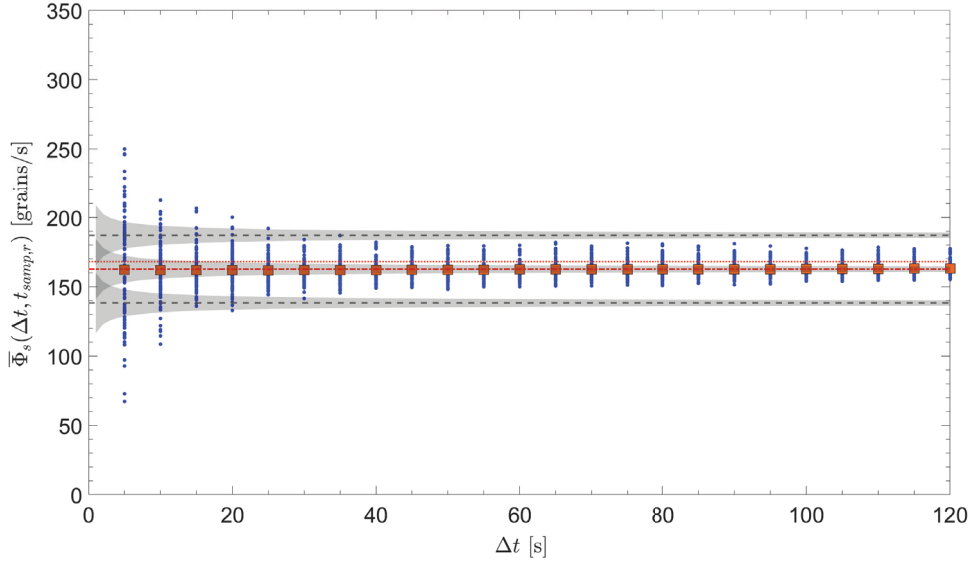
Figure 4.24: Series of $\overline{\Phi}_s(\Delta t, t_{samp,r})$ rates (blue dots) computed from the ED1 $\Phi_s(t)$ dataset for Δt-wide samples centred at times $t_{samp,r}$. The selected times $t_{samp,r}$ were equispaced of 3 seconds from $t = 4860$ s up to $t = 5140$ s. The orange squares indicate $\langle\overline{\Phi}_s\rangle_R(\Delta t)$ double-averaged rates. The horizontal dash-dotted red line indicates the mean of the $\langle\overline{\Phi}_s\rangle_R(\Delta t)$ rates for $\Delta t \geq 60$ (163 grains/s). The dotted red line denotes the T_3 time-averaged rate $\overline{\Phi}_{s,T3} = 168$ grains/s. The dashed black lines indicate the rate levels corresponding to the $\pm15\%$ deviation from the mean of $\langle\overline{\Phi}_s\rangle_R(\Delta t)$ rate for $\Delta t \geq 60$ (163 grains/s). The grey shaded areas identify the standard deviation limits that correspond to the Δt-intrinsic uncertainty (Eq. B12) around the constant rates indicated by the horizontal lines.

ED1: 2D-FFT spectral analysis of the antidune pattern during a quasi-steady phase

We conducted a 2D-FFT spectral analysis of the antidune pattern observed during the T_3 period (ED1, from $t = 4800$ s to $t = 5200$ s) primarily to understand how the antidune morphology and kinematics in TCW2 were affected by the increased bedload transport flux under similar local hydraulic forcing compared to the ES1 case (i.e. $q_{w,T3} = q_{w,ES1}$ and $\overline{\psi}_{TCW2,T3} \simeq \overline{\psi}_{TCW2,ES1}$). According to the framework already applied for the ES1 case (Section 4.3.1), we computed the $\lambda - c$ FFT spectrum for the $Z_{TCW2*,T3}([x_a = 4.06\,\text{m}\; x_b = 5.30\,\text{m}], [t_a = 4850\,\text{s}\; t_b = 5150\,\text{s}])$ sub-matrix in order to minimise the non-uniformities caused by the flume outlet (see Section 4.3.1). As indicated in the sub-matrix above, for this application we considered a slightly shorter period within T_3 ($\Delta t = 300$s) in order focus on a localised period and to avoid including the portion of the bed elevation perturbation matrix from $t = 5150$ s to $t = 5200$ s that could be already influenced by less steady conditions which reflected in the bedload transport rates measured at the flume outlet after $t = 5200$ s (however, a test revealed that the differences in the resulting spectra were negligible). We then calculated the $\lambda_N^* - c_N^*$ spectrum by applying the scaling relationships proposed by Pascal et al. (2021) (Eq. 4.4 and Eq. 4.3). The values of

the main parameters used for this analysis are summarised in Tab. 4.5.

$\overline{q}_{s,T3}$ [m^2 s^{-1}]	$\overline{\psi}_{TCW2,T3}$ [°]	$h_0 \simeq \langle \overline{h} \rangle$ [m]	λ_{R09} [m]	Fr [-]	Θ [-]	Θ_c [-]
$3.75 \cdot 10^{-5}$	2.7	0.01	0.13	1.42	0.107	0.065

Table 4.5: Parameters considered for computing the $\lambda_N^* - c_N^*$ spectrum from the $\lambda - c$ spectrum. Slope-dependent parameters estimated considering the slope angle average in TCW2* during T_3.

In Figure 4.25 (a) one can observe the contours of the $\lambda - c$ spectrum obtained for the $Z_{TCW2*,T3}$ sub-matrix and compare them with the equivalent ones of the spectrum computed for the $Z_{TCW2*,ES1}$ sub-matrix. Figure 4.25 (b) shows the associated dimensionless $\lambda_N^* - c_N^*$ spectra.

As expected due to the higher mean bedload transport rate during T_3, the $c \approx f(\lambda)$ trend for the T_3 case in Figure 4.25 (a) was steeper than the one of the ES1 case and also the wavelength variability was less pronounced (λ mostly in the range 0.7–1 λ_{R09}). The less variable antidune wavelength displayed during T_3 compared to the ES1 case was consistent with the diminished bedload transport intermittency. However, the spectrum in the dimensionless domain (Fig. 4.25 (b)) followed a $c_N^* \approx f(\lambda_N^*)$ trend less steep than the one predicted by the relationship proposed by Pascal et al. (2021) (Chapter 3). We identified a small increase of the mean antidune amplitude between ES1 and T_3 ($H_{AD,ES1} \simeq 5$ mm and $H_{AD,T3} \simeq 5.5$ mm, respectively). However, this amplitude change alone was not sufficient to explain the trend $c_N^* \approx f(\lambda_N^*)$ exhibited under the conditions of supply excess occurred in TCW2* during T_3 (compared to the mean bedload discharge during ES1). We remained careful in interpreting the c_N^* differences quantitatively as $\overline{q}_s$ differences because a slight overestimation error possibly affected the bedload transport rates measured during the ED1 phase (see comments in the introduction to the Results section 4.3). However, the relative magnitude of this potential monitoring error was of the order of 5% $\overline{q}_{s,T3}$ and thus the deviation in the $c_N^* \approx f(\lambda_N^*)$ trend was clearly significant. This different response in terms of dimensionless antidune celerity ($\sim$ 15–30%) suggests that a conspicuous fraction of the sediment load that travelled along the TCW2 sector during T_3 participated less frequently to the bedform migration by depositing on the stoss sides of the antidunes. A phenomenon that may explain this deviation from the predicted trend $c_N^* \approx f(\lambda_N^*)$ is the transit of a bedload sheet over the antidune sequence during T_3. We have already mentioned this possibility in Sec. 4.3.2 as a bedload sheet may also explain some peculiarity that was detected in the bedload flux statistics (especially the exponential distribution of the particle waiting times) as well as the enhanced transport capacity exhibited in the TCW2 sector during T_3 (under hydraulic conditions very similar to those set for the ES1 phase).
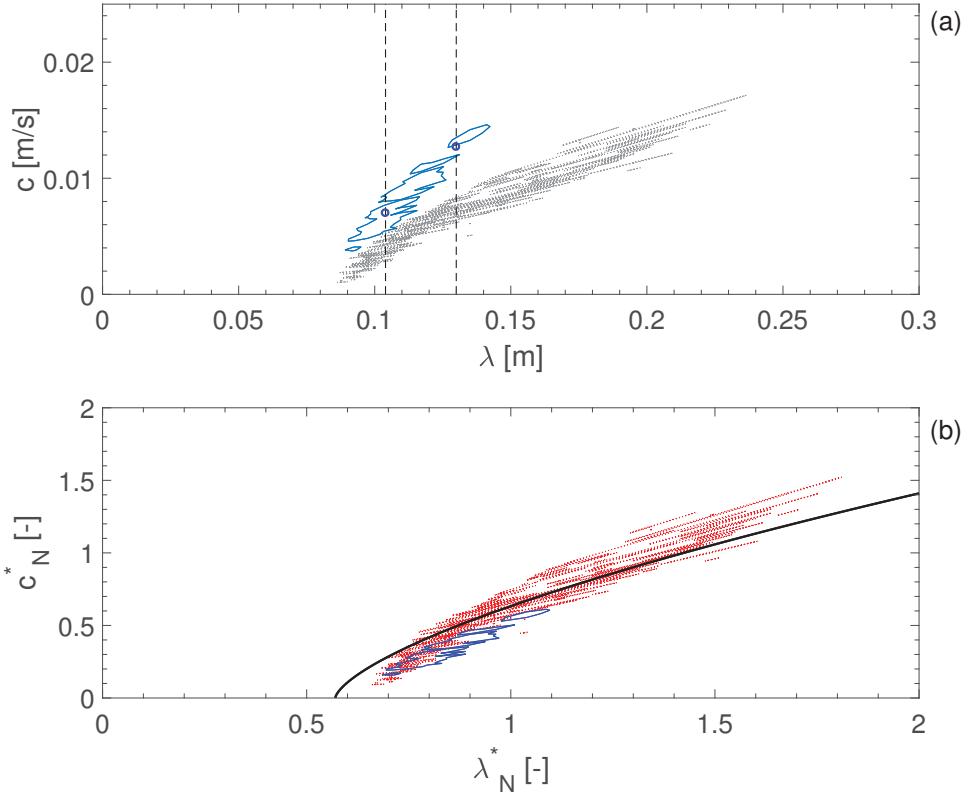
Figure 4.25: Sub-plot (a) $\lambda - c$ spectrum (light blue contour) computed for $Z_{TCW2*,T3}$. The vertical dashed lines identify the λ coordinates corresponding to $[0.8, 1]\lambda_{R09}$. The blue circles indicate the $\{\lambda, c\}$ pairs (Tab. 4.3) used to compute the $\overline{q}_{s,est(T3)}$ estimates (in the range 2.65–$3.15 \cdot 10^{-5}$ m^2 s^{-1}). The dotted grey contours indicate the spectrum computed for $Z_{TCW2*,ES1}$ (with equivalent contour level). Sub-plot (b) $\lambda_N^* - c_N^*$ dimensionless spectrum (blue contour) computed for $Z_{TCW2*,T3}$ considering the mean transport rate $\overline{q}_{s,T3}$. The solid black line indicates the dimensionless trend $c_N^* \approx f(\lambda_N^*)$ found by Pascal et al. (2021). The dotted red contours indicate the dimensionless spectrum computed for $Z_{TCW2*,ES1}$ (with equivalent contour level).

4.4 Conclusive remarks

The fluctuations in the bedload transport rate measured at the outlet of the long flume during ES1 were similar in both magnitude and periodicity to those observed during E1 (short flume run, Chapter 3). This similar fluctuation regime suggests that the antidunes exhibited similar morphology and behaviour during ES1 and E1 (at least close to the flume outlet).

The spectral analysis of the bed elevation perturbation confirmed that antidune geometry and celerity were consistent with those observed in the short flume. We found that the trend $c_N^* \approx f(\lambda_N^*)$ in the dimensionless spectra followed Eq. (3.16) (presented in the previous chapter). Accordingly, the estimates of $\overline{q}_{s,ES1}$ computed by using Eq. (3.17) were close to the actual value (relative errors in the 5–15 % range). The antidune wavelength did not vary systematically

along the migration path. This outcome contradicts the increase in λ that occurred for similar conditions in the numerical simulation made by Bohorquez and Ancey (2016).

The protocol and relationships presented in Chapter 2 allowed us to quantify the uncertainties of $\overline{\Phi}_s(\Delta t \mid t_{ref,i})$ estimates of the actual mean bedload transport rate for Δt sampling intervals centred at $t_{ref,i}$. The relationship for $\text{var}\,\overline{\Phi}_s(\Delta t \mid t)$ based on the renewal theory provided a good approximation of the trend exhibited by the empirical variance for large Δt values. At small Δt values, the theoretical trend often over predicted the empirical values. Furthermore, we studied the convergence of the $\overline{\Phi}_s(\Delta t, t_{samp,r})$ rates towards the run-averaged bedload transport rate ($\sim q_{s,in}$) for increasing Δt values. We found that sampling with $\Delta t \gtrsim 2T_{AD,fast} \simeq 40$ s was sufficient to approximate $q_{s,in}$ within the ±33% deviation range during the most stationary phase of bedload transport (period T_1 in ES1). Over the entire ES1 run duration, Δt intervals as long as 240 s ($\gtrsim 13T_{AD,fast}$) were required to reduce the uncertainty to ±15%.

Interestingly, the 1D wavelet spectra of the local bed perturbations $z(t \mid x_{fixed})$ indicate that the incipient antidune located close to the outlet septum often experienced a migration period notably longer than the typical migration period of antidunes situated far from the downstream boundary ($\sim$1.5–2 times longer, see Sec. 4.3.1). This evidence proves that the downstream boundary conditions may perturb bedform dynamics, even under supercritical flow conditions. The outlet septum inevitably influences the hyporheic flow conditions and indirectly affects the stability of the particles on the bed surface right upstream. Therefore, its design requires particular attention. This boundary effect may indirectly influence the convergence trend $\overline{\Phi}_s(\Delta t, t_{samp,r}) \rightarrow q_{s,in}$.

Concerning the ED1 run, we analysed the uncertainty of the $\overline{\Phi}_s(\Delta t \mid t_{ref,i})$ rates over a period T_3 (from $t = 4800$ s to $t = 5200$ s) during which the bedload transport process appeared quasi-steady at the flume outlet ($\overline{q}_{s,T3} \approx 2\overline{q}_{s,ES1}$), while the bed in the upstream sector of the flume was under degradation. During this phase of intense sediment supply, the relative uncertainty of the $\overline{\Phi}_s(\Delta t \mid t_{ref,i})$ estimates was lower than during ES1 for the same Δt value. This was likely due to the less intermittent transport under the influence of the large sediment supply. The convergence $\overline{\Phi}_s(\Delta t, t_{samp,r}) \rightarrow \overline{q}_{s,T3}$ was also notably faster compared to the trend observed for the ES1 run.

Applying the 2D-FFT to the bed elevation perturbation data of TCW2 and comparing the dimensionless spectrum $c_N^* - \lambda_N^*$ with the trend expressed by Eq. (3.16) made it possible to highlight an attenuated response in terms of dimensionless antidune celerity to the increased bedload supply during T_3. The reduced migration celerity appears coherent with the transit of a bedload sheet along TCW2 during T_3. This application allowed us to test the performances of Eq. (3.16) in a situation in which the temporarily increased bedload supply is the dominant forcing. Apparently, Eq. (3.16) tends to overestimate the antidune celerity (+ 15–30 %) in such

situations.

Supplementary information

C4 - S1
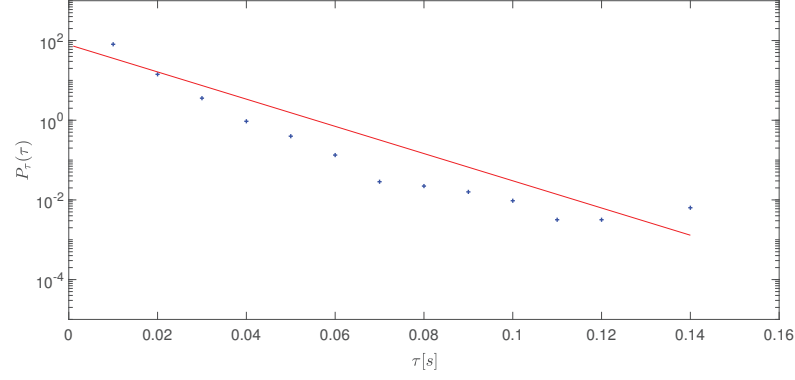
Figure 4.26: Arrival times empirical distribution at the middle cross-section of OCW ($\mathscr{S}_{OCW}$) during ED1 (T_3) (blue crosses). The exponential distribution fitted on the experimental data is indicated by a solid red line.

C4 - S2
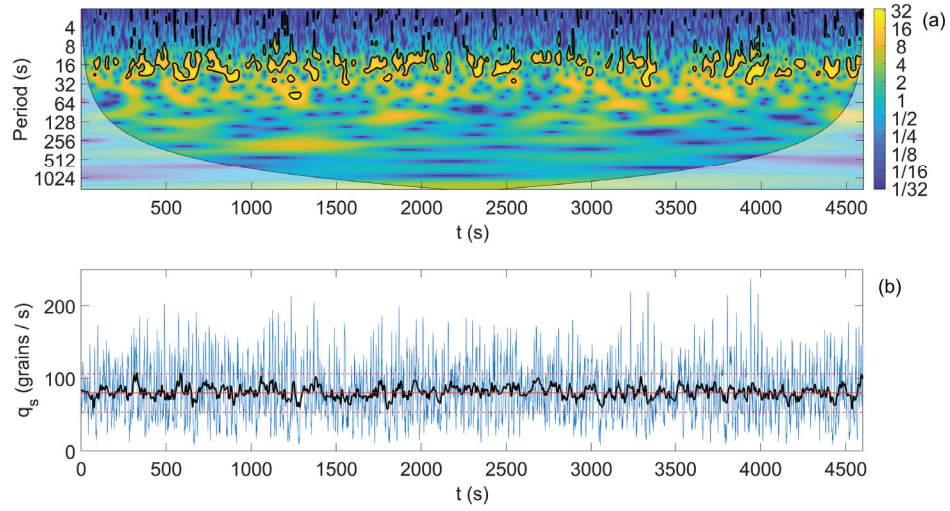
Figure 4.27: (a) Wavelet power scalogram (Morlet CWT) for the $\overline{q}_s(t \mid \Delta t = 1\mathrm{s})$ time series of the E1 run. The black lines indicate the contours that correspond to the 5% significance level (95% confidence). (b) Time series of $\overline{q}_s(t \mid \Delta t = 1\mathrm{s})$ (blue line) and $\overline{q}_s(t \mid \Delta t = 3T_{AD,fast} = 39\mathrm{s})$ for the entire duration of the E1 run. The solid red line indicates the run-averaged bedload flux $\overline{q}_{s,E1}$. The dashed red lines indicate the constant rates $1.33\overline{q}_{s,E1}$ and $0.67\overline{q}_{s,E1}$ which correspond to the ±33% deviation limits.
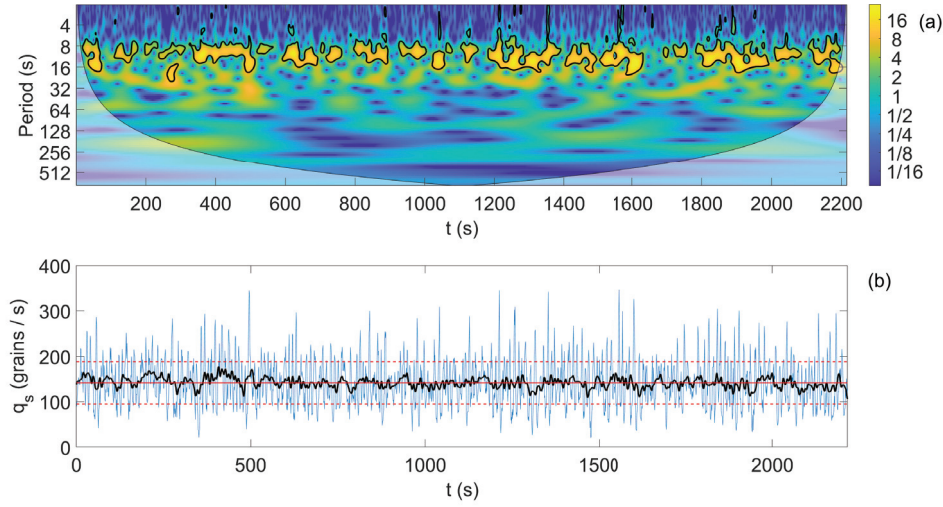
Figure 4.28: (a) Wavelet power scalogram (Morlet CWT) for the $\overline{q}_s(t \mid \Delta t = 1\text{s})$ time series of the E2 run. The black lines indicate the contours that correspond to the 5% significance level (95% confidence). (b) Time series of $\overline{q}_s(t \mid \Delta t = 1\text{s})$ (blue line) and $\overline{q}_s(t \mid \Delta t = 3T_{AD,fast} = 25\text{s})$ for the entire duration of the E2 run. The solid red line indicates the run-averaged bedload flux $\overline{q}_{s,E2}$. The dashed red lines indicate the constant rates $1.33\overline{q}_{s,E2}$ and $0.67\overline{q}_{s,E2}$ which correspond to the $\pm33\%$ deviation limits.
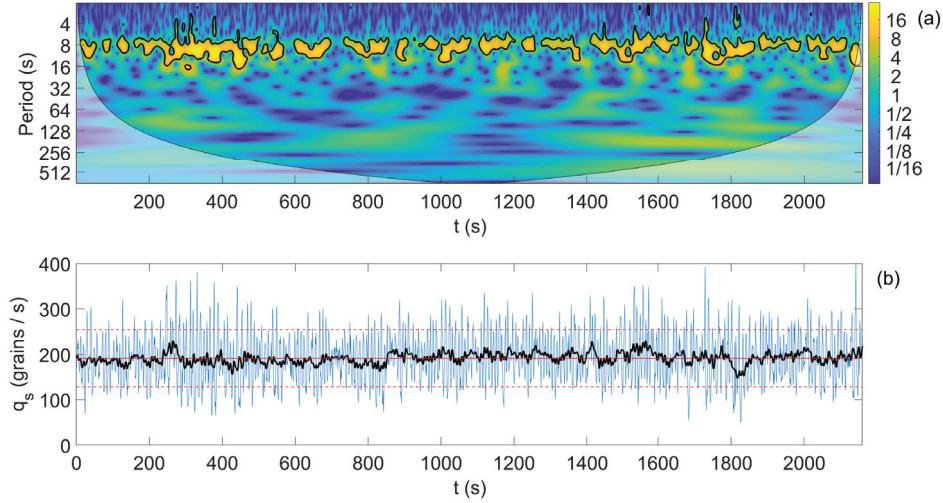
Figure 4.29: (a) Wavelet power scalogram (Morlet CWT) for the $\overline{q}_s(t \mid \Delta t = 1\text{s})$ time series of the E3 run. The black lines indicate the contours that correspond to the 5% significance level (95% confidence). (b) Time series of $\overline{q}_s(t \mid \Delta t = 1\text{s})$ (blue line) and $\overline{q}_s(t \mid \Delta t = 3T_{AD,fast} = 20\text{s})$ for the entire duration of the E3 run. The solid red line indicates the run-averaged bedload flux $\overline{q}_{s,E3}$. The dashed red lines indicate the constant rates $1.33\overline{q}_{s,E3}$ and $0.67\overline{q}_{s,E3}$ which correspond to the $\pm33\%$ deviation limits.

5 General conclusions and outlook

5.1 Summary of this thesis

The broad purpose of this research was to improve the understanding of bedload transport processes and bed morphodynamics in steep streams. As explained in the Introduction of this thesis, understanding the physical and statistical behaviour of bedload pulses and their relationships with bedform dynamics is crucial for improving our capacity to monitor and predict bedload transport processes in real-world rivers—especially, in mountain streams. I studied bedload transport rate fluctuations and their interplay with upstream migrating antidunes under steady-state conditions. The approach was distinctly experimental; I ran experiments in narrow flumes in which I applied image-based techniques to accurately monitor bedload transport rates and bed topography evolution. The research progressed in three stages that reflected the four main objectives presented in the Introduction chapter (see Sec. 1.3).

In Chapter 2, we described an experiment (P run) that was performed in the short flume under weak bedload transport conditions ($\Theta/\Theta_c \approx 1$ and $\langle \overline{\Phi}_s \rangle \simeq \Phi_{s,\text{feed}} \simeq 10$ grains/s). A high-speed camera was used to film the particles from above in a control volume while they were entrained, transported and deposited along the mobile bed. Applying a particle tracking procedure made it possible to reconstruct particle trajectories. This dataset was analysed to compute the volume-averaged bedload transport rate q_s and the particle flux Φ_s across a control surface for each time step.

The theoretical developments reported in Chapter 2 indicate that under steady-state conditions the double-averaged transport rates ($\langle \overline{q}_s \rangle$ and $\langle \overline{\Phi}_s \rangle$) converge towards the same value when the sampling time interval is much longer than the autocorrelation time t_c of the number of moving particles $N(t)$ ($\Delta t \gg t_c$). Although the ensemble variances of these rates are not equivalent, they share the same dependence

$$\text{var } \overline{\mathcal{Q}}_s \propto 1/\Delta t$$

where $\mathcal{Q}_s(t)$ is a time series of q_s or Φ_s rates.

A measurement protocol for assessing the variance (i.e. an uncertainty indicator) of time-averaged bedload transport rate estimates $\overline{\mathcal{Q}}_s$ was proposed. This framework holds for periods in which the behaviour of $\mathcal{Q}_s(t)$ is close to that of a stationary process. The best-case scenario is when the available data enable the resolution of discrete particle motion across a control surface $\mathcal{S}$ or within a control volume $\mathcal{V}$. In that situation, if the process satisfies the Markovian conditions, one can calculate the trend of var $\overline{\mathcal{Q}}_s$ (e.g. var$\overline{\Phi}_s(\Delta t \mid t) = \Lambda / \Delta t$, see Sec. 2.2.3) according to the model proposed by Ancey et al. (2008). If the process is not Markovian (e.g. the waiting times do not follow an exponential distribution), one can still find an asymptotic approximation (var $\overline{\mathcal{Q}}_s \approx K / \Delta t$ in the limit $t \to \infty$) by using renewal theory (see Supp. 2.8). We applied this protocol to the P run dataset and the overall agreement was good. However, we found that the waiting times were not exponentially distributed in our experiment. We could approximate the actual trend of var $\overline{\mathcal{Q}}_s$ but the Markovian assumption was not satisfied owing to the correlated intermittency caused by bedforms upstream of the control window. We also showed how to infer information on the uncertainty by using the central limit theorem when measurements are collected at low temporal frequencies.

In Chapter 3, the focus was on the variability of antidune morphology and celerity. We presented four experiments that were conducted in the short flume setup. For each run, we imposed a different sediment supply rate as well as the water flow rate required to maintain steady-state conditions at near-constant mean bed slope angle ($\overline{\psi} \approx 3$). We observed trains of upstream migrating antidunes. We showed that antidune geometry and migration period may vary considerably, even under such controlled conditions. According to our findings, the variabilities of antidune wavelength λ and celerity c are tightly interconnected. Typically, the longer the antidune the faster its migration. According to our spectral analysis of the bed elevation perturbation data collected during each run, wavelength variability decreases as the transport intensity increase. We proposed a scaling framework—based on Eq. 3.13 and Eq. 3.15—for which the spectra aligned onto a single trend. The associated dimensionless relationship (Eq. 3.16) summarises the behaviour exhibited by antidunes in our experiments and includes the dependency of c on the mean bedload transport rate:

$$\frac{c}{U_N} \approx f(\lambda_N^*) = \frac{[(\lambda / \lambda_{R09}) - 0.57]^{2/3}}{0.9},$$

where $U_N = \overline{q}_s / [d_{V,50}(1 - p)]$ is a virtual velocity for the sediment phase and λ_{R09} is the dominant antidune wavelength on steep slopes according to Recking et al. (2009). Eq. 3.16 can be converted into an explicit formula (Eq. 3.17) for estimating the mean bedload transport discharge associated with a sequence of upstream migrating antidunes. The first performance assessments of this relationship were satisfactory. Our results indicate that antidunes characterised by $\lambda \geq \lambda_{R09}$ tend to exhibit the shortest migration period. This characteristic period $T_{AD,fast}$ can be calculated using Eq. 3.16.

In Chapter 4, we presented an experiment (ES1) conducted under steady-state conditions in the new long flume in which we monitored the bed topography profile over long sectors of the flume. Based on the analysis of the 2D wavelength-celerity spectra (Sec. 4.3.1), we could conclude that no systematic increase of antidune wavelength occurred along the upstream migration path. Although such a wavelength increase has been observed in a numerical simulation by Bohorquez and Ancey (2016) under conditions similar to those of the ES1 run, this phenomenon is unlikely to arise for upstream migrating antidunes on steep slopes composed of well-sorted coarse sediments—at least under steady-state conditions with moderately intense sediment supply. The bed topography data collected during ES1 allowed us to conduct an additional performance assessment of Eq. 3.17 for estimating the steady-state mean bedload transport rate associated with upstream migrating antidunes. This test confirmed that this relationship might provide estimates of the steady-state bedload transport rate as accurate as $\pm 5 - -10\%$ (if applied in its validity domain).

We also monitored at high-frequency the particle flux at the outlet. The possibility to resolve the particle arrivals made it possible to apply the protocol presented in Chapter 2 with the approximation of $\mathrm{var}\,\overline{\Phi}_s(\Delta t \mid t)$ given by the renewal theory (Eq. 4.8, see Supp. 2.8). The trend predicted by Eq. 4.8 provided a conservative overestimation of the empirical variance values during ES1. The trend $\mathrm{var}\,\overline{\Phi}_s(\Delta t \mid t)$ was just above the empirical ensemble variance when t corresponded to a pulse peak with sudden increase of the particle flux followed by a slow decrease (or vice versa). Unfortunately, the variance was largely over predicted at small Δt when the particle flux was low. This comes as no surprise given the asymptotic limit behind Eq. 4.8 but remains a limitation of the protocol. This study confirmed that bedload pulses associated with antidune migration may notably affect the convergence of time-averaged rates towards the run-averaged rate, even when moderately intense sediment supply is imposed to the system. The minimum sampling time Δt required for ensuring a crude time-averaged estimate $\overline{\Phi}_s(t \mid \Delta t)$ of $q_{s,in}$ ($\pm 33\%$ error) was relatively short ($\Delta t \geq 2T_{AD,fast}$) when the bedload flux was very close to the stationary behaviour and the bedload pulses induced by antidune migration were characterised by a well-defined periodicity. When the periodicity was less regular, a minimum interval $\Delta t = 3T_{AD,fast}$ was required to estimating $q_{s,in}$ within the $\pm 33\%$ deviation range. For approximating the run-averaged rate within $\pm 15\%$, sampling intervals Δt longer than $10T_{AD,fast}$ were needed. Under less intense bedload transport conditions (e.g. run P, Chapter 2), under which an increased bedload transport intermittency is expected (according to Singh et al., 2009), the convergence may be even slower.

One might interpret $2T_{AD,fast}$ as the time interval associated to the migration of two antidunes near the flume outlet. As we showed in Sec. 4.3.1, the boundary conditions may often influence the migration period of the incipient antidune in contact with the outlet septum. Therefore, a period approximately equal to $2T_{AD,fast}$ may also correspond to the migration of a single antidune in those occasions. According to these observations, the behaviour of the incipient antidune close to the outlet may contribute to the deviations of the $\overline{\Phi}_s(t)$ signal from the periodicity $T \sim T_{AD,fast}$ that the dominant antidunes (those with $\lambda \geq \lambda_{R09}$) would tend to

impose most of the time. Indeed, we observed that far from the boundaries the variability of the migration period is notably lower than in the 20–cm-long sector located right upstream of the flume outlet. This outcome witnesses the attention that downstream boundary and hyporheic flow conditions deserve, even in streams under supercritical flow regime.

In Chapter 4, we also presented an experiment (ED1) conducted without active sediment feeding after ES1 (with the same water discharge). Analysing the bedload transport rate data collected during this experiment provided interesting insights on bedload fluctuations and antidune morphodynamics under bed degrading conditions. During a 400–s-long phase of ED1 (called T_3), the bedload flux at the flume outlet behaved as a quasi-stationary process. During the T_3 period, the mean bedload transport rate was approximately doubled with respect to the ES1 run-averaged transport rate (under the same hydraulic forcing). In this phase of ED1, the bedload transport process was quasi-steady at the flume outlet control section but the flume system could not be globally considered at equilibrium. The bed was preferentially eroded in the upstream part of the flume and this resulted in an increased bedload supply for the downstream flume sector. Under this temporarily enhanced sediment supply, bedload transport was less intermittent and the relative uncertainty of the local $\overline{\Phi}_s(\Delta t \mid t)$ rates was usually lower than that of rates sampled with the same Δt during ES1. Given the more uniform shape of antidunes and their faster migration under less intermittent sediment transport conditions, $\overline{\Phi}_s(\Delta t, t)$ rates collected during the T_3 phase of ED1 usually converged towards the representative mean bedload transport rate faster than those collected during ES1. We conducted spectral analyses of the bed elevation perturbation data collected in the downstream sector of the flume during T_3. This was useful to assess the order of magnitude of errors that may affect mean bedload transport rate estimates based on Eq. 3.17 in case of bedload sheets that interact with antidune sequences following a strong variation of sediment supply.

5.2 Future perspectives

5.2.1 Outcomes

As a whole, this research work concerned measurements and analyses of bedload transport rates and antidune morphodynamic features. These variables are prone to marked variability in supercritical flows characterised by high relative roughness.
Regarding the fluctuations in the bedload transport rate, our framework makes it possible to account for them when estimating time-averaged bedload transport rates. We showed how to infer information on the uncertainty related to these bedload transport rate estimates from the data. The proposed protocol for assessing the sampling time-related uncertainty of bedload transport rates is a robust and versatile tool for laboratory and field monitoring campaigns. This framework can be of great importance for a broad community of researchers and practitioners, a community that is slowly but progressively understanding the need

of taking into account the fluctuations of the bedload transport rates—thanks to recent literature contributions that stress this aspect (e.g. Ancey et al., 2014; Furbish et al., 2017; Ancey, 2020b; Gomez et al., 2022). The implementation of this protocol can also facilitate and make more consistent the comparisons between data collected in different environments and with different techniques.

Concerning the variability that affects antidune geometry and migration celerity, we showed how this variability can be quantified and how its interpretation can provide useful information on the antidune morphodynamics and their dependency on the sediment supply rate. As such, our investigations concerning the antidune morphodynamics in steep supercritical flows characterised by high relative roughness provided contributions that complement the findings made in previous experimental studies (especially those conducted by Recking et al. (2009) and Mettra (2014)). The dimensionless relationship that describes how antidune celerity varies with bedform wavelength under an imposed mean bedload transport rate is an important advance in the understanding of the antidune morphodynamics. Hopefully, this promising relationship will be further tested and possibly refined to extend its validity domain—for instance, to less laterally-confined channel configurations.

The combination of the approaches presented in Chapter 2 and Chapter 3 is helpful for studying the interplay between bedload transport and bedform migration. For instance, it enables to investigate how the sampling time required for the convergence of the time-averaged bedload transport rate towards the supply rate is interconnected with the migration period of antidunes. This aspect was addressed in the study presented in Chapter 4.

More specifically, the main contributions of each chapter are:

C. 2) (i) The theoretical analysis of the sampling time (Δt) influence on the uncertainty of time-localised mean bedload transport rates (Sec. 2.2), whose results were confirmed by experimental evidences. (ii) The measurement protocol—applicable in various bedload transport conditions and monitoring contexts—for assessing the case-specific trend of the Δt-related uncertainty of a mean bedload transport rate estimate (Sec. 2.2.7). (iii) The confirmation that the Markovian assumption for the population of moving particles is not accurate in presence of migrating bedforms, which cause a highly correlated behaviour in the bedload transport rate time series (that results in the hyper-exponential distribution of the particle waiting times).

C. 3) (i) The contribution to the assessment of the variability ranges of shape and celerity for the case of upstream migrating antidunes on steep slopes, a contribution that sums to those provided by Mettra (2014). (ii) The dimensionless relationship that describes how antidune celerity varies with bedform wavelength and mean bedload transport rate (Eq. 3.16).

C. 4) (i) The insights on the sampling time Δt required to estimate the run-averaged bedload transport rate (or supply rate) within a certain deviation range in presence of upstream migrating antidunes. (ii) The comparisons of this time scale with the expected migration

period of dominant antidunes and with the time interval needed to obtain an estimate within a given uncertainty range of the actual time-localised mean bedload transport rate. (iii) The assessment concerning the occurrence of a systematic increase in the antidune wavelength along the upstream migration path (see Bohorquez and Ancey, 2016)—no systematic increase was observed in our experiment. (iv) The identification of the local influence of the outlet bed discontinuity on the antidune migration period and consequently on the periodicity of bedload transport rate fluctuations measured at the flume outlet.

Detailed experimental insights on how the dynamics of antidunes and antidune trains are interrelated with the bedload transport rate fluctuations are of great importance to improve our understanding of bedload transport processes in steep streams. They can highlight which are the main mechanisms that links together the bedload flux and the morphodynamic evolution in these streams and their relative importance depending on the specific flow and sedimentary conditions (flow regime, bed slope, bedload transport intensity, etc.)—from the spatial scale of the single particle up to the scales of single bedforms and bedform sequences. The occurrence of bedform splitting and merging events has been seldom considered (or observed) in theoretical and numerical models aiming to reproduce bedform dynamics under supercritical flow conditions. As it stands out from this experimental study, antidune splitting and merging phenomena represent important contributions to the variability of the antidune shape and celerity, and thereby to the variable periodicity and magnitude of bedload pulses.

The experimental investigation presented in Chapter 4 (with comprehensive monitoring of bedload fluxes and bed topography) provided data that can be used for formulating and validating new theoretical and numerical models. Concerning the stochastic approach, there is a need of novel frameworks that embed the random nature of the particle motion but also the part of (spatially and temporally) correlated periodicity that the bedform migration (and/or other deviations from the steady-state conditions) may introduce in the bedload transport process. Such improved models would be a great advance for applications of the stochastic approach to field scenarios, in which migrating bedforms as well as time- and space-varying flow and sediment supply conditions are very likely to occur.

5.2.2 Open challenges

In the following paragraphs, I provide some perspectives for future developments. The focus is on investigations that can benefit of the flume setup built during this research work.

Further experiments with particle tracking over mobile bed at weak bedload transport intensity

One of the objectives of this research work was to monitor (at high temporal and spatial resolution) the trajectories of moving bedload particles in a control volume over a sloping erodible bed sheared by a free-surface flow. In the investigation presented in Chap. 2 (Ancey and Pascal, 2020) we focused on the sampling aspects that affect bedload transport rate estimates. We filmed the particles from above through a transparent plastic plate that was placed in contact with the water surface. This plate prevented light reflections and distortions due to the wavy free surface that would have disturbed the particle tracking procedure. We decided to adopt this solution to minimise tracking errors, since filming from the sidewall involved the issue of the particles that could mutually hide each other (especially during the particle bursts and when particles were rolling along the rough bed). The price to pay for this choice was the local flow confinement exerted by the plate, which inevitably introduced disturbances in the system. Presumably, the free-surface perturbation exacerbated antidunes near the downstream edge of the plate but it also prevented their migration towards the upstream sector of the flume.

The new flume presented in Chap. 4 was built with glass sidewalls. This feature makes it possible to collect images of higher quality than those collected in the flume setup used for the study presented in Chap. 2 (old plastic sidewalls). These improved imaging conditions could allow us to reach suitable tracking accuracy also in case of image acquisition from the sidewall—provided that the steady-state mean particle flux is notably lower than that imposed during the P run. Therefore, this new flume could enable monitoring of particle trajectories under free-surface flow conditions in a configuration of lesser lateral confinement ($d/W \simeq 16$) compared to the experiments conducted by Heyman et al. (2016) in which $d/W \simeq 5$ (and in which the flume was shorter). Preliminary tests conducted by the candidate under very low mean particle flux ($\langle \overline{\Phi}_s \rangle \approx 5$ grains/s) resulted moderately satisfactory but the sediment feeding system requires further adjustments to ensure steady sediment supply with this rate.

The new data would be a valuable contribution to the available datasets of particle trajectories collected under conditions representative of mountain streams (natural sediments, supercritical or near critical flow regime, high relative roughness d/h, bed slope above 1 %). Therefore, they would enable further tests of the existing stochastic frameworks. For instance, one could retrieve closure equations for the stochastic parameters and compare them with those found by (see Heyman et al., 2016). These comparisons might shed new light on the sensitivity of the stochastic parameters to changes in the local flow and bed conditions also influenced by differences in the boundary conditions (lateral confinement, distance of the sediment supply input, etc.).

Antidune migration at weak bedload transport intensity

During the experiments proposed in the previous section, it would be interesting to study also the variability of the antidune morphodynamics under mean bedload transport rate values lower than those imposed during the runs E1 and ES1. As mentioned in Sec. 3.3.3, a pronounced bedload transport intermittency is expected to influence antidune morphodynamics, especially in terms of migration celerity intended as a response to the forcing imposed by the sediment supply. Among other applications, the new bed topography data could be used to assess if (and to what extent) the longest antidune migration periods $T_{AD,slow}$ (see last part of Sec. 4.3.1) are predictable.

Flow over antidune sequences

Another aspect worth of investigation is the flow configuration over the antidune sequences. During his thesis, Mettra (2014) performed some tests with image-based analysis of the flow configuration over a fixed plane bed composed of natural grains to study the relationship $h = f(q_w)$ at different values of the bed slope angle ψ in his setup (in absence of bedload transport). He later conducted other tests with a shallow flow over a fixed sinusoidal-shaped bed with smooth surface. The wavelength of the antidune-like waves was set to a value similar to those observed in his experiments (see Appendix C in Mettra, 2014). Thereby, he observed the existence of an hysteresis cycle with occurrence of fully supercritical or transcritical flow conditions (hydraulic-jump) for variations in q_w (at constant mean bed slope angle $\overline{\psi}$).

Mettra's valuable tests would deserve to be repeated under conditions closer to those of experimental runs in which upstream migrating antidunes were observed, namely with porous rough bed. Monitoring the flow velocity profile along the antidune sequence by performing Particle Tracking Velocimetry (PTV) analysis (or similar analyses) would be another valuable possibility. These new experiments would be demanding challenges but they could clarify the potential role played by this hysteretic behaviour in the stability (or breaking) of upstream migrating antidunes sheared by shallow flows with high relative roughness. They could also contribute to explain the origin of the downstream travelling disturbances within the antidune sequences, which were observed during E1, E2 (see Sec. 3.3.4), ES1 (see Fig. 4.16) and ES2, apparently under supercritical flow regime. Last but not least, such tests would provide useful data to better clarify the magnitude of the form resistance possibly caused by antidunes.

This type of novel experiments is likely feasible and could even include analysis of the hyporheic flow in case of application of the Refractive Index Matching (RIM) technique (see Rousseau, 2019; Rousseau and Ancey, 2020). Concerning an analysis of the vertical velocity profile limited to the surface flow, I performed encouraging tests in the 5.8-–m-long flume (presented in Chap. 4) by developing an imaging solution (for PTV) that does not require the use of a laser—based on seeding with pollen powder (a quasi-neutrally buoyant tracer, see Greated

et al., 1992). One delicate aspect is finding a set of experimental conditions under which the erodible bed remains near the incipient motion condition—a condition under which these experiments would be particularly meaningful—and the bedload transport is not too intense. Intense bedload transport would cause two main issues. First, the transit of a large number of particles in the control window during the image collection would obviously complicate the analysis and would likely degrade the quality of the PTV data. Second, if the typical timescale of the bed topography changes is too close to (or smaller than) the timescale needed for a proper flow turbulence resolution the resulting PTV velocity field loses significance. These two issues could be avoided by using a fixed porous rough bed (or simply a fixed non-porous rough bed). These simplified conditions would likely facilitate the experiment implementation and improve the accuracy of the PTV results but would also be less similar to the actual conditions under which upstream migrating antidunes develop and migrate. A configuration with fixed non-porous rough bed with antidune topography based on available experimental data would probably represent a good starting point to assess the existence of the flow regime hysteresis.

Bedload transport monitoring based on the spectral analysis of the antidune patterns

This short section concerns the bedload transport monitoring method based on Eq. 3.17 and on the 2D-FTT spectral analysis of the antidune patterns (or alternatively, on bedform tracking). From the results presented in Chap. 4, it clearly stands out that this method cannot compete with the image-based high-frequency bedload transport monitoring in terms of pure measurement accuracy, at least when both are applied on similar sampling intervals Δt (see Sec. 4.3.1 and Sec. 4.3.1). This evidence was expected but deserves few additional considerations for future applications. Likewise other methods proposed by Simons et al. (1965), Nikora (1984) and Guala et al. (2014), one of the main advantages of this indirect method for bedload transport monitoring lies in its applicability to spatially windowed topographic data in order to extract information on the stream-wise variability of the bedload flux. Using bed topography data issued from techniques different from those used in this study is obviously possible (see Visconti et al. (2012), Dhont and Ancey (2018)). Furthermore, this method may be easily adapted to work with water surface profiles instead of bed topography profiles, since those two are substantially in phase for markedly supercritical flows over antidunes. This feature may represent a great advantage in case of opaque water or when remote-sensing techniques are required (see Ferreira et al., 2017). Therefore, this method based on the $\lambda_N^* - c_N^*$ spectrum may be a good candidate to complement spatially localized high-frequency q_s measurements (for instance, those based on high-speed cameras or accelerometers) in presence of upstream-migrating antidunes in a large variety of experimental conditions (even in some field site). In cases in which antidune sequences are subject to lesser lateral confinement, one might need to calibrate specific variants of Eq. 3.16 and Eq. 3.17 to obtain robust q_s estimates.

Bibliography

Alexander, J. (2008). Bedforms in froude-supercritical flow. In *Marine and River Dune Dynamics*, pages 1–5.

Alexander, J., Bridge, J., Cheel, R., and Leclair, S. (2001). Bedforms and associated sedimentary structures formed under supercritical water flows over aggrading sand beds. *Sedimentology*, 48(1):133–152.

Almedeij, J. H. and Diplas, P. (2003). Bedload transport in gravel-bed streams with unimodal sediment. *Journal of Hydraulic Engineering*, 129(11):896–904.

Ancey, C. (2010). Stochastic approximation of the Exner equation under lower-regime conditions. *Journal of Geophysical Research*, 115:F00A11.

Ancey, C. (2020a). Bedload transport: a walk between randomness and determinism. Part 1: State of the art. *Journal of Hydraulic Research*, 58:1–17.

Ancey, C. (2020b). Bedload transport: a walk between randomness and determinism. Part 2: Challenges and prospects. *Journal of Hydraulic Research*, 58:18–33.

Ancey, C., Böhm, T., Jodeau, M., and Frey, P. (2006). Statistical description of sediment transport experiments. *Physical Review E*, 74:011302.

Ancey, C., Bohorquez, P., and Bardou, E. (2014). Sediment transport in mountain rivers. *Ercoftac*, 89:37–52.

Ancey, C., Bohorquez, P., and Heyman, J. (2015). Stochastic interpretation of the advection diffusion equation and its relevance to bed load transport. *Journal of Geophysical Research: Earth Surface*, 120:2529–2551.

Ancey, C., Davison, A. C., Böhm, T., Jodeau, M., and Frey, P. (2008). Entrainment and motion of coarse particles in a shallow water stream down a steep slope. *Journal of Fluid Mechanics*, 595:83–114.

Ancey, C. and Heyman, J. (2014). A microstructural approach to bed load transport: mean behaviour and fluctuations of particle transport rates. *Journal of Fluid Mechanics*, 744:129–168.

Bibliography

Ancey, C. and Pascal, I. (2020). Estimating mean bedload transport rates and their uncertainty. *Journal of Geophysical Research: Earth Surface*, 125:e2020JF005534.

Anderson, A. G. (1953). The characteristics of sediment waves formed by flow in open channels. In *Proceedings of the Third Midwestern Conference on fluid mechanics*, pages 379–395. Am. Soc. of Civ. Eng. Reston, Va.

Andreotti, B., Claudin, P., Devauchelle, O., Durán, O., and Fourrière, A. (2012). Bedforms in a turbulent stream: ripples, chevrons and antidunes. *Journal of Fluid Mechanics*, 690:94–128.

Ashmore, P. (1991a). Channel morphology and bed load pulses in braided, gravel-bed streams. *Geografiska Annaler. Series A. Physical Geography*, 73 A:37–52.

Ashmore, P. E. (1991b). How do gravel-bed rivers braid? *Canadian Journal of Earth Sciences*, 28(3):326–341.

Badoux, A., Andres, N., Techel, F., and Hegg, C. (2016). Natural hazard fatalities in switzerland from 1946 to 2015. *Natural Hazards and Earth System Sciences*, 16(12):2747–2768.

Badoux, A., Andres, N., and Turowski, J. (2014). Damage costs due to bedload transport processes in Switzerland. *Natural Hazards and Earth System Science*, 14:279–294.

Bagnold, R. (1956). The flow of cohesionless grains in fluids. *Proceedings of the Royal Society of London*, 249:235–296.

Ballio, F., Nikora, V., and Coleman, S. (2014). On the definition of solid discharge in hydro-environment research and applications. *Journal of Hydraulic Research*, 52:173–184.

Ballio, F., Pokrajac, D., Radice, A., and Hosseini Sadabadi, S. A. (2018). Lagrangian and Eulerian description of bed-load transport. *Journal of Geophysical Research: Earth Surface*, 123:384–408.

Balmforth, N. and Provenzale, A. (2001). Patterns of dirt. In *Geomorphological fluid mechanics*, pages 369–393. Springer.

Barry, J., Buffington, J., and King, J. (2004). A general power equation for predicting bed load transport rates in gravel bed rivers. *Water Resources Research*, 40:W10401.

Benda, L. and Dunne, T. (1997). Stochastic forcing of sediment supply to channel networks from landsliding and debris flow. *Water Resources Research*, 33(12):2849–2863.

Böhm, T., Ancey, C., Frey, P., Reboud, J.-L., and Ducottet, C. (2004). Fluctuations of the solid discharge of gravity-driven particle flows in a turbulent stream. *Physical Review E*, 69:061307.

Bohorquez, P. and Ancey, C. (2015). Stochastic-deterministic modeling of bed load transport in shallow waterflow over erodible slope: Linear stability analysis and numerical simulation. *Advances in Water Resources*, 83:36–54.

152

Bohorquez, P. and Ancey, C. (2016). Particle diffusion in non-equilibrium bedload transport simulations. *Applied Mathematical Modelling*, 40:7474–7492.

Bohorquez, P., Cañada Pereira, P., Jimenez-Ruiz, P., and del Moral-Erencia, J. (2019). The fascination of a shallow-water theory for the formation of megaflood-scale dunes and antidunes. *Earth-Science Reviews*, 193:91–108.

Bose, S. K. and Dey, S. (2009). Reynolds averaged theory of turbulent shear flows over undulating beds and formation of sand waves. *Physical review E*, 80(3):036304.

Bravo-Espinosa, M., Osterkamp, W., and Lopes, V. L. (2003). Bedload transport in alluvial channels. *Journal of Hydraulic Engineering*, 129(10):783–795.

Breakspear, R. (2008). *Hydrodynamics and sedimentary structures of antidunes in gravel and sand mixtures*. PhD thesis, University of Southampton.

Bridge, J. and Dominic, D. (1984). Bed load grain velocities and sediment transport rates. *Water Resources Research*, 20(4):476–490.

Buffington, J. and Montgomery, D. (1997). A systematic analysis of eight decades of incipient motion studies, with special reference to gravel-bedded rivers. *Water Resources Research*, 33:1993–2029.

Bunte, K. and Abt, S. (2005). Effect of sampling time on measured gravel bed load transport rates in a coarse-bedded stream. *Water Resources Research*, 41:W11405.

Campagnol, J., Radice, A., and Ballio, F. (2012). Scale-based statistical analysis of sediment fluxes. *Acta Geophysica*, 60:1744–1777.

Campagnol, J., Radice, A., Nokes, R., Bulankina, V., Lescova, A., and Ballio, F. (2013). Lagrangian analysis of bed-load sediment motion: database contribution. *Journal of Hydraulic Research*, 51:589–596.

Cao, H. H. (1985). *Résistance hydraulique d'un lit de gravier mobile à pente raide étude expérimentale*. PhD thesis, École Polytechnique Fédérale de Lausanne.

Carling, P. A., Burr, D. M., Johnsen, T. F., and Brennand, T. A. (2009). A review of open-channel megaflood depositional landforms on Earth and Mars. In Burr, D., Carling, P., and Baker, V., editors, *Megaflooding on Earth and Mars*, pages 33–49. Cambridge University Press.

Carling, P. A. and Shvidchenko, A. B. (2002). A consideration of the dune: antidune transition in fine gravel. *Sedimentology*, 49(6):1269–1282.

Cartigny, M., Ventra, D., Postma, G., and Den Berg, J. H. (2014). Morphodynamics and sedimentary structures of bedforms under supercritical-flow conditions: New insights from flume experiments. *Sedimentology*, 61:712–748.

Bibliography

Chanson, H. (1998). Critical flow in rockbed streams with estimated values for manning's n-comment. *Geomorphology*, 25(3):279–282.

Chanson, H. (2001). Hydraulic design of stepped spillways and downstream energy dissipators. *Dam Engineering*, 11(4):205–242.

Charru, F., Mouilleron, H., and Eiff, O. (2004). Erosion and deposition of particles on a bed sheared by a viscous flow. *Journal of Fluid Mechanics*, 519:55–80.

Chin, A. (1999). The morphologic structure of step-pools in mountain streams. *Geomorphology*, 27(3):191–204.

Chin, A. and Wohl, E. (2005). Toward a theory for step pools in stream channels. *Progress in physical geography*, 29(3):275–296.

Church, M. (2006). Bed material transport and the morphology of alluvial river channels. *Annual Review of Earth and Planetary Sciences*, 34:325–354.

Church, M. (2010). Gravel-bed rivers. In Burt T, A. R., editor, *Sediment Cascades: An Integrated Approach*, pages 241–270. John Wiley and Sons, Chichester.

Church, M. and Ferguson, R. (2015). Morphodynamics: Rivers beyond steady state. *Water Resources Research*, 51(4):1883–1897.

Church, M., Hassan, M. A., and Wolcott, J. F. (1998). Stabilizing self-organized structures in gravel-bed stream channels: Field and experimental observations. *Water Resources Research*, 34(11):3169–3179.

Church, M. and Rice, S. P. (2009). Form and growth of bars in a wandering gravel-bed river. *Earth Surface Processes and Landforms*, 34(10):1422–1432.

Church, M. and Zimmermann, A. (2007). Form and stability of step-pool channels: Research progress. *Water Resources Research*, 43(3).

Coleman, S. and Fenton, J. (2000). Potential-flow instability theory and alluvial stream bed forms. *Journal of Fluid Mechanics*, 418:101–117.

Coleman, S. and Nikora, V. (2009). Exner equation: A continuum approximation of a discrete granular system. *Water Resources Research*, 45:W09421.

Colombini, M. (2004). Revisiting the linear theory of sand dune formation. *Journal of Fluid Mechanics*, 502:1–16.

Colombini, M., Seminara, G., and Tubino, M. (1987). Finite-amplitude alternate bars. *Journal of Fluid Mechanics*, 181:213–232.

Colombini, M. and Stocchino, A. (2005). Coupling or decoupling bed and flow dynamics: fast and slow sediment waves at high Froude numbers. *Physics of Fluids*, 17:036602.

Colombini, M. and Stocchino, A. (2008). Finite-amplitude river dunes. *Journal of Fluid Mechanics*, 611:283–306.

Colombini, M. and Stocchino, A. (2012). Three-dimensional river bed forms. *Journal of Fluid Mechanics*, 695:63–80.

Comiti, F., Cadol, D., and Wohl, E. (2009). Flow regimes, bed morphology, and flow resistance in self-formed step-pool channels. *Water Resources Research*, 45:W04424.

Comiti, F. and Lenzi, M. A. (2006). Dimensions of standing waves at steps in mountain rivers. *Water resources research*, 42(3).

Comiti, F. and Mao, L. (2012). Recent advances in the dynamics of steep channels. In *Gravel-Bed Rivers: Processes, Tools, Environments*, pages 351–377.

Cornish, V. (1899). On kumatology.(the study of the waves and wave-structures of the atmosphere, hydrosphere, and lithosphere). *The Geographical Journal*, 13(6):624–626.

Cox, D. and Miller, H. (1965). *The Theory of Stochastic Processes*. Chapman & Hall CRC, Boca Raton.

Crickmore, M. and Lean, G. (1962). The measurement of sand transport by means of radioactive tracers. *Proceedings of the Royal Society of London. Series A. Mathematical and Physical Sciences*, 266(1326):402–421.

Cudden, J. and Hoey, T. B. (2003). The causes of bedload pulses in a gravel channel: The implications of bedload grain-size distributions. *Earth Surface Processes and Landforms*, 28:1411–1428.

Curran, J. H. and Wohl, E. E. (2003). Large woody debris and flow resistance in step-pool channels, cascade range, washington. *Geomorphology*, 51(1-3):141–157.

D'Agostino, V. and Lenzi, M. A. (1999). Bedload transport in the instrumented catchment of the Rio Cordon: Part II: Analysis of the bedload rate. *Catena*, 36(3):191–204.

Davison, A. C. and Hinkley, D. V. (1997). *Bootstrap Methods andTheir Application*. Cambridge University Press, Cambridge.

Deigaard, R. (2006). Breaking antidunes: Cyclic behavior due to hysteresis. *Journal of Hydraulic Engineering*, 132(6):620–623.

Dhont, B. (2017). *Sediment Pulses in a Gravel-Bed Flume with Alternate Bars*. PhD thesis, École Polytechnique Fédérale de Lausanne.

Dhont, B. and Ancey, C. (2018). Are bedload transport pulses in gravel-bed rivers created by bar migration or sediment waves? *Geophysical Research Letters*, 45:5501–5508.

Dhont, B., Rousseau, G., and Ancey, C. (2017). Continuous monitoring of bedload transport in a laboratory flume using an impact sensor. *Journal of Hydraulic Engineering*, 143:04017005.

Bibliography

Di Cristo, C., Iervolino, M., and Vacca, A. (2006). Linear stability analysis of a 1-D model with dynamical description of bed-load transport. *Journal of Hydraulic Research*, 44(4):480–487.

Dietze, M., Lagarde, S., Halfi, E., Laronne, J., and Turowski, J. M. (2019). Joint sensing of bedload flux and water depth by seismic data inversion. *Water Resources Research*, 55:9892–9904.

Drake, T., Shreve, R., Dietrich, W., and Leopold, L. (1988). Bedload transport of fine gravel observed by motion-picture photography. *Journal of Fluid Mechanics*, 192:193–217.

Dressler, R. (1978). New nonlinear shallow-flow equations with curvature. *Journal of Hydraulic Research*, 16:205–222.

Dressler, R. F. and Yevjevich, V. (1984). Hydraulic-resistance terms modified for the Dressler curved-flow equations. *Journal of Hydraulic Research*, 22(3):145–156.

Drew, D. and Passman, S. (1999). *Theory of Multicomponent Fluids*. Springer, New York.

du Boys, P. (1879). Le Rhône et les rivières à lit affouillable – Étude du régime du Rhône et de l'action exercée par les eaux sur un lit à fond de graviers indéfiniment affouillable. *Annales des Ponts et Chaussées*, 49:141–195.

Ehrenberger, R. (1931). Direct bedload measurements on the danube at vienna and their results to date. *Die Wasserwirtschaft*, 34:1–9.

Einstein, H. (1937a). *Der Geschiebetrieb als Wahrscheinlichkeitproblem (Bedload transport as a probability problem)*. (english translation by W. W. Sayre, in Sedimentation (Symposium to honor H. A. Einstein), edited by H. W. Shen, Fort Collins, Colorado, 1972, C1–C105, ETHZ.

Einstein, H. (1937b). Die eichung des im rhein verwendeten geschiebefangers. *Schweizer Bauzeitung*, 110:29–32.

Einstein, H. (1942). Formulas for the transportation of bed load. *Transactions of the American Society of Civil Engineers*, 107:561–597.

Einstein, H. (1950). The bed-load function for sediment transportation in open channel flows. Technical Report Technical Report No. 1026, United States Department of Agriculture.

Engelund, F. (1970). Instability of erodible beds. *Journal of Fluid Mechanics*, 42:225–244.

Ettema, R. and Mutel, C. (2004). Hans Albert Einstein: Innovation and compromise in formulating sediment transport by rivers. *Journal of Hydraulic Engineering*, 130:477–487.

Exner, F. M. (1925). Über die wechselwirkung zwischen wasser und geschiebe in flüssen. *Akad. Wiss. Wien Math. Naturwiss. Klasse*, 134(2a):165–204.

Farge, M. (1992). Wavelet transforms and their applications to turbulence. *Annual review of fluid mechanics*, 24(1):395–458.

156

Fathel, S., Furbish, D., and Schmeeckle, M. (2015). An experimental demonstration of ensemble behavior in bed load sediment transport. *Journal of Geophysical Research: Earth Surface*, 120:2298–2317.

Ferguson, R. (1993). Understanding braiding processes in gravel-bed rivers: progress and unsolved problems. *Geological Society, London, Special Publications*, 75(1):73–87.

Ferguson, R. I. (2007). Flow resistance equations for gravel- and boulder-bed streams. *Water Resources Research*, 43:W05427.

Ferguson, R. I. (2021). Roughness calibration to improve flow predictions in coarse-bed streams. *Water Resources Research*, 57(6):e2021WR029979.

Ferreira, E., Chandler, J., Wackrow, R., and Shiono, K. (2017). Automated extraction of free surface topography using sfm-mvs photogrammetry. *Flow Measurement and Instrumentation*, 54:243–249.

FOEN (2021). Effects of climate change on swiss water bodies: Hydrology, water ecology and water management. Environmental studies UW-2101-E, Federal Office for the Environment (FOEN), https://www.bafu.admin.ch/bafu/en/home/topics/water/water–publications/publications-water/effects-of-climate-change-on-swiss-water-bodies.html. accessed on: 01.04.2021.

Foufoula-Georgiou, E. and Kumar, P., editors (1994). *Wavelets in Geophysics*. Academic Press.

Fredsøe, J. (1974). On the development of dunes in erodible channels. *Journal of Fluid Mechanics*, 64(1):1–16.

Frey, P., Ducottet, C., and Jay, J. (2003). Fluctuations of bed load solid discharge and grain size distribution on steep slopes with image analysis. *Experiments in fluids*, 35(6):589–597.

Froude, M. J., Alexander, J., Barclay, J., and Cole, P. (2017). Interpreting flash flood palaeoflow parameters from antidunes and gravel lenses: An example from montserrat, west indies. *Sedimentology*, 64(7):1817–1845.

Fuchs, R. (1952). On the theory of short-crested oscillatory waves. In *Gravity Waves, NBS Circular*, volume 521, pages 187–200. United States Department of Commerce, National Bureau of Standards.

Furbish, D., Fathel, S. L., and Schmeeckle, M. W. (2017). Particle motions and bedload transport theory: the entrainment forms of the flux and the Exner equation. In Tsutsumi, D. and Laronne, J. B., editors, *Gravel-Bed Rivers: Processes and Disasters*, pages 97–120. John Wiley & Sons, Chichester.

Furbish, D., Haff, P., Roseberry, J., and Schmeeckle, M. (2012). A probabilistic description of the bed load sediment flux: 1. Theory. *Journal of Geophysical Research*, 117:F03031.

Bibliography

Furbish, D. and Roering, J. (2013). Sediment disentrainment and the concept of local versus nonlocal transport on hillslopes. *Journal of Geophysical Research*, 118:937–952.

Ganti, V., Meerschaert, M., Foufoula-Georgiou, E., Viparelli, E., and Parker, G. (2010). Normal and anomalous dispersion of gravel tracer particles in rivers. *Journal of Geophysical Research*, 115:F00A12.

Gardiner, C. (1983). *Handbook of Stochastic Methods.* Springer Verlag, Berlin.

Gardiner, C. and Chaturvedi, S. (1977). The Poisson representation. I. A new technique for chemical master equations. *Journal of Statistical Physics*, 17:429–468.

Geay, T., Belleudy, P., Gervaise, C., Habersack, H., Aigner, J., Kreisler, A., Seitz, H., and Laronne, J. (2017). Passive acoustic monitoring of bedload discharge in a large gravel bed river. *Journal of Geophysical Research: Earth Surface*, 122:528–545.

Gilbert, G. K. and Murphy, E. C. (1914). The transportation of débris by running water. Technical report, U.S. Geological Survey Professional Paper vol. 86.

Gillespie, D. (1992). *Markov Processes: An Introduction for Physical Scientists.* Academic Press, San Diego.

Golly, A., Turowski, J. M., Badoux, A., and Hovius, N. (2019). Testing models of step formation against observations of channel steps in a steep mountain stream. *Earth Surface Processes and Landforms*, 44(7):1390–1406.

Gomez, B. (1991). Bedload transport. *Earth-Science Reviews*, 31:89–132.

Gomez, B. (2006). The potential rate of bed-load transport. *Proceedings of the National Academy of Sciences*, 103(46):17170–17173.

Gomez, B. and Church, M. (1989). An assessment of bed load sediment transport formulae for gravel bed rivers. *Water Resources Research*, 25:1161–1186.

Gomez, B., Naff, R., and Hubbell, D. (1989). Temporal variations in bedload transport rates associated with the migration of bedforms. *Earth Surface Processes and Landforms*, 14:135–156.

Gomez, B., Soar, P. J., and Downs, P. W. (2022). Good vibrations: Big data impact bedload research. *Earth Surface Processes and Landforms*, 47(1):129–142.

Graf, W. and Altinakar, M. (1993). *Hydraulique fluviale*, volume 2. Presses polytechniques et universitaires romandes, Lausanne.

Grant, G. E. (1994). Hydraulics and sediment transport dynamics controlling step-pool formation in high gradient streams: a flume experiment. In *Dynamics and geomorphology of mountain rivers*, pages 241–250. Springer.

Grant, G. E. (1997). Critical flow constrains flow hydraulics in mobile-bed streams: A new hypothesis. *Water Resources Research*, 33(2):349–358.

Gray, J. R., Laronne, J., and Marr, J. (2010). *Bedload-surrogate monitoring technologies*, volume Scientific Investigations Report 2010–5091. US Department of the Interior, US Geological Survey, Reston, Virginia.

Greated, C., Skyner, D., and Bruce, T. (1992). Particle image velocimetry (piv) in the coastal engineering laboratory. In *Proceedings International Conference Coastal Engineering 1992*, pages 212–225.

Greco, M., Iervolino, M., and Vacca, A. (2018). Analysis of bedform instability with 1-D two-phase morphodynamical models. *Advances in Water Resources*, 120:50–64.

Grimmett, G. and Stirzaker, D. (2008). *Probability and Random Processes*. Oxford University Press, Oxford, 3rd edition edition.

Grinsted, A., Moore, J. C., and Jevrejeva, S. (2004). Application of the cross wavelet transform and wavelet coherence to geophysical time series. *Nonlinear processes in geophysics*, 11(5/6):561–566.

Guala, M., Singh, A., BadHeartBull, N., and Foufoula-Georgiou, E. (2014). Spectral description of migrating bed forms and sediment transport. *Journal of Geophysical Research: Earth Surface*, 119:123–137.

Guo, J. (2015). Sidewall and non-uniformity corrections for flume experiments. *Journal of Hydraulic Research*, 53(2):218–229.

Guo, J. (2017). Exact procedure for einstein–johnson's sidewall correction in open channel flow. *Journal of Hydraulic Engineering*, 143(4):06016027.

Guy, H. P., Simons, D. B., and Richardson, E. V. (1966). *Summary of alluvial channel data from flume experiments, 1956-61*, volume 462. US Government Printing Office.

Hager, W. H. (2005). Du Boys and sediment transport. *Journal of Hydraulic Research*, 43:227–233.

Hamamori, A. (1962). A theoretical investigation on the fluctuations of bed load transport. Technical Report Report R4, Delft Hydraulics Laboratory.

Hassan, M. and Church, M. (1991). Distance of movement of coarse particles in gravel bed streams. *Water Resources Research*, 27:503–511.

Hayashi, T. (1970). Formation of dunes and antidunes in open channels. *Journal of the Hydraulics Division*, ASCE 96 (HY2):357—-366.

Herczynski, R. and Pienkowska, I. (1980). Toward a statistical theory of suspension. *Annual Review of Fluid Mechanics*, 12:237–269.

Bibliography

Heyman, J. (2014). *A study of the spatio-temporal behaviour of bed load transport rate fluctuations.* PhD thesis, École Polytechnique Fédérale de Lausanne.

Heyman, J. (2019). Tractrac: A fast multi-object tracking algorithm for motion estimation. *Computers & Geosciences*, 128:11–18.

Heyman, J., Bohorquez, P., and Ancey, C. (2016). Entrainment, motion, and deposition of coarse particles transported by water over a sloping mobile bed. *Journal of Geophysical Research: Earth Surface*, 121:1931–1952.

Heyman, J., Ma, H., Mettra, F., and Ancey, C. (2014). Spatial correlations in bed load transport: Evidence, importance, and modeling. *Journal of Geophysical Research: Earth Surface*, 119:1751–1767.

Heyman, J., Mettra, F., Ma, H., and Ancey, C. (2013). Statistics of bedload transport over steep slopes: Separation of time scales and collective motion. *Geophysical Research Letters*, 40(1):128–133.

Hino, M. (1968). Equilibrium-range spectra of sand waves formed by flowing water. *Journal of Fluid Mechanics*, 34:565–573.

Huang, L.-H. and Chiang, Y.-L. (2001). The formation of dunes, antidunes, and rapidly damping waves in alluvial channels. *International journal for numerical and analytical methods in geomechanics*, 25(7):675–690.

Hwa, T. and Kardar, M. (1992). Avalanches, hydrodynamics, and discharge events in models of sandpiles. *Phys. Rev. A*, 45:7002–7023.

Inoue, T., Watanabe, Y., Iwasaki, T., and Otsuka, J. (2020). Three-dimensional antidunes coexisting with alternate bars. *Earth Surface Processes and Landforms*, 45(12):2897–2911.

Jackson, R. G. (1975). Hierarchical attributes and a unifying model of bed forms composed of cohesionless material and produced by shearing flow. *Geological Society of America Bulletin*, 86(11):1523–1533.

Jain, S. and Kennedy, J. (1974). The spectral evolution of sedimentary bed forms. *Journal of Fluid Mechanics*, 63:301–314.

Jaqaman, K., Loerke, D., Mettlen, M., Kuwata, H., Grinstein, S., Schmid, S. L., and Danuser, G. (2008). Robust single-particle tracking in live-cell time-lapse sequences. *Nature Methods*, 5(8):695.

Jerolmack, D. J. and Paola, C. (2010). Shredding of environmental signals by sediment transport. *Geophysical Research Letters*, 37:L19401.

Johnson, J. W. (1942). The importance of side-wall correction in bed-load investigation. *Civil Engineering*, 12(6).

Kennedy, J. F. (1961). *Stationary waves and antidunes in alluvial channels.* PhD thesis, California Institute of Technology.

Kennedy, J. F. (1963). The mechanics of dunes and antidunes in erodible-bed channels. *Journal of Fluid mechanics*, 16(4):521–544.

Kennedy, J. F. (1969). The formation of sediment ripples, dunes, and antidunes. *Annual Review of Fluid Mechanics*, 1:147–168.

Kubo, Y. and Yokokawa, M. (2001). *Theoretical study on breaking of waves on antidunes.* Wiley Online Library.

Kuhnle, R. A. and Southard, J. B. (1988). Bed load transport fluctuations in a gravel bed laboratory channel. *Water Resources Research*, 24:247–260.

Lajeunesse, E., Malverti, L., and Charru, F. (2010). Bed load transport in turbulent flow at the grain scale: Experiments and modeling. *Journal of Geophysical Research*, 115:F04001.

Lamb, M., Dietrich, W., and Venditti, J. (2008). Is the critical Shields stress for incipient sediment motion dependent on channel-bed slope? *Journal of Geophysical Research*, 113:F02008.

Lamb, M. P., Brun, F., and Fuller, B. M. (2017). Hydrodynamics of steep streams with planar coarse-grained beds: Turbulence, flow resistance, and implications for sediment transport. *Water Resources Research*, 53(3):2240–2263.

Lavelle, J. W. and Mofjeld, H. O. (1987). Do critical stresses for incipient motion and erosion really exist? *Journal of Hydraulic Engineering*, 113(3):370–385.

Lenzi, M. A. (1999). Morfología y estabilidad de las secuencias en escalones (step pool) en los torrentes alpinos de elevada pendiente. *Ingeniería del agua*, 6(2):151–162.

Lenzi, M. A. (2001). Step–pool evolution in the rio cordon, northeastern italy. *Earth Surface Processes and Landforms*, 26(9):991–1008.

Leopold, L., Bagnold, R., Wolman, M., and Brush, L. (1960). Flow resistance in sinuous or irregular channels. Technical Report Professional Paper 282 D, U.S. Geological Survey.

Lhuillier, D. (1992). Ensemble averaging in slightly non-uniform suspensions. *European Journal of Mechanics B/Fluids*, 6:649–661.

Martin, R., Jerolmack, D., and Schumer, R. (2012). The physical basis for anomalous diffusion in bed load transport. *Journal of Geophysical Research*, 117:F01018.

Mendes, L., Antico, F., Sanches, P., Alegria, F., Aleixo, ., and Ferreira, R. (2016). A particle counting system for calculation of bedload fluxes. *Measurement Science and Technology*, 27(12):125305.

Bibliography

Mettra, F. (2014). *Morphodynamic mechanisms in steep channels: from local processes to large-scale evolution.* PhD thesis, École Polytechnique Fédérale de Lausanne.

Meyer-Peter, E., Favre, H., and Einstein, H. (1934). Neure Versuchsresultate über den Geschiebetrieb. *Schweizerische Bauzeitung*, 113:147–150.

Meyer-Peter, E. and Müller, R. (1948). Formulas for bed load transport. In IAHR, editor, *2nd meeting*, pages 39–64, Stockholm, Sweden.

Milliman, J. D. and Syvitski, J. P. (1992). Geomorphic/tectonic control of sediment discharge to the ocean: the importance of small mountainous rivers. *The journal of Geology*, 100(5):525–544.

Molnar, P., Densmore, A. L., McArdell, B. W., Turowski, J. M., and Burlando, P. (2010). Analysis of changes in the step-pool morphology and channel profile of a steep mountain stream following a large flood. *Geomorphology*, 124(1-2):85–94.

Montgomery, D. R. and Buffington, J. M. (1993). Channel classification, prediction of channel response, and assessment of channel condition. Technical Report Report TFW-SH10-93-002, University of Washington Seattle.

Montgomery, D. R. and Buffington, J. M. (1997). Channel-reach morphology in mountain drainage basins. *Geological Society of America Bulletin*, 109(5):596–611.

Mühlofer, L. (1933). Investigation into suspended load and bedload of the river Inn, near Kirchbichl, Tirol. *Die Wasserwirtsch*, 26:1–6.

Nikora, V. (1984). *The structure of turbulent flow and statistical characterisation of dune-covered river beds (with examples of field studies in rivers Turunchuk, Rioni, and Tsheniscali).* PhD thesis.

Nikora, V., Sukhodolov, A., and Rowinski, P. (1997). Statistical sand wave dynamics in one-directional water flows. *Journal of Fluid Mechanics*, 351:17–39.

Nordin, C. and Algert, J. (1966). Spectral analysis of sand waves. *Journal of Hydraulic Engineering*, 92:95–114.

Núñez-González, F. and Martín-Vide, J. P. (2011). Analysis of antidune migration direction. *Journal of Geophysical Research: Earth Surface*, 116(F2).

Palucis, M. and Lamb, M. (2017). What controls channel form in steep mountain streams? *Geophysical Research Letters*, 44(14):7245–7255.

Palucis, M. C., Ulizio, T. P., Fuller, B., and Lamb, M. P. (2018). Flow resistance, sediment transport, and bedform development in a steep gravel-bedded river flume. *Geomorphology*, 320:111–126.

Paola, C. and Voller, V. R. (2005). A generalized exner equation for sediment mass balance. *Journal of Geophysical Research: Earth Surface*, 110(F4).

Papa, D. (2020). *Morphology and morphodynamics of braided rivers: an experimental investigation.* PhD thesis, École Polytechnique Fédérale de Lausanne.

Parker, G. (1975). Sediment inertia as cause of river antidunes. *Journal of Hydraulic Division*, 101:211–221.

Parker, G. (1976). On the cause and characteristic scales of meandering and braiding in rivers. *Journal of Fluid Mechanics*, 76(3):457–480.

Parker, G., Klingeman, P. C., and McLean, D. G. (1982). Bedload and size distribution in paved gravel-bed streams. *Journal of the Hydraulics Division*, 108:544–571.

Parker, G., Paola, C., and Leclair, S. (2000). Probabilistic Exner sediment continuity equation for mixtures with no active layer. *Journal of Hydraulic Engineering*, 126:818–826.

Pascal, I., Ancey, C., and Bohorquez, P. (2021). The variability of antidune morphodynamics on steep slopes. *Earth Surface Processes and Landforms*, 46(9):1750–1765.

Piton, G. and Recking, A. (2019). Steep bedload-laden flows: Near critical? *Journal of Geophysical Research: Earth Surface*, 124(8):2160–2175.

Radice, A., Malavasi, S., and Ballio, F. (2006). Solid transport measurements through image processing. *Experiments in fluids*, 41(5):721–734.

Recking, A. (2006). *Etude expérimentale de l'influence du tri granulométrique sur le transport solide par charriage.* PhD thesis, Thèse de doctorat Mécanique des Fluides, INSA Lyon.

Recking, A. (2009). Theoretical development on the effects of changing flow hydraulics on incipient bed load motion. *Water Resources Research*, 45:W04401.

Recking, A. (2010). A comparison between flume and field bed load transport data and consequences for surface-based bed load transport prediction. *Water Resources Research*, 46:W03518.

Recking, A. (2012). Influence of sediment supply on mountain streams bedload transport. *Geomorphology*, 175-176:139–150.

Recking, A. (2013a). An analysis of nonlinearity effects on bed load transport prediction. *Journal of Geophysical Research*, 118:20090.

Recking, A. (2013b). Simple method for calculating reach-averaged bed-load transport. *Journal of Hydraulic Engineering*, 139:70–75.

Recking, A., Bacchi, V., Naaim, M., and Frey, P. (2009). Antidunes on steep slopes. *Journal of Geophysical Research*, 114:F04025.

Bibliography

Recking, A., Frey, P., Paquier, A., Belleudy, P., and Champagne, J. (2008). Feedback between bed load transport and flow resistance in gravel and cobble bed rivers. *Water Resources Research*, 44:W05412.

Recking, A., Leduc, P., Liébault, F., and Church, M. (2012a). A field investigation of the influence of sediment supply on step-pool morphology and stability. *Geomorphology*, 139:53–66.

Recking, A., Liébault, F., Peteuil, C., and Jolimet, T. (2012b). Testing bedload transport equations with consideration of time scales. *Earth Surface Processes and Landforms*, 37:774–789.

Redolfi, M. (2021). Free alternate bars in rivers: key physical mechanisms and simple formation criterion. *Water Resources Research*, 57(12):e2021WR030617.

Redolfi, M., Musa, M., and Guala, M. (2021). On steady alternate bars forced by a localized asymmetric drag distribution in erodible channels. *Journal of Fluid Mechanics*, 916.

Reynolds, A. J. (1965). Waves on the erodible bed of an open channel. *Journal of Fluid Mechanics*, 22(1):113–133.

Richardson, E. V., Simons, D. B., and Posakony, G. J. (1961). *Sonic depth sounder for laboratory and field use*, volume Circular 450. United States Geological Survey, Washington.

Richardson, K. and Carling, P. A. (2021). Morphology and origin of alluvial step-pools: A synthesis of experimental and field data from formative flows. *Earth-Science Reviews*, 222:103823.

Rickenmann, D. (2001). Comparison of bed load transport in torrents and gravel bed streams. *Water Resources Research*, 37:3295–3306.

Rickenmann, D. and Koschni, A. (2010). Sediment loads due to fluvial transport and debris flows during the 2005 flood events in switzerland. *Hydrological Processes: An International Journal*, 24(8):993–1007.

Rickenmann, D. and McArdell, B. (2008). Calibration of piezoelectric bedload impact sensors in the pitzbach mountain stream. *Geodinamica Acta*, 21(1-2):35–52.

Rickenmann, D. and Recking, A. (2011). Evaluation of flow resistance in gravel-bed rivers through a large field data set. *Water Resources Research*, 47:W07538.

Rickenmann, D., Turowski, J. M., Fritschi, B., Wyss, C., Laronne, J. B., Barzilai, R., Reid, I., Kreisler, A., Aigner, J., and Seitz, H. (2014). Bedload transport measurements with impact plate geophones: comparison of sensor calibration in different gravel-bed streams. *Earth Surface Processes and Landforms*, 39:928–942.

Roseberry, J., Schmeeckle, M., and Furbish, D. (2012). A probabilistic description of the bed load sediment flux: 2. Particle activity and motions. *Journal of Geophysical Research*, 117:F03032.

Rousseau, G. (2019). *Turbulent Flows over Rough Permeable Beds in Mountain Rivers: Experimental Insights and Modeling.* PhD thesis, École Polytechnique Fédérale de Lausanne.

Rousseau, G. and Ancey, C. (2020). Scanning piv of turbulent flows over and through rough porous beds using refractive index matching. *Experiments in Fluids*, 61(8):1–24.

Rousseau, G., Pascal, I., and Ancey, C. (2020). Modeling turbulent stream flows over rough permeable beds. In *River Flow 2020*, pages 22–30. CRC Press.

Saletti, M., Molnar, P., Zimmermann, A., Hassan, M. A., and Church, M. (2015). Temporal variability and memory in sediment transport in an experimental step-pool channel. *Water Resources Research*, 51:9325–9337.

Schindelin, J., Rueden, C. T., Hiner, M. C., and Eliceiri, K. W. (2015). The imagej ecosystem: An open platform for biomedical image analysis. *Molecular reproduction and development*, 82(7-8):518–529.

Schoklitsch, A. (1914). *Über schleppkraft und geschiebebewegung [Concerning Tractive Force and Bedload Movement].* Engelmann, Lepzig.

Schoklitsch, A. (1934). Der Geschiebetrieb und die Geschiebefracht. *Wasserkraft und Wasserwirtschaft*, 4:1–7.

Seizilles, G., Lajeunesse, E., Devauchelle, O., and Bak, M. (2014). Cross-stream diffusion in bedload transport. *Physics of Fluids*, 26:013302.

Seminara, G. (1998). Stability and morphodynamics. *Meccanica*, 33(1):59–99.

Shaw, J. and Kellerhals, R. (1977). Paleohydraulic interpretation of antidune bedforms with applications to antidunes in gravel. *Journal of Sedimentary Research*, 47(1):257–266.

Shields, A. (1936). Application of similarity principles and turbulence research to bed-load movement. Technical report, California Institute of Technology.

Simons, D. B., Richardson, E. V., and Nordin, C. F. (1965). Bedload equation for ripples and dunes. Technical Report Professional Paper 462 H, U.S. Geological Survey.

Singh, A., Fienberg, K., Jerolmack, D., Marr, J., and Foufoula-Georgiou, E. (2009). Experimental evidence for statistical scaling and intermittency in sediment transport rates. *Journal of Geophysical Research*, 114:2007JF000963.

Singh, A., Lanzoni, S., Wilcock, P. R., and Foufoula-Georgiou, E. (2011). Multiscale statistical characterization of migrating bed forms in gravel and sand bed rivers. *Water Resources Research*, 47:W12526.

Slootman, A. and Cartigny, M. J. (2020). Cyclic steps: Review and aggradation-based classification. *Earth-Science Reviews*, 201:102949.

Bibliography

Smart, G. and Jaeggi, M. (1983). Sedimenttransport in steilen Gerinnen. Technical Report 64, Mitteilungen 64 der Versuchanstalt für Wasserbau, Hydrologie und Glaziologie.

Strom, K., Papanicolaou, A. N., Evangelopoulos, N., and Odeh, M. (2004). Microforms in gravel bed rivers: Formation, disintegration, and effects on bedload transport. *Journal of Hydraulic Engineering*, 130:554–567.

Surell, A. (1841). *Étude sur les torrents des Hautes-Alpes*. Carilian-Goeury et Dalmont, Éditeurs.

Terwisscha van Scheltinga, R. C., Coco, G., and Friedrich, H. (2021). Sediment particle velocity and activity during dune migration. *Water Resources Research*, 57(5):e2020WR029017.

Terwisscha van Scheltinga, R. C., Coco, G., Kleinhans, M. G., and Friedrich, H. (2020). Observations of dune interactions from dems using through-water structure from motion. *Geomorphology*, 359:107126.

Tinevez, J.-Y., Perry, N., Schindelin, J., Hoopes, G. M., Reynolds, G. D., Laplantine, E., Bednarek, S. Y., Shorte, S. L., and Eliceiri, K. W. (2017). TrackMate: An open and extensible platform for single-particle tracking. *Methods*, 115:80–90.

Tinkler, K. J. (1997). Indirect velocity measurement from standing waves in rockbed rivers. *Journal of Hydraulic Engineering*, 123(10):918–921.

Tinkler, K. J. (1998). Critical flow in rockbed streams with estimated values for manning's n-reply. *Geomorphology*, 25(3):283–285.

Torrence, C. and Compo, G. (1998). A practical guide to wavelet analysis, b. am. meteorol. soc., 79, 61–78.

Tsakiris, A., Papanicolaou, A. N., and Lauth, T. (2014). Signature of bedload particle transport mode in the acoustic signal of a geophone. *Journal of Hydraulic Research*, 52:185–204.

Tucker, G. and Bradley, D. (2010). Trouble with diffusion: reassessing hillslope erosion laws with a particle-based model. *Journal of Geophysical Research*, 115:F00A10.

Turowski, J. (2010). Probability distributions of bed load transport rates: A new derivation and comparison with field data. *Water Resources Research*, 46:W08501.

Turowski, J. M. (2011). Probability distributions for bed form-dominated bed load transport: The Hamamori distribution revisited. *Journal of Geophysical Research*, 116(F2):F02017.

Turowski, J. M., Yager, E. M., Badoux, A., Rickenmann, D., and Molnar, P. (2009). The impact of exceptional events on erosion, bedload transport and channel stability in a step-pool channel. *Earth Surface Processes and Landforms*, 34(12):1661–1673.

van der Mark, C., Blom, A., and Hulscher, S. (2008). Quantification of variability in bedform geometry. *Journal of Geophysical Research*, 113:F03020.

Vesipa, R., Camporeale, C., and Ridolfi, L. (2012). A shallow-water theory of river bedforms in supercritical conditions. *Physics of Fluids*, 24:094104.

Vesipa, R., Camporeale, C., and Ridolfi, L. (2017). Effect of sampling time in the laboratory investigation of braided rivers. *Water Resources Research*, 53(6):5184–5197.

Vesipa, R., Camporeale, C., Ridolfi, L., and Chomaz, J.-M. (2014). On the convective-absolute nature of river bedform instabilities. *Physics of Fluids*, 26:124104.

Visconti, F., Stefanon, L., Camporeale, C., Susin, F., Ridolfi, L., and Lanzoni, S. (2012). Bed evolution measurement with flowing water in morphodynamics experiments. *Earth Surface Processes and Landforms*, 37(8):818–827.

Westoby, M. J., Brasington, J., Glasser, N. F., Hambrey, M. J., and Reynolds, J. M. (2012). 'structure-from-motion'photogrammetry: A low-cost, effective tool for geoscience applications. *Geomorphology*, 179:300–314.

Whittaker, J. G. and Jaeggi, M. (1982). Origin of step-pool systems in mountain streams. *Journal of the Hydraulics Division*, 108(6):758–773.

Wilcock, P. (1997a). The components of fractional transport rate. *Water Resources Research*, 33:247–258.

Wilcock, P. (1997b). Entrainment, displacement and transport of tracer gravels. *Earth Surface Processes and Landforms*, 22:1125–1138.

Wilcock, P. R. (1988). Methods for estimating the critical shear stress of individual fractions in mixed-size sediment. *Water Resources Research*, 24(7):1127–1135.

Wong, M. and Parker, G. (2006). Reanalysis and correction of bed-load relation of Meyer-Peter and Müller using their own database. *Journal of Hydraulic Engineering*, 132:1159–1168.

Wong, M., Parker, G., DeVries, P., Brown, T., and Burges, S. (2007). Experiments on dispersion of tracer stones under lower-regime plane-bed equilibrium bed load transport. *Water Resources Research*, 43:W03440.

Wyss, C. R., Rickenmann, D., Fritschi, B., Turowski, J. M., Weitbrecht, V., Travaglini, E., Bardou, E., and Boes, R. M. (2016). Laboratory flume experiments with the Swiss plate geophone bedload monitoring system. Part II: Application to field sites with direct bedload samples. *Water Resources Research*, 52:7760–7778.

Yager, E., Kirchner, J., and Dietrich, W. (2007). Calculating bed load transport in steep boulder bed channels. *Water Resources Research*, 43(7).

Yokokawa, M., Takahashi, Y., Yamamura, H., Kishima, Y., Parker, G., and Izumi, N. (2011). Antidunes and cyclic steps: Relating their features to a suspension index and a velocity coefficient. In *Japan Geoscience Union Meeting 2011*, pages SCG064–14. Japan Geoscience Union.

Bibliography

Zimmermann, A. and Church, M. (2001). Channel morphology, gradient profiles and bed stresses during flood in a step-pool channel. *Geomorphology*, 40:311–327.

Zimmermann, A. E., Church, M., and Hassan, M. A. (2008). Video-based gravel transport measurements with a flume mounted light table. *Earth Surface Processes and Landforms*, 33(14):2285–2296.

Zufferey, M. (2018). Navizence le 2 juillet 2018. https://youtu.be/hDTjCkXrpGA?t=137 Uploaded: 14-08-2018. Accessed: 21-04-2022.

EPFL ENAC IIC LHE
Station 18
Lausanne, Switzerland

IVAN PASCAL

OrcID: 0000-0001-6599-6222
pascivan@gmail.com
+41 77 974 54 01

Education

Ph.D. in Mechanics, École Polytechnique Fédérale de Lausanne (EPFL), Switzerland   (ongoing)
Thesis title: *Experimental study on bedload transport and antidunes: behaviour and interplay in steep turbulent streams.*
Advisor: Prof. Christophe Ancey
Specific field: Fluid Mechanics/Geomorphology

M.Sc. in Environmental Engineering, Politecnico di Torino, Italy   December 2015
Thesis title: *Geophysical and geochemical survey on the southern stretch of the Po River in Turin.*
Advisors: Prof. Luigi Sambuelli, Prof. Adriano Fiorucci

International Summer School "Geo-ecological problems of Preduralie"   1-12 August 2014
Perm State University, Perm, Russia.

B.Sc. in Environmental Engineering, Politecnico di Torino, Italy   December 2013
Thesis title: *Geophysical and geochemical survey on the southern stretch of the Po River in Turin.*
Advisor: Prof. Adriano Fiorucci

Employment history

École Polytechnique Fédérale de Lausanne, Switzerland (EPFL)   June 2017 – Present
Position: Doctoral assistant in Environmental Hydraulics
Advisor: Prof. Christophe Ancey
Responsibilities: Design and operation of experimental setups, analysis of results, writing of articles, supervision of students, field activities (e.g. equipment testing in demanding conditions).

Filters s.r.l, Piscina di Pinerolo, Italy   November 2016 – May 2017
Position: Deputy Document Controller-Technical Department
Responsibilities: Documents editing and control (i.e., maintenance manuals, technical datasheets), CAD design (filters, treatment systems and mechanical elements), analysis of filtration-related issues.

Scuola Italiana Sci Prali, Prali, Italy   January 2013 – March 2017
Position: Cross-country ski instructor

Scientific publications

Scientific publications in indexed journals

1. **Pascal, I.,** Ancey, C. and Bohorquez, P. (2021). **The variability of antidune morphodynamics on steep slopes.** *Earth Surface Processes and Landforms*, 46 (9), 1750-1765.

2. Ancey, C. and **Pascal, I.** (2020). **Estimating mean bedload transport rates and their uncertainty.** *Journal of Geophysical Research: Earth Surface*, 125(7), e2020JF005534.

3. L. Sambuelli, A. Fiorucci, P. Dabove, **I. Pascal**, C. Colombero, C. Comina (2017). **Case History: a 5-km long waterbone geophysical survey along the Po River within the city of Turin (NW Italy).** *Geophysics, 82 (6), B189-B199.* https://doi.org/10.1190/geo2017-0071.1

Conference presentations

1. B. De Graffenried, **I. Pascal**, T. Liardon, C. Ancey (2021). **Analyse de l'évolution morphologique d'une rivière de montagne**. *In: Webinaire "Transport sédimentaire: rivières et barrages réservoirs" CFBR (11.03.2021).*

2. **I. Pascal**, C. Ancey, P. Bohorquez (2019). **Antidunes on steep slopes: variability of wave geometry and migration celerity.** *In: RCEM 2019, 11th Symposium on River Coastal and Estuarine Morphodynamics, Auckland (NZ).*

3. B. Dhont, **I. Pascal,** P. Bohorquez & C. Ancey (2018). **How bar generate sediment transport pulses in gravel-bed channels**. *In: 5th IAHR Europe Congress, Trento (IT).*

Conference papers

1. G. Rousseau, **I. Pascal**, C. Ancey (2020). **Modeling turbulent stream flows over rough permeable beds**. *In River Flow 2020. CRC Press.*

2. L. Sambuelli**,** C. Comina, A. Fiorucci, P. Dabove, **I. Pascal**, C. Colombero (2015): **A 5-km long waterborne CVES survey on the Po River in the town of Turin: preliminary results**. *In : 34° Convegno Nazionale Gruppo Nazionale di Geofisica della Terra Solida, Trieste, Volume : 3.*

Teaching experiences

Teaching assistant EPFL, Switzerland   Summer 2017 - Spring 2021

Fluid mechanics, ~60 students, 5 ECTS. Exercise assistance and exams correction.   4 semesters
Hydrological risks, ~20 students, 3 ECTS. Exercise assistance and exams correction.   4 semesters

Peer reviewing

Article reviewing
Computer & Geoscience

Personal skills

Languages Italian (native speaker), English (C1, IELTS Band Score 6.5), French (C1)
Programming languages Matlab, Latex, C++, Python (basics)
Software TrackMate-ImageJ, QGIS, Pix4Dmapper, GCD, Photoscan, Fudaa LS-PIV, ArcMap, AutoCAD, ENVI, HEC-RAS, RES2DINV, Office
Operating systems Windows, macOS
Geomatics: Experience with GPS/GNSS systems also combined with RTK
Field skills: Survey experience in rivers and mountain areas (also in snowy conditions), UAV surveys, equipment testing, installation and running of discharge measurements setups (e.g. ADCP, LS-PIV), grain size distribution data collection.

Others

Professional licenses
Licensed Professional Engineer (Italy)
Session: July-September 2016
Licensed Cross-country Ski Instructor (Italy)
Session: Spring 2012

Volunteer experience
Volunteer of the National Mountain Rescue (CNSAS)   January 2014 - P r e s e n t
CNSAS Prali Val Germanasca, Prali, Italy